

# **Exciton Dynamics in 2D Organic Assemblies for Realization of Next-generation Optoelectronic Devices**

**Thèse N° 9486**

Présentée le 26 avril 2019

à la Faculté des sciences et techniques de l'ingénieur  
Unité de rattachement pour scientifiques IMX  
Programme doctoral en science et génie des matériaux

pour l'obtention du grade de Docteur ès Sciences

par

**Surendra Babu ANANTHARAMAN**

Acceptée sur proposition du jury

Dr Y. Leterrier, président du jury  
Prof. F. Nüesch, Dr J. Heier, directeurs de thèse  
Prof. J. Rabe, rapporteur  
Prof. F. Castro, rapporteur  
Prof. M. Graetzel, rapporteur

2019



Take up one idea.  
Make that one idea your life -  
think of it, dream of it, live on that idea.  
Let the brain, muscles, nerves, every part of your body, be full of that idea,  
and just leave every other idea alone.  
This is the way to success.

— *Swami Vivekananda*  
(Indian Monk, 1863-1902)

To my parents...





# Acknowledgements

First of all, my sincere gratitude to my thesis director, Frank Nüesch, for accepting my candidacy and supporting me to pursue my Ph.D research in his lab. I thank him for being kind and educating me on the fundamentals of exciton dynamics and photophysics in J-aggregates with greater clarity and thought provoking questions. These experiences motivated me to be a teaching assistant for his course on Modern Photovoltaics Technologies. It needs to be mentioned here, the freedom of research, flexibility, quest for in-depth work and continuous support from my thesis co-director, Jakob Heier has brought a successful completion to the thesis work. Special thanks to Frank and Jakob for showing their continuous support towards me to be a delegate in the President's Council for Student Advisors (PCSA) and represent EPFL in The American Ceramics Society.

The major and most exciting part of my journey during my Ph.D goes along with the “dream team – The IBMers” – Thilo Stöferle and Rainer Mahrt. I completely loved all the discussions during our meetings, paying attention to details while disseminating the knowledge, brainstorming ideas, geek jokes and the humor, all these memories makes a very special moments for me to cherish any day in my life. Thank you for being so nice with me. Special mention to Thilo for the confidence and his courage to leave no stone unturned to understand the exciton dynamics in the J-aggregates, made me to enjoy the extra mile effortlessly even in difficult times.

Moving on to the fabrication of narrowband photodetectors, the immense support of Roland, with his up to date knowledge in this field, fruitful collaboration with Karen and Matthias was helpful to successfully realize a J-aggregate photodetector. Many thanks go to Agnes for current noise measurements and Erwin for ellipsometry measurements. Also, I gratefully acknowledge Mohammed for giving introduction to thermal evaporator and Anand for inkjet printing.

I am very thankful for the timely help from Joachim Kohlbrecher, PSI for the small-angle neutron scattering studies, which provided detailed insights in the bright J-aggregates. Many thanks to Jay for showing his interest in coordinating with my experiments as a part of his internship work. I thank my colleagues at ETH Zürich - Gabriele Raino, Sergii Yakunin and Maksym Kovalenko, for extending their support with TRPL, low temperature PL and quantum yield measurements.

Special thanks to Daniel and Dieter Schlüter, ETH Zürich for not only providing the dendronized polymers (DPs) but also sharing a lot of information behind the polymer science on monolayer formation, stability of DPs and for interesting discussions. Many thanks to Amin

## Acknowledgements

---

for the successful collaboration which was helpful in using X-rays for characterizing polymers and to understand the self-assemble of cyanine dye molecules.

The work in this thesis will not be made in time without the organization support from Beatrice and Isabella. Furthermore, I appreciate their efforts for providing me a conducive and silent workplace and making my office work to be more efficient. Thanks to Dani for allowing me to use the mechanical shaker (as he calls, its shaking!) which facilitate the growth of thin films. I thank Ullrich Müller for giving an introduction and training to atomic force microscope which was extensively used in this study.

I gratefully acknowledge the JSPS fellowship to visit Takeshi Shimomura lab, TUAT, to learn nanoscale electrode fabrication. Thanks to Shinji Kanehasi and Naoki Sugihara for taking care of me during my stay in Japan. Also, I met lot of friends – Nishino, Ito, Goto, Yagi. It was so much fun to spend time with you guys to enjoy the work in the lab and life outside lab.

As our laboratory name stands for FUNctional polymer, one cannot miss having fun while going for lunch, coffee breaks, nitrogen ice creams, barbeques and more. I thank my friends and colleagues – Mohammed, Elena, Jose, Yauhen, Leila, Alessandra, Simon, Song, Philip, Sina, Lei, Anna, Nicolas, Karen, Matthias, Sandra and Donatas. It was so much fun working with you guys. Thanks to Elena for her kindness to invite for casual dinner and lot of tips for cooking meals in short time. Also, thanks to Jose for keeping your doors open to help me when I am in need.

The motivation for Monday mornings would have not been possible without the Indian friends outside lab. Thanks goes to Alok, Gitika, Jagan, Sudheer, Valliyappa, Manoj, Tutu, Prashant, Subhu and Piyush for being extremely fun people, organizing get together events, hiking and outdoor activities. I thank Sakshi and Anand for all the good times we had during dinner with nice discussions and those kept me out of homesick. I appreciate your kindness towards me for making a nice evening after a long day in the lab.

My highest appreciation is addressed to my parents – Selvi and Anantharaman, for going through a lot of hardship to raise me and supporting my decisions in life. I am indebted to your love and I owe you both a lot. My two little precious brothers – Ajay and Asik, for bringing smile on my face with their playfulness and naughtiness. To my uncle, Asokan for his unconditional love, support and advise at several occasions. I was late with my graduation to make you proud and I dedicate this work to you.

My special thanks to my girlfriend – Archana for her love, motivation and being a pillar of support in all my endeavors. You have seen my hidden capabilities and eagerness to pursue higher studies. Thank you for being so supportive, a best friend to share my thoughts and a strong personality in a distant land to pursue your dream. I can't thank you enough for all your support since you knew me, and I owe you a lot for that. I can't wait to see your successful graduation.

Last, but not least, I thank all my teachers from the bottom of my heart who taught me to think, to dream and achieve big things in life.

*Düßeldorf, 15 February 2019*

*Surendra Babu Anantharaman*

# Abstract

Supramolecular assemblies of cyanine dye molecules formed by weak van der Waals forces have gained immense attention for their distinct optical properties (high extinction coefficient, narrow absorption and photoluminescence line-width and small Stokes shift) compared to their monomer counterparts. Strong light-matter interaction in the J-aggregates causes coherent exciton migration and high color purity emission. This motivates to fabricate J-aggregate thin films for different optoelectronic devices such as solar cells, where J-aggregates serve as exciton transport channels, organic light emitting diodes (OLEDs) and polariton lasers. Exciton migration and photoluminescence quantum yield (PLQY) of the J-aggregates in thin films dictate the efficiency of energy harvesting and light emitting devices, respectively. The main focus of this thesis is the development of a new J-aggregate growth route which favors the formation of large, coherent domains of 2D J-aggregate thin films and to investigate the exciton dynamics. Furthermore, non-radiative decay channels suppressing the PLQY of J-aggregates in thin film and in solution were identified.

The coherent crystalline domain size in thin films is typically limited to nanoscale length because dye molecules spontaneously self-assemble already in solution. This can be overcome by maintaining equilibrium between monomers and the critical nucleus of a J-aggregate in solution. This approach is shown here as a successful route to achieve large coherent domains on a functionalized substrate. The growth model was further confirmed with small-angle x-ray scattering (SAXS) studies. Using time-resolved photoluminescence (TRPL) spectroscopy, non-radiative decay channels limiting the exciton migration were identified. The results suggest that the increase in domain size and order is directly proportional to the increased radiative decay of the excitons. Furthermore, the PLQY of J-aggregates in water at room temperature is typically ~5%. Upon addition of alkylamine, the quantum yield was drastically improved while maintaining line-width and peak position. Using small-angle neutron scattering (SANS), a two-phase region was identified in the water-dye-alkylamine ternary phase diagram in which high PLQY J-aggregates form. From TRPL studies, an increase in radiative lifetime is in agreement with the increase in PLQY.

As an application, ultra-narrowband photodetectors were explored owing to the narrow line-width of J-aggregate absorption. The concept proved advantageous over other strategies for narrowing the response width, with competing figure of merits. Realization of an inkjet printed prototype with higher frequency response compared to spin-coated devices highlights

## Abstract

---

their potential for industrial applications.

Excitonic channels using J-aggregate nanowires were formed by complexing J-aggregates with dendronized polymers. SAXS studies revealed a core-shell configuration of the DP-J-aggregate hybrid structure. A correlation between polymer conformation and J-aggregates allowed to assemble J-aggregate nanowires as thin films.

Centrosymmetric cyanine dimers are known for their non-luminescent nature. Twisted dimer packing of dye molecules in a polymer matrix are confirmed from circular dichroism spectroscopy studies. This explains a strongly red-shifted photoluminescence with high quantum yield in the thin film.

**Keywords:** J-aggregates, exciton-charge quenching, narrowband organic photodetectors, J-aggregate nanowires, high PLQY.

# Zusammenfassung

Supra-molekulare Anordnungen von Cyanine Molekülen die sich durch schwache van der Waals Wechselwirkungen ausbilden, gewannen wegen Ihrer ausserordentlichen optischen Eigenschaften (hoher Extinktionskoeffizient, schmale Absorptions- und Photolumineszenzlinienbreite und geringe Stokes Verschiebung) grosse Aufmerksamkeit. Eine starke Wechselwirkung zwischen Licht und Materie in diesen J-aggregaten bewirkt kohärente Exzitonmigration und hohe Farbreinheit der Ausstrahlungscharakteristik.

Das ist Motivation genug um J-aggregat Dünnschichten herzustellen, welche in verschiedensten opto-elektronischen Bauteilen eingesetzt werden können, sei es als Exzitonentransportkanal in Solarzellen, in organischen Lichtemittierdioden oder Polaritonlasern. Exzitonmigration und die Quantenausbeute der Photolumineszenz (PLQY) von J-aggregaten in dünnen Schichten bestimmen die Effizienz von Energiegewinnungs- und Lichtemittierbauteilen.

Der Schwerpunkt dieser Doktorarbeit liegt in der Entwicklung einer neuen Wachstumsroute für J-aggregate, in welcher sich grosse, kohärente 2-dimensionale Domänen ausbilden, und der Untersuchung der Dynamik der Exzitonen. Nicht-radiative Zerfallsrouten, welche eine hohe Quantenausbeute in Schichten und der Lösung verhindern, wurden aufgefunden.

Die Grösse der kohärenten Domänen in dünnen Schichten ist typischerweise auf Nanometerdimensionen beschränkt, da die Moleküle schon in Lösung spontan aggregieren. Dies kann überwunden werden, wenn man in der Lösung ein Gleichgewicht zwischen Monomeren und kritischen Keimen von J-aggregaten etabliert. Wir zeigen hier dass mit diesem Ansatz grosse kohärente Domänen erfolgreich hergestellt werden können. Dieses Wachstumsmodell wurde mit Kleinwinkelstreuungsmessungen (SAXS) bestätigt. Mit zeitaufgelöster Photolumineszenzspektroskopie (TRPL) konnten nicht-radiative Zerfallskanäle, welche Exzitonmigration begrenzen, bestimmt werden. Diese Ergebnisse legen nahe, dass Domänengrösse und Ordnung direkt mit dem Strahlungszerrfall von Exzitonen zusammenhängen. Typische Werte für die PLQY von J-aggregaten in Wasser bei Raumtemperatur sind um die 5%. Durch das Hinzufügen von Alkylaminen konnte die Quanteneffizienz erheblich gesteigert werden, während Linienbreite und Position des Maximums erhalten blieben. Mit Kleinwinkel-Neutronenstreuungen (SANS) konnte im Wasser-Farbstoff-Alkylamine Phasendiagramm eine Region bestimmt werden in welcher sich J-aggregate mit hoher PLQY ausbilden. TRPL Studien bestätigen, dass ein Anstieg der radiativen Lebensdauer mit Erhöhung der PLQY zusammenhängen.

## Zusammenfassung

---

Als Anwendungsbeispiel untersuchten wir Photodetektoren mit ultra-dünner Bandbreite basierend auf J-aggregaten. Das Konzept erwies sich als vorteilhaft gegenüber anderen Methoden die Bandbreite zu begrenzen. Die Verwirklichung eines Prototyps welcher mit einem Tintenstrahldrucker hergestellt wurde zeigt das Potential dieses Bauteiles für industrielle Fertigung.

Exzitonen-Kanäle aus J-aggregate-Nanodrähten wurden durch Bildung eines Komplexes mit einem dendritischem Polymers gebildet. SAXS enthüllte eine Kern-Schalen Struktur.

Zentrosymmetrische Cyanin Dimere zeichnen sich durch ihren nicht-lumineszierenden Charakter aus. Eine starke rot-verschobene Lumineszenz des Cyanin Farbstoffs konnte durch gegeneinander verdrillte Farbstoffmoleküle erklärt werden. Der Nachweis wurde mit Cirkulardichrosimus Messungen erbracht.

**Schlüsselwörter:** J-aggregat, Exziton-Ladungs Quenching, schmall-bandige Photodetektoren, J-aggregat-Nanodrähte, hohe PLQY.

# Contents

<b>Acknowledgements</b>	<b>i</b>
<b>Abstract (English/Deutsch)</b>	<b>iii</b>
<b>List of Figures</b>	<b>xi</b>
<b>List of Tables</b>	<b>xvii</b>
<b>1 Introduction</b>	<b>1</b>
1.1 Advancing from Electronic Age to Excitonic Age . . . . .	1
1.2 Organic Semiconductors . . . . .	2
1.3 Electronic Properties in Organic Semiconductors . . . . .	2
1.4 Förster and Dexter Type Energy Transfer . . . . .	11
1.5 Supramolecular Assemblies in Cyanine Dyes . . . . .	13
1.6 Corelation between Structural Packing and Optical Properties in J-aggregates .	15
1.6.1 1D J-aggregates . . . . .	16
1.6.2 2D J-aggregates . . . . .	18
1.7 Growth Model of Thin Films . . . . .	20
1.8 Exciton Dynamics in J-aggregates . . . . .	22
1.9 Perspective on Exciton Migration in J-aggregates . . . . .	23
1.10 Recent Applications of J-aggregates in Optoelectronic Devices . . . . .	24
1.10.1 Narrowband photodetectors . . . . .	24
1.10.2 Polariton lasers . . . . .	29
1.10.3 Excitonic channels and PL enhancers . . . . .	30
1.11 Aim of the Thesis . . . . .	31
<b>2 Exciton Dynamics and Effects of Structural Order in Morphology-controlled J-aggregate Assemblies</b>	<b>41</b>
2.1 Introduction . . . . .	42
2.2 Results and Discussion . . . . .	43
2.2.1 Growth mechanism of J-aggregates with different morphologies in solid-state films . . . . .	43
2.2.2 Optical properties of platelet and lamellar films . . . . .	46
2.2.3 Exciton dynamics in platelet and lamellar films at low temperature (6 K) .	48

2.3	Conclusion . . . . .	53
2.4	Experimental Section . . . . .	53
2.5	Supporting Information . . . . .	60
<b>3</b>	<b>Unprecedented Enhancement of J-aggregate Photoluminescence Quantum Yield at Room Temperature by Suppressing Non-radiative Decay Channels</b>	<b>69</b>
3.1	Introduction . . . . .	70
3.2	Results and Discussion . . . . .	71
3.2.1	Optical properties of J-aggregate in the solution . . . . .	71
3.2.2	Structural properties of J-aggregate in the solution . . . . .	77
3.3	Conclusion . . . . .	83
3.4	Experimental Section . . . . .	83
3.5	Supporting Information . . . . .	87
<b>4</b>	<b>Filter-free Ultra-narrowband Organic Photodetectors with Inkjet Printing Compatibility</b>	<b>91</b>
4.1	Introduction . . . . .	92
4.2	Results and Discussion . . . . .	94
4.2.1	Solvent engineering approach for J-aggregate thin films . . . . .	94
4.2.2	Narrowband photodetectors . . . . .	97
4.2.3	Current noise . . . . .	100
4.2.4	Response time and -3dB values . . . . .	101
4.2.5	Demonstration of inkjet printed narrowband photodetectors . . . . .	104
4.3	Conclusion . . . . .	106
4.4	Experimental Section . . . . .	106
4.5	Supporting Information . . . . .	112
<b>5</b>	<b>Excitonic Channels from Bio-inspired Templated Supramolecular Assembly of J-aggregate Nanowires</b>	<b>119</b>
5.1	Introduction . . . . .	120
5.2	Results and Discussion . . . . .	123
5.2.1	Dye aggregation in solution . . . . .	123
5.2.2	Conformation of different generation DPs on glass substrates and anchoring J-aggregates . . . . .	123
5.2.3	Complexation of J-aggregate and dendronized polymers in solution studied by SAXS . . . . .	127
5.2.4	Layer-by-layer deposition of DP/J-aggregate nanowires . . . . .	130
5.3	Conclusion . . . . .	133
5.4	Experimental Section . . . . .	134
5.5	Supporting Information . . . . .	140



<b>6 Strongly Red-shifted Photoluminescence Band Induced by Molecular Twisting in Cyanine (Cy3) Dye Films</b>	<b>149</b>
6.1 Introduction . . . . .	150
6.2 Results and Discussion . . . . .	151
6.3 Conclusion . . . . .	160
6.4 Experimental Section . . . . .	160
6.5 Supporting Information . . . . .	165
<b>7 Conclusion and Outlook</b>	<b>171</b>
<b>Curriculum Vitæ</b>	<b>175</b>



# List of Figures

1.1	Atomic orbitals of carbon in ground state (a) along with possible "new" hybrid orbitals by linear combination of s- and p- orbitals like (b) $2sp^3$ (c) $2sp^2$ and (d) $2sp$ . The hybridized and remaining $p_z$ orbitals are marked only in (d). . . . .	3
1.2	Molecular orbital of ethene shown for C=C bond without carbon-hydrogen bonds for clarity. . . . .	6
1.3	Two dipoles with dipole moment - $\vec{\mu}_1$ and $\vec{\mu}_2$ arranged randomly (a) and with head-to-tail arrangement (b) separated by a distance r. . . . .	7
1.4	Electronic coupling between two identical molecules ( $M_1$ and $M_2$ ) showing energy splitting for H-Dimer and J-Dimer . . . . .	9
1.5	Vibronic excitons in H and J-aggregates showing the influence of optically allowed transitions (bold lines) in the absorption spectrum. . . . .	10
1.6	Absorption and fluorescence spectrum of donor and acceptor (a). Non-radiative energy transport - Förster (b) and Dexter (c) and radiative energy transfer (d). . . . .	13
1.7	Typical cyanine dye with hydrophobic edges shown in red and hydrophilic edges shown in blue (a). Illustrating delocalisation of $\pi$ -electron along the polymethine chain (b). . . . .	14
1.8	Example of three cyanine dyes with increasing chain length for (a) $n = 1$ , (b) $n = 2$ , and (c) $n = 3$ . (d) Attenuance of the monomer (in dotted lines) and their corresponding J-aggregate (filled) solution spectrum are shown in energy scale. . . . .	15
1.9	Chemical structure of the C8S3 dye showing hydrophilic and hydrophobic edges (a). Schematic of double walled tubular J-aggregate showing inner cylinder and outer cylinder with a cryo-TEM image (b). The absorption spectrum of J-aggregates and its corresponding monomer (c). . . . .	17
1.10	Schematic of complete double wall nanotube (a), Oxidized outer wall (b), Mutual arrangement of dye molecules in the inner wall (c) and extension of this model to outer wall (d). . . . .	17
1.11	Schematic of Langmuir-Blodgett (LB) growth technique showing the set-up (a) used to form Langmuir films (b) and then transferred on glass substrates (c). . . . .	19
1.12	Schematic of Layer-by-Layer (LBL) deposition technique showing the functionalization of glass substrate with electrolyte (cationic or anionic)(a) followed by deposition of cyanine dyes (anionic or cationic)(b), respectively. . . . .	20
1.13	Starting with a glass substrate (a) a schematic of three distinct growth models - Volmer-Weber (b), Stranski-Krastanov (c) and Frank-van der Merwe model (d) . . . . .	21

## List of Figures

---

1.14 Visualization of photoluminescence <i>versus</i> laser fluence trends showing constant emission and exciton-exciton annihilation (EEA) (a). Formation of bi-exciton showing exciton quenching during annihilation (b). . . . .	23
1.15 Working principle of Conventional and Charge-Collection Narrowing (CCN) OPDs	25
1.16 Illustration of response time calculation from the light pulse . . . . .	27
1.17 Schematic showing different jetting types in ink-jet printing . . . . .	28
1.18 Hybrid microcavity LED structure showing bottom and top DBR with J-aggregates and inorganic (GaN) quantum wells and electrical contacts (a). Reflectivity and PL spectra recorded for GaN and J-aggregates at 25 K (b). . . . .	30
1.19 Absorption spectra for J-aggregate (LHNs) coupled with inorganic quantum dot (PbS <sub>980</sub> ) in a sucrose-trehalose (sugar) matrix (shown in purple), in comparison with individual PbS <sub>980</sub> (black line) and LHNs (blue line) (a). PL spectra of LHNs coupled with PbS <sub>980</sub> and PbS <sub>980</sub> control sample excited at 532 nm; inset: normalized PL enhancement of QDs over time. The samples were kept under room light, and the PL enhancement was measured after 12 days. . . . .	31
2.1 (a) Chemical structure of the <b>TDBC</b> dye. (b) Schematic showing methodologies to control J-aggregates growth following Volmer-Weber and Stranski-Krastanov growth models. (c) Attenuance of dye solution by varying the monomer and J-aggregate phase content leads to different types of J-aggregate morphologies like (d) platelets, (e) quasi-epitaxial crystals and (f) lamellar on glass substrates functionalized with PAMAM, as observed with scanning probe microscopy. Presence of mixed leaf-like and stripe J-aggregates in lamellar films are marked with white rings in (f). . . . .	45
2.2 (a) Attenuance, absorbance and steady-state photoluminescence of monomers in methanolic solution, platelets and lamellar film measured at 300 K. Photoluminescence signals of the thin films are recorded with an excitation wavelength of 530 nm (450 nm for monomers) in an integrating sphere. (b) Relative quantum yield for the platelets and lamellar films from 6 to 100 K, normalized to the quantum yield of platelets films at 6 K, with pulsed excitation wavelength at 400 nm and 80 MHz repetition rate. The corresponding full-width at half-maximum (FWHM) of the photoluminescence of the thin films, as shown in Table S2.1, are plotted as a function of temperature. The error bars from the fit are smaller than the symbol size. . . . .	47

2.3	(a) Spectrally- and temporally-integrated photoluminescence acquired with continuous-wave and ultrafast excitation at 400 nm and 550 nm for platelets and lamellar films at 6 K. (b) Time-resolved spectrally-integrated dynamics (fluence of $78 \text{ nJ cm}^{-2}$ ) with the lines representing the fits of an exponential decay to the data between 0 and 50 ps. Cross-sections plotted for small time intervals (4 ps bin size) from the streak camera image recorded with an excitation wavelength of 400 nm for platelets (c) and lamellar films (d). (e) Transient red-shift in peak center energies from (c) and (d) with error bars for the peak energies corresponding to the time. . . . .	49
2.4	Schematic representation of exciton dynamics in lamellar (a) and platelet (b) films when excited at 550 nm. In comparison, charge generation in the bulk films for lamellar (c) and platelets (d) leads to exciton quenching when excited at 400 nm. ① - exciton diffusion and radiative recombination, ② - non-radiative recombination at disordered sites, ③ - charge-carrier generation and ④ - exciton-charge quenching in the bulk along with ②. . . . .	52
3.1	(a) Chemical structure of the <b>TDBC</b> dye. (b) Attenuance of the monomer form of <b>TDBC</b> dye in methanol, and J-aggregates formed in water and ethylamine-water (1:1 vol%, <b>EA:Water</b> ) with its corresponding photoluminescence (PL). The PL for J-aggregate in water is scaled 10 times. (c) Dye solution in water and ethylamine-water ( <b>EA:Water</b> ) mixture under ambient light (top left). Photoluminescence from the samples when exposed to UV light (top right) and 532 nm laser (bottom). (d) Normalized attenuance, photoluminescence excitation spectra (PLE) and PL for J-aggregates in ethylamine-water solution. . . . .	72
3.2	Absolute photoluminescence quantum yield for J-aggregates measured in different solvents – water, 0.1 M NaOH, ethanolamine-water (1:1, <b>EtOHAm:Water</b> ), ethanolamine ( <b>EtOHAm</b> ) and ethylamine-water ( <b>EA:Water</b> ). Self-absorption corrected PLQY for J-aggregates in water and ethylamine-water ( <b>EA:Water</b> ) system are shown as circles. . . . .	73
3.3	Time-resolved photoluminescence (TRPL) studies for the J-aggregate emission recorded for the dyes dispersed in water (a) and in ethylamine:water ( <b>EA:Water</b> ) (b) at different excitation power as mentioned in the labels. (c) TRPL for J-aggregates formed at different dye concentration in ethylamine solution ( <b>EA:Water</b> ) with excitation power $\sim 0.41 \mu\text{W}$ compared with the 1 mM dye solution in water (excitation power $\sim 0.82 \mu\text{W}$ ). . . . .	74
3.4	(a) SANS spectra of blends of $\text{D}_2\text{O}$ and HA with different volume ratios of $\text{D}_2\text{O}$ to HA. (b) Scattering invariant ( $Q^*$ ) and characteristic dimension ( $d_0$ ) for blends of $\text{D}_2\text{O}$ and HA. From the two-phase region, only the HA-rich phase is shown. (c) Schematic of morphology in the blended phases from the 1-phase region (left) and HA-rich phase from the 2-phase region (right). . . . .	79
3.5	SANS spectra of the J-aggregates in different solutions as mentioned in the labels. 80	

## List of Figures

3.6	Overlapping optical phase content (monomer, high PLQY J-aggregates, pristine J-aggregates) with phase boundaries (lines) observed from SANS studies in water-hexylamine-dye ternary phase diagram. . . . .	82
4.1	Chemical structure of the (a) <b>J580</b> , (b) <b>J780</b> and (c) <b>J980</b> dye. (d) Comparison of attenuance peaks of aggregate thin films when suspended aggregates are directly deposited from solution (solid line) or obtained in-situ during spin coating from a monomer solution (dotted line). . . . .	95
4.2	Difference in film morphology of <b>J780</b> dye aggregates fabricated by the direct method (a) or in-situ method (b) from TFE solution on ITO/ TiO <sub>2</sub> substrates. . . . .	96
4.3	(a) Device structure of narrowband photodetectors with J-aggregates as active layer investigated in this study. The device active area is 3.1 mm <sup>2</sup> . (b) Energy level diagram of the device for <b>J580</b> (optical gap) with TAPC layer. Current density – voltage characteristics for the <b>J580</b> (c) <b>J580</b> with TAPC layer (d), <b>J780</b> (e) and <b>J980</b> (f) devices. The device structure is ITO/TiO <sub>2</sub> /J-aggregate layer ( <b>J580</b> , or <b>J580</b> +TAPC (50 nm) or <b>J780</b> or <b>J980</b> )/MoO <sub>3</sub> (10 nm)/Ag (12 nm). The integrated current density (ICD) values calculated from the external quantum efficiency (shown later) are marked with filled circles over the J-V curves. . . . .	98
4.4	External quantum efficiency (EQE) and responsivity (shown in open circles) of photodetectors showing wavelength-selectivity at 586 nm (a - without TAPC, b - with TAPC), 780 nm (c) and 980 nm (d) for <b>J580</b> , <b>J780</b> and <b>J980</b> respectively, measured at an interval of 2 nm at different bias voltage. . . . .	99
4.5	Noise power spectral density recorded as a function of frequency for <b>J580</b> (a), <b>J580</b> with TAPC (b), <b>J780</b> (c) and <b>J980</b> (d) devices. The spectra were obtained at the indicated DC bias levels. . . . .	100
4.6	Temporal response of the <b>J780</b> device illuminated with 10 kHz light pulse and measured at different bias voltage (a). Summary of -3dB values for all devices measured without and with preconditioning (b). . . . .	102
4.7	Schematic of inkjet printed device (cross-section) structure showing printed layers (c-TiO <sub>2</sub> , m-TiO <sub>2</sub> and J-aggregate as active layer) followed by vacuum processed layers (a). Current density-voltage curves showing an increase in charge extraction upon addition of m-TiO <sub>2</sub> layer (b). EQE for inkjet printed device structure with J-aggregate as active layer on c-TiO <sub>2</sub> (c) and c-TiO <sub>2</sub> /m-TiO <sub>2</sub> (d). -3dB value recorded for inkjet printed device (IJP J580) with c-TiO <sub>2</sub> /m-TiO <sub>2</sub> at different bias voltage (e) and the values are shown in comparison with spin-coated device (without m-TiO <sub>2</sub> layer) (f). . . . .	105
5.1	Chemical structures of the DPs featured in this thesis (DP1, DP2, DP3 and DP4) as shown in (a-d) and the cyanine dye <b>J560</b> used for J-aggregate formation (e). . . . .	122
5.2	Attenuance (normalized) for <b>J560</b> dye dissolved in methanol, water and 100 mM acetate buffer. . . . .	124
5.3	AFM height images (tapping mode) of DPs – (a) DP1, (b) DP2, (c) DP3 and (d) DP4 deposited on glass. . . . .	125

5.4	AFM topographies (tapping mode) of J-aggregates deposited on DP2-functionalized glass substrates from (a) 0.2 mM, (b) 0.6 mM and (c) 2 mM solutions of J560 in 100 mM acetate buffer (pH $\approx$ 4).	126
5.5	Attenuance of monomers and J-aggregates deposited on DP functionalized glass substrates from $c_{J560} = 0.6$ mM dye solution in 100 mM acetate buffer.	127
5.6	(a) The experimental $I(q)$ profiles of DP2 and its mixture with <b>J560</b> dye shown in dots, and their corresponding theoretical curves shown as solid lines calculated from the IFT analysis. For better representation, the curves are shifted vertically. (b) $p(r)$ functions corresponding to the theoretical curves shown (a). (c) $I \times q$ <i>versus</i> $q$ curves for DP2 and polymer-dye mixtures representing cross-section scattering intensities. These curves analyzed by IFT to obtain detailed cross sectional information. For better representation, the curves are shifted vertically. (d) $p(r)$ functions, obtained by IFT assuming cylindrical symmetry for the $I \times q$ shown in (c).	128
5.7	(a) The experimental $I(q)$ profiles of DP4 and its mixture with <b>J560</b> dye shown in dots, and their corresponding theoretical curves shown as solid lines calculated from the IFT analysis. For better representation, the curves are shifted vertically. (b) $p(r)$ functions corresponding to the theoretical curves shown (a). (c) $I \times q$ <i>versus</i> $q$ curves for DP2 and polymer-dye mixtures representing cross-section scattering intensities. These curves analyzed by IFT to obtain detailed cross sectional information. For better representation, the curves are shifted vertically. (d) $p(r)$ functions, obtained by IFT assuming cylindrical symmetry for the $I \times q$ shown in (c).	131
5.8	Elongated DP2 (a) and DP4 (b) deposited from complexed DP and J-aggregate solution ( $c_{J560} = 0.6$ mM dye in acetate buffer) on their corresponding DP pre-functionalized glass substrates. For DP4, <i>super-structures</i> were observed with local ordering when they are covered with dye molecules as shown in (c).	132
5.9	Attenuance for DP4-premixed with dye solution ( $c_{J560} = 0.6$ mM) and deposited on DP4 functionalized glass substrates.	133
6.1	Attenuance and PL spectra for Cy3-T in CB solution and spin-coated film (a). PL spectra from cyanine films with different counterions (b). Excitation spectra for Cy3-T films when emission was monitored at the monomer (587 nm) and dimer (679 nm) peak (c).	152
6.2	Temperature-dependent fluorescence studies of the cyanine films (Cy3-T) recorded from 92 K to room temperature on cooling (a, b) and on heating (c, d, e).	155
6.3	Emission spectra for different concentrations of Cy3-P dye dispersed in a PVME matrix (a). The dimer and monomer emission are normalized with the dye concentration in the PVME matrix (b). Circular dichroism (CD) spectra for different concentration of Cy3-P dye dispersed in the PVME matrix (c).	157
6.4	Lifetime measurement for the monomer and dimer emission from Cy3-T and Cy3-P spin-coated films.	158

## List of Figures

---

- 6.5 Blends of NOPF<sub>6</sub>/Cy3-P show that the dimer is quenched more efficiently than the monomer emission (a). Nonquenchable emission intensity from Cy3-P films spin-coated on C<sub>60</sub> decreases with increase in the film thickness. The ratio of monomer to dimer intensity with film thickness is shown in the inset (b). . . . 159



## List of Tables

2.1	Exciton lifetime values obtained from mono- and bi-exponential decay fits. . .	50
3.1	Exciton lifetime values obtained from mono- and bi-exponential decay fits. . .	75
4.1	Summary of figures of merit for solution processed narrowband photodetectors with EQE < 100 nm. . . . .	103
5.1	Maximum elongated dimension ( $D_L$ ) and maximum cross-section dimension ( $D_{cs}$ ) for DP2 and DP4 at different dye loadings. Note that these dimensions are underestimates, due to the inherently limited access to low q values in the Guinier regime. . . . .	130



# 1 Introduction

## 1.1 Advancing from Electronic Age to Excitonic Age

In the electronic age, with the advent of transistors mankind has realized high speed memory devices and gadgets. “*Transistor density on integrated circuit doubles about every two years*” was predicted by Gordon Moore<sup>[1]</sup> in 1965. With the rapid advancement of technology to achieve miniaturization of the devices thereby lowering the cost and enhancing the computing power of the system has pushed the transistor technology close to Moore’s law. It is unambiguous that research and development in silicon semiconductor have played a pivotal role in achieving such a tremendous growth in the semiconductor device technology, so far. One of the main prerequisites in the advancement of device technology is to have devices working at low operating voltage with fast data transmission. Today in optical communications, electrical signals and optical signals are converted for data transfer. The switching between optical and electrical signal is irreplaceable. All optical switching would overcome the loss due to electrical signal conversion. A missing part of merging the photonics and electronics in semiconductor device technologies or gadgets and overcoming the switching between optical and electrical signal in communication networks goes unnoticed to enhance the capability of these devices.

Recently, researchers have advanced in this direction to a new mode of data transport using “excitonic devices” that have evolved into excitonic integrated circuits, excitonic transistors (EXOT)<sup>[2–5]</sup> to build emergent *opto-excitonic devices* where the major focus is on tuning and controlling exciton migration in the device. Different from electronic transport, the prime carrier is an exciton which can be directly generated using light, store them as light, transport them as energy and again release as light. An exciton is a neutral quasiparticle with a bound electron-hole pair generated from strong light-matter interaction or by electrical injection. Excitons play a vital role in naturally occurring light harvesting antennas. For instance, in the photosynthesis reaction, the antenna complexes (pigments or chlorophyll) harvest sun light to create excitons which are transported as excitation energy to the reaction center. These excitons are called Frenkel excitons. Today artificial 2D systems built from two-dimensional (2D) organic assemblies and inorganic materials such as transition metal dichalcogenides

(TMDCs) such as MoS<sub>2</sub>, WS<sub>2</sub> and its hetero-structures are at the focus of research interest.<sup>[3,6,7]</sup> Understanding exciton transport in these artificial 2D organic assemblies have attracted immense interest among researchers to build efficient devices such as organic solar cells and organic light emitting diodes. Focusing on exciton dynamics in organic assemblies and its application in optoelectronic devices forms the subject of this thesis. This chapter introduces organic assemblies of cyanine dye molecules, growth, fabrication of devices and the characterization techniques which were followed in the subsequent chapters of this thesis.

### 1.2 Organic Semiconductors

Organic molecules composed of hydrogen, carbon and heteratoms such as sulphur and nitrogen form the building block for organic semiconductors (OSCs). These materials can exist in an amorphous or crystalline form depending on the molecular structure and the bonding nature. In general, OSC are insulators, however, they can be tuned into semiconductors by doping, charge injection from electrodes or optical excitation and dissociation of photogenerated charge carriers. This makes the OSCs an extrinsic semiconductor. Furthermore, the charge carriers are localized and the transport occurs through thermally activated hopping. Carrier mobility in organic materials are  $\sim 1 \text{ cm}^2/\text{Vs}$ .<sup>[8,9]</sup> The high electrical conductivity in  $\pi$ -conjugated polymers called “polyacetylenes” was shown in 1975. With further explorations, an eleven-fold improvement was achieved by doping polyacetylenes. The Nobel prize in chemistry was awarded jointly to Alan J. Heeger, Alan G. MacDiarmid and Hideki Shirakawa for the “discovery and development of conductive organic polymers” in 2000.<sup>[10]</sup> Along the research in the domain of organic electronic materials, researchers paid special attention to optical properties in OSCs like absorption and emission. Therefore, understanding the fundamentals from atomic to molecular level will help to appreciate the electron and exciton migration in OSCs.

### 1.3 Electronic Properties in Organic Semiconductors

#### Atomic Orbitals and their Hybridization

As carbon constitutes the backbone in the organic molecules, interaction between carbon atoms form the basis for understanding charge transport in organic materials. The electronic configuration of carbon is  $1s^2 2s^2 2p^2$  with a completely filled 1s orbital (inner electronic level) and four electrons (two s electron and two p electron) in the outer electronic level. This forms the ground state configuration of carbon atom (Figure 1.1a). Changing this current configuration of carbon by promoting an electron from 2s- to 2p- orbital opens up several combinations of atomic orbitals. Using linear combinations of atomic orbitals (LCAO), “new” hybrid orbitals can be formed while the total number of the orbitals is conserved. The hybrid orbitals named *molecular orbitals* are  $2sp^3$ ,  $2sp^2$  and  $2sp$  depending on the hybridization between s and p orbitals as shown in Figure 1.1 (b-d). The hybridized and remaining  $p_z$

orbitals are marked only in Figure 1.1d for clarity.

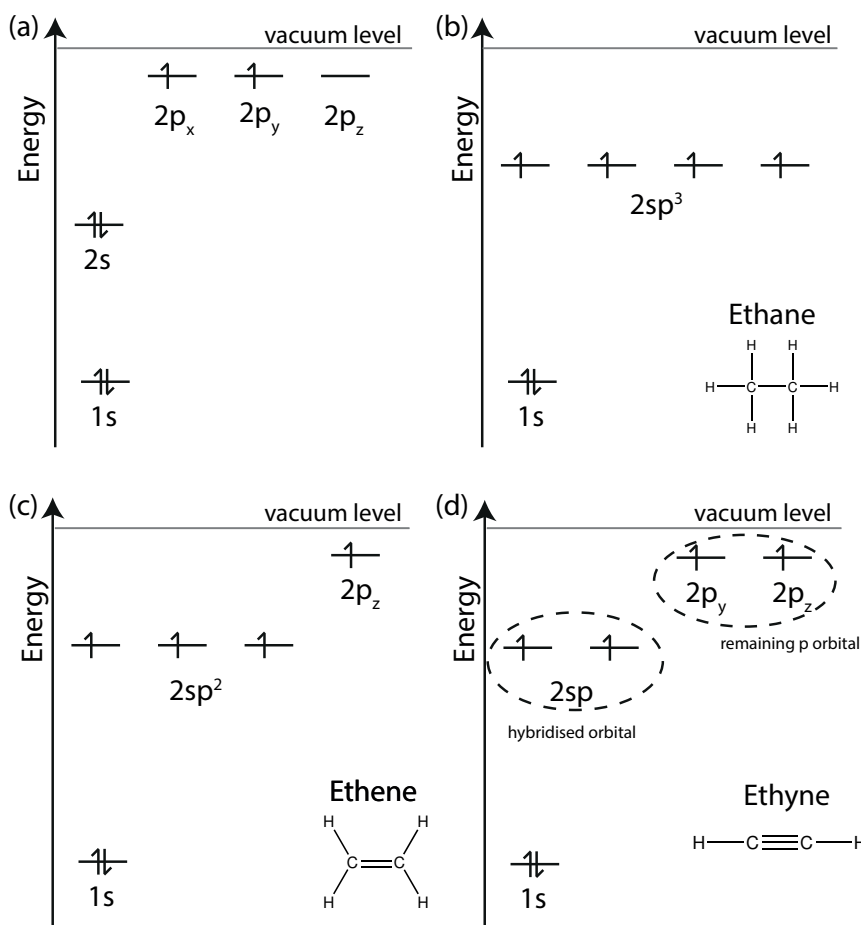


Figure 1.1 – Atomic orbitals of carbon in ground state (a) along with possible "new" hybrid orbitals by linear combination of s- and p- orbitals like (b) 2sp<sup>3</sup> (c) 2sp<sup>2</sup> and (d) 2sp. The hybridized and remaining p<sub>z</sub> orbitals are marked only in (d).

Here, different types of hybridization are elaborated with an example:

- sp<sup>3</sup> hybridization:** For ethane (H<sub>3</sub>C-CH<sub>3</sub>), the promotion of an electron in the carbon atom from the 2s orbital in the ground state to the p<sub>z</sub> orbitals opens the possibility to bond with four atoms (Figure 1.1b). The energy required for such excitation of an electron is much lower than the energy released from bonding with four additional bonds. In ethane, one of the 2sp<sup>3</sup> orbital in the carbon atom aligned on the internuclear axis with the other carbon atom strongly interacts to form a  $\sigma$  bond and the other three  $\sigma$  bonds are formed between carbon and hydrogen.
- sp<sup>2</sup> hybridization:** For ethene (H<sub>2</sub>C=CH<sub>2</sub>), the first bond between two carbon atoms is a  $\sigma$ -bond by overlapping 2sp<sup>2</sup> orbitals and other two 2sp<sup>2</sup> orbitals between carbon and hydrogen (Figure 1c). The remaining (p<sub>z</sub>) orbital forms a  $\pi$ -bond with the carbon atom

perpendicular to the hybridization plane, which results in C=C.

- **sp hybridization:** For ethyne ( $\text{HC}\equiv\text{CH}$ ), the two carbons are bound by a  $\sigma$ -bond and the remaining unhybridized orbitals ( $p_y$  and  $p_z$ ) form two  $\pi$ -bonds (Figure 1.1d).

The above mentioned hybridization are the first step of changes that can be observed in optical band gap due to interactions of atoms (here, carbon and hydrogen) to form molecules with new "hybrid orbitals". For simplicity, the terminology for interactions observed between two hydrogen atoms will be introduced. Subsequently, these terminologies will be used to explain the interaction between two carbon atoms.

Considering the interaction between two hydrogen atoms, the electron configuration of hydrogen can be represented as wavefunctions such as  $\psi_a$  and  $\psi_b$  in quantum mechanics. Here,  $\psi_a$  and  $\psi_b$  represents the 1s hydrogen orbital centered on proton a and b, respectively. The molecular orbital emerging from the interaction between  $\psi_{1s}$  orbitals, can be represented by using linear combination of atomic orbitals (LCAO) as,

$$\psi_{\pm} = c_1\psi_a \pm c_2\psi_b$$

where  $c_1$  and  $c_2$  are the mixing coefficients determining the extent of mixing the atomic orbitals. There are three conditions to be fulfilled by atomic orbitals to interact and form molecular orbitals as mentioned here. The atomic orbitals must have same symmetry, similar energy and spatial overlap. The new orbitals are called bonding ( $\psi_+$ ) and antibonding ( $\psi_-$ ) orbitals. The energies of these molecular orbitals can be approximately determined from the Hückel molecular orbital theory. Hückel approximation is limited to conjugated hydrocarbons which can be extended from simple system like benzene to long conjugated molecules. In this method, only  $\pi$  electrons are included as it influences the optical and chemical properties of the molecules, while  $\sigma$  electrons form the framework of the molecule. This method is based on applying variational principle to the LCAO with simplified assumptions regarding the overlapping atomic orbitals.<sup>[11]</sup> Briefly, the terminologies used in Hückel model is discussed here considering the interaction between two hydrogen atoms. The bonding between hydrogens to form  $\text{H}_2$ , leads to several interactions which can be defined by three terms:

1. **Overlap integral (S):** A quantitative measure of the extent of overlap between two orbitals located on different hydrogen atoms in the same region of space is represented as,

$$S = \int \psi_a \psi_b d\tau$$

The overlap integral (S) can take values between zero and one, where, (i) zero (when no overlap), (ii) small (limited overlap) or (iii) one (large overlap).

2. **Coulomb integral ( $\alpha$ ):** The Coulomb interaction between an electron of one nucleus

with the other nucleus is represented as,

$$\alpha = \int \psi_a \hat{H} \psi_a d\tau$$

The Hamiltonian or energy operator,

$$\hat{H} = -\frac{\hbar}{2m} \frac{\partial}{\partial x^2} + \hat{V}$$

and  $\hat{V}$  is the potential experienced by the particle.

3. **Resonance integral ( $\beta$ ):** An interaction between a nucleus and the overlap of two atomic orbitals located on different centers, which is represented as,

$$\beta = \int \psi_a \hat{H} \psi_b d\tau$$

A cumulative effect of all these three terms on orbital splitting leads to new energy levels as,

$$E_{\pm} = \frac{(\alpha \pm \beta)}{1 \pm S}$$

Now, extending the molecular orbital formation for ethene, considering only the C=C bond details the electronic and optical transitions like  $\sigma - \sigma^*$  (in red) and  $\pi - \pi^*$  (in blue), respectively as shown in Figure 1.2. First, considering the innermost  $1s^2$  orbitals, which are completely filled and the electrons are tightly bound close to the nuclei, gives a negligible resonance interaction ( $\beta$ ) and a very small splitting in molecular orbitals. In the  $2sp^2$  orbital, one of the orbital pointing along the internuclear axis induces a large resonance interaction between the carbon atoms forming a  $\sigma$  bond. This results in strong splitting of the  $\sigma - \sigma^*$  molecular orbital. Furthermore, the  $2p_z$  orbital located very far from the carbon nuclei has small interactions, which again generates small splitting of  $\pi - \pi^*$  molecular orbital compared to  $\sigma - \sigma^*$ .

Due to large splitting in  $\sigma - \sigma^*$ , the transitions are probed in the ultra-violet region, while small splitting in  $\pi - \pi^*$  transitions are observed in visible region. Here, the energy level of  $\pi$  and  $\pi^*$  denotes the highest occupied molecular orbital (HOMO) and lowest unoccupied molecular orbital (LUMO), respectively. The energy gap between HOMO and LUMO is called optical band gap, which is different from the electronic band gap. From the above mentioned hybridization, two types of bonds-  $\sigma$  and  $\pi$  bonds contribute to the electronic wavefunction of the molecules. Furthermore, considering that the nuclei are not stationary in the real molecules, they are oscillating around an equilibrium position with a certain vibrational frequency (say  $\omega$ ).<sup>[8,9]</sup> Therefore, the total wavefunction of the molecular state ( $\psi$ ) is a product of the electronic wavefunction ( $\psi_{el}$ ), spin wavefunction ( $\psi_{spin}$ ) and vibrational wavefunction ( $\psi_{vib}$ ), that is given as  $\psi = \psi_{el} \psi_{spin} \psi_{vib}$ . Molecular interactions with the electromagnetic radiation can be

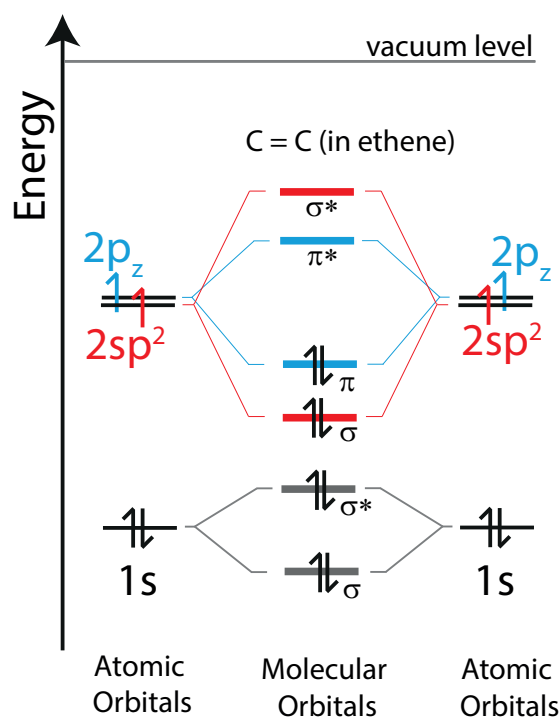


Figure 1.2 – Molecular orbital of ethene shown for C=C bond without carbon-hydrogen bonds for clarity.

observed from the changes in optical transitions from  $\pi$  and  $\pi^*$ . The optical excitation of an electron from HOMO to LUMO forms a tightly bound exciton (electron-hole pair) which is stable at room temperature. Furthermore, when molecules are coupled, the interaction between excitons leads to interesting effects. As a next step, the changes in optical properties upon interaction between two molecules will be discussed.

### Exciton Model in Optical Spectroscopy

Generally, molecules can interact with each other by weak van der Waals force in the ground state. Kasha derived a model to explain the intermolecular interaction between weakly coupled molecules forming resonance interaction.<sup>[12]</sup> The model is explained here to underscore the importance of interaction parameters influencing the exciton energy levels. Detailed derivations are available in textbooks for reference.<sup>[9,13]</sup>

Considering two identical molecules ( $M_1$  and  $M_2$ ), which have the same ground state energy levels ( $E_1$  and  $E_2$ ) with wavefunction  $\psi_1$  and  $\psi_2$ , respectively for  $2p_z$  orbital. The overall wavefunction of the two-molecule system in the ground state can be approximated as the



product of the wavefunctions of the individual molecules,

$$\Psi_g = \Psi_1 \Psi_2 \quad (1.1)$$

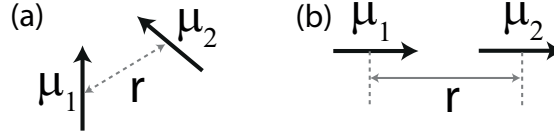


Figure 1.3 – Two dipoles with dipole moment -  $\vec{\mu}_1$  and  $\vec{\mu}_2$  arranged randomly (a) and with head-to-tail arrangement (b) separated by a distance  $r$ .

Considering these molecules as two-particle system, the Hamiltonian function can be described as,

$$\hat{H} = \hat{H}_1 + \hat{H}_2 + \hat{V}_{12} \quad (1.2)$$

where,  $\hat{H}_1$  and  $\hat{H}_2$  are the operators for individual molecules,  $\hat{V}_{12}$  is the inter-molecular perturbation potential. Using point-dipole interaction, the transition dipole of the molecules ( $\vec{\mu}_1$  and  $\vec{\mu}_2$ ) can be randomly oriented as shown in Figure 1.3a or in a head-to-tail arrangement (Figure 1.3b).

Using point dipole approximation, the exciton coupling energy for random orientation can be given as,

$$J_{12} = \frac{1}{4\pi\epsilon_0} \left[ \frac{\vec{\mu}_1 \cdot \vec{\mu}_2}{r^3} - \frac{3(\vec{\mu}_1 \cdot \vec{r})(\vec{\mu}_2 \cdot \vec{r})}{r^5} \right] \quad (1.3)$$

Upon dipole alignment (head-to-tail), the exciton coupling energy ( $J_{12}$ ) reduces to

$$J_{12} = -\frac{1}{4\pi\epsilon_0} \frac{2\vec{\mu}_1 \cdot \vec{\mu}_2}{r^3} \quad (1.4)$$

Using equation 1.1 and 1.2, the ground state of the system can be obtained by invoking Schrödinger equation. Therefore, the ground state energy of two identical molecules is,

$$E_g = \langle \Psi_1 \Psi_2 | H_1 + H_2 + V_{12} | \Psi_1 \Psi_2 \rangle = E_1 + E_2 + D \quad (1.5)$$

## Chapter 1. Introduction

---

where,  $D = \langle \Psi_1 \Psi_2 | V_{12} | \Psi_1 \Psi_2 \rangle$ . This term reflects the interaction between two molecules, that depends on orientation and distance between the molecules as explained in eqn 1.3 and 1.4, and corresponds to the van der Waals interaction energy. Also, the negative component in this term lowers the ground state energy of the system (two-molecules) compared to the individual molecule.

So far, we discussed the ground state interaction between two identical molecules. Now, if we can optically excite one of the molecules, the excited state ( $\Psi_e$ ) can be  $\Psi_e = \Psi_1^* \Psi_2 = \Psi_1 \Psi_2^*$ . Here,  $\Psi_1^*$  and  $\Psi_2^*$  are the excited state wavefunctions for molecule 1 and molecule 2, respectively. This describes that exciting either of the molecules will result in the same excited energy. Therefore, the excited state can oscillate between both the configurations. By linear combination of both these situations, the overall wave-function for the excited state is,

$$\Psi_E = c_1 \Psi_1^* \Psi_2 + c_2 \Psi_1 \Psi_2^* \quad (1.6)$$

where,  $c_1$  and  $c_2$  are equal for identical molecules. The normalized symmetric and anti-symmetric contributions for the eigenfunctions ( $\Psi_{E\pm}$ ) with respective energies ( $E_{\pm}$ ) can be represented as,

$$\Psi_{E\pm} = \frac{1}{\sqrt{2}} (\Psi_1^* \Psi_2 \pm \Psi_1 \Psi_2^*) \quad (1.7)$$

Applying eqn. 1.7 and 1.2 into the Schrödinger equation gives

$$E_{E\pm} = E_1^* + E_2 + D' \pm J_{12} \quad (1.8)$$

Here, it is assumed that molecule 1 is excited and molecule 2 is in its ground state, and their corresponding energies are  $E_1^*$  and  $E_2$ , respectively. The third term,  $D'$  is analogous to  $D$  in eqn 1.5 but here, it is an interaction between molecules in excited-state and ground-state. The fourth term ( $J_{12}$ ) is the resonance interaction energy between two configurations which is analogous to resonance integral as explained in section 1.3.

From the above derivations on electronic (or excitonic) coupling between identical molecules, the interactions between molecules can be optically probed. Precisely, the above equation 1.8, represents the transition energy ( $\Delta E_{total}$ ) between the ground state and excited state as

shown in Figure 1.4 and represented as,

$$\Delta E_{total} = (E_1^* + E_2 + D' \pm J_{12}) - (E_1 + E_2 + D) = \Delta E_1 + \Delta D \pm J_{12} \quad (1.9)$$

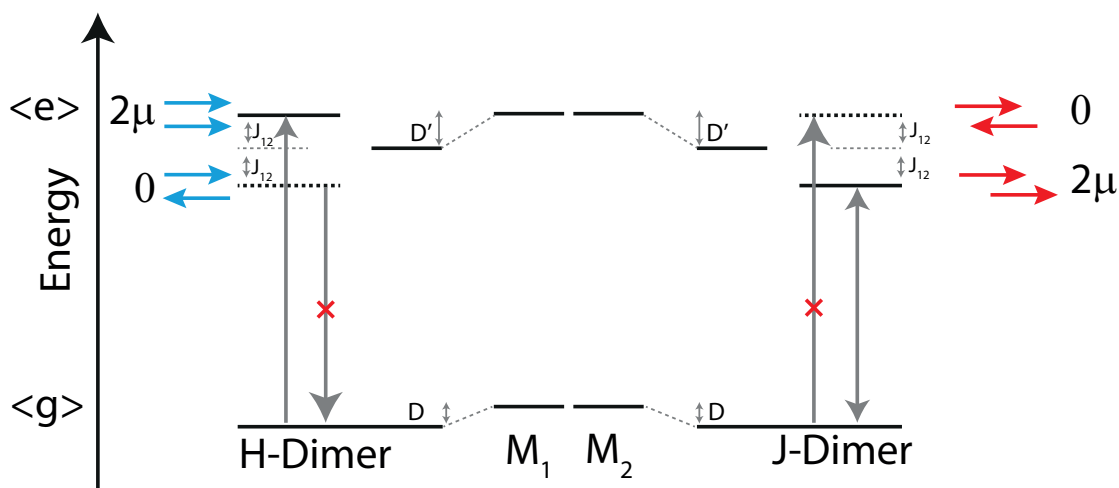


Figure 1.4 – Electronic coupling between two identical molecules ( $M_1$  and  $M_2$ ) showing energy splitting for H-Dimer and J-Dimer

The transition energy ( $\Delta E_{total}$ ) is dependent on dipole orientation as shown in Figure 1.4. Considering molecules as point-dipoles and orienting this dipole in different combinations, two situations with a valid net dipole moment arises as explained below:

1. **H-Dimer:** When the molecules are arranged in coplanar fashion with head-to-tail interaction, the transition dipole moment aligned in anti-parallel direction in the lower energy state cancels out. As a consequence, the optical transition is not allowed. On the other hand, when the molecules stack as head-to-head interaction, the transition dipole moment adds to  $2\mu$ . This is an allowed optical transition, hence an absorption band blue-shifted to the monomer state can be observed. Upon excitation, however, the electron relaxes to the lower energy state which has a forbidden transition. This explains the weak or even vanishing fluorescence from H-aggregates. In some cases, a slight misorientation or twist in the molecules can still give rise to an emission as explained in Chapter 6. Also, thermal motion can naturally induce such twisted geometries.
2. **J-Dimer:** When the molecules are arranged in co-linear fashion by dislodging the center of the molecule in head-to-tail interaction, the net transition dipole moment for the lower energy state becomes optically active for absorption and fluorescence. This optically allowed lower energy state gives a red-shift (bathochromic) in the absorption band compared to the monomer.

### Huang-Rhys (S) parameter

From the above discussion on electronic coupling between two identical molecules, the allowed transition energy for H-dimer and J-dimer was explained. However, this two-molecule or dimer model as explained by Kasha is incomplete for organic molecules. This is due to the interplay of electron-phonon interactions, which gives rise to intramolecular vibrations along with the electronic transition. This electron-phonon coupling strength is denoted as Huang-Rhys (S) parameter. A seminal work of Spano<sup>[14,15]</sup> extends the two-molecule exciton model considering the effect of this S parameter. In a strong electron-phonon coupling regime, the single energy states as described earlier in Figure 1.4 with energy level splitting of  $2J_{12}$  turns into a band with  $4J_{12}$  (Figure 1.5a and c) due to *vibronic excitons*. Figure 1.5 shows monomer energy levels with vibrational levels (as lines on the left) and its corresponding vibronic exciton band for H-aggregates (Figure 1.5a) and J-aggregates (Figure 1.5c). The bold arrows indicate the optically allowed transitions. From the absorption spectra, different transitions can be identified as 0-0 or 0-1, which is helpful to classify the main transition peak and the vibronic peak. In the case of J-aggregates, the excitons stay in the bottom energy level (0-0) unlike H-aggregates (0-1). This gives a strong absorption band with increased oscillator strength for J-aggregates in the 0-0 band, while other 0-1, 0-2 transitions are dictated by weak vibronic coupling (Figure 1.5b and d). Later, Spano<sup>[16]</sup> showed that the ratio of intensity between  $I^{0-0}/I^{0-1}$  from a fluorescence spectrum can give an estimate of coherently coupled neighbouring molecules.

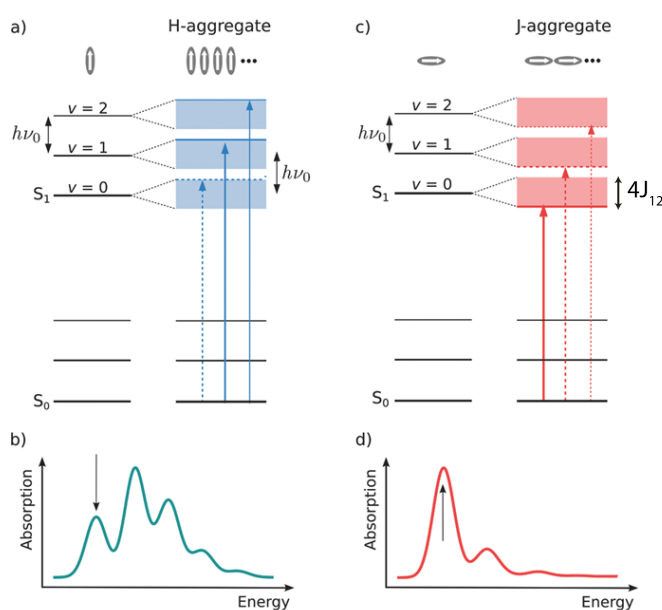


Figure 1.5 – Vibronic excitons in H and J-aggregates showing the influence of optically allowed transitions (bold lines) in the absorption spectrum. Adapted with permission<sup>[17]</sup>

From this theory as explained by Spano,<sup>[14]</sup> it is possible to predict how the absorption or fluorescence spectra changes depending on the electronic coupling among the interacting

chromophores and disorder in the system. Moreover, this can be used to identify a weak-coupling and strong-coupling regime in aggregates. For instance, weakly coupled J-aggregates will show the  $S_1 \leftarrow S_0$  transition with a shift in the absorption band from monomer while having resonance in absorption and fluorescence. With strong coupling, the oscillator strength increases reflecting this effect in fluorescence.

In summary, J-aggregates show a very strong fluorescence with a small Stokes' shift (difference between absorption and emission maxima). A narrow absorption width (about 10-20 nm) and small Stokes' shift in J-aggregates signifies a strong exciton coupling and resonant behaviour of excitons. These properties of J-aggregates intrigued several researchers to also explore this aggregation effect in porphyrins,<sup>[18,19]</sup> chlorin,<sup>[20,21]</sup> perylene bisimide,<sup>[22,23]</sup> merocyanines,<sup>[24,25]</sup> hydroazaheptacene tetraimides<sup>[26]</sup> and BODIPY<sup>[27]</sup> dyes. Despite the effect of aggregation was observed in a broad range of molecules, cyanine dyes even today attract significant attention due to their unique properties - a high polarizability already present in the ground state giving rise to strong interaction between molecules over a large distance. For instance, the polarizability is almost thrice compared to polyenes of similar size.<sup>[28]</sup> This polarizability effect leads to giant pseudo-dipole formation in the excited state. Extensive review articles on J-aggregates in cyanines,<sup>[28]</sup> perylene bisimide<sup>[29]</sup> with a special mention on exciton dynamics in J-aggregates<sup>[17]</sup> are available in literature.

## 1.4 Förster and Dexter Type Energy Transfer

We here introduce the two main mechanisms of how energy can be transported between molecules. Consider two molecules which act as donor and acceptor with absorption ( $D_a$  and  $A_a$ ) and fluorescence ( $D_f$  and  $A_f$ ) spectra as shown in Figure 1.6a. An exciton created in a donor molecule by an external stimuli can be transferred to the acceptor molecule by non-radiative energy transport - Förster and Dexter type and/or radiative energy transport.

### Förster transport

In the year 1946, Förster developed a model explaining exciton transport in molecules which are placed apart at a considerably larger distance compared to their molecular size and the coupling between the molecules is provided by electromagnetic dipole-dipole interaction. This resulted in coherent transport of exciton from donor to acceptor without any release of energy in the intermediate step as shown in Figure 1.6b. This mode of exciton transport was named Förster resonance energy transfer (FRET). The efficiency ( $E_{FRET}$ ) of a FRET transport can be defined as,

$$E_{FRET} = \frac{k_{ET}}{k_f^0 + k_{ET} + \sum k_i} \quad (1.10)$$

## Chapter 1. Introduction

---

where,  $k_{ET}$  - rate of FRET,  $k_f^0$  - rate of natural radiative relaxation (i.e., fluorescence rate in the absence of any other deactivation processes), and  $k_i$  - non-radiative relaxation rate (e.g., internal conversion, intersystem crossing, external conversion etc).

Between donor and acceptor, the orientation and distance between them are related to the Coulomb interaction energy ( $\beta_c$ ) and transfer rate ( $k_{ET}$ ) as,

$$\beta_c \propto \frac{|\mu_D| |\mu_A|}{R^3} k_{ET} \quad (1.11)$$

$$k_{ET} = \frac{1}{\tau_D} \left( \frac{R_0}{R} \right)^6 \quad (1.12)$$

where,  $\mu_D$  and  $\mu_A$  represent transition dipole moments of donor and acceptor,  $R$ - donor-acceptor distance and  $k$  - orientation factor,  $\tau_D$  - fluorescence lifetime of donor in the absence of acceptor,  $R_0$  - Förster radius at which FRET rate is 50%. Donor-acceptor distance is a very crucial factor to influence exciton transport in FRET mode due to its  $R^6$  dependence. To enhance the FRET, a high quantum yield of donor fluorescence and high extinction coefficient of acceptor gives an overlap integral ( $J$ ) as shown in Figure 1.6a

$$J = \int D_f(\lambda) \epsilon_a(\lambda) \lambda^4 d\lambda \quad (1.13)$$

$D_f$  - normalized emission spectrum of the donor,  $\epsilon_a$  - molar absorption coefficient of the acceptor and  $\lambda$  - the wavelength.

### Dexter transport

Another non-radiative process, which can transfer excitons by electronic coupling  $\beta_e$  between a donor and acceptor is Dexter transport. Besides a large overlap integral ( $J$ ), an additional overlap of electron wavefunctions is required to have an exchange of electron between donor and acceptor, where the efficiency is distance dependence. The rate of Dexter transport ( $k_D$ ) is,

$$k_D \propto e^{-(2R/L)} \quad (1.14)$$

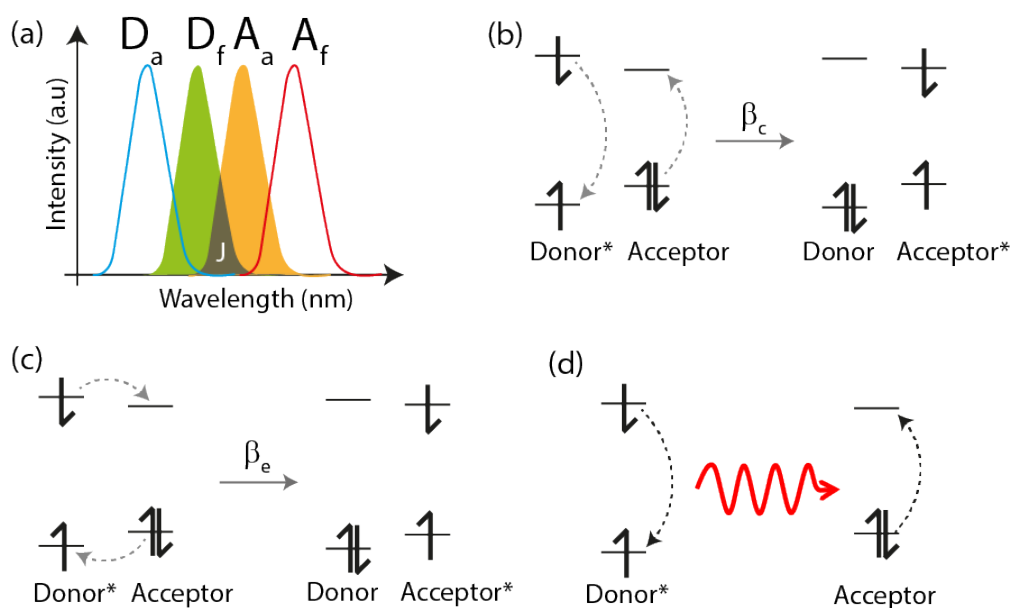


Figure 1.6 – Absorption and fluorescence spectrum of donor and acceptor (a). Non-radiative energy transport - Förster (b) and Dexter (c) and radiative energy transfer (d).

**Radiative energy transport** occurs by emission from donor molecule followed by absorption of the acceptor molecule. The efficiency of exciton transfer is very low in this process as shown in Figure 1.6d.

## 1.5 Supramolecular Assemblies in Cyanine Dyes

Cyanine dyes, as the name "cyan" suggests, are blue-green dyes which were synthesized for the first time by Greville Williams a century ago in 1856.<sup>[30–32]</sup> Cyanines have very strong molar extinction coefficients ( $\sim 10^5 \text{ M}^{-1} \text{ cm}^{-1}$ ) and optical absorption tunable for wide range of wavelength of interest from 400 to 900 nm. Despite researchers possessing very well-established synthesis route to tune the material, very recently in 2017, Lin et al.<sup>[33]</sup> have shown that the absorption edge can be tuned upto 1500 nm. This speaks for continued efforts of researchers in building new cyanine chromophores due to their strong extinction coefficient. Structurally, cyanines are organic salts with an anionic (cationic) chromophore and cationic (anionic) counter-ion (Figure 1.7a). The chromophore of the cyanine dyes belong to polymethine group, with odd number of methine groups ( $-\text{CH}=\text{}$ ) linked with alternate single and double bonds and nitrogen end groups. The presence of alternate single and double bonds introduces conjugation in the polymethine chain. This enables the lone pair of electron in the nitrogen atom to delocalize along the polymethine chain (Figure 1.7b). The presence of Cl in the corner (in magenta) participates in organic assemblies and also it can influence the HOMO and LUMO of the cyanine dye to a greater extent.<sup>[34]</sup> The hydrophobic side chains (in red) can be tuned to modify the morphology of the cyanine dyes.<sup>[35]</sup> The presence of sulphonate group (in blue) renders water solubility of the cyanine dyes.

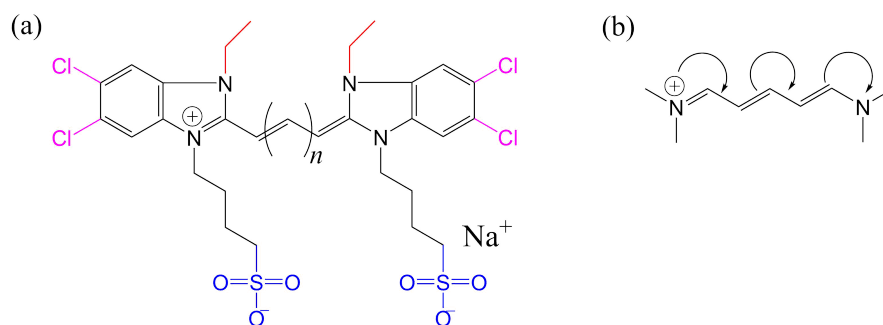


Figure 1.7 – Typical cyanine dye with hydrophobic edges shown in red and hydrophilic edges shown in blue (a). Illustrating delocalisation of  $\pi$ -electron along the polymethine chain (b).

Tuning the optical and chemical properties of cyanine dyes starts from beginning of the synthesis.<sup>[36]</sup> For instance, the chain length of the cyanine dye can be increased from  $n = 0$  (monomethine),  $n = 1$  (trimethine),  $n = 2$  (pentamethine) and  $n = 3$  (heptamethine) (Figure 1.8a-c). Correspondingly, the peak absorption can be bathochromically shifted by ca. 100 nm (Figure 1.8d). Longer chains (for instance,  $n = 4$ ) are prone to oxidation of double bonds, thereby disintegration of polymethine chain and deterioration of optical properties of cyanines.<sup>[37]</sup> Using the particle-in-a-box model, the absorption maximum (in energy scale) of the dye can be correlated to the length between nitrogen atoms.

$$\Delta E = \frac{(2n + 1)h^2}{8mL^2} \quad (1.15)$$

where,  $\Delta E$  - difference in HOMO and LUMO (optical band gap),  $n$  - number of electrons,  $h$  - Planck's constant,  $m$  - mass of the electron and  $L$  - length of the conjugated system (here, it is between two nitrogen atoms).

In 1936, Jelley<sup>[38,39]</sup> and Scheibe<sup>[40,41]</sup> independently discovered molecular aggregation in the cyanine dye (1,1'-diethyl-2,2'-cyanine 1,1'-diethyl-2,2'-cyanine chloride (pseudoisocyanine, **PIC**)). These newly formed aggregates were named "J-aggregates". The optical absorption band of these J-aggregates were found to be characterized by a very narrow and red-shifted from their individual molecules (monomers). For comparison, the J-aggregates formed in solution for three different cyanine dyes are shown in Figure 1.8d. A higher level ordering which is dependent on concentration, temperature and reversibility was proposed. Later, Scheibe and Kandler<sup>[42]</sup> showed that the direction of the absorption dipole is parallel to the aggregate axis using linear dichroism experiments. With these fundamentals, Förster<sup>[43]</sup> again confirmed that the molecules are aligned in J-aggregates as reported by Scheibe and Kandler.<sup>[42]</sup> Davydov<sup>[44]</sup> and Kasha<sup>[12]</sup> proposed a basic model of excitonic (or electronic) coupling between two molecules as shown in section 1.3. Although, it is a simplified model, it is robust enough and applicable while scaling up to molecular aggregates to provide more



## 1.6. Corelation between Structural Packing and Optical Properties in J-aggregates

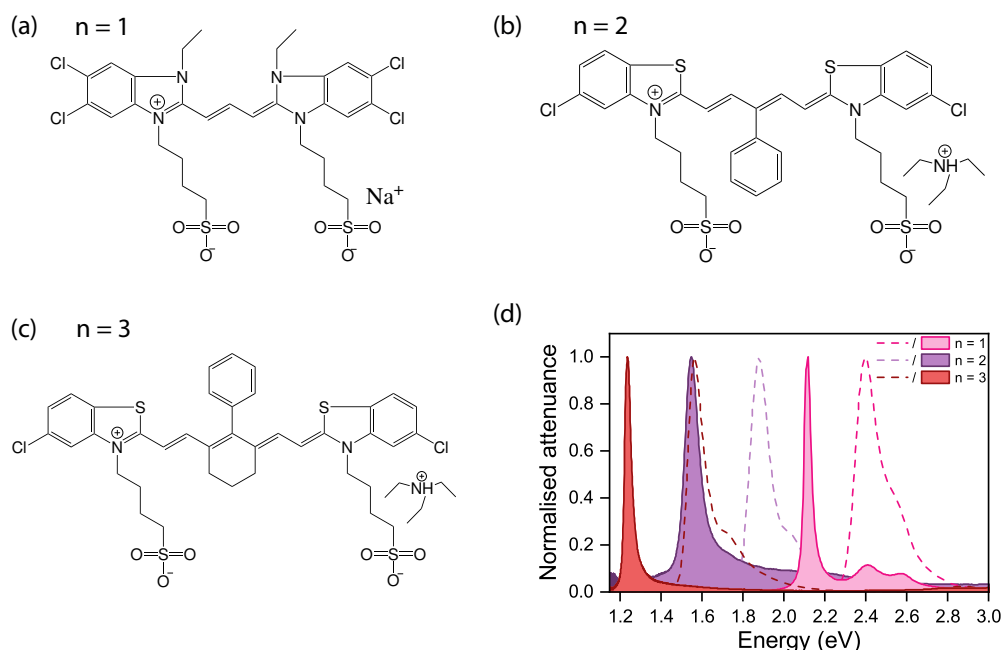


Figure 1.8 – Example of three cyanine dyes with increasing chain length for (a)  $n = 1$ , (b)  $n = 2$ , and (c)  $n = 3$ . (d) Attenuance of the monomer (in dotted lines) and their corresponding J-aggregate (filled) solution spectrum are shown in energy scale.

insights in their optical properties.

## 1.6 Corelation between Structural Packing and Optical Properties in J-aggregates

Strong dipole-dipole interaction in the J-aggregates along the molecular axis makes it compelling to study its exciton dynamics compared to their monomers. Exciton dynamics in J-aggregates are studied for different morphologies. The morphology of J-aggregates can be tuned between 1D - cylindrical objects and 2D - thin films by changing the dye structure. Formation of different J-aggregate morphologies and growth models and correlation to the optical properties will be described here.

From the exciton theory as mentioned before in section 1.3, the self-association of dye molecules to form a J-aggregates in solution depends on several factors like dye structure, concentration, solvent polarity, pH, ionic strength and temperature.<sup>[45]</sup> An extensive work on cyanine dye aggregation in solution was reported by Herz.<sup>[45]</sup> The role of  $\pi$ - $\pi$  dispersive interactions between polarizable groups and electrostatic interaction between opposite charge facilitates aggregation. Furthermore, the planarity of cyanines renders close packing of molecules thereby reducing the distance between the molecules. This can substantially increase the exciton coupling energy as shown in eqn.1.3. In the J-aggregate configuration, the whole molecular assembly acts as a single entity with strongly coupled transition dipole

moment.<sup>[29]</sup> The strong absorption coefficient (oscillator strength) for J-aggregates compared to their monomer counterparts comes from the square dependence of transition dipole moment. As a result of this excitonic coupling, the optical properties of J-aggregates are distinct from their individual monomers. For strongly coupled chromophores in a J-aggregate, an exciton possesses coherent properties due to the rapid exchange of excitation energy between the  $N$  molecules constituting the latter. As a result of this dominant exchange interaction, the excited state of the aggregate is decoupled from its environment, leading to an extremely narrow absorption band that scales with  $1/N$  and is devoid of vibrational transitions. These characteristic features are accompanied by a short radiative lifetime scaling with  $1/N$  and a vanishing Stokes shift of the narrow fluorescence line. In real aggregates, the number of coherently coupled molecules (coherence size) strongly depends on imperfections, disorder induced by the environment or thermal motion as well as size distributions of the molecular assemblies. In rough terms these effects will lead to larger bandwidth, lowered extinction coefficient as well as a clear albeit small Stokes shift.<sup>[46–48]</sup> Furthermore, this square dependence of transition dipole moment to the oscillator strength also reflects in the fluorescence properties.

In general, the fluorescence quantum yield ( $\Phi$ ) of a system is defined as

$$\Phi = \frac{k_r^0}{k_r^0 + k_{nr}} \quad (1.16)$$

where,  $k_r^0$  and  $k_{nr}$  are radiative and non-radiative decay rate, respectively.

The fluorescence lifetime ( $\tau$ ) is,

$$\tau = \frac{1}{k_r^0 + k_{nr}} \quad (1.17)$$

In the case of J-aggregates, an increased radiative rates ( $k_r^0$ ) with shortening of fluorescence lifetime compared to their monomer counterparts was observed. This increased radiative decay rate in J-aggregates was called "superradiance".<sup>[49,50]</sup> Most importantly, the exciton lifetime for J-aggregates is much shorter than the monomers depending on the coherently coupled monomers by a factor  $\sim 1/N$ .<sup>[51]</sup> The exciton coherence in J-aggregates leads to collective behaviour in fluorescence quenching called "super-quenching". This characteristic feature was exploited later for several donor-acceptor systems, energy transfer and PL enhancers.<sup>[52–54]</sup>

### 1.6.1 1D J-aggregates

Formation of 1D J-aggregates (tubular aggregates) in solution was studied using a cyanine dye 3,3-bis(2-sulphopropyl)-5,5,6,6-tetrachloro-1,1-dioctylbenzimidacarbocyanine (C8S3).<sup>[57–59]</sup> The chemical structure of C8S3 dye is shown in Figure 1.9a. As the sulphonate groups (marked

## 1.6. Corelation between Structural Packing and Optical Properties in J-aggregates

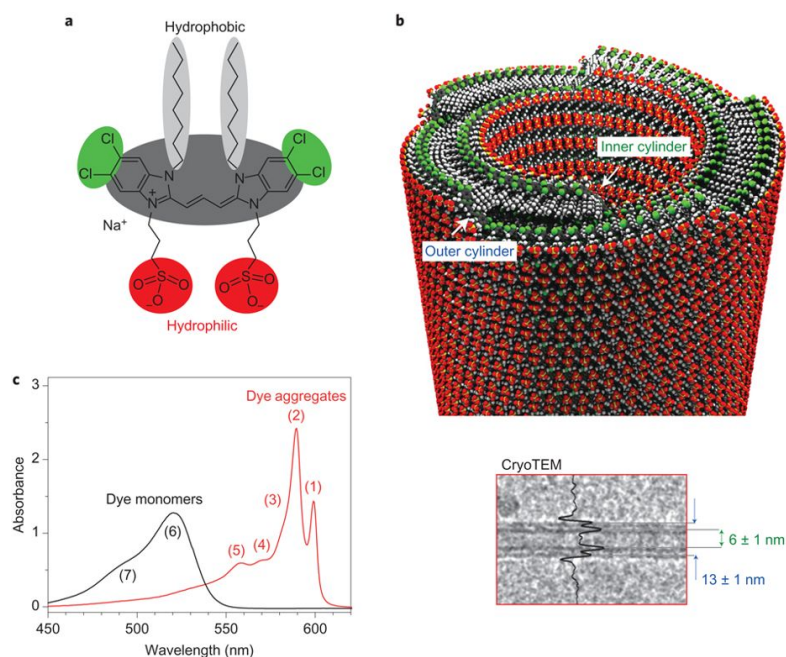


Figure 1.9 – Chemical structure of the C8S3 dye showing hydrophilic and hydrophobic edges (a). Schematic of double walled tubular J-aggregate showing inner cylinder and outer cylinder with a cryo-TEM image (below), (b). The absorption spectrum of J-aggregates and its corresponding monomer (c). Adapted with permission.<sup>[55]</sup>

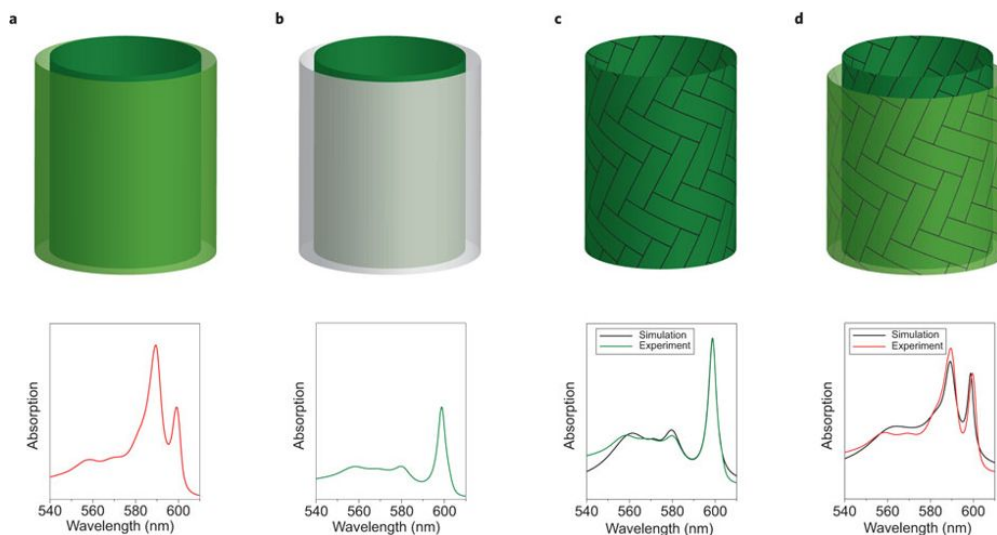


Figure 1.10 – Schematic of complete double wall nanotube (a), Oxidized outer wall (b), Mutual arrangement of dye molecules in the inner wall (c) and extension of this model to outer wall (d). The corresponding absorption and simulated spectra are shown below. Adapted with permission.<sup>[56]</sup>

in red) render water solubility, the hydrophobic interaction (marked in grey) from the alkyl groups in 1,1' nitrogen positions leads to double-walled tubular J-aggregates with an inner wall and outer wall as shown schematically in Figure 1.9b along with the cryo-TEM (below) as observed by Berlepsch et al.<sup>[58]</sup> The tubular aggregates showed unique inner wall and outer wall thickness with distinct absorption behavior. As shown in Figure 1.9c, the monomers have a weak and broad absorption band (6) along with a vibronic band (7), while tubular J-aggregates show two strong absorption peaks from the inner (1) and outer wall (2).<sup>[57,59]</sup> It can be noted that along with the main absorption peak, there are other small absorption peaks (3),(4) and (5) present at the high energy side (Figure 1.9c). This is different from the monomer absorption peak (6). Further insights into the absorption spectrum and correlating to the molecular packing in this double-walled tubular J-aggregate was shown by Eisele et al.<sup>[55]</sup> Addition of silver nitrate ( $\text{AgNO}_3$ ) solution to a freshly prepared double-walled tubular J-aggregate solution leads to selective oxidation of the outer wall that suppressed its optical response and only the absorption peak of the inner wall ( $\sim 600$  nm) can be observed as shown in Figure 1.10b. The molecular packing of monomers and orientation of dipoles can explain this observation in greater detail. In contrast to the typical bricklayer structure, the authors showed that the molecular packing in the inner wall follows a herringbone structure with molecules rotated out-of-the-plane instead of being planar in structure. This new model was named as *extended herringbone* structure. The presence of molecules in the out-of-plane direction gives rise to high energy peaks in the absorption spectrum along with the inner wall absorption as shown in Figure 1.10b. This was verified further by using simulations and compared with the experimental data (Figure 1.10c). Extending this model to the outer wall was in complete agreement as observed for the inner wall (Figure 1.10d). It was also concluded that in this double-walled tubular aggregates the excitons between the inner and outer wall don't interact and therefore, this can be imagined as two uncoupled tubes.

### 1.6.2 2D J-aggregates

Kirstein et al.<sup>[60]</sup> observed 2D growth of J-aggregates on ammonium amphiphile. Kirstein and Möhwald<sup>[61]</sup> investigated the optical transitions in 2D J-aggregates and confirmed a Herringbone packing of molecules. The formation of 2D J-aggregate films propelled the application of J-aggregates as sensitizers on silver halide crystals for photography.<sup>[62,63]</sup> Steiger et al.<sup>[64]</sup> have shown that the edges and corners of AgBr crystals act as nucleation site to form J-aggregates from monomer solution. Also, thin films of J-aggregates were formed by mixing PIC-Br dye with polyvinylalcohol (PVA) in water and highly oriented J-aggregates were obtained by using "vertical spin-coating route".<sup>[65]</sup> Here, two different growth techniques which are widely used even today to obtain 2D J-aggregate thin films are explained below:

#### 1. Langmuir-Blodgett (LB) growth

A typical set-up for manufacturing Langmuir-Blodgett films consists of a trough filled with water where cyanine dye molecules with limited solubility are dispersed in water and con-

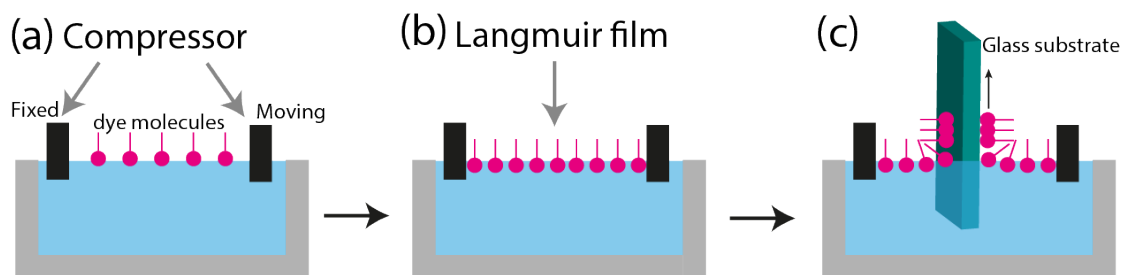


Figure 1.11 – Schematic of Langmuir-Blodgett (LB) growth technique showing the set-up (a) used to form Langmuir films (b) and then transferred on glass substrates (c).

trolled by compressor plates (fixed and moving barrier) as shown in Figure 1.11a. Presence of hydrophobic and hydrophilic part of the cyanine dyes results in extending the hydrophobic part at the air-water interface and hydrophilic part in the water. As the dye molecules disperse uniformly a thin film is formed which is called "*Langmuir film*". Subsequently, using compressor plates the molecules are compressed slowly by monitoring the compression in the Wilhelmy balance. Then, a cleaned glass substrate will be immersed in the liquid and withdrawn at controlled speed, so that the monolayer is transferred to the glass substrate (Figure 1.11a). The compressor plates are developed to keep very high surface pressure so that the molecules can be transferred efficiently on the substrates in a continuous process as the amount of dye molecules decreases with repeated cycles. Several factors like surface tension, surfactants and substrate nature influences the film formation. Although this technique is a very slow process, this was the first step to achieve J-aggregate monolayers in 1970s. Hada et al.<sup>[66]</sup> were the first research group to show the implementation of the LB technique for cyanine J-aggregates.

As J-aggregates in PIC dyes form at very high concentration ( $c = 5 \text{ mM}$ ), PIC dye was modified to thiacyanine or thiocarbocyanine like 5,6-dichloro-2-[[5,6-dichloro-1-ethyl-3-(4-sulfobutyl)-benzimidazol-2-ylidene]-propenyl]-1-ethyl-3-(4-sulfobutyl)-benzimidazolium hydroxide, inner salt, sodium salt (**TDBC**) dye which formed J-aggregates at very low concentration ( $c = 0.1 \text{ }\mu\text{M}$ ).<sup>[67]</sup> Further studies on 2D J-aggregate formation using (**TDBC**) dye will be discussed as this forms the Chapter 2 of this thesis. The chemical structure of the TDBC dye is shown in Figure 1.8a.

## 2. Layer-by-Layer (LBL) deposition

The layer-by-layer (LBL) technique was first implemented by Kirkland<sup>[68]</sup> and Iler<sup>[69]</sup> in 1966 to deposit alternating layers of oppositely charged particles. Fukumoto and Yonezawa<sup>[70]</sup> showed multilayer J-aggregates deposited using LBL with thiacyanine and thiocarbocyanine dyes, separately as anionic dyes with poly(diallyldimethylammonium chloride) (PDDA) as cationic surfactant. This process involves depositing a monolayer of polyelectrolyte (PDPA here) by immersing a cleaned glass (or quartz) substrate into the polyelectrolyte bath at room temperature for 30 min and rinsing with the same solvent (water) to remove weakly adsorbed

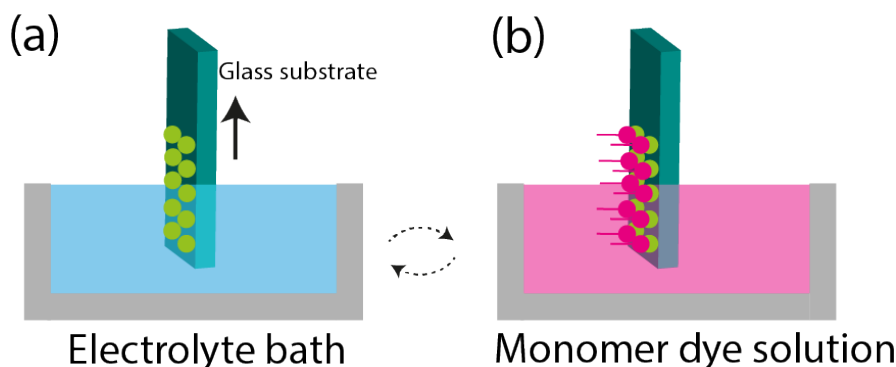


Figure 1.12 – Schematic of Layer-by-Layer (LBL) deposition technique showing the functionalization of glass substrate with electrolyte (cationic or anionic)(a) followed by deposition of cyanine dyes (anionic or cationic)(b), respectively.

excess material (Figure 1.12a). Subsequently, the PDDA functionalized substrate will be immersed in the dye solution to form a J-aggregate monolayer (Figure 1.12b). This technique allows much faster and easier deposition of monolayers to multilayer films compared to the LB technique. Later, this technique was explored by Bulović<sup>[71]</sup> group to deposit J-aggregates using **TDBC** dye to study the optical properties of J-aggregates and to build advanced opto-electronic devices. Furthermore, Bradley et al.<sup>[71]</sup> showed that the film formation of J-aggregate in LBL technique follows a "Stranski-Krastanov (S-K)" growth model. This growth model is followed even recently to deposit J-aggregate thin films using **TDBC** dye.<sup>[72]</sup> The influence of polyelectrolyte on exciton dynamics will be discussed later and an alternate growth model of J-aggregate thin film will be discussed in Chapter 2 in this thesis which negates the S-K growth model as explained by Bradley et al.<sup>[71]</sup> In the next section, we will discuss different growth model of thin films to appreciate the routes to form J-aggregate monolayer and coherent crystals.

## 1.7 Growth Model of Thin Films

In general, growth of thin films and crystals are very distinct phenomenon. Growth of single crystals from a supersaturated solution is based on approaching towards an equilibrium state while thin-film formation is more dynamic favoring non-equilibrium processes. In the case of vapor phase deposited thin films, the chemical potential between the vapour phase and the solid phase acts as driving force for film formation (Figure 1.13a). So, the growth of thin films involves both thermodynamics and growth kinetics which makes it a complicated growth route. Growth of J-aggregates on solid substrates as mentioned above, occurs from a solution to substrate. This involves the film-substrate interface free energy ( $\gamma_i$ ) as an important parameter. Broadly, thin film growth follows three distinct growth models.<sup>[73]</sup>

1. **Volmer-Weber growth model:** When small clusters are nucleated on the substrate, the

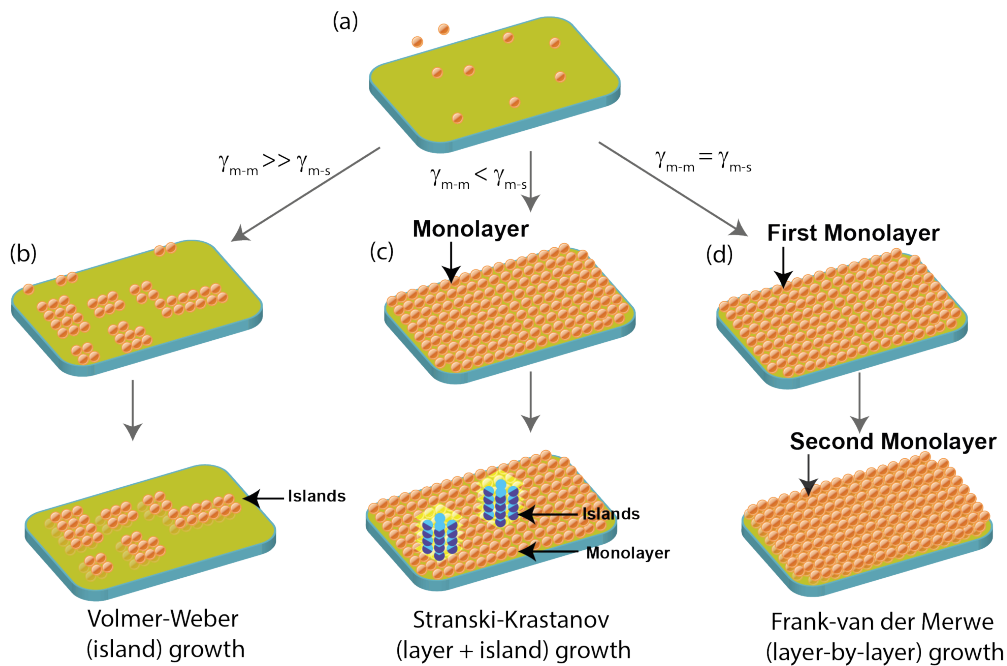


Figure 1.13 – Starting with a glass substrate (a) a schematic of three distinct growth models - Volmer-Weber (b), Stranski-Krastanov (c) and Frank-van der Merwe model (d)

clusters grow together to form large crystals. The interaction between molecules are much stronger than the molecule-substrate interaction (i.e  $\gamma_{m-m} \gg \gamma_{m-s}$ ). This leads to island formation as molecules hold together by weak van-der Waals force (Figure 1.13b).

2. **Stranski-Krastanov growth model:** Unlike the Volmer-Weber growth model, when the interaction between molecule is reduced and the molecule-substrate interaction is enhanced (i.e  $\gamma_{m-m} < \gamma_{m-s}$ ), this acts as driving force to form a monolayer of molecules on the substrate (Figure 1.13c). Further deposition of the molecules, limits its interaction to the first monolayer formed on the substrate, thereby initiating island formation of molecules on top of the monolayer.
3. **Frank-van der Merwe growth model:** When there is no energy barrier between the molecule-molecule and molecule-substrate interaction (i.e  $\gamma_{m-m} = \gamma_{m-s}$ ), monolayer formation is highly feasible. Furthermore, in this growth technique, the monolayer completion tends to be more dominant than the island formation. This is because, formation of islands before completion of first monolayer will have an energy penalty making it an energetically unfavorable situation. After formation of the first monolayer, the next monolayer starts developing (Figure 1.13d)<sup>[74]</sup>

### 1.8 Exciton Dynamics in J-aggregates

Following the growth of J-aggregate thin films, understanding the exciton dynamics is the prime focus of this thesis. Unlike in molecular crystals, the exciton migration length in J-aggregates was reported to be orders of magnitude larger. Exciton migration in J-aggregates are treated as coherent (or band type) or incoherent (or hopping type). In the case of coherent transport, the exciton moves in a wave-like fashion before getting scattered by defects or phonons, where it loses coherence.<sup>[46,75,76]</sup> The characteristic time at which coherence is lost is called *dephasing time* and tuning this time can be helpful in studying the coherent diffusion length in J-aggregates.<sup>[50]</sup> For instance, as phonons are thermally excited, cooling the system minimizes exciton-phonon coupling and thereby increasing the dephasing time. This implies longer diffusion length at low temperatures. On the other hand, structural defects like grain boundaries or crystal imperfections are independent of temperature. In this situation, the excitons can hop from one site to another in random fashion, to initiate incoherent exciton transfer. Nevertheless, it is generally observed that the diffusion length for incoherent hopping is much smaller than coherent diffusion.<sup>[48]</sup> To have coherent exciton migration at room temperature, the exciton coupling needs to be much larger than  $kT$  and energetic disorder in the system. Although, J-aggregates possess high exciton coupling ( $\sim 500\text{-}1000\text{ cm}^{-1}$ ), the static disorder, in particular, 2D J-aggregates influence the exciton migration as elucidated in Chapter 2.

Exciton migration length in J-aggregates (both 1D and 2D) were studied using several techniques:

#### 1. Quenching experiments

Preliminary experiments by Scheibe<sup>[41]</sup> showed that the photoexcitation in J-aggregates (donor) can be quenched by adding small amounts of quenching molecules (acceptor), signifying an extended exciton migration length. Later, exciton migration length in monolayers were studied to understand the diffusion length over several molecules at room temperature.<sup>[51,77]</sup> Initially, Möbius and co-workers<sup>[77,78]</sup> proposed that the rate of energy transfer from donor to acceptor decreases with temperature. Later, Scheblykin<sup>[79]</sup> showed that the exciton migration is strongly  $T$ -dependent and observed *exciton-exciton annihilation* at low temperatures. A quantitative description on static and dynamic disorder effects on exciton migration was described.<sup>[79]</sup>

#### 2. Exciton-Exciton Annihilation (EEA)

Unlike quenching experiments, the EEA technique requires only pristine J-aggregates films to calculate the exciton migration length. The photoluminescence (PL) of the J-aggregates are recorded with increase in laser fluence. From the relation between PL intensity *versus* fluence ( $\text{PL} \propto I^n$ ), two different mechanism can be inferred (Figure 1.14a). When  $n=1$ , the



PL trend remains to be linear, signifying a constant emission as more photons are pumped in with increase in fluence. On the other hand, with increase in exciton density, the excitons ((1) and (2)) can migrate (coherent or hop) to collide with each other. In this situation, a bi-exciton is formed, by suppression of one exciton (1) and transferring the other exciton to form a bi-exciton (3). Quick relaxation of electron from  $\langle e2 \rangle$  state to  $\langle e1 \rangle$  state, results in reduction of two-exciton to one-exciton with reduced PL intensity (Figure 1.14b). This trend leads to sub-linearity ( $n < 1$ ) behaviour, which is generally observed during excitation at very high densities ( $1 \mu\text{J cm}^{-2}$ ).<sup>[80]</sup> This nonradiative recombination of excitons can be represented as,

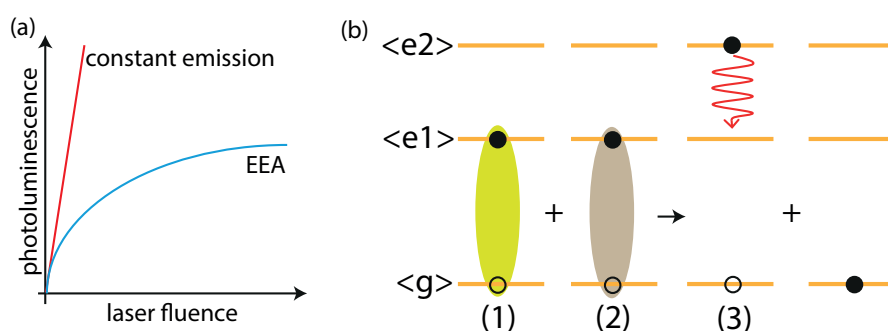
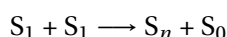


Figure 1.14 – Visualization of photoluminescence *versus* laser fluence trends showing constant emission and exciton-exciton annihilation (EEA) (a). Formation of bi-exciton showing exciton quenching during annihilation (b). Here  $\langle g \rangle$ ,  $\langle e1 \rangle$  and  $\langle e2 \rangle$  represents ground state, first excited state and second excited state, respectively.

In chapter 2, we will introduce a new exciton quenching mechanism - "*charge-exciton quenching*" in the presence of excess excitation energy (instead of fluence) which is different from exciton-exciton annihilation.

## 1.9 Perspective on Exciton Migration in J-aggregates

Using one of the above mentioned techniques, researchers have measured (or estimated) the exciton migration length in J-aggregates. For 1D J-aggregates, tubular J-aggregate are already present in solution and preparation of solid-state thin films is very simple. Eisele<sup>[81]</sup> used drop-casting route by dropping the J-aggregate solution on cleaned glass substrate and characterized them using near-field scanning optical microscopy (NSOM). Later, Caram et al.<sup>[35]</sup> showed that dispersing the tubular J-aggregates in a sucrose-trehalose matrix reduces the photo-bleaching effect and used EEA studies to characterize the exciton migration length. Room temperature exciton migration length of  $\sim 1.6 \pm 1 \mu\text{m}$  was reported, which is also the highest reported value so far.<sup>[35]</sup>

For 2D J-aggregates, Akselrod<sup>[80]</sup> followed LBL approach to deposit TDBC J-aggregates and

conducted exciton-exciton annihilation studies. An exciton migration length of  $\sim 44$  nm was estimated despite having uniform J-aggregate films as claimed by Bradley et al.<sup>[71]</sup> Sorokin et al.<sup>[82]</sup> showed exciton self-trapping in the J-aggregate films deposited by LBL route. Considering a multi-layer J-aggregate film deposited by LBL route, presence of polyelectrolyte between two J-aggregate layer inhibits exciton coupling. Furthermore, the stacking defects like grain boundaries acts as fluorescence (or exciton) quencher, thereby limiting the exciton migration length in 2D J-aggregates. In organic crystals, exciton quenching at the grain boundaries promotes free-charge carrier formation at the grain boundaries and these charge carriers can accelerate exciton quenching.<sup>[83]</sup>

Therefore, growing coherent, large 2D J-aggregates thin films and minimizing the interference of polyelectrolyte layer forms the motivation of this work. This was achieved by exploiting the growth route shown by Steiger et al.<sup>[64]</sup> as detailed in Chapter 2 of this thesis.

### 1.10 Recent Applications of J-aggregates in Optoelectronic Devices

J-aggregates were initially used as spectral sensitizers in photographic films,<sup>[62,84]</sup> optical recording<sup>[85]</sup> and fluorescent labels for bio-medical applications.<sup>[86,87]</sup> Here, some recent applications where J-aggregates are currently explored will be discussed below:

#### 1.10.1 Narrowband photodetectors

Devices which can convert optical to electrical signals are called photodetectors. Cyanine dyes are mostly used as photodetectors with a focus on extending the light absorption to the infrared region.<sup>[33,36,88–90]</sup> Osedach et al.<sup>[89]</sup> demonstrated the concept of using J-aggregates in photodetectors to extend the infrared absorption limit. On the other hand, narrowband photodetectors are gaining attention for several applications in medicine, aerospace, surveillance and robotic sensors. The main feature of narrowband photodetector material is to have an absorption spectrum with full-width at half maximum (FWHM) less than 100 nm with high external quantum efficiency (EQE meaning number of charge carriers collected to the number of photons incident on the device)  $\sim 15\%$ .

Several techniques like fabricating micro-cavity to generate charge carriers from the charge-transfer (CT) state,<sup>[91]</sup> charge-collection narrowing (CCN)<sup>[92]</sup> and from plasmon states<sup>[93]</sup> are reported. In general, CCN technique gained more attention among researchers in perovskite and organic electronics, that was followed up to further development like improving the EQE beyond 100 % (gain) using photomultiplication effect.<sup>[94–96]</sup> Therefore, it is worth detailing the CCN mechanism as a motivation for narrowband photodetectors demonstrated so far.

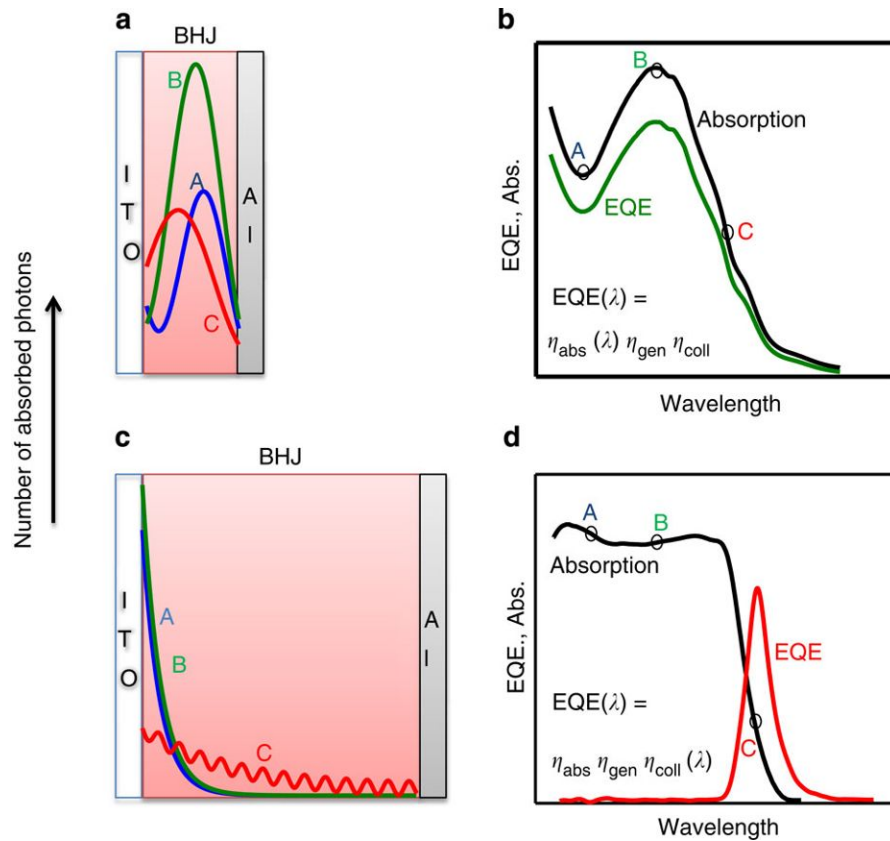


Figure 1.15 – Conventional photodiode (a) using bulk-heterojunction (BHJ) photo-active layer for charge generation using photoexcitation for all three wavelengths (A,B and C) of the absorption spectrum as shown in (b). Charge-collection narrowing (CCN) with a thick (BHJ) device where collection is enhanced only for wavelength marked "C" (c) resulting in a narrow EQE (d). Adapted with permission from Armin et al.<sup>[97]</sup>

### Working principle of charge-collection narrowing (CCN)

Armin et al.<sup>[97]</sup> have used PCDTBT:PC<sub>70</sub>BM [(poly[N-9-heptadecanyl-2,7-carbazole-alt-5,5-(4,7-di-2-thienyl-2,1,3- benzothiadiazole)]:PC<sub>70</sub>BM] as donor:acceptor blend which normally has a broadband absorption. A conventional photodiode was fabricated by spin-coating PCDTBT:PC<sub>70</sub>BM blend on an indium tin oxide (ITO) substrate with evaporated aluminum as top electrode to complete the device (Figure 1.15a). The absorption and EQE are shown in Figure 1.15b, where EQE almost follows the profile of absorption. It can be noted that the spectral distribution for all the three wavelengths are similar as shown in Figure 1.15a.

Upon increasing the film thickness of the active layer from 700 nm to ~2  $\mu$ m, the spectral distribution gets altered. The photons at shorter wavelength are strongly absorbed at the ITO interface, while long wavelength photons (marked C) penetrate longer distance into the device (Figure 1.15c). This effect enhanced the collection efficiency ( $\eta_{coll}$ ) in the EQE for longer wavelength while suppressing the shorter wavelength due to imbalanced charge carrier

## Chapter 1. Introduction

---

transport. Collectively, a narrowband photodetector with FWHM of the EQE in sub-100 nm range was demonstrated (Figure 1.15d).

This requirement of high EQE with FWHM in sub-100 nm range motivates to explore the ultra-narrow absorption bands with FWHM < 50 nm in J-aggregates for narrowband photodetection. Moreover, the wavelength of the absorption edge can be tuned from visible to infra-red region by extending the polymethine bridge length. This will be discussed in detail in Chapter 3 in this thesis. The figure-of-merit for narrowband photodetectors are EQE, response time and noise current. These characterization techniques will be elaborated here.

### External Quantum Efficiency (EQE)

External quantum efficiency or incident photon to converted electron ratio (IPCE) is defined as number of electrons extracted per second to the number of photons incident per second on the device. This relation is given as,

$$EQE = \frac{\text{number of extracted electrons/s}}{\text{number of incident photons/s}} = \frac{h \cdot c \cdot I}{e \cdot \lambda \cdot P} \quad (1.18)$$

where,  $h$  - Planck constant,  $c$  - speed of the light in vacuum,  $I$  - current generated from the device,  $e$  - elementary charge,  $\lambda$  - wavelength and  $P$  - power of the incident light.

In an ideal case, if all the absorbed photons are converted into charge carriers and extracted, then the EQE of the device is unity (or 100 %). Generally, other effects like charge-recombination, scattering of incident photon affects the IPCE. To determine the number of incident photons at different wavelengths, standard Silicon photodiode with a known spectral response is first measured. With this reference sample, the devices are connected and measured for wavelength of interest under different bias condition. Different from solar cells, the photodetector functions in reverse bias.

Based on the EQE values, one can calculate  $IQE$  and responsivity ( $R$ ) using the following equations,

$$IQE = \frac{EQE}{\text{number of absorbed photons/s}} = \frac{EQE}{A_t} \quad (1.19)$$

$$\text{Responsivity (R)} = \frac{EQE \cdot \lambda}{1240} (A/W) \quad (1.20)$$

$IQE$  is the internal quantum efficiency taking absorption into account, whereby  $EQE$  is divided by the true absorbance ( $A_t$ ) of the active layer. Responsivity ( $R$ ) gives the ratio of photocurrent generated to the incident radiant energy ( $W$ ). This can be calculated from the  $EQE$  as shown in eqn.1.20. The unit of  $R$  is  $A/W$ .

### Transient photocurrent response characterizations

One of the main figures-of-merit for a photodetector is response time - the time required for a photodetector to respond to an incident photon. The photocurrent response upon illumination with white light will be measured. From the photocurrent, the rise time ( $\tau_r$ ) will be calculated from the difference between the time taken to rise from 10% to 90% of the photocurrent (Figure 1.16).

To understand the dynamic behaviour of the photodetector, the response time measured will be performed for light pulses with different frequencies. From this data, the cut-off frequency ( $f_{-3dB}$ ) will be determined. This -3dB point is the frequency at which the input signal power drops by 50% (in other words, the measured photocurrent decreases to 0.71 of the initial value)<sup>[98]</sup>

The above mentioned concept on narrowband photodetectors are studied using J-aggregates and discussed in Chapter 4 in this thesis. Furthermore, these photodetectors are mostly pixelated devices and additive manufacturing techniques using solution-processing route to fabricate these photodetectors for large volumes, will push this concept for industrialization. The next section will introduce one of the manufacturing technique - inkjet printing which was followed in this thesis work to demonstrate the capability of printing these narrowband photodetectors as discussed in Chapter 4.

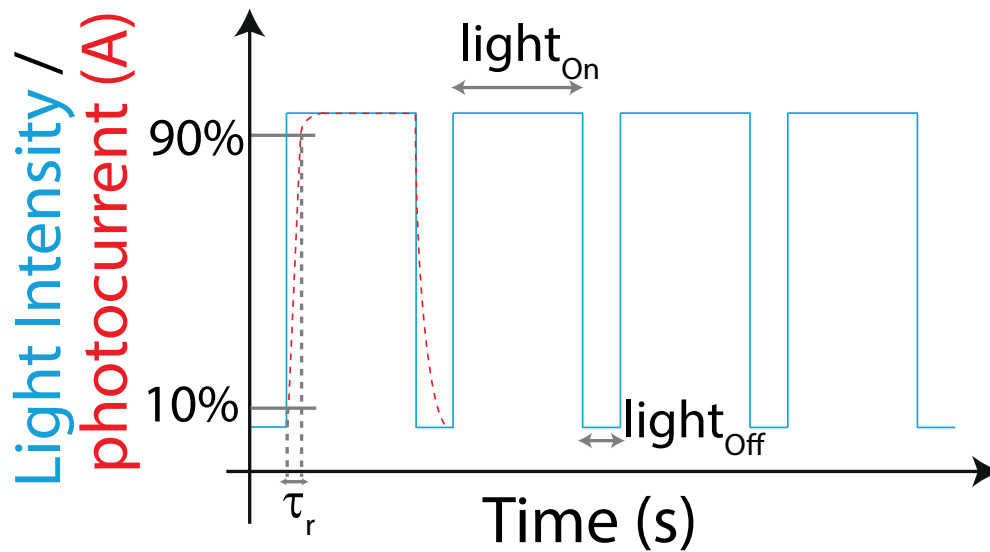


Figure 1.16 – Illustration of response time calculation from the light pulse

### Inkjet printing

Inkjet printing (IJP) evolves from the patented work of Lord William Kelvin for direction of droplets using electrostatic forces, which was developed for graphics printing and used for printing functional materials. Direct deposition of solutions onto a substrate in a non-contact, mask-less mode with a possibility to pattern a required structure without lithography technique and later transforming into solid structures appeals this technology among wide community. The pattern resolution is limited by the droplet volume and spreading diameter of the droplet on the substrate, which promoted this technique to build several prototypes of new device stacks in lab-scale. In organic electronics, IJP has been used to completely print organic light emitting diodes (OLEDs),<sup>[99]</sup> organic field-effect transistors (OFETs),<sup>[100]</sup> and organic photovoltaics (OPVs).<sup>[101]</sup>

In general, continuous inkjet printing (CIJ) was the primary technique to transfer the material from the liquid container to the substrate which was developed further to print in a controlled manner and called as drop-on-demand (DOD) technique. In CIJ technique, a stream of liquid droplets formed due to Rayleigh instability of the liquid is ejected through a nozzle onto the substrate. The droplets are accelerated by applying voltage to the deflector plates thereby charging the liquid droplet and to drive them towards the substrate. It is a continuous process, where the system continues to dispense the droplet even when there is no requirement for printing, where the excess material is removed through the gutter. This leads to wastage in the case of non-reusable or expensive inks. Further development of this technique lead to drop-on-demand (DOD) technique, where an external stimuli, either thermal or mechanical force enables the drop formation (Figure 1.17a and b). This was advantageous in printing the inks under controlled manner. We have used a piezoelectric actuator to control the droplet formation, by applying a voltage waveform with frequencies in the acoustic range (1-20 kHz) which resonates between the electrodes thereby forming a droplet and guiding

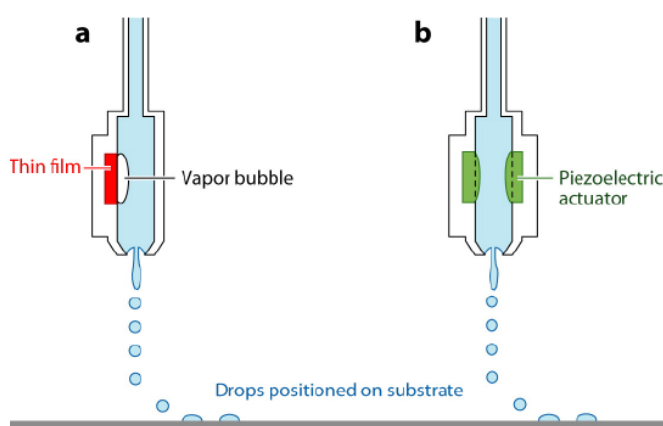


Figure 1.17 – Schematic illustration showing drop-on-demand (DOD) inkjet printing system with a liquid filled container facilitated with a thin film heater (a) or by mechanical actuation (b) to form droplets. Adapted with permission from Brain Derby<sup>[102]</sup>

the droplet to the substrate. It is noteworthy to mention that this ink-jet printing technology has stringent requirements to process inorganic and organic component inks for printing. Although, inorganics are stable across several solvents to match the criteria for printing, organic materials suffer from solubility issues which is difficult to process. This limitation of solubility of the organic component was circumvented by devising an organic vapor jet printing (OVJP), which is a combination of molecular evaporation and carrier gas controlled jet printing.<sup>[103]</sup> Briefly, a hot carrier gas (Argon or Neon) with the molecular vapor is passed through a nozzle which forms a collimated gas beam. Upon getting in contact with the cold substrate, the molecules condense to form a thin layer. The advantage of OVJP over conventional ink-jet printing is reduction of nozzle clogging and much more control over pattern resolution.

In this thesis work, the photodetector involves both inorganic ( $\text{TiO}_2$ , as electron acceptor) and organic (J-aggregates) components, which are printed using a DOD technique to demonstrate the manufacturing capability of the narrowband photodetector.

### 1.10.2 Polariton lasers

Conventional lasers are generated by stimulated emission from the electrons which are pumped to higher energy states undergoing relaxation to the lower state to give an emission. In this case, an electron in a higher energy level, at a different time interval, can emit a photon to reach the low-energy state. This process introduces incoherence in the emitted photon with random phase. The most favorable condition will be, to have all the electrons populated to one excited state. This advancement would benefit in building lasers with low power excitation, however, due to the Pauli exclusion principle, more than two electrons (with different spin) cannot occupy the same quantum state. This can be obviated when electrons are substituted by excitons. Creating a Bose-Einstein (BE) condensate will lead to funnel all the occupancy to the lowest quantum state. Generally, BE condensates are feasible for inorganics at low temperature, however, BE condensates were observed at room temperature using polymers.<sup>[104]</sup>

The design of a polariton laser involves an optical micro-cavity developed with reflecting mirrors (dielectric Bragg reflectors, DBR) and filled with an organic active layer. This design leads to the formation of strong coupling between excitons and cavity photons, a state of composite Bosonic quasi-particle called as exciton-polaritons, which is half-light and half-matter. The coupling between exciton and photons gives rise to two new states - upper polariton branch (UPB, higher energy) and lower polariton branch (LPB, lower energy). Lidzey<sup>[105]</sup> introduced tetra-(2,6-t-butyl)phenol-porphyrin zinc (organic material) in a micro-cavity and observed a strong-coupling regime in exciton-photon interaction.

As J-aggregates show a coherent state when they are excited with a photon and this motivated the researchers to explore J-aggregates as a lasing material. First studies were conducted to use J-aggregates as active layer in a microcavity and strong coupling between excitons-polariton was observed.<sup>[107]</sup> When J-aggregates are coupled to a cavity, exciton-exciton annihilation

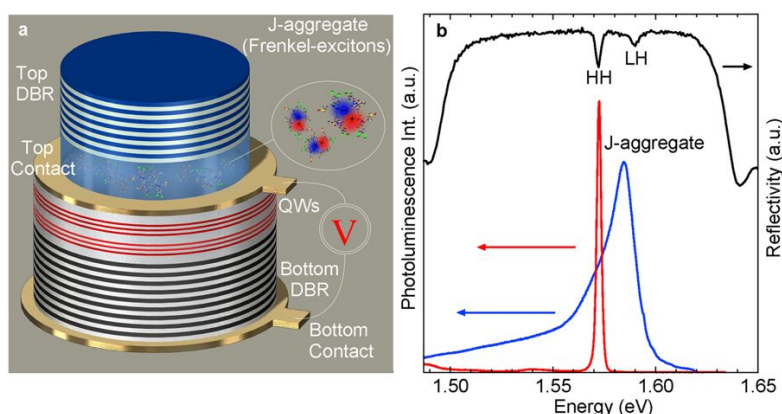


Figure 1.18 – Hybrid microcavity structure using J-aggregates in top DBR and GaN quantum wells in bottom DBR (a). Reflectivity and PL spectra recorded for GaN and J-aggregates at 25 K (b). Credit: Paschos et al<sup>[106]</sup> Link to license <https://creativecommons.org/licenses/by/4.0/>

was observed as competing to polariton formation.<sup>[80]</sup> Recently, a polariton laser (upto 200 K) was demonstrated using organic-inorganic hybrid structure with J-aggregates as the organic component and GaN as inorganic component (Figure 1.18a).<sup>[106]</sup> The reflectivity of the bottom cavity and PL spectra for GaN and J-aggregates are shown in Figure 1.18b. Although this demonstration of J-aggregate for polariton lasers are interesting, the quantum yield of the J-aggregates are mostly limiting their application in such light emitting devices. Typical, photoluminescence quantum yield of J-aggregates in solution is ~5%. In Chapter 3, ways to improve the quantum yield of J-aggregates in solution from 4% to 60% at room temperature will be discussed.

### 1.10.3 Excitonic channels and PL enhancers

Initially, linear helical J-aggregates are formed by anchoring dimers to the DNA that extends to J-aggregates. This became a topic of interest to study energy transfer using FRET and in recent time, programming controlled exciton migration on linear templates are gaining significant attention and need for 1D J-aggregates.<sup>[108,109]</sup> Researchers have explored 1D J-aggregates as *exciton-bridge* and PL enhancers as explained below.

Similar to J-aggregate films deposited using LBL as described in section 1.6.2, inorganic quantum dots are also deposited using LBL approach to fabricate devices.<sup>[110]</sup> Wang and Weiss<sup>[7]</sup> showed that replacing the polyelectrolyte layer by J-aggregates between lead sulfide quantum dots have shown a 20-fold improvement in energy transfer rate. Thanks to the high FRET rate in the J-aggregates, which act as *exciton-bridge* in this case.

Furthermore, with the long exciton migration achieved in tubular J-aggregates, which are also called as light-harvesting nanotubes (LHNs), they are used for PL enhancers in inorganic quantum dots. Freyria et al.<sup>[54]</sup> have coupled LHNs to inorganic quantum dots to explore the unique properties of LHNs - the strong absorption coefficient and long range exciton



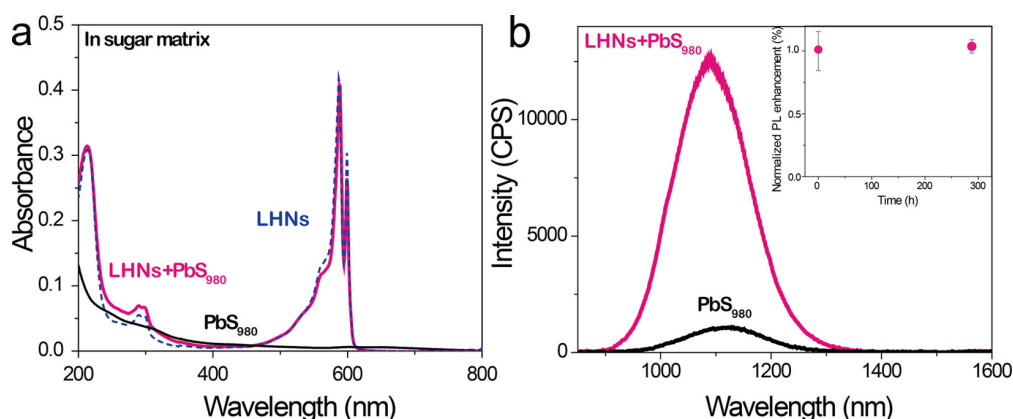


Figure 1.19 – Absorption spectra for J-aggregate (LHNs) coupled with inorganic quantum dot ( $\text{PbS}_{980}$ ) in a sucrose-trehalose (sugar) matrix (shown in purple), in comparison with individual  $\text{PbS}_{980}$  (black line) and LHNs (blue line) (a). PL spectra of LHNs coupled with  $\text{PbS}_{980}$  and  $\text{PbS}_{980}$  control sample excited at 532 nm; inset: normalized PL enhancement of QDs over time. The samples were kept under room light, and the PL enhancement was measured after 12 days. Reprinted and Adapted with permission from Freyria et al.<sup>[54]</sup> ©2017 American Chemical Society

migration in J-aggregates (LHNs). Here, the extinction coefficient of quantum dots ( $\text{PbS}_{980}$ ) are extremely low compared to the LHNs (Figure 1.19a). When excited at 532 nm, the energy transfer from J-aggregates to  $\text{PbS}_{980}$  leads to strong increase in fluorescence (Figure 1.19b). It can be observed that, in both cases the same cyanine dye molecule forming tubular J-aggregates are exploited for energy transfer. On the other hand, using DNA templates have their own limitation due to dimer formation, which can trap exciton transport. In Chapter 5, linear templates like dendronized polymers (DPs) are explored to form J-aggregate nanowires. Different generation of DPs show different template length which was helpful to control the length of the nanotubes and the aggregate length. A unique growth of J-aggregates on DP was observed unlike the case of DNA templates. From this growth modification, a high quality (high J-aggregate to monomer absorption) J-aggregate nanowires were obtained. Furthermore, in Chapter 6, we show that dimers which are non-emissive can be turned into highly emissive dimers in solid-state.<sup>[111]</sup> This modification was used to develop highly emissive organic light emitting electrochemical cells (OLECs).<sup>[112]</sup>

## 1.11 Aim of the Thesis

J-aggregates are a very active field of research due to their both foundational and application-oriented aspects of their strong light-matter interaction. The wide interest ranges from polaritons over photovoltaics to light emitting devices. Despite the fact that optical properties of J-aggregates have been studied extensively in solution, the growth routes to obtain solid-state 2D J-aggregate assemblies are very limited. The present growth routes (like LBL or spin-coating) have their own disadvantage on exciton dynamics, demanding a better growth

technique. This key challenge is tackled here with a simple growth route to obtain large coherent domains which can suppress non-radiative decay channels thereby facilitating better exciton migration. Furthermore, their low quantum yield, that has been a roadblock for many emissive applications (e.g., narrowband organic LEDs, polariton condensates) are addressed in this thesis. 1D J-aggregates are recently receiving immense attraction for excitonic channels and PL enhancers in the NIR region. With the limitation on the chemical structure to tune for 1D J-aggregates, researchers have focussed on utilising the DNA templates to fabricate 1D J-aggregate nanowires. An alternate template, dendronized polymers are used here to develop high quality J-aggregate nanowires. Apart from growth route and optical properties, the J-aggregates are implemented in a device stack to explore them as narrowband photodetectors. The wavelength-selectivity, narrowband absorption and excellent device performance motivated to demonstrate ink-jet printable device which opens new avenue for solution processable next-generation photodetectors. Overall, this thesis work focusses on the understanding the fundamentals of exciton dynamics in 2D J-aggregates by tuning their growth morphology, fabricating devices for narrowband photodetector application and demonstrating an additive manufacturing route - inkjet printability. The structure of the thesis is detailed below as a guide to the reader.

In Chapter 2, the growth model to obtain 2D J-aggregates in thin films on a dendrimer functionalized glass substrate will be described. The parameters to control the growth of coherent J-aggregate crystals by overcoming the disorders as reported in the LBL process will be explained. Furthermore, the effect of disorder (static and energetic) on exciton dynamics in 2D J-aggregate thin films will be studied using optical spectroscopy (at room temperature) and femtosecond spectroscopy at low temperature (6 K). The outcome of this study will demonstrate the enhancement in radiative decay of excitons in the large J-aggregate crystals, which overcomes the non-radiative channel - "charge-exciton quenching" that are strongly influencing the exciton migration in spin-coated and conventional J-aggregate films will be discussed.

Beyond absorption, exploring the photoluminescence properties of J-aggregate in solution will be the focus of Chapter 3. J-aggregates show very narrow photoluminescence (FWHM  $< 20$  nm), which are interesting for color purity emitters, however, the quantum yield of the J-aggregates are  $\sim 5\%$ . As explored in Chapter 2 in this thesis, despite growing coherent large crystals the quantum yield in thin films improved by 2-fold (absolute quantum yield  $\sim 4\%$ ). A significant amount of non-radiative decay channel present in the J-aggregate solution will be addressed by adding alkylamines, where a drastic increase in photoluminescence quantum yield of J-aggregates from 5% to 60% was achieved. Using small-angle neutron scattering (SANS), the structural reorganization in the J-aggregates which suppresses non-radiative decay will be discussed. Guidelines to achieve high quantum yield J-aggregates in a ternary phase diagram will be shown in Chapter 3.

An application of J-aggregate as narrowband photodetectors to obtain reasonable EQE with FWHM  $< 25$  nm for three different J-aggregates showing spectral response in visible (580 nm)

to infra-red region (1000 nm) will be discussed in Chapter 4. To the extent these detectors are solution processable by spin-coating the electron transport layer and active layer, the devices are inkjet printed to demonstrate the capability of printing this device. Optimized inkjet printed devices shows similar performance as spin-coated devices. Figure-of-merits like EQE, responsivity, response time and noise current will be discussed.

1D J-aggregates which showed efficient energy transfer was limited to only one (C8S3) cyanine dye. To open the possibilities to have 1D tubular J-aggregates which can mimic the naturally occurring LHA architecture, 1D tubular aggregates were constructed by using a linear dendronized polymer (DP) scaffold and to adsorb J-aggregates on the DP surface. This forms the focus of Chapter 5, where a solution complexation route with dendronized polymer and J-aggregates from a trimethine cyanine dye, leading to high quality supramolecular J-aggregate nanowires in the solid state is unravelled. By first complexing polymer and dye in solution instead of adsorbing dye onto a monolayer DP template, restrictions of J-aggregate growth due to immobilized DPs is minimized. Using a layer-by-layer technique, these high quality nanowires are selectively deposited on a substrate. This growth mechanism is demonstrated for the first time in the literature. Small-angle x-ray scattering (SAXS) revealed a core-shell configuration of the J-aggregate – DP hybrid structure.

While 1D tubular aggregates are deposited on DNA substrates, the presence of dimers in the edges can strongly localize the exciton. Dimers are present in most of the solution processed cyanine devices which affects the optical properties of the device, for instance, by quenching photoluminescence. So, it is important to overcome this dimers in thin films to enhance the properties of optoelectronic devices. In Chapter 6, a strongly red-shifted photoluminescence peak observed from dimers will be explained from the aspect of molecular packing. A long lifetime with high photoluminescence quantum yield from these dimers which are important parameters for light emitting devices was helpful in another study.<sup>[112]</sup>



# Bibliography

- [1] G. E. Moore, *Electronics* **1965**, 38, 114–117.
- [2] G. Grosso, J. Graves, A. T. Hammack, A. A. High, L. V. Butov, M. Hanson, A. C. Gossard, *Nature Photonics* **2009**, 3, 577–580.
- [3] D. Unuchek, A. Ciarrocchi, A. Avsar, K. Watanabe, T. Taniguchi, A. Kis, *Nature* **2018**, 560, 340–344.
- [4] N. P. D. Sawaya, D. Rappoport, D. P. Tabor, A. Aspuru-Guzik, *ACS Nano* **2018**, 12, 6410–6420.
- [5] A. A. High, E. E. Novitskaya, L. V. Butov, M. Hanson, A. C. Gossard, *Science* **2008**, 321, 229–231.
- [6] B. J. Walker, V. Bulović, M. G. Bawendi, *Nano Letters* **2010**, 10, 3995–3999.
- [7] C. Wang, E. A. Weiss, *Nano Letters* **2017**, 17, 5666–5671.
- [8] A. Köhler, H. Bässler in *Electronic Processes in Organic Semiconductors*, John Wiley Sons, Ltd, **2015**, Chapter 1, pp. 1–85.
- [9] M. Pope, C. E. Swenberg, *Electronic processes in organic crystals and polymers*, 2nd ed, Rev. ed. of: *Electronic processes in organic crystals*. 1982, New York : Oxford University Press, **1999**.
- [10] A. J. Heeger, A. G. MacDiarmid, H. Shirakawa, **2000**.
- [11] Y. Liwschitz, *Israel Journal of Chemistry* **1963**, 1, 121–121.
- [12] M. Kasha, H. R. Rawls, M. Ashraf El-Bayoumi, *Pure and Applied Chemistry* **1965**, 11, 371–392.
- [13] A. Köhler, H. Bässler in *Electronic Processes in Organic Semiconductors*, John Wiley Sons, Ltd, **2015**, Chapter 2, pp. 87–191.
- [14] F. C. Spano, *Accounts of Chemical Research* **2009**, 43, 429–439.
- [15] F. C. Spano, C. Silva, *Annual Review of Physical Chemistry* **2014**, 65, 477–500.
- [16] F. C. Spano, H. Yamagata, *The Journal of Physical Chemistry B* **2010**, 115, 5133–5143.
- [17] T. Brixner, R. Hildner, J. Köhler, C. Lambert, F. Würthner, *Advanced Energy Materials* **2017**, 7, 1700236–1700269.

## Bibliography

---

- [18] H. Kano, T. Kobayashi, *The Journal of Chemical Physics* **2002**, *116*, 184–195.
- [19] N. Micali, V. Villari, M. A. Castriciano, A. Romeo, L. Monsù Scolaro, *The Journal of Physical Chemistry B* **2006**, *110*, 8289–8295.
- [20] V. Huber, M. Katterle, M. Lysetska, F. Würthner, *Angewandte Chemie International Edition* **2005**, *44*, 3147–3151.
- [21] S. Sengupta, F. Würthner, *Accounts of Chemical Research* **2013**, *46*, 2498–2512.
- [22] T. E. Kaiser, H. Wang, V. Stepanenko, F. Würthner, *Angewandte Chemie* **2007**, *119*, 5637–5640.
- [23] H. Wang, T. E. Kaiser, S. Uemura, F. Würthner, *Chemical Communications* **2008**, 1181–1183.
- [24] F. Nüesch, J. Moser, V. Shklover, M. Grätzel, *Journal of the American Chemical Society* **1996**, *118*, 5420–5431.
- [25] A. Liess, A. Lv, A. Arjona-Esteban, D. Bialas, A.-M. Krause, V. Stepanenko, M. Stolte, F. Würthner, *Nano Letters* **2017**, *17*, 1719–1726.
- [26] K. Cai, J. Xie, D. Zhao, *Journal of the American Chemical Society* **2013**, *136*, 28–31.
- [27] Z. Chen, Y. Liu, W. Wagner, V. Stepanenko, X. Ren, S. Ogi, F. Würthner, *Angewandte Chemie International Edition* **2017**, *56*, 5729–5733.
- [28] J. L. Bricks, Y. L. Slominskii, I. D. Panas, A. P. Demchenko, *Methods and Applications in Fluorescence* **2017**, *6*, 012001.
- [29] F. Würthner, T. E. Kaiser, C. R. Saha-Möller, *Angewandte Chemie International Edition* **2011**, *50*, 3376–3410.
- [30] M. Q. Doja, *Trans.Roy.Soc.Edinburgh* **1856**, *31*, 377.
- [31] M. Q. Doja, *Chemical Reviews* **1932**, *11*, 273–321.
- [32] A. Mishra, R. K. Behera, P. K. Behera, B. K. Mishra, G. B. Behera, *Chemical Reviews* **2000**, *100*, 1973–2012.
- [33] Q. Lin, Z. Wang, M. Young, J. B. Patel, R. L. Milot, L. Martinez Maestro, R. R. Lunt, H. J. Snaith, M. B. Johnston, L. M. Herz, *Advanced Functional Materials* **2017**, *27*, 1702485.
- [34] S. Pascal, A. Haefele, C. Monnereau, A. Charaf-Eddin, D. Jacquemin, B. Le Guennic, C. Andraud, O. Maury, *The Journal of Physical Chemistry A* **2014**, *118*, 4038–4047.
- [35] J. R. Caram, S. Doria, D. M. Eisele, F. S. Freyria, T. S. Sinclair, P. Rebentrost, S. Lloyd, M. G. Bawendi, *Nano Letters* **2016**, *16*, 6808–6815.
- [36] A. C. Véron, H. Zhang, A. Linden, F. Nüesch, J. Heier, R. Hany, T. Geiger, *Organic Letters* **2014**, *16*, 1044–1047.
- [37] P.-A. Bouit, C. Aronica, L. Toupet, B. Le Guennic, C. Andraud, O. Maury, *Journal of the American Chemical Society* **2010**, *132*, 4328–4335.
- [38] E. E. Jelley, *Nature* **1936**, *138*, 1009.

- [39] E. E. Jelley, *Nature* **1937**, 139, 631.
- [40] G. Scheibe, *Angewandte Chemie* **1937**, 50, 212–219.
- [41] G. Scheibe, A. Schöntag, F. Katheder, *Die Naturwissenschaften* **1939**, 27, 499–501.
- [42] G. Scheibe, L. Kandler, *Naturwissenschaften* **1938**, 26, 412–413.
- [43] T. Förster, *Annalen der physik* **1948**, 437, 55–75.
- [44] A. S. Davydov, *Physics-Uspekhi* **1964**, 7, 145–178.
- [45] A. Herz, *Advances in Colloid and Interface Science* **1977**, 8, 237–298.
- [46] S. Kirstein, S. Daehne, *International Journal of Photoenergy* **2006**, 2006.
- [47] H. Fidder, J. Knoester, D. A. Wiersma, *The Journal of Chemical Physics* **1991**, 95, 7880–7890.
- [48] T. Kobayashi, *J-Aggregates*, World Scientific, **1996**.
- [49] H. Fidder, J. Knoester, D. A. Wiersma, *Chemical Physics Letters* **1990**, 171, 529–536.
- [50] S. De Boer, D. A. Wiersma, *Chemical Physics Letters* **1990**, 165, 45–53.
- [51] H. Kuhn, C. Kuhn in *J-Aggregates*, Chapter 1, pp. 1–40.
- [52] G. M. Akselrod, B. J. Walker, W. A. Tisdale, M. G. Bawendi, V. Bulovic, *ACS Nano* **2011**, 6, 467–471.
- [53] B. J. Walker, G. P. Nair, L. F. Marshall, V. Bulovic, M. G. Bawendi, *Journal of the American Chemical Society* **2009**, 131, 9624–9625.
- [54] F. S. Freyria, J. M. Cordero, J. R. Caram, S. Doria, A. Dodin, Y. Chen, A. P. Willard, M. G. Bawendi, *Nano Letters* **2017**, 17, 7665–7674.
- [55] D. M. Eisele, C. W. Cone, E. A. Bloemsma, S. M. Vlaming, C. G. F. van der Kwaak, R. J. Silbey, M. G. Bawendi, J. Knoester, J. P. Rabe, D. A. Vanden Bout, *Nature Chemistry* **2012**, 4, 655–662.
- [56] J. Köhler, *Nature Chemistry* **2012**, 4, 598.
- [57] C. Didraga, A. Pugžlys, P. R. Hania, H. von Berlepsch, K. Duppen, J. Knoester, *The Journal of Physical Chemistry B* **2004**, 108, 14976–14985.
- [58] H. von Berlepsch, S. Kirstein, R. Hania, A. Pugžlys, C. Böttcher, *The Journal of Physical Chemistry B* **2007**, 111, 1701–1711.
- [59] J. L. Lyon, D. M. Eisele, S. Kirstein, J. P. Rabe, D. A. VandenBout, K. J. Stevenson, *Journal of Physical Chemistry C* **2008**, 112, 1260–1268.
- [60] S. Kirstein, H. Möhwald, M. Shimomura, *Chemical Physics Letters* **1989**, 154, 303–308.
- [61] S. Kirstein, H. Möhwald, *Advanced Materials* **1995**, 7, 460–463.
- [62] T. Tani in *J-aggregates*, World Scientific, **1996**, pp. 209–228.
- [63] K. Hosoi, A. Hirano, T. Tani, *Journal of Applied Physics* **2001**, 90, 6197.
- [64] R. Steiger, R. Pugin, J. Heier, *Colloids and Surfaces B: Biointerfaces* **2009**, 74, 484–491.

## Bibliography

---

- [65] K. Misawa, T. Kobayashi in *J-aggregates*, World Scientific, **1996**, pp. 41–65.
- [66] H. Hada, Y. Yonezawa, H. Inaba, *Berichte der Bunsengesellschaft für physikalische Chemie* **1981**, *85*, 425–430.
- [67] S. Daehne, U. De Rossi, J. Moll, *Journal of The Society of Photographic Science and Technology of Japan* **1996**, *59*, 250–259.
- [68] J. Kirkland, *Analytical Chemistry* **1965**, *37*, 1458–1461.
- [69] R. Iler, *Journal of Colloid and Interface Science* **1966**, *21*, 569–594.
- [70] H. Fukumoto, Y. Yonezawa, *Thin Solid Films* **1998**, *327-329*, 748–751.
- [71] M. S. Bradley, J. R. Tischler, V. Bulović, *Advanced Materials* **2005**, *17*, 1881–1886.
- [72] H. Aviv, Y. R. Tischler, *Journal of Luminescence* **2015**, *158*, 376–383.
- [73] J. Venables, *Introduction to Surface and Thin Film Processes*, Cambridge University Press, **2000**.
- [74] E. Bauer, *Zeitschrift für Kristallographie-Crystalline Materials* **1958**, *110*, 372–394.
- [75] I. Scheblykin, O. Y. Sliusarenko, L. Lepnev, A. Vitukhnovsky, M. Van der Auweraer, *The Journal of Physical Chemistry B* **2001**, *105*, 4636–4646.
- [76] C. Spitz, S. Daehne, *International Journal of Photoenergy* **2006**, *2006*, 1–7.
- [77] D. Möbius, H. Kuhn, *Journal of Applied Physics* **1988**, *64*, 5138–5141.
- [78] D. Möbius, H. Kuhn, *Israel Journal of Chemistry* **1979**, *18*, 375–384.
- [79] I. Scheblykin, O. Y. Sliusarenko, L. Lepnev, A. Vitukhnovsky, M. Van der Auweraer, *The journal of physical chemistry B* **2001**, *105*, 4636–4646.
- [80] G. M. Akselrod, Y. R. Tischler, E. R. Young, D. G. Nocera, V. Bulovic, *Phys. Rev. B* **2010**, *82*, 113106.
- [81] D. M. Eisele, J. Knoester, S. Kirstein, J. P. Rabe, D. A. Vanden Bout, *Nature Nanotechnology* **2009**, *4*, 658–663.
- [82] A. V. Sorokin, N. V. Pereverzev, I. I. Grankina, S. L. Yefimova, Y. V. Malyukin, *The Journal of Physical Chemistry C* **2015**, *119*, 27865–27873.
- [83] R. R. Lunt, J. B. Benziger, S. R. Forrest, *Advanced Materials* **2010**, *22*, 1233–1236.
- [84] R. S. Eachus, A. P. Marchetti, A. A. Muentner, *Annual Review of Physical Chemistry* **1999**, *50*, 117–144.
- [85] C. Ishimoto, H. Tomimuro, J. Seto, *Applied physics letters* **1986**, *49*, 1677–1679.
- [86] M. Reers, T. W. Smith, L. B. Chen, *Biochemistry* **1991**, *30*, 4480–4486.
- [87] M. Shakiba, K. K. Ng, E. Huynh, H. Chan, D. M. Charron, J. Chen, N. Muhanna, F. S. Foster, B. C. Wilson, G. Zheng, *Nanoscale* **2016**, *8*, 12618–12625.
- [88] H. Zhang, S. Jenatsch, J. De Jonghe, F. Nüesch, R. Steim, A. C. Véron, R. Hany, *Scientific Reports* **2015**, *5*, 9439.



- [89] T. P. Osedach, A. Iacchetti, R. R. Lunt, T. L. Andrew, P. R. Brown, G. M. Akselrod, V. Bulović, *Applied Physics Letters* **2012**, *101*, 113303.
- [90] M. Young, J. Suddard-Bangsund, T. J. Patrick, N. Pajares, C. J. Traverse, M. C. Barr, S. Y. Lunt, R. R. Lunt, *Advanced Optical Materials* **2016**, *4*, 1028–1033.
- [91] B. Siegmund, A. Mischok, J. Benduhn, O. Zeika, S. Ullbrich, F. Nehm, M. Boehm, D. Spoltore, H. Froeb, C. Koerner, K. Leo, K. Vandewal, *Nature Communications* **2017**, *8*, DOI 10.1038/ncomms15421.
- [92] Q. Lin, A. Armin, P. L. Burn, P. Meredith, *Nature Photonics* **2015**, *9*, 687.
- [93] A. Sobhani, M. W. Knight, Y. Wang, B. Zheng, N. S. King, L. V. Brown, Z. Fang, P. Nordlander, N. J. Halas, *Nature Communications* **2013**, *4*, 1643.
- [94] W. Wang, F. Zhang, M. Du, L. Li, M. Zhang, K. Wang, Y. Wang, B. Hu, Y. Fang, J. Huang, *Nano Letters* **2017**, *17*, 1995–2002.
- [95] Y. Zhong, T. J. Sisto, B. Zhang, K. Miyata, X. Y. Zhu, M. L. Steigerwald, F. Ng, C. Nuckolls, *Journal of the American Chemical Society* **2017**, *139*, 5644–5647.
- [96] Y. Fang, Q. Dong, Y. Shao, Y. Yuan, J. Huang, *Nature Photonics* **2015**, *9*, 679.
- [97] A. Armin, R. D. Jansen-van Vuuren, N. Kopidakis, P. L. Burn, P. Meredith, *Nature Communications* **2015**, *6*, 6343.
- [98] M. Kielar, O. Dhez, G. Pecastaings, A. Curutchet, L. Hirsch, *Scientific Reports* **2016**, *6*, 39201.
- [99] Z. Shu, E. Beckert, R. Eberhardt, A. Tünnermann, *Journal of Materials Chemistry C* **2017**, *5*, 11590–11597.
- [100] T. Carey, S. Cacovich, G. Divitini, J. Ren, A. Mansouri, J. M. Kim, C. Wang, C. Ducati, R. Sordan, F. Torrisi, *Nature Communications* **2017**, *8*, 1202.
- [101] T. Eggenhuisen, Y. Galagan, A. Biezemans, T. Slaats, W. Voorthuijzen, S. Kommeren, S. Shanmugam, J. Teunissen, A. Hadipour, W. Verhees, et al., *Journal of Materials Chemistry A* **2015**, *3*, 7255–7262.
- [102] B. Derby, *Annual Review of Materials Research* **2010**, *40*, 395–414.
- [103] M. Shtein, P. Peumans, J. B. Benziger, S. R. Forrest, *Advanced Materials* **2004**, *16*, 1615–1620.
- [104] J. D. Pluimhof, T. Stöferle, L. Mai, U. Scherf, R. F. Mahrt, *Nature Materials* **2014**, *13*, 247.
- [105] D. G. Lidzey, D. Bradley, M. Skolnick, T. Virgili, S. Walker, D. Whittaker, *Nature* **1998**, *395*, 53.
- [106] G. G. Paschos, N. Somaschi, S. I. Tsintzos, D. Coles, J. L. Bricks, Z. Hatzopoulos, D. G. Lidzey, P. G. Lagoudakis, P. G. Savvidis, *Scientific Reports* **2017**, *7*, 11377.
- [107] J. R. Tischler, M. S. Bradley, V. Bulović, J. H. Song, A. Nurmikko, *Physical Review Letters* **2005**, *95*.

## Bibliography

---

- [108] P. K. Dutta, R. Varghese, J. Nangreave, S. Lin, H. Yan, Y. Liu, *Journal of the American Chemical Society* **2011**, *133*, 11985–11993.
- [109] É. Boulais, N. P. Sawaya, R. Veneziano, A. Andreoni, J. L. Banal, T. Kondo, S. Mandal, S. Lin, G. S. Schlau-Cohen, N. W. Woodbury, et al., *Nature Materials* **2018**, *17*, 159.
- [110] H. Jin, S. Choi, H. J. Lee, S. Kim, *The Journal of Physical Chemistry Letters* **2013**, *4*, 2461–2470.
- [111] S. B. Anantharaman, S. Yakunin, C. Peng, M. V. G. Vismara, C. F. Graeff, F. A. Nüesch, S. Jenatsch, R. Hany, M. V. Kovalenko, J. Heier, *The Journal of Physical Chemistry C* **2017**, *121*, 9587–9593.
- [112] S. Jenatsch, L. Wang, N. Leclaire, E. Hack, R. Steim, S. B. Anantharaman, J. Heier, B. Ruhstaller, L. Penninck, F. Nüesch, et al., *Organic Electronics* **2017**, *48*, 77–84.

## 2 Exciton Dynamics and Effects of Structural Order in Morphology-controlled J-aggregate Assemblies

Surendra B. Anantharaman<sup>1,2</sup>, Thilo Stöferle<sup>3</sup>, Frank A. Nüesch<sup>1,2</sup>, Rainer F. Mahrt<sup>3</sup> and Jakob Heier<sup>1</sup>

<sup>1</sup>Laboratory for Functional Polymers, Swiss Federal Laboratories of Materials Science and Technology, Empa, Überlandstrasse 129, CH-8600 Dübendorf, Switzerland.

<sup>2</sup>Institut des Matériaux, Ecole Polytechnique Fédérale de Lausanne, EPFL, Station 12, CH-1015 Lausanne, Switzerland.

<sup>3</sup>IBM Research-Zürich, Säumerstrasse 4, 8803, Rüschlikon, Switzerland.

**Keywords:** Energetic disorder, Exciton-quenching, J-aggregates, Morphology, Narrow-band emitters.

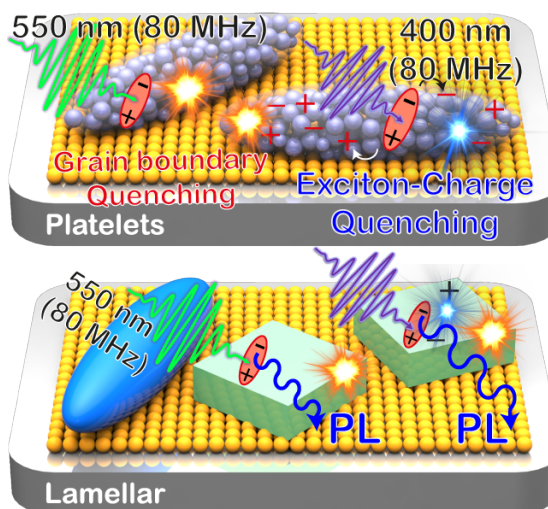
Adapted with permission from Advanced Functional Materials  
©2018 WILEY-VCH Verlag GmbH & Co. KGaA, Weinheim

*Adv. Funct. Mater.*, **2018**, X (X), 1806997, DOI: 10.1002/adfm.201806997  
<https://onlinelibrary.wiley.com/doi/full/10.1002/adfm.201806997>

**Author Contributions:** J.H and F.A.N. wrote the proposal on crystal growth of J-aggregate assemblies on solid substrates. S.B.A developed from this idea to understand the effect of structural order on exciton dynamics in J-aggregate assemblies and planned the work. S.B.A prepared all the samples and characterised them. T.S conducted the ultrafast spectroscopy under the supervision of R.F.M. S.B.A analysed the data and wrote the manuscript with inputs from all co-authors.

### Abstract

Narrow-band photoluminescence (PL) together with high quantum efficiency from organic molecules is essential for high color purity emitters. Supramolecular assemblies like J-aggregates are promising materials due to their narrow PL signal with full-width at half-maximum (FWHM) < 20 nm. However, their micro-crystalline nature and coherent exciton migration results in strong non-radiative exciton recombination at the grain boundaries that diminish the photoluminescence quantum yield (PLQY), and possibilities for improving the crystallinity by tuning the growth mechanism were limited. Here, we demonstrate two distinct routes to



grow different J-aggregate morphologies like platelets and lamellar crystals with improved crystallinity by surface-guided molecular assembly thereby suppressing non-radiative decay and improving PLQY. Both platelets and lamellar crystals show similar absorbance at room temperature. However, temperature-dependent photoluminescence studies show seven-fold (two-fold) higher PLQY for lamellar films compared to platelets at 6 K (300 K). Using time-resolved photoluminescence spectroscopy, different non-radiative decay pathways were identified. The dependence of exciton diffusion on energetic disorder and non-radiative decay will be discussed. The results suggest that the difference in domain size and order gives rise to significantly enhanced radiative decay from lamellar films as compared to platelets or films formed by spin-coating.

### 2.1 Introduction

Supramolecular assemblies have attracted immense interest for adding new functionalities to materials. They are widely explored as energy harvesters,<sup>[1–3]</sup> sensors,<sup>[4]</sup> plasmonic antennas,<sup>[5]</sup> polariton lasers,<sup>[6]</sup> and to build emergent devices like nano-scale exciton-mechanical systems (NEXMS),<sup>[7]</sup> optical and excitonic switches.<sup>[8]</sup> Understanding the supramolecular

chemistry and the resulting structure–property relation paves the way to bridge the gap from molecular assemblies at the nano-scale to optoelectronic devices at the micron-scale. In particular, packing these molecules one-dimensionally (1D) and two-dimensionally (2D) has revealed unique exciton migration properties, one of the important factors for energy harvesting.<sup>[9]</sup> Exciton migration distances in amorphous systems of individual monomers are typically on the order of 10 to 20 nm at room temperature, only. Interestingly, self-assembling organic molecules by non-covalent forces can result in strong coupling of the individual transition dipole moments, leading to giant excited state dipoles as observed in J-aggregates.<sup>[10–12]</sup> These 1D J-aggregates have shown an unprecedented exciton migration up to 1  $\mu\text{m}$  due to low static and energetic disorder.<sup>[13,14]</sup> Although some 1D aggregates are regarded as the rolled-up form of 2D aggregates, the exciton dynamics in the latter is still ambiguous. For instance, exciton transport reported from 2D assemblies is only 60 nm, which is well within the individual domain size ( $\sim 100$  nm) of the crystal ( $\sim 1$   $\mu\text{m}$ ).<sup>[15,16]</sup> As self-assembly is known to be a spontaneous organization process, its 2D control on a solid substrate is highly challenging.<sup>[17]</sup> This spontaneity in self-assembly dictates the crystal size, grain boundaries and energetic disorder which hamper exciton migration.<sup>[18,19]</sup> Reducing the energetic disorder in the J-aggregates can improve the nature of exciton transport from hopping to band-like transport. Besides exciton migration, 2D assemblies show narrowband emission enabling applications in near-monochromatic, high color purity displays.<sup>[18]</sup> However, in large area devices, stacking defects in fluorescent 2D assemblies lead to self-quenching, rendering the growth of such structures with high quantum yield very challenging.<sup>[2]</sup> Finally, growing 2D assemblies on a solid substrate in an aqueous medium is equally demanding for solution-processed printing to fabricate large-area devices. Therefore, it is still necessary to develop an aqueous solution route to grow 2D assemblies on a solid substrate with large crystalline domains thereby enhancing the fluorescence quantum yield for excitonic devices and organic displays.

The focus of the present study, is to demonstrate the growth of different J-aggregates morphologies on functionalized glass substrates. The key control parameters and growth mechanism to obtain high-quality J-aggregate crystals with large coherent domains (3  $\mu\text{m}$ ) will be discussed. Furthermore, the influence of the microscopic environment (like grain boundaries, disorder) of the different morphologies on exciton dynamics and fluorescence quenching at low temperature (6 K) will be investigated.

## 2.2 Results and Discussion

### 2.2.1 Growth mechanism of J-aggregates with different morphologies in solid-state films

We used a solution-processing route to deposit the anionic cyanine dye - **TDBC** (5,6-dichloro-2-[[5,6-dichloro-1-ethyl-3-(4-sulfobutyl)-benzimidazol-2-ylidene]-propenyl]-1-ethyl-3-(4-sulfobutyl)-benzimidazolium hydroxide, inner salt, sodium salt) on functionalized substrates to unravel the growth mechanism of 2D J-aggregates and their optical properties. The chemi-

cal structure of the **TDBC** dye is shown in Figure 2.1a. In the first system, **TDBC** was dissolved in water ( $c = 0.2 \times 10^{-3}$  M) to form J-aggregates in the solution. The molar extinction coefficient and FWHM of the J-aggregate peak at a wavelength of 587 nm in the solution were determined to be  $2.071 \times 10^5 \text{ cm}^{-1}$  and  $\sim 16$  nm ( $479 \text{ cm}^{-1}$ ), respectively, by means of steady-state absorption spectroscopy. The peak-fitting for J-aggregate attenuation is shown in Figure S2.1. Figure 2.1b shows a schematic of the growth mechanism of J-aggregates from three different dye solutions containing J-aggregates (solution 1), monomers (solution 2) as major phase and mixed monomer and J-aggregate phase (solution 3). The stable phase content in the solution has been achieved by tuning the dye content and solvent mixture, as confirmed from the attenuation in Figure 2.1c. Cleaned glass substrates were treated with oxygen plasma and immersed in methanolic polyamidoamine (PAMAM) dendrimer solution ( $c = 1.0 \times 10^{-6}$  M) and soaked overnight to functionalize the surface. Subsequently, the PAMAM substrates were protonated and immersed in the dye solution to transfer the J-aggregates onto the substrate.<sup>[20]</sup> The J-aggregates deposited on the PAMAM monolayer substrates were rinsed with Millipore water to remove loosely adsorbed J-aggregate layers. Increasing the PAMAM concentration leads to self-aggregation instead of monolayer formation (Figure S2.2a and S2.2b, Supporting Information). Consequently, this resulted in poor J-aggregate formation (irrespective of the solution phase) on the PAMAM substrates, as confirmed by the decrease in J-aggregate absorption (Figure S2.2c, Supporting Information).

By increasing the immersion time of PAMAM substrates in dye solution ( $c = 0.2 \times 10^{-3}$  M, solution 1) to 12 h, the deposited J-aggregates formed a *platelets-like* morphology following a ‘Volmer-Weber (V-W)’ growth model (Figure 2.1d). The platelets obtained from this growth show numerous small domains isolated by grain boundaries. The V-W growth model is a typical model reported for J-aggregates adsorbed from solution onto AgBr substrates devoid of any J-aggregate monolayer,<sup>[21]</sup> and is distinctly different from the Stranski-Krastanov (S-K) growth model reported for the same dye, too.<sup>[22]</sup>

In the second system, the dye solution ( $c = 0.2 \times 10^{-3}$  M, solution 2) with an equi-volume ratio mixture of methanol:water (50:50) contains monomers as major phase and J-aggregates in a “critical nucleus state”. This configuration resulted in selective nucleation of J-aggregates on the PAMAM surface followed by J-aggregate monolayer formation after 12 h. With prolonged time (48 h), the amphiphilic nature of the dye molecule triggered the growth of quasi-epitaxial crystals on top of the J-aggregate monolayer, conforming to a ‘S-K’ growth model (Figure 2.1e). The S-K growth process can be explained by the growth of a charged layer on top of the first monolayer of the molecules, complying with charge neutrality. Our findings suggest that templated molecular assembly is a highly efficient process to realize different solid-state J-aggregate morphologies like platelets, monolayers, and quasi-epitaxial crystals. To confirm the difference in thin film molecular packing between platelets and quasi-epitaxial crystals, we have investigated their crystalline nature using small-angle x-ray scattering (SAXS) using a synchrotron source. From the SAXS data (Figure S2.3), we can confirm that molecules are randomly oriented in platelets, signifying polycrystallinity, whereas they are uni-directionally oriented for quasi-epitaxial crystals. It should be noted that the x-ray diffraction intensity is

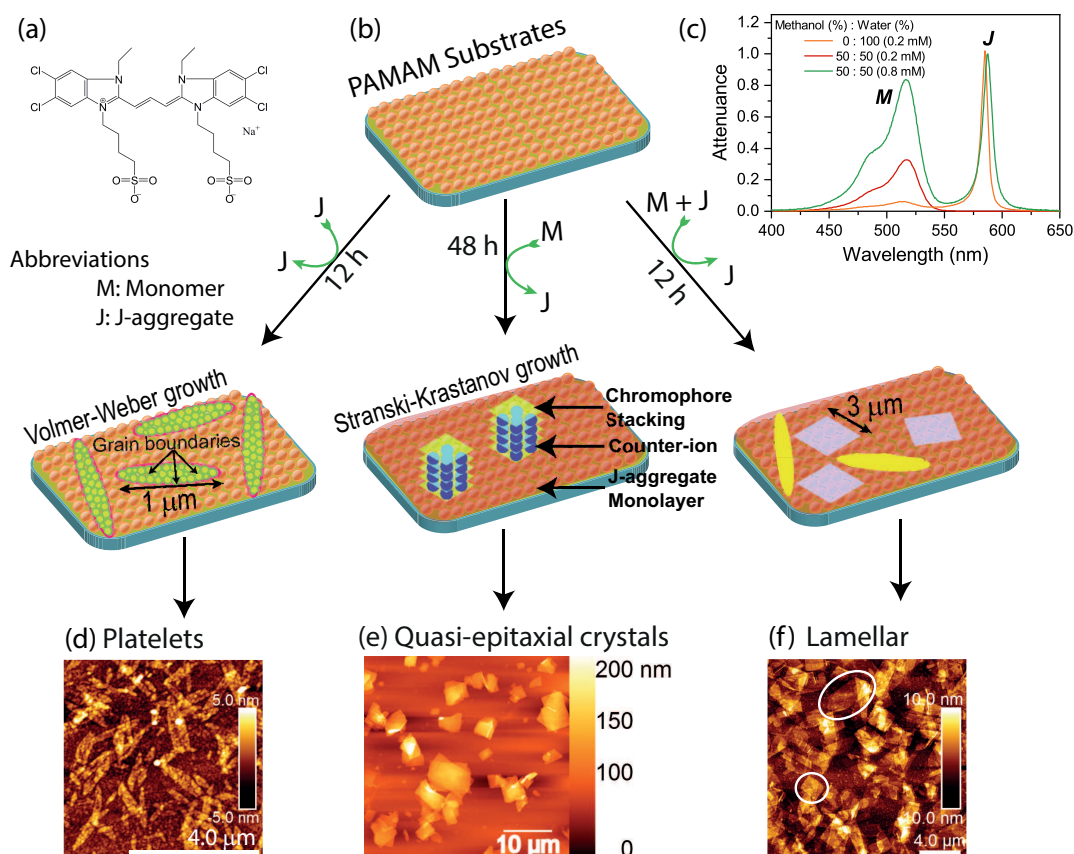


Figure 2.1 – (a) Chemical structure of the **TDBC** dye. (b) Schematic showing methodologies to control J-aggregates growth following Volmer-Weber and Stranski-Krastanov growth models. (c) Attenuance of dye solution by varying the monomer and J-aggregate phase content leads to different types of J-aggregate morphologies like (d) platelets, (e) quasi-epitaxial crystals and (f) lamellar on glass substrates functionalized with PAMAM, as observed with scanning probe microscopy. Presence of mixed leaf-like and stripe J-aggregates in lamellar films are marked with white rings in (f).

very significant from a thin film ( $\sim 10$  nm, “platelets”), and the absence of diffraction peaks in quasi-epitaxial crystals ( $\sim 150$  nm) is not due to a reduced scattering volume.

Based on these observations, we have developed a new strategy to grow J-aggregate crystals of the TDBC dye with reduced grain boundaries on the PAMAM substrate. This is achieved by adjusting the ratio of monomers and J-aggregates in an equi-volume ratio solution of methanol and water ( $c = 0.8 \times 10^{-3}$  M, solution 3) such that J-aggregates anchor on the substrate, and monomers are fed from the solution to grow high quality crystals. The morphology obtained from this new route is subsequently referred to as lamellar films (Figure 2.1f). It is evident from the scanning force microscopy images that the crystalline domains in the lamellar film are significantly larger ( $\sim 3 \mu\text{m}$ ) compared to the platelets ( $\sim 30$ – $50$  nm). Histograms of height and domain size for platelets and lamellar films are shown in Figure S2.4 (Supporting Information). For comparison with the V-W route, as shown in Figure 2.1d, we have deposited

J-aggregates from a high dye concentration ( $0.8 \times 10^{-3}$  M) in water for 12 h, which did not lead to larger aggregate domains. This confirms that the controlled growth of aggregates from a dye solution containing J-aggregates supplemented by free monomers is key to form high quality lamellar crystals in the solid-state. This condition is achieved by employing a methanol-water co-solvent system with high dye concentration.

Following the discussion above, it turns out that at low dye concentration (0.2 mM, 0.175 mg/ml) with J-aggregates as major phase in the water solution, platelets (leaves-like) are the only morphology obtained. However, keeping the same dye concentration (0.2 mM, 0.175 mg/ml) with monomers as major phase and J-aggregates in critical nucleus 50:50 methanol:water solution, quasi-epitaxial crystals (stripes) were observed. Upon increasing the dye concentration (0.8 mM, 0.7 mg/ml) in the binary solvent mixture containing both monomers and J-aggregates leads to a mixed morphology of leaf-like morphology and stripes in lamellar films. This concurs with the morphological arrangements for a similar carbocyanine dye molecule reported by Prokhorov et.al.,<sup>[23]</sup> where high dye concentration (0.5 mg/ml) has led to the formation of both leaves and stripe J-aggregate morphology. Note that the dye concentration used in this work to obtain lamellar films is close to the concentration reported by Prokhorov et.al.<sup>[23]</sup> Here, we demonstrate that tuning the dye concentration to control the monomer and J-aggregate content in solution allows obtaining distinct morphologies in thin films.

### 2.2.2 Optical properties of platelet and lamellar films

Optical properties of monomers in solution and J-aggregate films of platelets and lamellar structures are compared in Figure 2.2a. The monomer dye solution exhibits an absorption peak around 518 nm followed by vibronic progression and its corresponding photoluminescence (PL) peak at 541 nm, with a large spectral shift of about 23 nm ( $821 \text{ cm}^{-1}$ ). Upon formation of J-aggregates, the transition dipole moments of the monomer molecules are strongly coupled, leading to a red-shifted narrow absorption band peaked at 587 nm with a FWHM of  $\sim 13$  nm ( $393 \text{ cm}^{-1}$ ). Although lamellar films showed higher attenuation than platelets, the absorbance of the films measured in an integrating sphere was almost the same. This points towards stronger light scattering of the lamellar films compared to the platelet's films, as expected from the much larger domain size. In addition, the PL signals of the J-aggregate films were recorded in an integrating sphere at room temperature. Despite the presence of J-aggregate monolayers in lamellar films that can cause strong reabsorption, lamellar films showed more intense PL than the platelets when comparing the spectrally integrated PL intensity. The absolute quantum yield values obtained for platelets and lamellar films following deMello's<sup>[24]</sup> method and PL spectrum corrected for reabsorption<sup>[25]</sup> are 2.34% and 4.59%, respectively. The true absorbance for both films at the excitation wavelength (550 nm) was similar (0.04). Furthermore, as an external reference standard, the absolute PLQY for Rhodamine 101 dye solution was measured as reported by Würth et al.,<sup>[26]</sup> showing only little deviation (86% instead of 91% as reported by Würth et al.<sup>[26]</sup>). The spectral shift for both J-aggregate films



is only  $\sim 5$  nm ( $144$   $\text{cm}^{-1}$ ). Small spectral shift, narrow PL signal and higher PLQY suggest that the lamellar films could be more promising than platelets regarding energy transport properties.

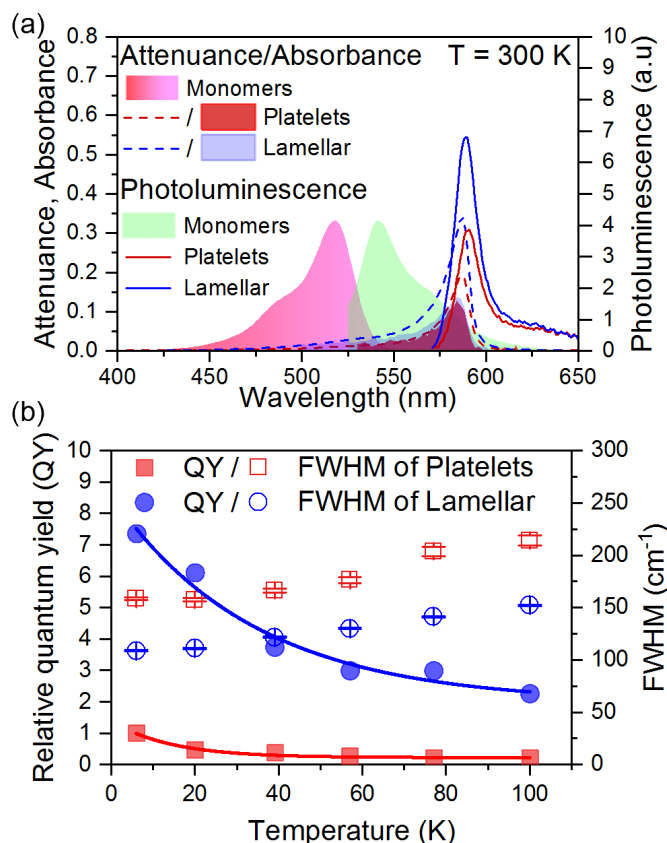


Figure 2.2 – (a) Attenuance, absorbance and steady-state photoluminescence of monomers in methanolic solution, platelets and lamellar film measured at 300 K. Photoluminescence signals of the thin films are recorded with an excitation wavelength of 530 nm (450 nm for monomers) in an integrating sphere. (b) Relative quantum yield for the platelets and lamellar films from 6 to 100 K, normalized to the quantum yield of platelets films at 6 K, with pulsed excitation wavelength at 400 nm and 80 MHz repetition rate. The corresponding full-width at half-maximum (FWHM) of the photoluminescence of the thin films, as shown in Table S2.1, are plotted as a function of temperature. The error bars from the fit are smaller than the symbol size.

Deeper insight into the exciton dynamics is gained by investigating the fluence dependence of the PL at various temperatures ranging from 6 K up to 100 K for both platelets and lamellar films. A pulsed laser with an excitation wavelength of 400 nm, 80 MHz repetition rate, 100 fs pulse duration, and incident fluence of up to  $100$   $\text{nJ cm}^{-2}$  was used for excitation. The exciton density is very low within this range, safely ruling out singlet-singlet exciton annihilation.<sup>[13,15]</sup> At 6 K, the relative quantum yield of lamellar films was almost seven-fold higher compared to platelets (Figure 2.2b). Moreover, the FWHM of the PL signal was much narrower for the lamellar films, pointing towards a larger coherent domain size and an enhanced PLQY.<sup>[18]</sup> It

should be noted that no long-wavelength components were observed unlike in 1D aggregates, which are reported to be exciton traps.<sup>[27]</sup> From 6 K to 100 K (Figure 2.2b) and even at room temperature (Figure 2.2a) the relative quantum yield of the lamellar films remained higher compared to platelet films, suggesting that less non-radiative decay channels are present. Furthermore, the PL intensity did not follow a linear decrease with temperature, in good agreement with a recent report.<sup>[19]</sup>

### 2.2.3 Exciton dynamics in platelet and lamellar films at low temperature (6 K)

Figure 2.3a summarizes the PL intensity *versus* excitation fluence recorded at 6 K. Power-law fits to the emitted intensity allowed to identify density-dependent quenching mechanisms for the different morphologies and excess photon energies resulting in a sub-linear behavior (exponent <1). Upon exciting with a pulsed laser at 550 nm (80 MHz, 100 fs pulse duration) a linear increase ( $PL \propto I^{1.0(0.94 \pm 0.05)}$ ) in PL intensity with increasing pump fluence  $I$  for lamellar (platelet) films was observed. However, exciting with high energy photons (400 nm, 80 MHz repetition rate, 100 fs pulse duration) a pronounced sub-linear behavior in platelets ( $PL \propto I^{0.77 \pm 0.05}$ ) compared to the lamellar ( $PL \propto I^{0.94 \pm 0.05}$ ) films has been observed. Continuous-wave (CW) excitation at 405 nm shows similar sub-linear behavior ( $PL \propto I^{0.86 \pm 0.05}$ ) for both films. Due to the very low excitation densities, the observed sub-linear behavior cannot be attributed to exciton-exciton annihilation (EEA), as observed in experiments with high excitation fluence.<sup>[13,15]</sup> Hence, we consider the sub-linear behavior to be an indirect consequence of the excess energy of the optical excitation, which will be discussed below.

By means of time-resolved PL spectroscopy, the exciton dynamics was investigated for platelets, lamellar and spin-coated films with 400 nm pulsed laser excitation at 6 K, as shown in Figure 2.3b. The temporal PL decay was fitted by a mono-exponential, and alternatively, a bi-exponential function. The fitting parameters are summarized in Table 2.1. The goodness of fit (G.O.F) does not significantly improve by using a bi-exponential fit compared to a mono-exponential fit, confirming the results reported by Lindrum et al.<sup>[28]</sup> showing that a mono-exponential fit is the best approximation for the PL decay at low temperature ( $T \leq 20$  K) and a bi-exponential fit is applicable for room temperature measurements. Therefore, we used mono-exponential decay fitting in our study, implying that one excited state dictates the exciton dynamics. However, one has to take into account that disorder like a non-uniform distribution of domain sizes typically leads to a non-exponential decay behavior. Lamellar films showed faster decay dynamics compared to platelets and spin-coated films. This observation in conjunction with the higher PLQY suggests that larger coherent domains are present in the lamellar film.<sup>[29]</sup> By increasing the fluence, the PL intensity increased, concomitant with a slight decrease in the lifetime (Table S2.2, Supporting Information). In addition, lifetime measurements for lower excitation fluence of  $26 \text{ nJ cm}^{-2}$  are shown in Figure S2.7, Supporting Information.

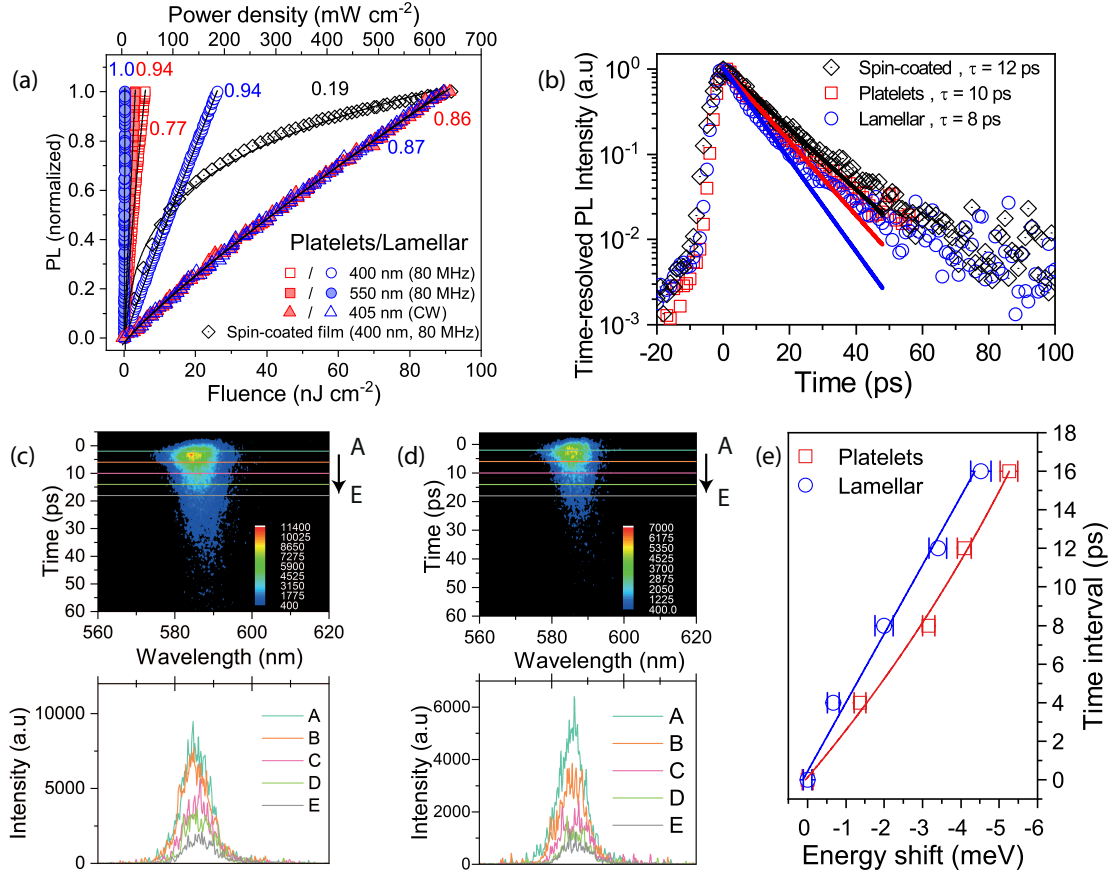


Figure 2.3 – (a) Spectrally- and temporally-integrated photoluminescence acquired with continuous-wave and ultrafast excitation at 400 nm and 550 nm for platelets and lamellar films at 6 K. For comparison, spin coated films were studied with ultrafast excitation at 400 nm, 80 MHz at 6 K. The exponents from the power-law fits ( $PL \propto I^n$ ) are added as labels to the curves (See Figure S2.5, SI for unnormalized raw data). For reversibility, see Figure S2.6, SI. The top horizontal axis represents the power density range used for the CW excitation. (b) Time-resolved spectrally-integrated dynamics (fluence of 78 nJ cm<sup>-2</sup>) with the lines representing the fits of an exponential decay to the data between 0 and 50 ps. From this, the exciton lifetime for the films was extracted (mono exponential decay times are shown in the legend). Cross-sections plotted for small time intervals (4 ps bin size) from the streak camera image recorded with an excitation wavelength of 400 nm for platelets (c) and lamellar films (d). (e) Transient red-shift in peak center energies from (c) and (d) with error bars for the peak energies corresponding to the time. Lines are a guide to the eye.

Table 2.1 – Exciton lifetime values obtained from mono- and bi-exponential decay fits.

Sample	Mono-exponential fit			Bi-exponential fit			
	Amplitude (A)	Lifetime (t), in ps	G.O.F. <sup>a</sup>	Amplitude (A <sub>1</sub> )	Lifetime (t <sub>1</sub> ), in ps	Amplitude (A <sub>2</sub> )	Lifetime (t <sub>2</sub> ), in ps
Lamellar	1.03±0.01	8	0.9895	0.94±0.03	6	0.12±0.03	26
Platelets	1.02±0.01	10	0.9887	0.88±0.08	6	0.29±0.09	18
Spin-coated films	1.02±0.01	12	0.99188	0.93±0.06	10	0.10±0.06	34

<sup>a</sup>goodness of fit

The polydispersity of the crystalline domains of the platelets or spin-coated films, due to the presence of intra-granular sub-structures<sup>[30]</sup> (see Figure 2.1b), results in an inhomogeneously broadened density of states (DOS), similar to observations in ensembles of perovskite nanocrystals and colloidal quantum dots.<sup>[31,32]</sup> Excitons in the vicinity of inter-grain boundaries will be immediately quenched non-radiatively and therefore decrease the PLQY.<sup>[33,34]</sup> On the other hand, monodispersity and less topological disorder in lamellar films are accompanied by comparatively less energetic disorder. Direct evidence of energetic disorder can be drawn from the streak camera images (Figure 2.3c, d), and spectra taken at different times (cross-sections from the images), showing a slightly more pronounced red-shift that increased with time more for platelets compared to lamellar films (Figure 2.3e).

From the experimental results described above, the following conclusion can be drawn: the sub-linear power-dependence and the dependence on the excess energy of the pump photons suggest that the observed PL behavior stems from a charge generation mechanism resulting in non-radiative quenching of excitons. The generation of charges depends on the excitation photon energy as well as on the excitation laser fluence. An excitation generated in a localized state subsequently executes a random walk within a manifold of positionally and energetically disordered sites towards the tail states of the DOS because under non-equilibrium conditions and at low temperatures (6 K) downward jumps in energy dominate the random walk. This behavior is schematically shown in Figure 2.4a and b. Exciting the films at 505 nm, 1 kHz repetition rate (2.45 eV) with an excess energy of only  $\sim 200$  meV relative to the  $S_1 - S_0$  transition, and taking into account that the laser fluence in this experiment was significantly higher (Table S2.2) leading to higher exciton densities and possibly to additional quenching mechanisms, still a substantially longer exciton lifetime was observed compared to excitation at 400 nm (80 MHz repetition rate) with an excess energy of  $\sim 850$  meV (see Table S2.2). This signifies that the excess energy for excitation at 505 nm is insufficient to generate free charges, and therefore grain boundaries and/or other permanent non-radiative traps like H-type aggregates are the dominating exciton quenching sites.<sup>[35]</sup> The observed increase in lifetime with excitation density could indicate that these traps are gradually filled. Lifetime measurements with low-fluence pulses at 550 nm and 80 MHz repetition could not be done due to technical constraints in the setup. However, excitation at 400 nm led to the creation of free charges as observed also in conjugated polymers<sup>[36–39]</sup> and aggregates<sup>[40]</sup> (Figure 2.4c and d). Here, the excess energy created a vibrationally hot excitation (bound electron-hole pair) which can subsequently dissociate. Once separated, the carriers have a reduced probability to recombine again, leading to free charge carriers.<sup>[36,41]</sup> The calculations for the charge recombination time and the diffusion length are detailed in the Supporting Information. The lifetime of the free charges (15  $\mu$ s) is much longer than the exciton lifetime ( $\sim 10$  ps) which results in exciton-charge quenching. Furthermore, as seen in Figure 2.3a, such exciton-charge quenching is independent of the excitation mode (CW (405 nm) and pulsed laser (400 nm)) which leads to sub-linear behavior.

Owing to low mobility of the free charge carriers at low temperatures, the charges are trapped in the immediate vicinity of defects. This residing charge species form a *trap state* preferentially

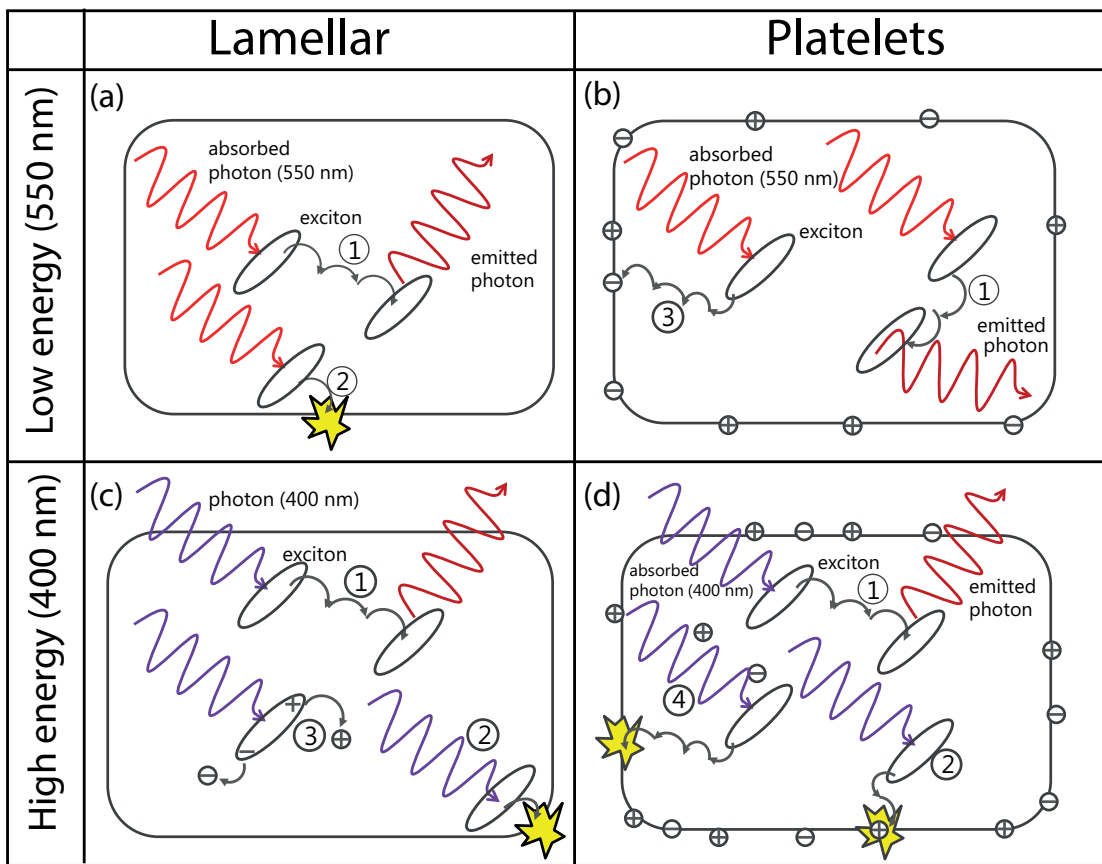


Figure 2.4 – Schematic representation of exciton dynamics in lamellar (a) and platelet (b) films when excited at 550 nm. In comparison, charge generation in the bulk films for lamellar (c) and platelets (d) leads to exciton quenching when excited at 400 nm. ① - exciton diffusion and radiative recombination, ② - non-radiative recombination at disordered sites, ③ - charge-carrier generation and ④ - exciton-charge quenching in the bulk along with ②.

at the grain boundaries, quenching the excitons.<sup>[34]</sup> Such additional non-radiative process explains both the sub-linearity and the lower QY in platelets compared to lamellar films. Consequently, lamellar films with a comparably low number of granular boundaries result in higher PLQY. In addition, spin coated films (topography is shown in Figure S2.8) were investigated under similar conditions with power-dependent PL measurements, yielding a power-law exponent of 0.19. Hence, photo-induced charge generation efficiency increased with disorder in the film, thus confirming this model. It should be noted that by increasing the defect concentration (grain boundaries) from lamellar films to platelets to spin-coated films, the lifetime increased and the power-law exponent of the power-dependent PL intensity was more pronounced sub-linear (0.94 to 0.19). This cannot be consistently explained from the coherent domain size and exciton lifetime alone and may be due to additional defects introduced in the film during processing that can lead to further charge generation and luminescence quenching. For instance, matrix immobilization of J-aggregates has shown Lévy (non-Gaussian) type of disorder in the films.<sup>[42]</sup> Such Lévy-type of defects are reported

to significantly funnel excitons to trap states present in the film.<sup>[43]</sup> On the other hand, such disorder can also induce exciton self-trapping.<sup>[44]</sup>

We note that both the almost linear PL intensity as a function of excitation fluence in lamellar films as well as the sub-linear behavior in platelets remained constant (in the error range for the exponent of  $\pm 0.05$ ) within the temperature range of the measurements (Figure S2.9, Supporting Information). This suggests a temperature-independent charge generation and trapping rate and a minor role of temperature-driven exciton or charge diffusion for this kind of quenching process. The larger energetic disorder in platelets leads to increased charge generation, and consequently, to stronger exciton quenching compared to lamellar films, resulting in stronger sub-linearity in the former. In contrast, the lower energetic disorder in lamellar films can inhibit photocarrier generation, and therefore circumvent exciton quenching, allowing for enhanced exciton diffusion. Our observations manifest the interplay of topological and energetic disorder, which can strongly dictate exciton dynamics in the absence of exciton-phonon interaction.

## 2.3 Conclusion

In summary, two different routes to form molecular assemblies of cyanine dyes on solid substrates following two different growth models were introduced. The presence of critical J-aggregate nuclei is pivotal to switch its growth mode on solid substrates. Using different excitation schemes (CW, pulsed, varying the excess energy) as well as time-resolved PL spectroscopy, different non-radiative decay pathways were identified. The interplay of energetic disorder and non-radiative decay are dominant factors affecting the exciton transport. The results show that the difference in domain size and order give rise to significantly enhanced radiative decay for lamellar films as compared to platelets or films deposited by spin-coating. This growth methodology can be employed to design crystalline and highly fluorescent 2D materials which will have potential for future optoelectronic devices.

## 2.4 Experimental Section

**Growth of J-aggregate films:** PAMAM dendrimers (10 wt% in methanol, Sigma Aldrich) with ethylene diamine core, generation 4.0 solution was used for functionalizing the glass substrates. The anionic cyanine dye 5,6-dichloro-2-[[5,6-dichloro-1-ethyl-3-(4-sulfobutyl)-benzimidazol-2-ylidene]-propenyl]-1-ethyl-3-(4-sulfobutyl)-benzimidazolium hydroxide, inner salt, sodium salt (**TDBC**) was purchased from FEW chemicals, Germany and used without any further purification. **TDBC** was dissolved in water (Millipore water, 18.2 M $\Omega$ -cm resistivity at 25 °C) and in methanol-water (50:50) mixture, separately with a dye concentration ( $c$ ) of  $c = 0.2 \times 10^{-3}$  M (0.175 mg/ml), to study the self-assembly of dyes towards formation of J-aggregates on functionalized surface. Also, a high dye concentration ( $c = 0.8 \times 10^{-3}$  M) solution was prepared by dissolving 0.7 mg/ml in methanol-water (50:50) mixture. 5 mg of dye was dissolved in 1 ml

of water and stirred overnight before spin coating on glass substrates at 4000 rpm for 60 s.

**Surface functionalization and film formation:** Glass substrates were cleaned following a standard procedure by ultra-sonicating them in 0.2 % Hellmanex solution, water, acetone, ethanol for 10 min individually. Followed by cleaning, glass substrates were treated with oxygen plasma with a power setting of 45 W for 5 min. Plasma-treated glass was immediately immersed in PAMAM ( $c = 1 \times 10^{-6}$  M) methanolic solution for 18 h to functionalize the surface. Such functionalized layer was rinsed with methanol to remove loosely adsorbed PAMAM while leaving behind a monolayer. Subsequently, the PAMAM-coated substrates were protonated in acidic ( $\text{pH} < 3$ ) medium to activate the amine groups for anchoring anionic dye molecules.<sup>[20]</sup> Protonated PAMAM-coated substrates were immersed in the dye solution for various time schedules with mild shaking and rinsed with Millipore water to obtain J-aggregate films.

**Scanning probe microscopy (SPM):** SPM studies were conducted using a Bruker Dimension Icon in tapping mode to map the topography and phase contrast of the J-aggregate films. Antimony-doped Si cantilevers (RTESP-300) procured from Bruker with a tip radius of 12 nm, force constant of  $40 \text{ Nm}^{-1}$  and operating at resonant frequency of 300 kHz were used. The SPM images were analyzed using the NanoScope software using particle analysis with a threshold height to the maximum of the height histogram to deduce height and domain size histograms.

**Grazing incidence small angle x-ray diffraction studies (SAXS):** SAXS measurements for the platelets and quasi-epitaxial crystals were performed at the Elettra synchrotron facility (Trieste, Italy). A 1D gas detector (Gabriel type) calibrated with silver behenate for the scattering vector ( $q$ ) values was used to collect the scattered x-rays from the sample. The sample-to-detector distance was fixed at 176 cm with a fixed wavelength ( $\lambda = 1.54 \text{ \AA}$ ). The scattering vector ( $q$ ) is defined as  $q = 4\pi \sin(\theta) / \lambda$ , where  $2\theta$  is the scattering angle.

**Attenuance and steady-state photoluminescence:** Attenuance for monomer solution and J-aggregate films were characterized using a Varian Cary 50 UV-Vis spectrophotometer. Absorbance and steady-state photoluminescence spectra of the deposited J-aggregate films and monomer solution were studied using a Horiba Jobin-Yvon Fluorolog spectrofluorometer equipped with an integrating sphere. The absolute quantum yield for the platelet and lamellar films were measured at room temperature using an integrating sphere.<sup>[24]</sup> Furthermore, as an external standard to evaluate the deviation of quantum yield values as determined from our instrument, we have measured a Rhodamine 101 dye solution using a quartz-cuvette (10 x 10 mm) following the protocol mentioned elsewhere.<sup>[26]</sup> Due to small Stokes' shift in J-aggregate thin films, the reabsorption of the fluorescence spectrum was corrected by following the approach proposed by Cao and Sletten.<sup>[25]</sup> Briefly, the true fluorescence ( $I(\lambda)$ ) was obtained



by correcting for reabsorption from the overlap between absorption and emission spectra as,

$$I(\lambda) = I_0(\lambda) \left[ \frac{-\ln(10^{-OD(\lambda)})}{1 - (10^{-OD(\lambda)})} \right] \quad (2.1)$$

where,  $I_0(\lambda)$  is the experimental value,  $OD(\lambda)$  is the optical density of the sample.

### Laser fluence studies and time-resolved photoluminescence spectroscopy (TRPL):

J-aggregate thin films were mounted in a liquid Helium cryostat maintained in Helium exchange gas and cooled to 6 K. Excitation fluence series for the films were acquired by using excitation either at 400 nm by a frequency-doubled mode-locked Ti:Sapphire laser or alternatively at 550 nm by an optical parametric oscillator (OPO) pumped by the mode-locked Ti:Sapphire, with a pulse duration of about 100 fs and a repetition rate of 80 MHz, respectively. For comparison, additional PL experiments by means of a continuous-wave laser with an excitation wavelength at 405 nm have been carried out. A travelling-wave parametric amplifier pumped by a Ti:Sapphire regenerative amplifier (800 nm, 1 kHz) seeded by the Ti:Sapphire laser was used to excite the films at 505 nm with a pulse duration of about 250 fs and 1 kHz repetition rate. Time- and spectrally-resolved PL for excitation at 400 nm (80 MHz) and 505 nm (1 kHz) laser was measured by means of a streak camera (Hamamatsu, nominal time resolution 2 ps) coupled to a spectrometer. Temperature-dependent PL signals were recorded at different temperatures ranging from 6 K to 100 K. The integrated area of the PL signal was normalized to PL from platelet films (as a reference for relative quantum yield) at 6 K. For plotting the full-width at the half-maximum (FWHM) of the PL signal at different temperatures, the PL spectrum at 6 K was fitted using Voigt function to determine the Gaussian ( $\Delta\omega_G$ ) and Lorentzian ( $\Delta\omega_L$ ) width. As Gaussian width represents static energetic disorder (T-independent) and Lorentzian width represents T-dependent perturbations, the value of Gaussian width calculated at 6 K was fixed as constant while applying Voigt fitting for other temperatures up to 100 K. From the Gaussian width and Lorentzian width, the FWHM of the PL signal is calculated as,

$$FWHM = (0.5346 \times \Delta\omega_L) + \sqrt{(0.2169 \times \Delta\omega_L^2) + \Delta\omega_G^2} \quad (2.2)$$

For plotting the transient energetic shift, the spectral data points are binned in time intervals of 4 ps. The data points were fitted to a Gaussian profile to determine the peak energy for the transient energetic shift along with the error in the peak energy value from the fitting.

**Acknowledgements** The authors gratefully acknowledge funding from the Swiss National Science Foundation grant number: 200021-157135 to conduct this research work. We acknowledge the Scanning Probe Microscopy user laboratory at Empa for providing access to the instrument. This work was partly supported by the Swiss State Secretariat for Education, Research and Innovation (SERI) and the European Union's Horizon-2020 framework programme through the Marie-Sklodowska Curie ITN network SYNCHRONICS (H2020-MSCA-ITN-643238). We thank Stefan Salentinig, Laboratory for Biointerfaces, Empa St. Gallen for the SAXS measurement and access to the Elettra facility.

# Bibliography

- [1] J.-L. Brédas, E. H. Sargent, G. D. Scholes, *Nature Materials* **2016**, 16, 9.
- [2] H. Peng, Y. Chen, Y. Zhao, Q. Yang, L. Wu, C. Tung, L. Zhang, Q. Tong, *Angewandte Chemie International Edition* **2012**, 51, 2088–2092.
- [3] S. Sengupta, F. Würthner, *Accounts of Chemical Research* **2013**, 46, 2498–2512.
- [4] W. Liang, S. He, J. Fang, *Langmuir* **2014**, 30, 805–811.
- [5] A. Cacciola, C. Triolo, O. Di Stefano, A. Genco, M. Mazzeo, R. Saija, S. Patanè, S. Savasta, *ACS Photonics* **2015**, 2, 971–979.
- [6] G. G. Paschos, N. Somaschi, S. I. Tsintzos, D. Coles, J. L. Bricks, Z. Hatzopoulos, D. G. Lidzey, P. G. Lagoudakis, P. G. Savvidis, *Scientific Reports* **2017**, 7, 11377.
- [7] P. Deotare, Nanoscale Exciton-Mechanical Systems (NEXMS), Accessed: April 2018, <http://eecs.umich.edu/eecs/about/articles/2016/parag-deotare-receives-afosr-young-investigator-award.html>.
- [8] G. Grosso, J. Graves, A. T. Hammack, A. A. High, L. V. Butov, M. Hanson, A. C. Gossard, *Nature Photonics* **2009**, 3, 577–580.
- [9] A. G. Dijkstra, H.-G. Duan, J. Knoester, K. A. Nelson, J. Cao, *The Journal of Chemical Physics* **2016**, 144, 134310.
- [10] D. Möbius, H. Kuhn, *Journal of Applied Physics* **1988**, 64, 5138–5141.
- [11] D. Möbius, *Advanced Materials* **1995**, 7, 437–444.
- [12] S. Kirstein, H. Möhwald, *Advanced Materials* **1995**, 7, 460–463.
- [13] J. R. Caram, S. Doria, D. M. Eisele, F. S. Freyria, T. S. Sinclair, P. Rebentrost, S. Lloyd, M. G. Bawendi, *Nano Letters* **2016**, 16, 6808–6815.
- [14] D. M. Eisele, J. Knoester, S. Kirstein, J. P. Rabe, D. A. Vanden Bout, *Nature Nanotechnology* **2009**, 4, 658–663.
- [15] G. M. Akselrod, Y. R. Tischler, E. R. Young, D. G. Nocera, V. Bulovic, *Phys. Rev. B* **2010**, 82, 113106.
- [16] S. Valleau, S. K. Saikin, M.-H. Yung, A. A. Guzik, *The Journal of Chemical Physics* **2012**, 137, 034109.

## Bibliography

---

- [17] S. Cai, W. Zhang, R. N. Zuckermann, Z. Li, X. Zhao, Y. Liu, *Advanced Materials* **2015**, 27, 5762–5770.
- [18] J. Knoester, *Advanced Materials* **1995**, 7, 500–502.
- [19] A. Eisfeld, C. Marquardt, A. Paulheim, M. Sokolowski, *Physical Review Letters* **2017**, 119, 097402.
- [20] R. Steiger, R. Pugin, J. Heier, *Colloids and Surfaces B: Biointerfaces* **2009**, 74, 484–491.
- [21] H. Saijo, M. Shiojiri, *Journal of Imaging Science and Technology* **1997**, 41, 266–271.
- [22] M. S. Bradley, J. R. Tischler, V. Bulović, *Advanced Materials* **2005**, 17, 1881–1886.
- [23] V. V. Prokhorov, S. I. Pozin, D. A. Lypenko, O. M. Pereyagina, E. I. Mal'tsev, A. V. Vannikov, *Chemical Physics Letters* **2012**, 535, 94–99.
- [24] J. C. de Mello, H. F. Wittmann, R. H. Friend, *Advanced Materials* **1997**, 9, 230–232.
- [25] W. Cao, E. M. Sletten, *Journal of the American Chemical Society* **2018**, 140, 2727–2730.
- [26] C. Würth, M. Grabolle, J. Pauli, M. Spieles, U. Resch-Genger, *Nature Protocols* **2013**, 8, 1535–1550.
- [27] M. Vacha, M. Furuki, T. Tani, *The Journal of Physical Chemistry B* **1998**, 102, 1916–1919.
- [28] M. Lindrum, A. Glismann, J. Moll, S. Daehne, *Chemical Physics* **1993**, 178, 423–432.
- [29] F. C. Spano, J. R. Kuklinski, S. Mukamel, D. V. Brumbaugh, M. Burberry, A. A. Muentert, *Molecular Crystals and Liquid Crystals* **1991**, 194, 331–336.
- [30] H. Asanuma, T. Tani, *The Journal of Physical Chemistry B* **1997**, 101, 2149–2153.
- [31] H.-H. Fang, L. Protesescu, D. M. Balazs, S. Adjokatse, M. V. Kovalenko, M. A. Loi, *Small* **2017**, 13, 1700673.
- [32] G. M. Akselrod, F. Prins, L. V. Poulikakos, E. M. Y. Lee, M. C. Weidman, A. J. Mork, A. P. Willard, V. Bulović, W. A. Tisdale, *Nano Letters* **2014**, 14, 3556–3562.
- [33] R. R. Lunt, J. B. Benziger, S. R. Forrest, *Advanced Materials* **2010**, 22, 1233–1236.
- [34] J. D. A. Lin, O. V. Mikhnenko, T. S. van der Poll, G. C. Bazan, T.-Q. Nguyen, *Advanced Materials* **2015**, 27, 2528–2532.
- [35] O. P. Dimitriev, Y. P. Piryatinski, Y. L. Slominskii, *The Journal of Physical Chemistry Letters* **2018**, 9, 2138–2143.
- [36] V. I. Arkhipov, E. V. Emelianova, H. Bässler, *Physical Review Letters* **1999**, 82, 1321–1324.
- [37] C. Deibel, D. Mack, J. Gorenflot, A. Schöll, S. Krause, F. Reinert, D. Rauh, V. Dyakonov, *Physical Review B* **2010**, 81, 085202.
- [38] D. J. Carswell, L. E. Lyons, *Journal of the Chemical Society (Resumed)* **1955**, 1734–1740.
- [39] E. Hendry, M. Koeberg, J. M. Schins, H. K. Nienhuys, V. Sundström, L. D. A. Siebbeles, M. Bonn, *Physical Review B* **2005**, 71, 125201.
- [40] Z. Guo, D. Lee, H. Gao, L. Huang, *The Journal of Physical Chemistry B* **2015**, 119, 7666–7672.

- [41] D. M. Basko, E. M. Conwell, *Physical Review B* **2002**, 66, 155210.
- [42] L. Lüer, S. K. Rajendran, T. Stoll, L. Ganzer, J. Rehault, D. M. Coles, D. Lidzey, T. Virgili, G. Cerullo, *The Journal of Physical Chemistry Letters* **2017**, 547–552.
- [43] A. Merdasa, Á. J. Jiménez, R. Camacho, M. Meyer, F. Würthner, I. G. Scheblykin, *Nano Letters* **2014**, 14, 6774–6781.
- [44] A. V. Sorokin, N. V. Pereverzev, I. I. Grankina, S. L. Yefimova, Y. V. Malyukin, *The Journal of Physical Chemistry C* **2015**, 119, 27865–27873.

## 2.5 Supporting Information

### S1. Charge generation and recombination time for excitation at 400 nm

In the following, the conditions for charge carrier build-up at 400 nm excitation are estimated. Furthermore, we show that the distance between two charges is much farther (715 nm) than the film thickness ( $\sim 5$  nm) of the J-aggregates used in this study. This implies the 2D recombination is a more appropriate model than 3D. In the simplest approach, the charge carrier density is given by the charge generation rate  $G(\lambda, T, I)$  and a bimolecular recombination rate  $R(N, T)$ , where  $\lambda$  is the photon wavelength,  $T$  the temperature,  $I$  the fluence and  $N$  the two-dimensional carrier density.<sup>[S1]</sup>

$$\frac{dN}{dt} = G(\lambda, T, I) - R(N, T) \quad (\text{S2.1})$$

$$\frac{dN}{dt} = G_0(\lambda, T, I) \cdot \eta - N/\tau \quad (\text{S2.2})$$

Here,  $G_0$  is the photon flux averaged over time,  $\eta$  is the efficiency of the charge generation, and  $\tau$  is the carrier recombination time, which is given by

$$\tau = \frac{8\varepsilon_0\varepsilon}{15\sqrt{\pi}e\mu} N^{-3/2} \quad (\text{S2.3})$$

In our experiment (we consider a large number of pulses),  $G'_0 (= 1.60 \cdot 10^{23} \text{ s}^{-1} \text{ m}^{-2})$  measured with a power meter needs to be multiplied by the absorbance ( $= 0.003 \pm 0.001$ ) to yield the effective absorbed photon flux:  $G_0 = 5.248 \pm 1.89 \cdot 10^{20} \text{ s}^{-1} \text{ m}^{-2}$ .  $\eta$  can be assumed to be rather large, otherwise charge-exciton quenching would not be able to compete with the major non-radiative process in the system: we assumed  $\eta=0.5$  in the following calculation. Furthermore, the relative dielectric constant,  $\varepsilon=4$  is used. For well-ordered lamellar films, the carrier mobility can reach  $10^{-3} \text{ m}^2 \text{ V}^{-1} \text{ s}^{-1}$  ( $=10 \text{ cm}^2 \text{ V}^{-1} \text{ s}^{-1}$ ). At equilibrium,  $\frac{dN}{dt} = 0$ , which enables to calculate the equilibrium charge density

$$G_0 \cdot \eta - \frac{N}{\tau} = 0 \quad (\text{S2.4})$$

Substituting equation (S1.3) in equation (S1.4) gives,

$$N^{5/2} = \frac{8\varepsilon_0\varepsilon G_0\eta}{15\sqrt{\pi}e\mu} \quad (\text{S2.5})$$

$$N^{5/2} = \frac{8 \times 8.854 \times 10^{-12} \text{CV}^{-1}\text{m}^{-1} \times 4 \times (5.248 \pm 1.89) \times 10^{20} \text{s}^{-1}\text{m}^{-2} \times 0.5}{15\sqrt{\pi} \times 1.602 \times 10^{-19} \text{C} \times 10^{-3} \text{m}^2 \text{V}^{-1} \text{s}^{-1}} \quad (\text{S2.6})$$

$$N^{5/2} = 1.7 \pm 0.6 \cdot 10^{31} \text{m}^{-5} \quad (\text{S2.7})$$

$$N = 3.1 \pm 2.1 \cdot 10^{12} \text{m}^{-2} \quad (\text{S2.8})$$

In other words, the average distance between charge carriers would be about 564 nm, which is much larger than the platelet size and roughly the size of lamellar crystals. As static disorder is increased in the system, the mobility may be much lower than the highest mobility observed in 3D molecular crystals.<sup>[S2]</sup> Based on the above estimation, we infer that in such a bulk carrier quenching model, charge carriers would have to be trapped more severely in order to account for charge – exciton quenching in platelets or spin coated films (corresponding to charge carrier mobilities of about  $10^{-8}$  to  $10^{-6} \text{cm}^{-2} \text{V}^{-1} \text{s}^{-1}$  at low temperature). Following this argument to the end, the charge carrier mobility of  $10^{-6} \text{cm}^{-2} \text{V}^{-1} \text{s}^{-1}$  would imply a carrier lifetime of  $\tau = 15 \mu\text{s}$  and a two-dimensional diffusion length ( $L_D$ ) of,

$$L_D = 2 \cdot \sqrt{D \cdot \tau} = 2 \cdot \sqrt{\frac{\mu k T \tau}{e}} = 1.8 \text{nm}$$

conforming to long-lived charges that are closely localized near their generation sites.

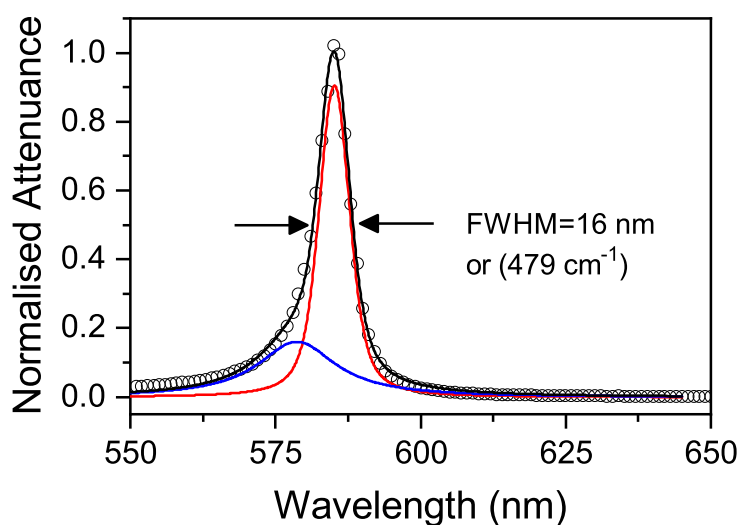


Figure S2.1 – The normalized attenuance of the J-aggregate peak measured from dye dissolved in water was de-convoluted to determine the full-width at half-maximum (FWHM). The measured J-aggregate peak is shown as scatter points, which is de-convoluted into two peaks – main J-aggregate peak as red line and the contribution from uncoupled molecules as blue line. The fitted J-aggregate curve is represented as black line.

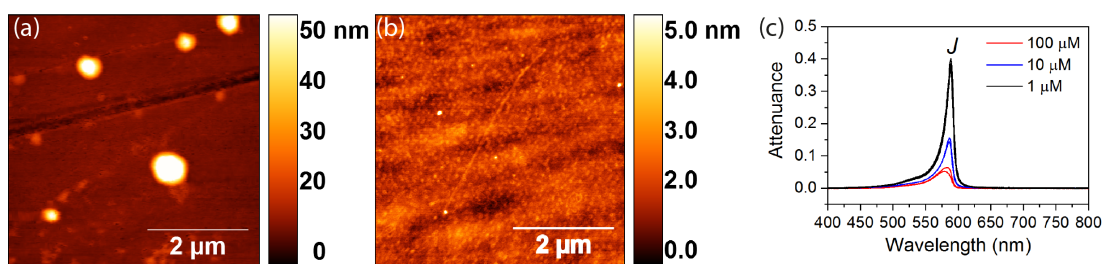


Figure S2.2 – PAMAM deposited on glass substrates at (a) high concentration (100  $\mu\text{M}$ ) and (b) low concentration (1  $\mu\text{M}$ ), forming PAMAM aggregates and a PAMAM monolayer, respectively. The J-aggregates are deposited on glass substrates functionalised with different PAMAM concentration. (c) The attenuance shows strong absorption from J-aggregate films deposited on the PAMAM monolayer. The spectra acquired at multiple spots from the sample are shown overlaid in same colour.



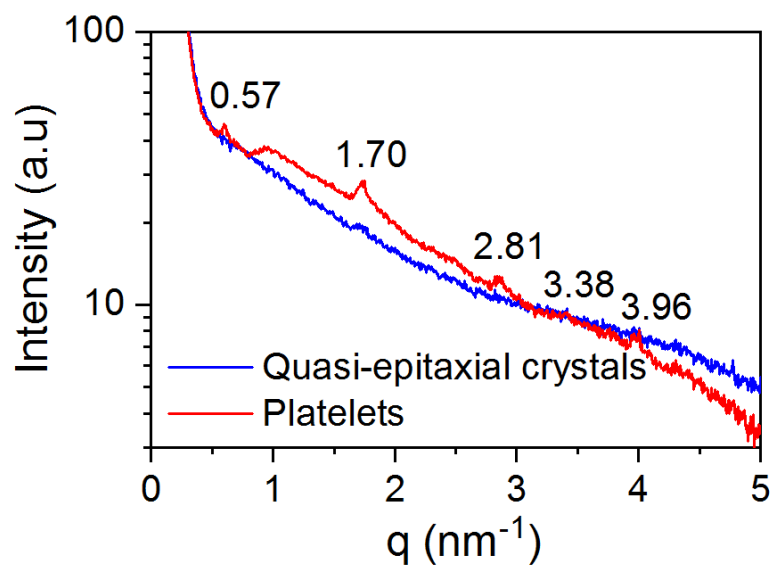


Figure S2.3 – Synchrotron SAXS measurement for platelets and quasi-epitaxial crystal thin films.

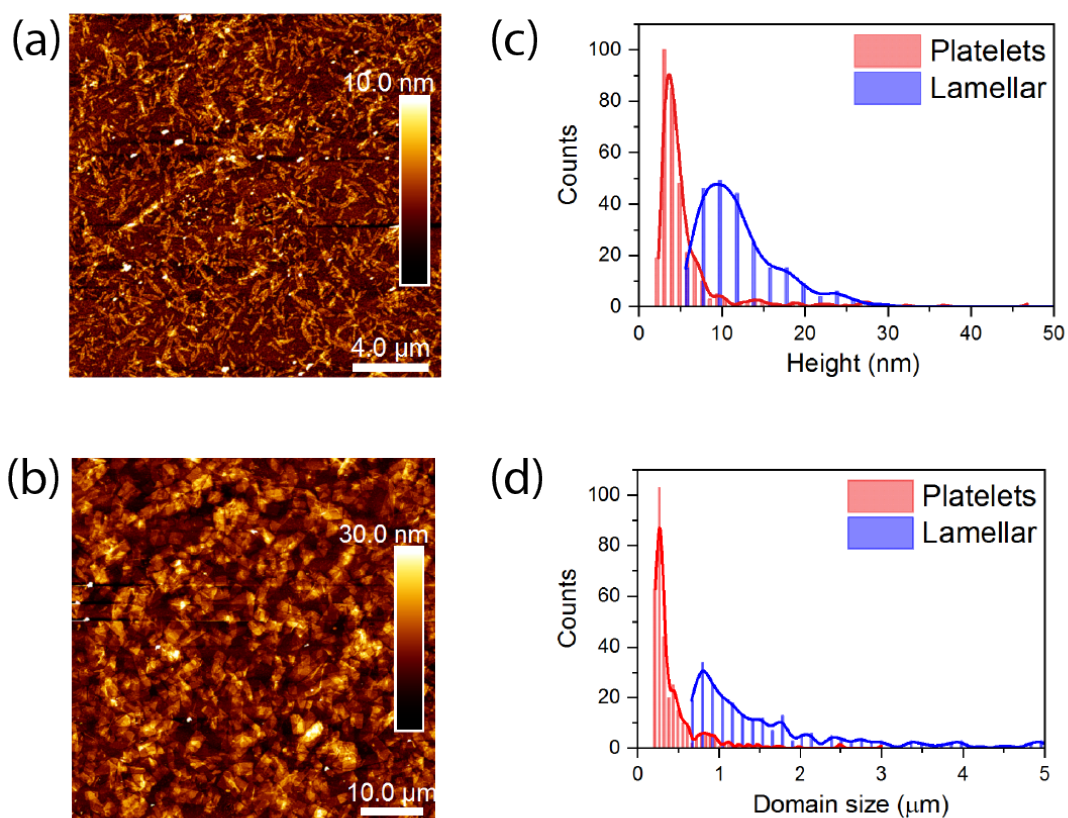


Figure S2.4 – Topographical image of platelets (a) and lamellar films (b) with their corresponding height (c) and domain size (d) distributions. The thickness of the platelets and lamellar films are  $\sim 4$  nm and 10 nm, respectively as shown in (c).

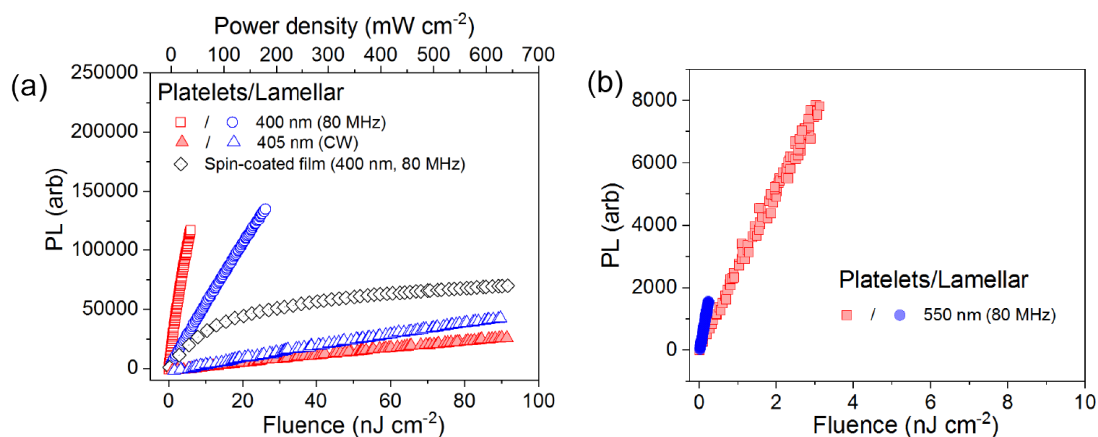


Figure S2.5 – Integrated PL intensity *versus* fluence acquired for continuous-wave and pulsed ultrafast excitation at 400 nm (a) and 550 nm (b) for platelets and lamellar films at 6 K. For comparison, spin-coated films were studied with ultrafast excitation at 400 nm, 80 MHz at 6 K.

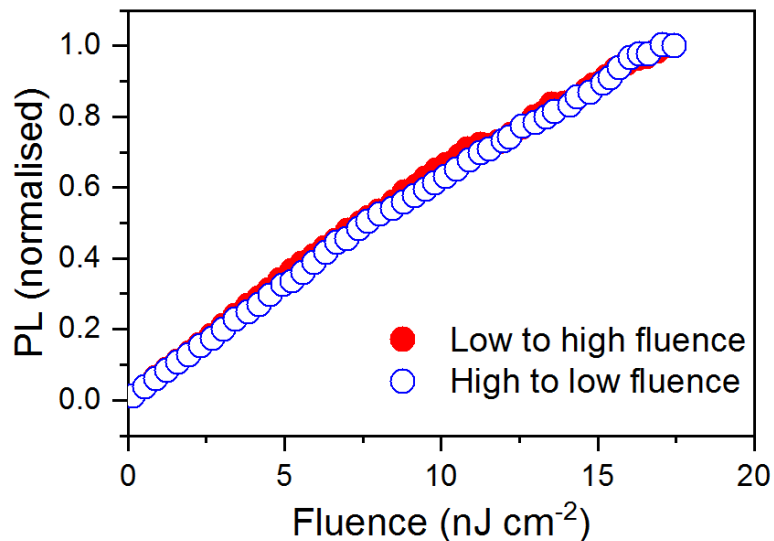


Figure S2.6 – Normalised PL *versus* fluence for platelets excited at 400 nm, 80 MHz at 6 K from low to high fluence and vice-versa to demonstrate reversibility of the process. From a power-law fit we obtain an exponent of 0.77 for both curves.

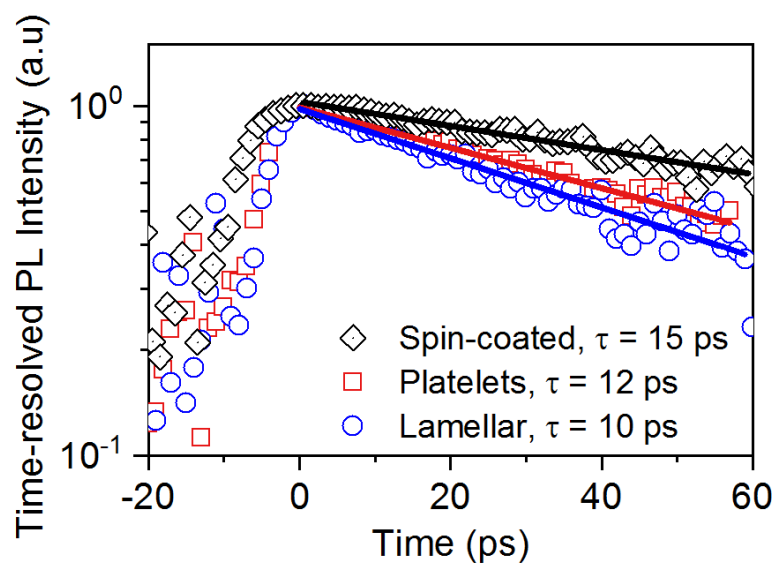


Figure S2.7 – Time-resolved spectrally-integrated dynamics (fluence of  $26 \text{ nJ cm}^{-2}$ ) with the lines representing the fits of an exponential decay to the data between 0 and 60 ps.

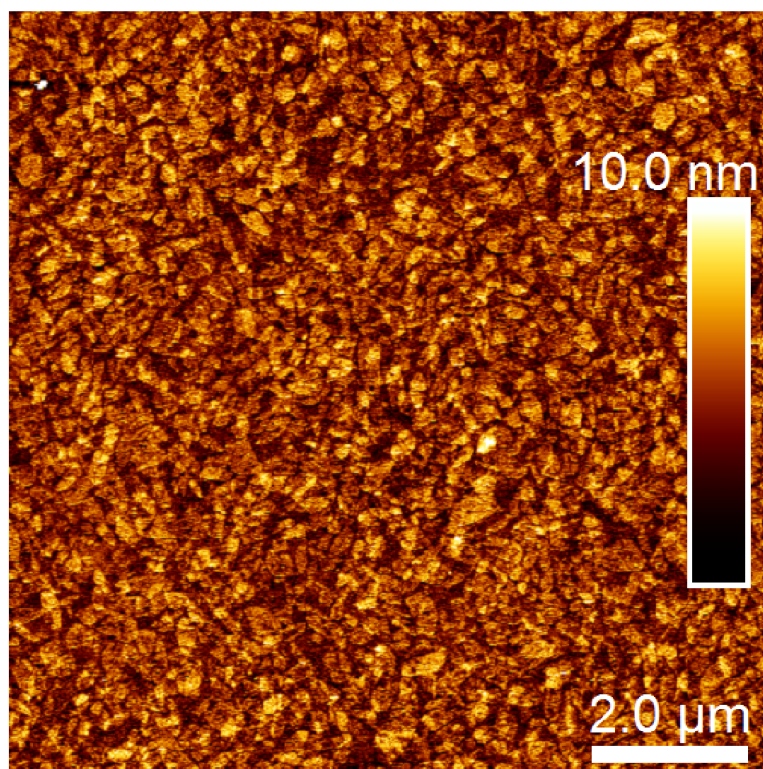


Figure S2.8 – Topography of spin-coated film obtained from J-aggregate dye solution (5 wt% dye) in water.

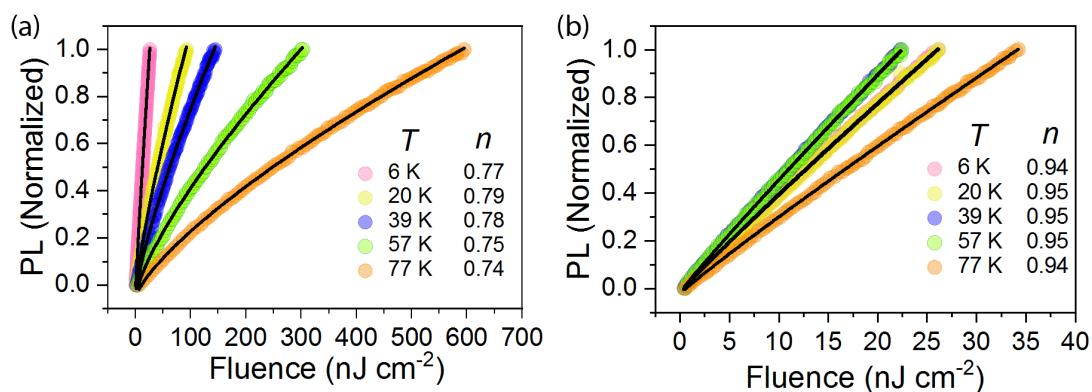


Figure S2.9 – PL intensity *versus* fluence recorded at different temperatures for (a) platelets and (b) lamellar films, keeping the excitation wavelength at 400 nm. The respective exponents  $n$  from power-law fits to the data are shown in the legend. It should be noted that, at 77 K, an enormous amount of pump power is required for acquiring PL in platelets ( $\sim 500 \text{ nJ cm}^{-2}$ ), unlike lamellar films ( $< 50 \text{ nJ cm}^{-2}$ ).

Table S2.1 – Full-width at half-maximum (FWHM) of the photoluminescence spectrum collected as a function of temperature for platelets and lamellar films.

Temperature (K)	Platelets			Lamellar		
	Gaussian width (cm <sup>-1</sup> )	Lorentzian width (cm <sup>-1</sup> )	FWHM (cm <sup>-1</sup> )	Gaussian width (cm <sup>-1</sup> )	Lorentzian width (cm <sup>-1</sup> )	FWHM (cm <sup>-1</sup> )
6	100.27 ± 3.83	92.33 ± 3.69	158.45 ± 1.45	58.64 ± 2.58	75.78 ± 2.12	108.94 ± 0.95
	100.27	91.07 ± 2.04	157.55 ± 1.46	58.64	78.61 ± 0.90	111.14 ± 0.71
39	100.27	103.27 ± 2.54	166.41 ± 1.87	58.64	91.91 ± 0.90	121.72 ± 0.73
57	100.27	116.52 ± 3.74	176.29 ± 2.83	58.64	102.01 ± 0.82	129.99 ± 0.68
77	100.27	151.83 ± 5.54	203.84 ± 4.45	58.64	115.58 ± 0.81	141.37 ± 0.69
100	100.27	164.51 ± 5.75	214.11 ± 4.70	58.64	128.23 ± 0.81	152.22 ± 0.70

Table S2.2 – Lifetime of the singlet exciton in platelets and lamellar films measured at 6 K for different laser fluence.

Laser fluence (nJ cm <sup>-2</sup> )	400 nm, 80 MHz		Laser fluence (mJ cm <sup>-2</sup> )	505 nm, 1 kHz	
	Platelets (ps)	Lamellar (ps)		Platelets (ps)	Lamellar (ps)
26	11.7	9.8	2.08	43	39.5
50	10.6	8.8	4.15	50	61.4
78	10.1	8	6.24	51.7	71.4

## Subbibliography

[S1] A. V. Nenashev, F. Jansson, S. D. Baranovskii, R. Österbacka, A. V. Dvurechenskii, F. Gebhard, *Applied Physics Letters* **2010**, 96, 213304.

[S2] G. Schweicher, Y. Olivier, V. Lemaure, Y. H. Geerts, *Israel Journal of Chemistry* **2014**, 54, 595.

# 3 Unprecedented Enhancement of J-aggregate Photoluminescence Quantum Yield at Room Temperature by Suppressing Non-radiative Decay Channels

Surendra B. Anantharaman<sup>1,2</sup>, Jay Patel<sup>1</sup>, Gabriele Rainò<sup>3</sup>, Sergii Yakunin<sup>3,4</sup>, Joachim Kohlbrecher<sup>5</sup>, Maksym Kovalenko<sup>3,4</sup>, Frank A. Nüesch<sup>1,2</sup>, and Jakob Heier<sup>1</sup>

<sup>1</sup>Laboratory for Functional Polymers, <sup>4</sup>Laboratory for Thin Films and Photovoltaics, Swiss Federal Laboratories of Materials Science and Technology, Empa, Überlandstrasse 129, CH-8600 Dübendorf, Switzerland.

<sup>2</sup>Institut des Matériaux, Ecole Polytechnique Fédérale de Lausanne, EPFL, Station 12, CH-1015 Lausanne, Switzerland.

<sup>3</sup>Laboratory of Inorganic Chemistry, Department of Chemistry and Applied Biosciences, ETH Zürich, Vladimir Prelog-Weg 1, Zürich, CH-8093, Switzerland.

<sup>5</sup>Laboratory for Neutron Scattering and Imaging (LNS), Paul Scherrer Institute, CH-5232 Villigen, Switzerland.

**Keywords:** J-aggregates, room temperature quantum yield, radiative excitons, small-angle neutron scattering.

*The contents of this chapter is under preparation for submission to a peer-reviewed journal publication*

**Author Contributions:** S.B.A conceived the idea, planned the project and performed quantum yield measurements. J.P prepared the samples and recorded PL under the supervision of S.B.A. S.B.A prepared the samples and analyzed the data for the TRPL measurements performed by G.R and the quantum yield measurements using thin capillaries by S.Y under the supervision of M.K. J.K, J.H and S.B.A conducted small-angle neutron scattering studies and J.K analyzed the data. E.N helped with the discussion on photophysics and structural assembly and provided valuable inputs. S.B.A wrote the manuscript with inputs from all co-authors.

### Abstract

Narrowband photoluminescence with high quantum yield are of paramount importance for light emitting devices. Supramolecular assemblies from organic dyes forming J-aggregates have shown a narrowband photoluminescence with full-width at half maximum < 20 nm. However, the quantum yield is very low for J-aggregates from cyanine dyes formed in solution. Here, we propose that spontaneous self-assembly of dye molecules to form J-aggregates introduce crystallographic defects, which lead to non-radiatively quench the excitons. Overcoming this non-radiative exciton quenching site by restructuring molecular assemblies in solution by adding alkylamine helps in passivating these defects, thereby leading to an unprecedented increase in quantum yield. Time-resolved photoluminescence (TRPL) studies showed an increase in the exciton lifetime with one-order of magnitude decrease in non-radiative rate. Combining the optical characterization with structural analysis of the J-aggregate solution using small-angle neutron scattering, a two-phase region in the ternary system (water-alkylamine-dye) was identified to achieve high PLQY in the J-aggregates.

### 3.1 Introduction

Two-dimensional assemblies (J-aggregates) of organic dye molecules have recently attracted interest among researchers in the field of polariton lasers,<sup>[1]</sup> organic light emitting devices,<sup>[2]</sup> hybrid energy transfer systems<sup>[3–5]</sup> and to build emerging opto-excitonic devices. Dye molecules held together by weak van-der-Waals forces may show different optical properties such as absorption and photoluminescence. A strong coupling of transition dipole moments leads to a narrow absorption and photoluminescence (PL) peak with small Stokes' shift. Such properties are exploited for narrowband photodetectors and high color purity emitters.<sup>[2]</sup> Furthermore, exploiting the high extinction coefficient of J-aggregates as donor material in hybrid organic/inorganic systems (in particular, J-aggregate/quantum dots) has shown to significantly improve the properties of the hybrid system,<sup>[3,4,6]</sup> thanks to the efficient Förster resonance energy transfer (FRET) process operating between the donor (J-aggregates) and acceptor (quantum dots). Although, FRET is a non-radiative energy transfer process, the photoluminescence quantum yield (PLQY) of the donor in the absence of acceptor is of paramount importance to minimize the non-radiative recombination of excitons and increase the FRET efficiency.



J-aggregates from a cyanine dye (5,6-dichloro-2-[[5,6-dichloro-1-ethyl-3-(4-sulfobutyl)-benzimidazol-2-ylidene]-propenyl]-1-ethyl-3-(4-sulfobutyl)-benzimidazolium hydroxide, inner salt, sodium salt, famously known as **TDBC** have been used in light emission devices such as hybrid polariton lasers<sup>[1,2]</sup> and hybrid energy transport systems.<sup>[3]</sup> The J-aggregates formed from the **TDBC** dye have a full-width at half maximum (FWHM) of absorption and PL of 13 nm ( $393\text{ cm}^{-1}$ ) and 5 nm ( $144\text{ cm}^{-1}$ ), respectively. For device applications, manufacturing of J-aggregate thin films is important and the quantum yield in thin films was reported to be  $\sim 2\%$ .<sup>[7]</sup> Recently, we have shown that the quantum yield in thin films can be improved up to  $\sim 5\%$  at room temperature and a seven-fold increase at 6 K was achieved by growing high quality J-aggregate crystals in the thin film.<sup>[8]</sup> It can be noted that the quantum yield is not so high, and this motivates us to revisit the aggregate formation in solution, as a first step to enhance its quantum yield at room temperature. To the present date, for comparison, J-aggregates from perylene bisimide in solution have shown a near 100 % PLQY at room temperature.<sup>[9]</sup>

In this work, we introduce a new mechanism for J-aggregate formation with high PLQY ( $\sim 60\%$ ) in a solution of colloidal water droplets in amines at room temperature. This facilitates to stabilize J-aggregates in the polar environment while monomers are stabilized in the non-polar environment. The structural transformation in the J-aggregates was studied using small-angle neutron scattering (SANS). This observation confirms a “mini-emulsion” formation, which is different from the literature models (micelles).<sup>[10,11]</sup> From time-resolved photoluminescence studies, an increase in lifetime of J-aggregates was observed with increase in PLQY, which confirms the suppression of non-radiative decay channels in the J-aggregates.

## 3.2 Results and Discussion

### 3.2.1 Optical properties of J-aggregate in the solution

The chemical structure of the cyanine dye (**TDBC**) used in this work is shown in Figure 3.1a. Upon dissolving the dye in methanol, only monomers were present. Dispersing the dye ( $c = 1\text{ mM}$ ) in water, immediately led to the formation of J-aggregates with peak absorption at 587 nm (Figure 3.1b). However, dispersing the dye at the same concentration in ethylamine solution, forms a reduced amount of J-aggregate (as observed from the decrease in optical density of the J-aggregate peak), with a concomitant increase in monomer phase content. The photoluminescence (PL) peak for both the solutions was recorded at an excitation wavelength ( $\lambda_{ex}$ ) of 550 nm by placing the samples inside an integrating sphere (Figure 3.1b). It can be clearly confirmed that the photoluminescence quantum yield from J-aggregates have significantly improved upon addition of ethylamine, while keeping the narrow full-width at half-maximum and peak position of the PL. The absolute photoluminescence quantum yield was initially calculated by following the method introduced by de-Mello.<sup>[12]</sup> The photoluminescence observed from both the solutions exposed to an UV lamp ( $\lambda_{ex}=366\text{ nm}$ ) and a laser ( $\lambda_{ex}=532\text{ nm}$ ) are shown in Figure 3.1c. The photoluminescence excitation (PLE) spectra recorded for the J-aggregates in ethylamine solution completely overlaps with the attenuation

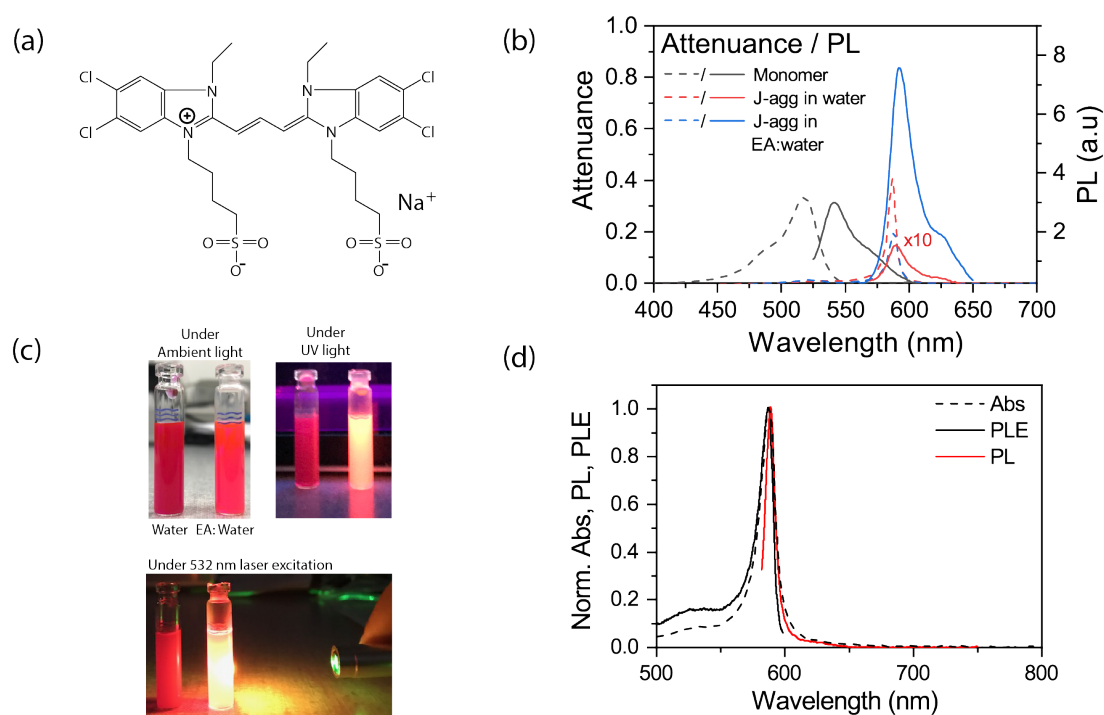


Figure 3.1 – (a) Chemical structure of the **TDBC** dye. (b) Attenuance of the monomer form of **TDBC** dye in methanol, and J-aggregates formed in water and ethylamine-water (1:1 vol%, **EA:Water**) with its corresponding photoluminescence (PL). The PL for J-aggregate in water is scaled 10 times. (c) Dye solution in water and ethylamine-water (**EA:Water**) mixture under ambient light (top left). Photoluminescence from the samples when exposed to UV light (top right) and 532 nm laser (bottom). (d) Normalized attenuance, photoluminescence excitation spectra (PLE) and PL for J-aggregates in ethylamine-water solution.

measured from UV-Vis spectroscopy, signifying that there is no excited state process present in the system. Furthermore, no additional peaks were observed at longer wavelengths as reported elsewhere.<sup>[13]</sup>

From the above results, it is clear that the addition of alkylamine has resulted in an increase in PL intensity. To quantify the absolute quantum yield and to understand the role of solvents, the dye solution was prepared using different solvents such as 0.1 M NaOH, ethanolamine, ethanolamine:water (1:1) and ethylamine:water (1:1) and in water as reference, while keeping the same dye concentration (1 mM). The absolute quantum yield was measured by taking the solution in 1mm glass capillaries to minimize reabsorption (Figure S3.1, Supporting Information).<sup>[14]</sup> Typically, cyanine J-aggregates are formed in NaOH solution to minimize protonation of the dye and allow stable J-aggregate formation.<sup>[15,16]</sup> A similar step followed here shows no increase in PLQY compared to J-aggregates formed in millipore water (Figure 3.2). Addition of ethanolamine to J-aggregate solution in 1:1 volume ratio resulted in a small increase in PLQY (< 5%). Nevertheless, addition of dye solution directly to the ethanolamine solution improved the PLQY to ~12%. From these observations, it can be clearly said that the

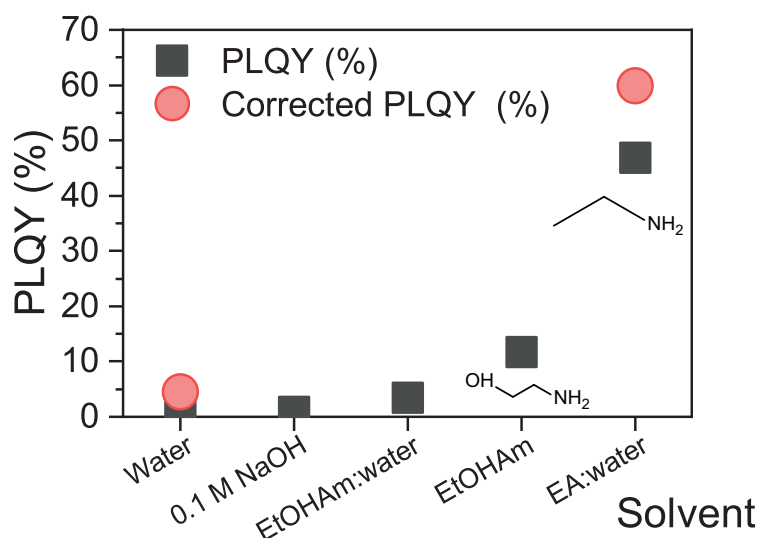


Figure 3.2 – Absolute photoluminescence quantum yield for J-aggregates measured in different solvents – water, 0.1 M NaOH, ethanolamine-water (1:1, **EtOHAm:Water**), ethanolamine (**EtOHAm**) and ethylamine-water (**EA:Water**). Self-absorption corrected PLQY for J-aggregates in water and ethylamine-water (**EA:Water**) system are shown as circles.

-OH group had minor influence compared to the amine group, which showed an improvement in the PLQY. Upon addition of ethylamine to J-aggregate dye solution in 1:1 volume ratio by maintaining the final dye concentration to 1 mM resulted in unprecedented improvement in PLQY to ~46.9 % (without reabsorption correction). It can be confirmed that a 3-fold increase in PLQY by replacing ethanolamine to ethylamine signifies the role of end group (-OH) in the guest molecules are very important. Wavelength dependent PLQY measured from 500 to 600 nm in 2 nm intervals showed a slightly lower PLQY from 500 to 540 nm, corresponding to monomer absorption band (Figure S3.2, Supporting Information). Although, a Förster resonance energy transfer is possible from monomer to J-aggregates, the limited energy transfer efficiency from monomer to J-aggregate can be a possible reason for slightly lower PLQY. Nevertheless, the PLQY was almost constant above the monomer absorption peak (520 nm) upto J-aggregate peak absorption (586 nm). Due to small Stokes' shift between J-aggregate absorption and photoluminescence, reabsorption was corrected for J-aggregates in water and ethylamine solution as reported by Ahn et al.<sup>[14]</sup> It can be noted that the reabsorption corrected PLQY for J-aggregates in water and ethylamine are 4.5 % and 60.6 %, respectively. Further increase in alkylchain length from ethyl- to hexyl-, while keeping the same dye concentration (1 mM) resulted in disintegration of J-aggregates to monomers (Figure S3.3, Supporting Information). Nevertheless, it will be shown later, with increase in dye concentration, J-aggregates with high PLQY can be retained in hexylamine solution.

Deeper insights to understand the increase in the J-aggregate's PLQY upon addition of ethylamine were pursued by characterizing the exciton lifetime and structural order in the solution. The time-resolved photoluminescence spectroscopy (TRPL) studies were performed with

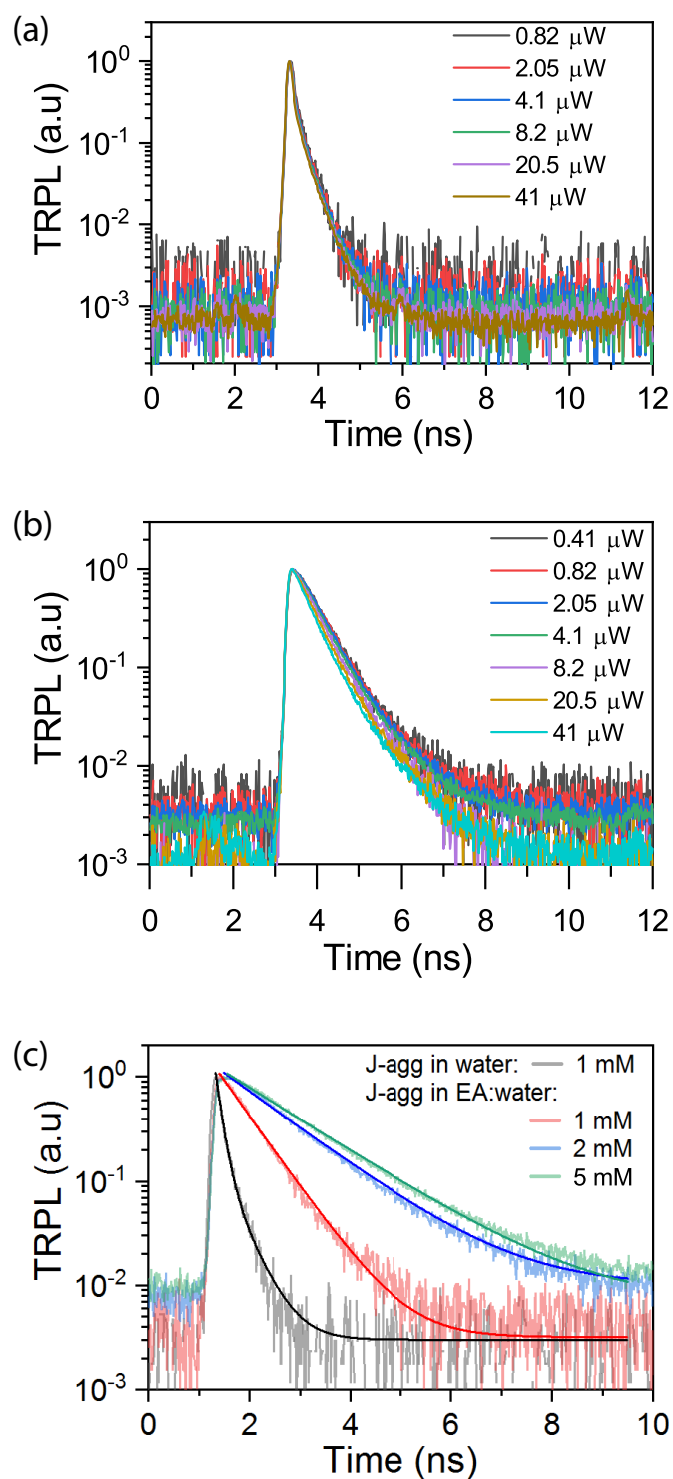


Figure 3.3 – Time-resolved photoluminescence (TRPL) studies for the J-aggregate emission recorded for the dyes dispersed in water (a) and in ethylamine:water (**EA:Water**) (b) at different excitation power as mentioned in the labels. (c) TRPL for J-aggregates formed at different dye concentration in ethylamine solution (**EA:Water**) with excitation power  $\sim 0.41 \mu\text{W}$  compared with the 1 mM dye solution in water (excitation power  $\sim 0.82 \mu\text{W}$ ).

Table 3.1 – Exciton lifetime values obtained from mono- and bi-exponential decay fits.

Solution	Dye conc. (mM)	Excitation power ( $\mu\text{W}$ )	Fitting	Amplitude (A) and decay time (t)
J-aggregates in water	1	0.82	Bi-exponential	$A_1 = 0.94$ ; $t_1 = 114\text{ps}$ $A_2 = 0.16$ ; $t_2 = 383\text{ps}$ Average decay time, $\langle\tau_{avg}\rangle = 153\text{ ps}$
J-aggregates in EA:water	1	0.41	Mono-exponential	638 ps
	2	0.41		1231 ps
	5	0.41		1426 ps

J-aggregate solutions in water and a EA:water system in 1 mm path length cuvettes. A pulsed laser with excitation wavelength at 400 nm with 80 MHz repetition rate was used in this study and the TRPL data are shown in Figure 3.3 (a and b). TRPL decay for J-aggregates in water showed a bi-exponential decay profile at room temperature in agreement with the findings of Lindrum et al.<sup>[17]</sup> The fast decay component ( $t_1$ ) is assigned to the natural exciton lifetime and the slow decay component ( $t_2$ ) denotes the presence of non-radiative decay channels. The average exciton lifetime for J-aggregates in water was 153 ps (excitation power = 0.82  $\mu\text{W}$ , Table 1). With increase in excitation power from 2.05  $\mu\text{W}$  to 41  $\mu\text{W}$ , a similar average exciton lifetime (153-178 ps) and bi-exponential exciton decay dynamics was observed (Figure S3.4a and b, Supporting Information). For the same dye concentration (1 mM) in the ethylamine-water system, the exciton lifetime increased drastically to 638 ps (0.41  $\mu\text{W}$ ) and 641 ps (0.82  $\mu\text{W}$ ). Furthermore, a mono-exponential fitting has a convergence and goodness of fit with the data. The TRPL fitted data profile for J-aggregates in water and in ethylamine-water for two different excitation powers are shown in Figure S3.4, Supporting Information. From these observations it can be concluded that the non-radiative decay channels are obviated upon addition of ethylamine to the J-aggregates. For reference, the exciton lifetime of monomers ( $\tau_{monomer}$ ) for the same dye calculated from the Strickler-Berg relation was reported to be 2.4 ns.<sup>[18]</sup> From the relation between lifetime of monomers and J-aggregates ( $\tau_{J-agg} = \tau_{monomer}/N$ ),<sup>[19]</sup> the number of molecules coupled in an aggregate domain in the water and EA:water system is calculated to be  $\sim 15$  and 4, respectively. Muneter et al.<sup>[20]</sup> have investigated the influence of the J-aggregate size on photoluminescence lifetime and quantum yield. They reported that with increase in aggregate size, the funneling of excitons to non-radiative decay channels becomes a dominant process. Also, small J-aggregates are expected to have a higher efficiency of electron transfer from J-aggregates to AgBr conduction band. Taking this size effect of J-aggregates onto PLQY into account, we can say that addition of ethylamine to J-aggregate solution may reduce the physical size of J-aggregates, thereby minimizing the non-radiative decay channels (grain boundaries, defects) present in large J-aggregate crystals (for example, J-aggregates in water). Later, we will confirm that the size of the J-aggregates changes upon addition of alkylamine using small-angle neutron scattering studies.

Using the photoluminescence quantum yield,  $\phi_f$  (4.5 % and 60 % for water and EA:water system, respectively) and exciton lifetime (153 ps and 638 ps for the water and EA:water system, respectively) we have calculated the radiative ( $k_r$ ) and non-radiative rate ( $k_{nr}$ ) from equation 3.1 and equation 3.2.

$$\phi_f = \frac{k_r}{k_r + k_{nr}} \quad (3.1)$$

$$\tau = \frac{1}{k_r + k_{nr}} \quad (3.2)$$

The radiative rate ( $k_r$ ) for J-aggregates in water and EA:water system are  $0.294 \times 10^9 \text{ s}^{-1}$  and  $0.94 \times 10^9 \text{ s}^{-1}$ , respectively. The non-radiative rate ( $k_{nr}$ ) for J-aggregates in water and EA:water system are  $6.241 \times 10^9 \text{ s}^{-1}$  and  $0.627 \times 10^9 \text{ s}^{-1}$ , respectively. It can be clearly observed that a 1-order of magnitude decrease in non-radiative rate is achieved upon addition of ethylamine to the J-aggregate solution. This is reflected by an increase in PLQY from 4.5% to 60%. Furthermore, at high excitation intensities ( $41 \mu\text{W}$ ), also the EA:water system showed a bi-exponential decay with shortening of lifetime (342 ps, Figure S3.4d, Supporting Information). Decrease in lifetime, high PLQY and an additional exciton decay component can be ascribed to exciton-exciton annihilation in the EA:water system. However, no change in exciton lifetime, or change in fitting functions was observed for J-aggregates in water. With limited PLQY in this system, the non-radiative decay channels (grain boundaries) can be the dominant exciton quenching site.

To further understand the role of dye content in the EA:water system, we have increased the dye concentration from 1 mM to 2 mM and 5 mM. Using the same excitation power ( $0.41 \mu\text{W}$ ), the lifetime of J-aggregates increased while still having a mono-exponential decay fitting (Figure 3.1c). However, PL peak position shows a pronounced red-shift and broadening (Figure S3.5, Supporting Information). This can be due to a strong reabsorption of the photons facilitated by the overlap integral between absorption and photoluminescence at high dye concentrations. With high PLQY in EA:water system, at high dye concentration the increased overlap integral area between absorption and photoluminescence, can trap the photons, thereby giving rise to longer exciton lifetime. A similar observation on increasing the exciton lifetime in the case of  $\text{CsPbI}_3$  perovskite microwires<sup>[21]</sup> and its influence in performance of perovskite solar cells are reported.<sup>[22]</sup> Considering the small Stokes shift and high PLQY of J-aggregates in the EA:water system, and similar to the case of perovskite nanowires, we ascribe the lengthening of exciton lifetime at high dye concentration to *photon recycling*.

### 3.2.2 Structural properties of J-aggregate in the solution

The structure of J-aggregates from cyanine dyes is well-known to undergo modifications upon addition of surfactant or salt. In such cases, small-angle neutron scattering (SANS) studies have provided deeper insights into the structural modification.<sup>[23,24]</sup> In our case, we have shown that the addition of ethylamine to J-aggregates in water leads to high PLQY in the solution. However, the structural order of ethylamine-water-dye falls below the resolution limit of SANS set-up. Alternatively, we have chosen hexylamine-water-dye system which also gives high PLQY similar to the addition of ethylamine to J-aggregate solution.

Different from the EA:Water system, the HA:Water system macro-phase separates into two phases for HA volume fractions between 5 and 50 % (Figure S3.6, Supporting Information). The highly luminescent J-aggregate is only formed in the HA-rich phase. Even more interesting, the dye is completely expelled from the water-rich phase. Similar to the EA:water system, in the one-phase region at high amine content, the non-fluorescent aggregate forms. Some of the factors such as interactions of the dye with the amine groups, stabilization of J-aggregates and monomers depending on the solvent environment play an important role in forming J-aggregates with high PLQY.

To fully understand the role of HA in the stabilization of a highly emissive J-aggregate, we probe the phases of the D<sub>2</sub>O and HA system and investigate the effect of HA addition to a J-aggregate solution with SANS. To minimize the background scattering, we have used D<sub>2</sub>O instead of H<sub>2</sub>O for the SANS measurement. Details of the phase morphology are obtained from SANS studies. Generally, scattering techniques and especially SANS have proven extremely useful to probe colloidal suspensions and fractal aggregates in the range from 2 nm to 300 nm. An important quantity to consider is the magnitude of the scattering wave vector  $q$ , which acts as probe for structures of size  $1/q$ . The scattering intensity,  $I(q)$  is typically described as the product of form factor  $P(q)$  and the structure factor  $S(q)$ . At large  $q$  the form factor  $P(q)$  is relevant, which describes the scattering function from a single primary particle and is directly connected to the autocorrelation function of the primary particle. At small  $q$ , the variations in scattering intensity are dominated by the structure factor  $S(q)$  which describes the spatial correlation between particles.

We first investigate the plain D<sub>2</sub>O:HA system. For D<sub>2</sub>O:HA volume ratios between 95:05 and 50:50, the solution separates into two macroscopic phases separated by a clearly visible phase boundary, similarly to the ternary system including the dye. A water rich phase remains at the bottom of the vial, while a HA-rich phase segregates to the top (Figure S3.6, Supporting Information). These findings are consistent with literature reports of a water-HA phase diagram.<sup>[25]</sup> SANS spectra of extracted HA-rich and the blended phase of the D<sub>2</sub>O:HA system at different volume fraction are shown in Figure 3.4a. All solution spectra show a characteristic ring in the high  $q$ -region, which translates into a signature peak in the radially integrated spectra. Such a peak is typical for scattering from amorphous soft materials and polycrystalline colloids, where the characteristic distance ( $d_0$ ) between scattering heterogeneities is given by

the d-spacing,

$$d_0 = \frac{2\pi}{q_0} \quad (3.3)$$

where,  $q_0$  is the peak position. The scattering invariant ( $Q^*$ ) can be calculated by,

$$Q^* = \int_0^{\infty} q^2 I(q) dq \quad (3.4)$$

A best fit to the form factor of the spectra suggests ellipsoidal shaped D<sub>2</sub>O droplets in the nanometer range with a small attractive interaction (sticky ball model). For a sample with D<sub>2</sub>O:HA volume ratios of 70:30 the structural dimension corresponds to radius  $r_1 = 0.4$  nm and  $r_2 = 1.5$  nm. Figure 3.4b shows the value of the scattering invariant and the characteristic dimension  $d_0$  of the structure factor (extracted from the scattering peak position). We identify  $d_0$  as the average distance between water droplets. For D<sub>2</sub>O:HA volume fractions 95:5, 90:10, 80:20, 70:30 and 60:40, scattering invariant and peak position remain practically constant, which indeed should be the case for all starting compositions within a two phase region. Decreasing the D<sub>2</sub>O volume fraction further, the scattering invariant decreases approximately linearly, proving that the D<sub>2</sub>O droplets are indeed the source of scattering. Similarly, at large  $q$  the scattering intensity increases with decreasing D<sub>2</sub>O volume fraction because of increased incoherent scattering from HA (Figure 3.4a). The 99:1 sample does not show any contribution to scattering, which signifies that the composition is within the solubility limit of HA in water (1-phase region) (Figure 3.5). Surprisingly, the characteristic distance between scattering centers is decreasing from 4.4 nm to 2.2 nm for the 10:90 sample.

The data require a refinement of the suggested phase structure to explain how less scattering material still gives rise to a smaller characteristic distance. Starting from a pure HA solution, addition of water results in the formation of colloidal water droplets in the HA-matrix. With increasing water content, the droplet size increases. At a 60:40 volume fraction, the water droplets reached an equilibrium size at most dense packing (Figure 3.4c, left side). By increasing the water content further, excess water separates from the HA-rich phase, forming its own, water-rich phase. In the two phase region, the morphology of the HA-rich phase stays the same. On the HA rich side of the diagram, the scattering originates from smaller features, while the volume fraction of water decreases. Here one needs to assume that the individual water droplets form clusters within the HA matrix (Figure 3.4c, right side). The scattering ring stems from the characteristic length-scale of water droplets within the clusters. The emulsion is stabilized by the charges of the amine head-groups assembling in the water droplets.

One source of photoluminescence quenching in J-aggregates is assigned to local traps present



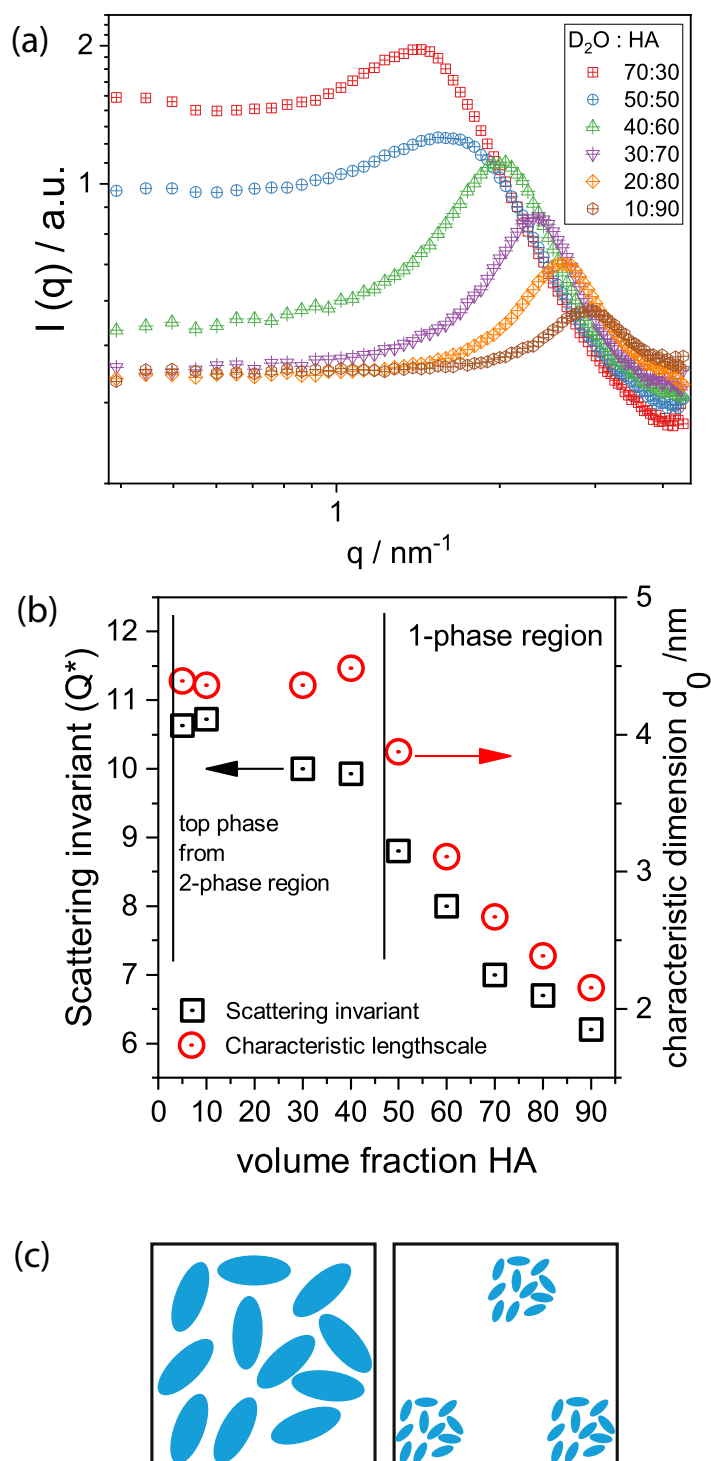


Figure 3.4 – (a) SANS spectra of blends of  $\text{D}_2\text{O}$  and HA with different volume ratios of  $\text{D}_2\text{O}$  to HA. (b) Scattering invariant ( $Q^*$ ) and characteristic dimension ( $d_0$ ) for blends of  $\text{D}_2\text{O}$  and HA. From the two-phase region, only the HA-rich phase is shown. (c) Schematic of morphology in the blended phases from the 1-phase region (left) and HA-rich phase from the 2-phase region (right).

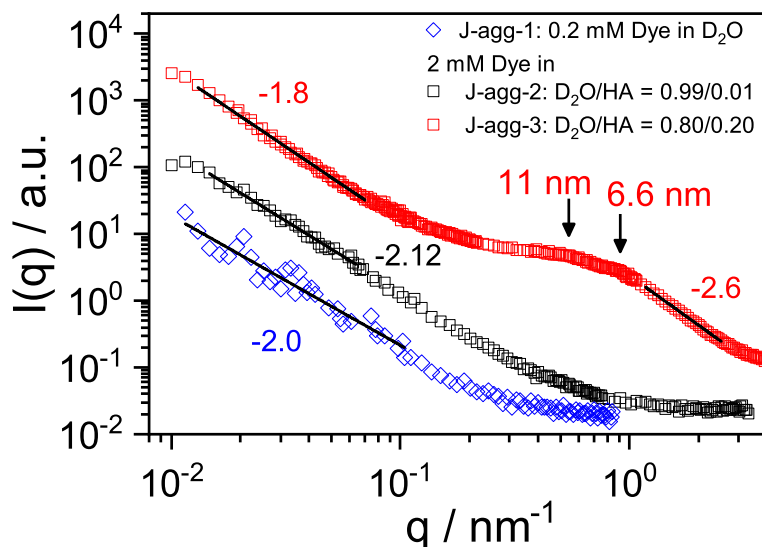


Figure 3.5 – SANS spectra of the J-aggregates in different solutions as mentioned in the labels.

at the contact sites between individual aggregates.<sup>[26]</sup> Breaking aggregates into single crystalline units without grain boundaries could thus eliminate non-radiative decay pathways.<sup>[8]</sup> Similarly, dye molecules loosely attached to the J-aggregate interfaces and not integrated into the J-aggregate crystal lattice act as quenching sites. Removing these molecules by dissolving them in a solvent that does not attack the J-aggregate, will also improve the fluorescence quantum yield.

We claim both mechanisms described above can be of relevance in our system. To further validate the relative changes in the physical size of the J-aggregate upon addition of hexylamine, we present SANS spectra of a diluted J-aggregate solution (J-agg-1), a J-aggregate solution where a small amount of HA has been added to but has not changed the emissive properties (J-agg-2) and a solution where a sufficient amount of HA has been added so that phase separation occurs, leading to an highly emissive aggregate (J-agg-3), (Figure 3.5). As described before, adding larger amounts of HA to a J-aggregate solution (1-phase region) will fully disintegrate the J-aggregate into monomers, and the colloidal water suspension was formed (Figure S3.6, Supporting Information).

For all samples, at low  $q$  (Guinier –regime), no plateau value was reached, indicating that for all cases the aggregate is larger than the 300 nm probed with SANS. All spectra show scaling behavior of the structure factor for  $0.015 \text{ nm}^{-1} \leq q \leq 0.10 \text{ nm}^{-1}$ . The least-squares fitting for J-agg-1 and J-agg-2 yielded potential laws of  $\alpha \approx 2.0$ , from where different interpretations are possible.  $\alpha = 2.0$  can be attributed to Gaussian chain behavior or a 2-dimensional platelet structure. In the latter model dye monomers directly assemble into a large 2-D aggregate structure, which is consistent with common models of J-aggregate structures. But, also the

similarity of the fractal structure of J-aggregates and more conventional fractal nanoparticle composites has been pointed out.<sup>[27]</sup> Following this formalism, we can interpret  $\alpha$  as the mass fractal dimension of the aggregate.<sup>[28]</sup> Adding small amounts of HA (volume fraction 0.01, J-agg-2) increases the scattering intensity. In J-agg-3 enhanced scattering in the medium to high  $q$ -range was observed, which now allows to extract information on the building block of the aggregate and proves that the emissive J-aggregate structure differs significantly from the “original” aggregate.

It can be concluded that the most interesting composition range is the region where the system separates into two phases. Here the emissive aggregate segregated with HA into the HA-rich phase – the water rich phase remained free of J-aggregates even though in the HA free system large J-aggregates form as hydrates in water. For the SANS experiments the top phase was extracted, the SANS spectra of the solution is also shown in Figure 3.5. The spectra differ greatly from the spectra of the pure aggregates or the D<sub>2</sub>O/HA blend. The presence of nano-colloidal water droplets as seen before can be excluded, meaning the dye inhibits the formation of a nano-emulsion upon adding HA to the solution. The onset of scaling for  $q$ -values  $< 0.1 \text{ nm}^{-1}$  indicates weakly coupled aggregation. The scaling exponent smaller than 2 suggests a break-up of the 2D-platelet structure into a fractal structure, or a decrease of dendritic branching. Two “bumps” at  $q=0.95 \text{ nm}^{-1}$  and  $q=0.55 \text{ nm}^{-1}$  indicate that the building block is characterized by the two length scales,  $l = 6.6 \text{ nm}$  and  $l = 11 \text{ nm}$ . The scaling factor of -2.6 for large  $q$  deviates from a pure Porod-law. Good fits to the data could be obtained with different structure factor profiles. All profiles suggest stacking of elongated particles ranging from 1 nm to 6 nm in size, with different stacking geometries.

In the one-phase region, HA forms the majority phase (Figure 3.4c), and HA being a good solvent for the cyanine dye quickly destroys the J-aggregate. In the opposite region (water rich), the “original aggregate” remains but seems to be reduced in size (less branches). In the two-phase region, the emissive aggregate will segregate with HA into the HA-rich phase. It is notable that the water rich phase will remain free of J-aggregates (and dye) even though large J-aggregates form as hydrates in water. It seems energetically more favorable to encapsulate the aggregate in the water colloids. This confinement of J-aggregates into nano-droplets of water has been reported before for water emulsions.<sup>[29]</sup> Adding HA to a J-aggregate solution will initiate two processes: HA will encapsulate small volumes of water. This colloidal system will macroscopically segregate from a plane water phase. At this point, J-aggregate hydrates are too large to be incorporated in the water droplets. At the same time HA will decompose the J-aggregate. Especially branching points and defect molecules at the interface are prone to HA attack because of the good solubility of the dye in HA.

At equilibrium, a J-aggregate of limited size is confined in a water droplet stabilized by the HA matrix. The water droplets are larger than the droplets in the original water:HA system as the addition of the cationic dye shields the charges of HA and stabilizes larger colloids. The J-aggregate morphology is of high quality as high energy defect sites are “removed” by HA. It is also known that the interfaces of colloidal suspensions show a high degree of molecular order

which may also improve the quality of the J-aggregate.

Collectively, the increase in PLQY for J-aggregates in hexylamine-water-dye system has a strong correlation with the structural changes in the system as confirmed from SANS studies. The optical properties from Figure S3.6 are used to summarize the findings. As guidelines, the results from both optical and structural properties of J-aggregates in the ternary phase diagram are summarized in Figure 3.6. The optical property and assembly type are marked as scatter points and the line represents the two phase region obtained from SANS studies. At low dye concentration ( $1\ \mu\text{M}$ ), J-aggregates are immediately formed in water, that dissolves into monomer upon addition of hexylamine. Nevertheless, with increase in dye concentration, the presence of HA-rich phase in water forms J-aggregates with high PL as explained above. Further increasing the hexylamine content leads to destabilize this phase and in turn lower the PLQY in J-aggregates (low PLQY J-agg).

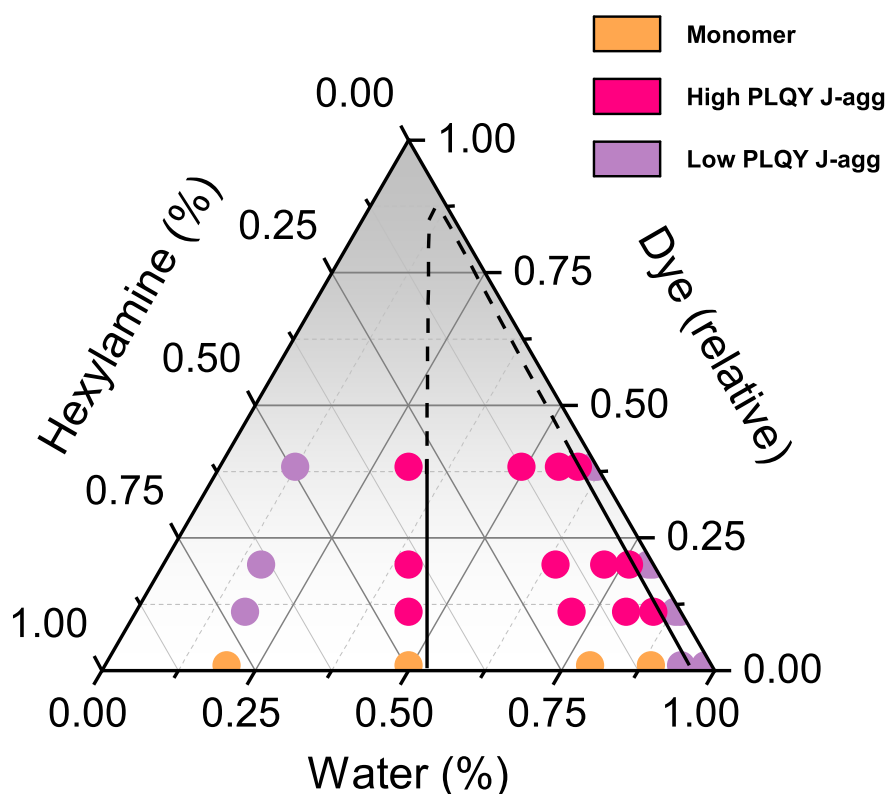


Figure 3.6 – Overlapping optical phase content (monomer, high PLQY J-aggregates, pristine J-aggregates) with phase boundaries (lines) observed from SANS studies in water-hexylamine-dye ternary phase diagram.

### 3.3 Conclusion

Spontaneous self-assembly of dye molecules to form large microcrystals in solution introduces crystallographic defects which are deleterious to high PL quantum yields. Modifying the dye solution by adding hexylamine (or ethylamine) passivates these defects by reassembling the molecules at the water/alkylamine interface and suppresses the edge-defects. This leads to an increase in the quantum yield from 5% to 60%, with an order of magnitude decrease in non-radiative rate and increase in exciton lifetime as inferred from the time-resolved photoluminescence studies. Small-angle neutron scattering studies confirm a two-phase region – HA-rich and water-rich in the ternary system (water-hexylamine-dye). Confinement of J-aggregates inside the water droplets formed in HA-rich phase is prerequisite to significantly minimize the non-radiative decay channels. A correlation between structural transition and increasing photoluminescence quantum yield in a ternary phase diagram is established in this study.

### 3.4 Experimental Section

**J-aggregate Preparation:** The cyanine dye (5,6-dichloro-2-[[5,6-dichloro-1-ethyl-3-(4-sulfobutyl)-benzimidazol-2-ylidene]-propenyl]-1-ethyl-3-(4-sulfobutyl)-benzimidazolium hydroxide, inner salt, sodium salt (**TDBC**)) procured from FEW chemicals, Germany was used without further purification. Ethylamine solution (70 wt% in H<sub>2</sub>O), propylamine, hexylamine and ethanolamine were purchased from Sigma Aldrich. The TDBC dye was dissolved in Millipore water to form J-aggregates. After an idle period of 24 h, the J-aggregate solution was mixed with ethylamine and hexylamine in different ratios.

#### Characterization

**Optical Properties:** Absorption of the J-aggregate solution was measured using a Varian Cary 50 UV-Vis spectrophotometer. Photoluminescence of the dye solution was measured using glass capillaries with 1 mm path length to minimize reabsorption in an integrating sphere. The absolute photoluminescence quantum yield was measured using a Quantaaurus-QY C11347 spectrometer from Hamamatsu followed by reabsorption correction as reported by Ahn et al.<sup>[14]</sup> Briefly, the dye solution taken in the glass capillary was placed in the integrating sphere to record the emission ( $F_{obs}(\lambda)$ , including reabsorption). The emission for the same solution was measured without integrating sphere ( $F'(\lambda)$ ). The reabsorption factor ( $a$ ) was calculated using

$$\frac{\int_0^{\infty} F_{obs}(\lambda) d\lambda}{\int_0^{\infty} F'(\lambda) d\lambda} = 1 - a \quad (3.5)$$

The reabsorption factor is used to correct the observed quantum yield ( $QY_{obs}$ ) as

$$QY = \frac{QY_{obs}}{1 - a} \quad (3.6)$$

Photoluminescence excitation (PLE) spectra for the J-aggregate emission wavelength were acquired in the Fluorolog spectrometer.

**Time-resolved Photoluminescence (TRPL):** A frequency-doubled mode-locked Ti:Sapphire laser to generate a 400 nm excitation with 80 MHz repetition rate was used to excite the sample. The room temperature time-resolved photoluminescence for the J-aggregates in water and ethylamine:water solution were studied with a time-correlated single photon counting setup equipped with a SPC-130-EM counting module (Becker & Hickl GmbH) and an IDQ-ID-100-20-ULN avalanche photodiode (Quantique) for recording the decay traces. Average exciton lifetime ( $\langle \tau_{avg} \rangle$ ) from bi-exponential fit were calculated from

$$\langle \tau_{avg} \rangle = \frac{\sum_i A_i t_i^2}{\sum_i A_i t_i} \quad (3.7)$$

where,  $A_i$  and  $t_i$  are the corresponding amplitudes and exponential decay parameters in a bi-exponential fitting.

**Small-angle Neutron Scattering (SANS):** For SANS measurement, the dye was dissolved in  $D_2O$  and then the desired amount of hexylamine was added to understand the phase formation/separation in the solution. For reference, different amount of hexylamine to  $D_2O$  ratio was prepared to understand the interaction in the matrix. The dye solution and the matrix solution was filled in cylindrical quartz cuvettes and sealed with Teflon cap to perform SANS measurements at PSI, Swiss Spallation Neutron Source (SINQ) facility, Switzerland. To minimize the background scattering,  $D_2O$  was used instead of  $H_2O$ . Empty cuvette, deuterium oxide ( $D_2O$ , 99.9%, Cambridge Isotope Laboratories, Inc.) was used for baseline correction.

**Acknowledgements** The authors gratefully acknowledge funding from the Swiss National Science Foundation grant numbers: 200021-157135 and 169695 to conduct this research work. We acknowledge the Scanning Probe Microscopy user laboratory at Empa for providing access to the instrument. We acknowledge the Small Angle Neutron Scattering Facility at PSI (Switzerland). J.P acknowledges The International Association for the Exchange of Students for Technical Experience (IAESTE) which enabled him to take part in this work at Empa.

# Bibliography

- [1] G. G. Paschos, N. Somaschi, S. I. Tsintzos, D. Coles, J. L. Bricks, Z. Hatzopoulos, D. G. Lidzey, P. G. Lagoudakis, P. G. Savvidis, *Scientific Reports* **2017**, 7, 11377.
- [2] N. Christogiannis, N. Somaschi, P. Michetti, D. M. Coles, P. G. Savvidis, P. G. Lagoudakis, D. G. Lidzey, *Advanced Optical Materials* **2013**, 1, 503–509.
- [3] Q. Zhang, T. Atay, J. R. Tischler, M. S. Bradley, V. Bulović, A. V. Nurmikko, *Nature Nanotechnology* **2007**, 2, 555–559.
- [4] B. J. Walker, V. Bulović, M. G. Bawendi, *Nano Letters* **2010**, 10, 3995–3999.
- [5] D. M. Coles, N. Somaschi, P. Michetti, C. Clark, P. G. Lagoudakis, P. G. Savvidis, D. G. Lidzey, *Nature Materials* **2014**, 13, 712–719.
- [6] F. S. Freyria, J. M. Cordero, J. R. Caram, S. Doria, A. Dodin, Y. Chen, A. P. Willard, M. G. Bawendi, *Nano Letters* **2017**, 17, 7665–7674.
- [7] S. Wang, T. Chervy, J. George, J. A. Hutchison, C. Genet, T. W. Ebbesen, *The journal of physical chemistry letters* **2014**, 5, 1433–1439.
- [8] S. B. Anantharaman, T. Stöferle, F. A. Nüesch, R. F. Mahrt, J. Heier, *Advanced Functional Materials* **2018**, 1806997.
- [9] T. E. Kaiser, H. Wang, V. Stepanenko, F. Würthner, *Angewandte Chemie* **2007**, 119, 5637–5640.
- [10] G. Y. Guralchuk, I. K. Katrunov, R. S. Gryniov, A. V. Sorokin, S. L. Yefimova, I. A. Borovoy, Y. V. Malyukin, *The Journal of Physical Chemistry C* **2008**, 112, 14762–14768.
- [11] R. Humphry-Baker, M. Graetzel, R. Steiger, *Journal of the American Chemical Society* **1980**, 102, 847–848.
- [12] J. C. de Mello, H. F. Wittmann, R. H. Friend, *Advanced Materials* **1997**, 9, 230–232.
- [13] O. P. Dimitriev, Y. P. Piryatinski, Y. L. Slominskii, *The Journal of Physical Chemistry Letters* **2018**, 9, 2138–2143.
- [14] T.-S. Ahn, R. O. Al-Kaysi, A. M. Müller, K. M. Wentz, C. J. Bardeen, *Review of Scientific Instruments* **2007**, 78, 086105.
- [15] M. S. Bradley, J. R. Tischler, V. Bulović, *Advanced Materials* **2005**, 17, 1881–1886.

## Bibliography

---

- [16] I. A. Struganova, H. Lim, S. A. Morgan, *The Journal of Physical Chemistry B* **2002**, *106*, 11047–11050.
- [17] M. Lindrum, A. Glismann, J. Moll, S. Daehne, *Chemical Physics* **1993**, *178*, 423–432.
- [18] J. Moll, S. Daehne, J. R. Durrant, D. A. Wiersma, *The Journal of chemical physics* **1995**, *102*, 6362–6370.
- [19] S. Kirstein, S. Daehne, *International Journal of Photoenergy* **2006**, *2006*.
- [20] A. A. Muentert, D. V. Brumbaugh, J. Apolito, L. A. Horn, F. C. Spano, S. Mukamel, *The Journal of Physical Chemistry* **1992**, *96*, 2783–2790.
- [21] I. Dursun, Y. Zheng, T. Guo, M. De Bastiani, B. Turedi, L. Sinatra, M. A. Haque, B. Sun, A. A. Zhumekenov, M. I. Saidaminov, et al., *ACS Energy Letters* **2018**.
- [22] L. M. Pazos-Outón, M. Szumilo, R. Lamboll, J. M. Richter, M. Crespo-Quesada, M. Abdi-Jalebi, H. J. Beeson, M. Vrućinić, M. Alsari, H. J. Snaith, et al., *Science* **2016**, *351*, 1430–1433.
- [23] H. v. Berlepsch, C. Böttcher, *Physical Chemistry Chemical Physics* **2018**, *20*, 18969–18977.
- [24] H. Von Berlepsch, C. Böttcher, A. Ouart, M. Regenbrecht, S. Akari, U. Keiderling, H. Schnablegger, S. Dähne, S. Kirstein, *Langmuir* **2000**, *16*, 5908–5916.
- [25] J. Glinski, G. Chavepeyer, J. Platten, C. De Saedeleer, *Journal of colloid and interface science* **1994**, *162*, 129–134.
- [26] Y. V. Malyukin, A. Sorokin, S. Yefimova, A. Lebedenko, *Journal of luminescence* **2005**, *112*, 429–433.
- [27] N. Micali, V. Villari, L. M. Scolaro, A. Romeo, M. A. Castriciano, *Physical Review E* **2005**, *72*, 050401.
- [28] G. Bushell, Y. Yan, D. Woodfield, J. Raper, R. Amal, *Advances in Colloid and Interface Science* **2002**, *95*, 1–50.
- [29] M. A. Castriciano, A. Romeo, V. Villari, N. Micali, L. M. Scolaro, *The Journal of Physical Chemistry B* **2004**, *108*, 9054–9059.



### 3.5 Supporting Information

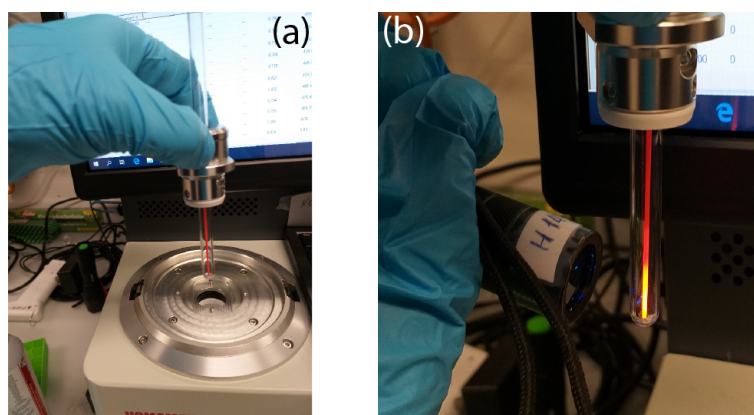


Figure S3.1 – Absolute photoluminescence quantum yield measurement set-up using integrating sphere with J-aggregate solution taken in 1mm glass capillaries (a) and exposed to UV light (b).

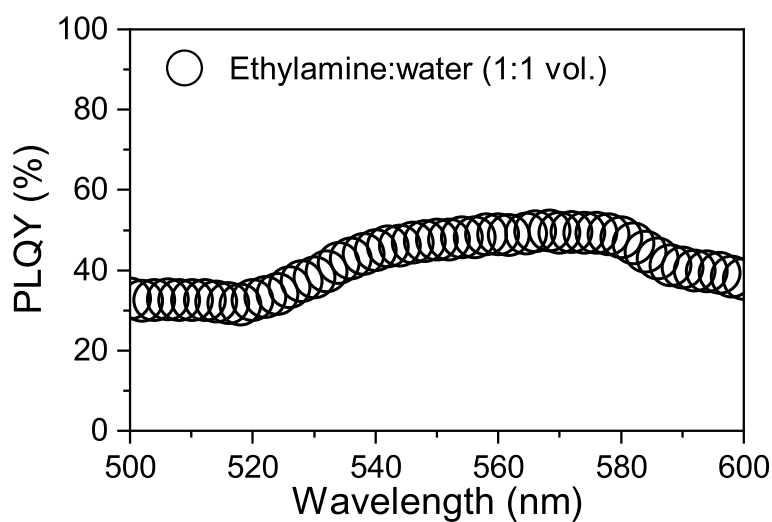


Figure S3.2 – Wavelength dependent PLQY measurement for J-aggregates in ethylamine:water in 1:1 volume ratio.

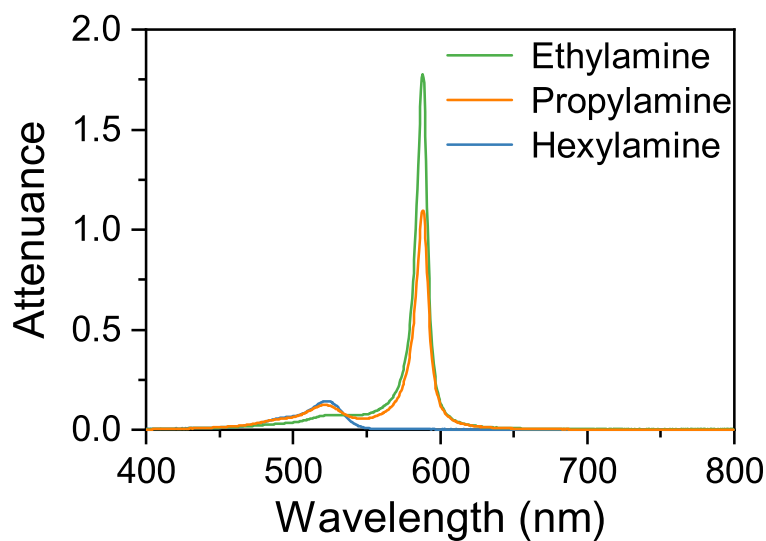


Figure S3.3 – Increasing the chain length of the alkylamine from ethyl- to hexyl- resulted in disintegration of J-aggregates to monomers.

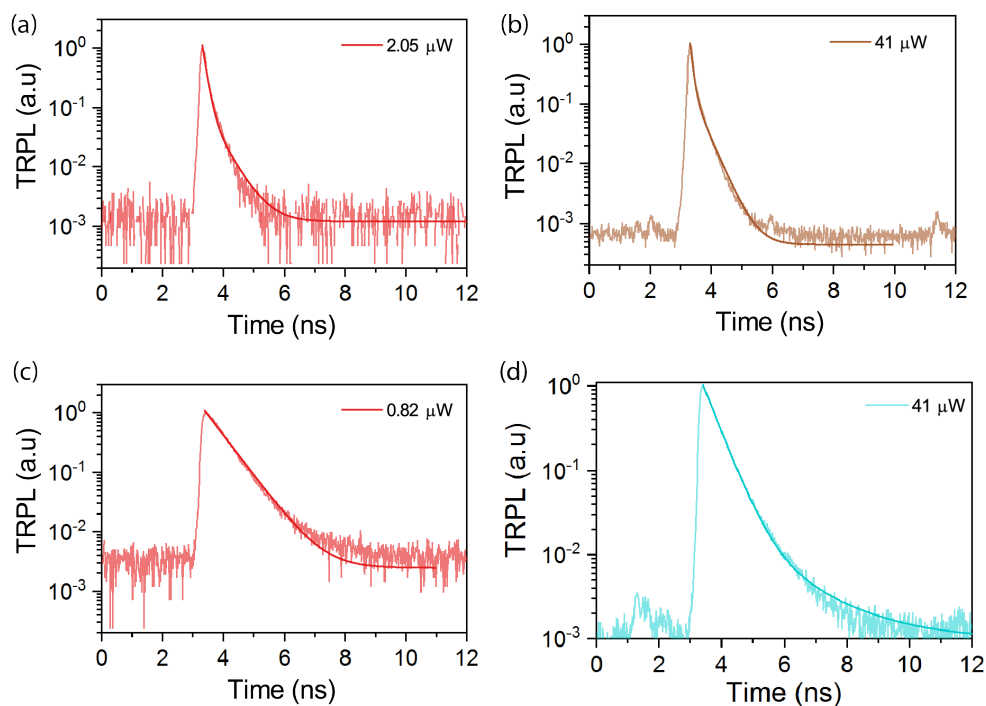


Figure S3.4 – Time-resolved spectrally integrated dynamics for J-aggregates in water (a,b) and ethylamine:water (c,d) with excitation power mentioned in the plots. The solid lines correspond to the fitted lines.

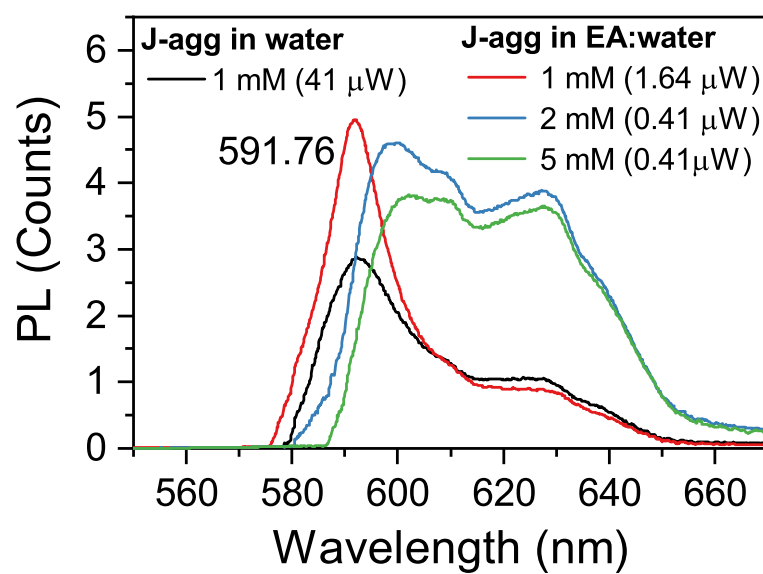


Figure S3.5 – PL recorded for J-aggregates in water and ethylamine:water (EA:water) at different dye concentration.

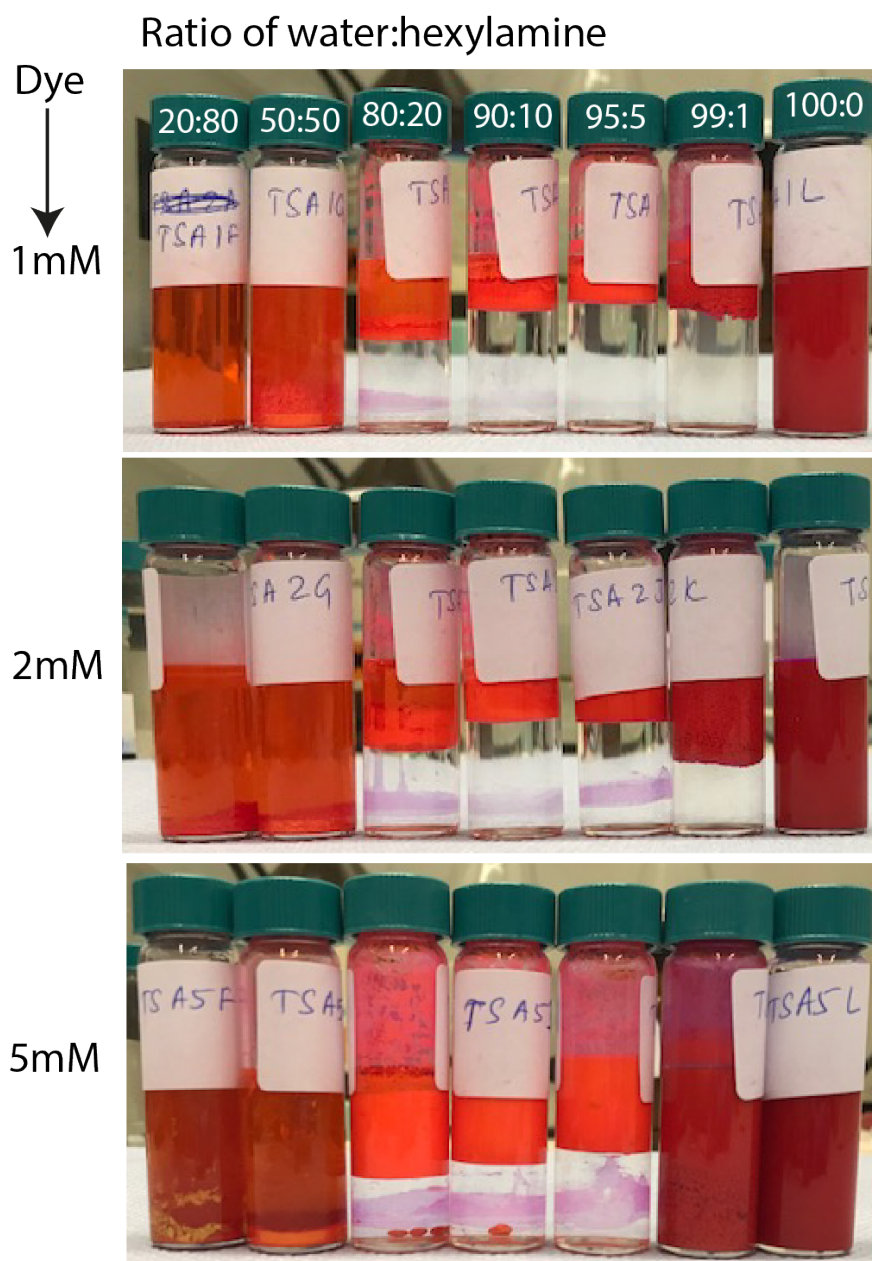


Figure S3.6 – Photograph of the dyes dissolved in water at different concentration (1 mM, 2 mM and 5 mM) followed by addition of hexylamine in different ratio as mentioned on the top of the vials. The final dye concentration in the solution is mentioned on the left column.

## 4 Filter-free Ultra-narrowband Organic Photodetectors with Inkjet Printing Compatibility

Surendra B. Anantharaman<sup>1,2</sup>, Karen Strassel<sup>1,3</sup>, Matthias Diethelm<sup>1,2</sup>, Agnes Gubicza<sup>4</sup>, Erwin Hack<sup>4</sup>, Roland Hany<sup>1</sup>, Frank A. Nüesch<sup>1,2</sup>, and Jakob Heier<sup>1</sup>

<sup>1</sup>Laboratory for Functional Polymers, Swiss Federal Laboratories of Materials Science and Technology, Empa, Überlandstrasse 129, CH-8600 Dübendorf, Switzerland.

<sup>2</sup>Institut des Matériaux, Ecole Polytechnique Fédérale de Lausanne, EPFL, Station 12, CH-1015 Lausanne, Switzerland.

<sup>3</sup>Institute of Chemical Sciences and Engineering, École Polytechnique Fédérale de Lausanne, EPFL, CH-1015 Lausanne, Switzerland.

<sup>4</sup>Transport at Nanoscale Interfaces, Swiss Federal Laboratories for Materials Science and Technology, Empa, Überlandstrasse 129, CH-8600 Dübendorf, Switzerland.

**Keywords:** Ultra-narrowband photodetectors, color selective, organic dyes, J-aggregates, inkjet printing

*The contents of this chapter has been submitted to a peer-reviewed journal publication*

**Author Contributions:** S.B.A conceived the idea, fabricated the devices, characterized and analyzed them. K.S fabricated the J980 devices and carried out the J-V and EQE measurements. A.G conducted the current noise measurement and M.D performed response time measurement for all the devices fabricated by S.B.A. S.B.A inkjet printed the devices and characterized them. E.H performed ellipsometry measurements for all the samples and fitted the data. R.H., F.A.N and J.H supervised the project and provided valuable inputs. S.B.A and F.A.N wrote the manuscript with inputs from all co-authors.

### Abstract

Narrowband photodetectors are useful for myriad applications involving color discrimination. For this purpose, prevalent devices use broadband photodetectors in combination with electric (charge collection narrowing, photo multiplication) and optical strategies (optical cavity) to achieve a narrowband photodetector response with concomitant drawbacks in the figures-of-merits. Organic materials with true narrowband absorption for photodetectors are not well explored. Here we exploit strong coupling in cyanine dyes to form J-aggregates with a narrow absorption band (FWHM~13-50 nm) and high extinction coefficients. Thin film narrowband photodetectors are fabricated for three different dyes with absorption maxima ranging from the visible to the near-infrared. External quantum efficiency (EQE), responsivity, noise equivalent power, specific detectivity and response speed are determined. The advantage of using narrowband absorption materials is reflected in competitive values for the figures of merit. Furthermore, ultra-narrow bandwidth ( $< 50$  nm) photodetectors fabricated by inkjet printing the active organic (J-aggregate) and inorganic layers showed higher frequency response ( $f_{-3dB}$ ) compared to spin-coated devices, thus underlining their industrial relevance.

### 4.1 Introduction

The largest class of photodetectors is based on inorganic semiconductors such as GaSb, silicon, InGaAs or germanium. Conventional photodiodes consist of a p-i-n device architecture and show broadband absorption from the ultra-violet to the near-infrared (NIR) region. Typical figures of merit of such devices are external quantum efficiency (EQE), responsivity and response time. For a GaSb/GaInSb laboratory device these values can be as high as  $10^4\%$ ,  $10^3$  A/W and 2 ms, respectively, when operated as a near-infrared photodetector at the optical communication wavelength ( $1.55 \mu\text{m}$ ).<sup>[1]</sup> Commercially, inorganic photodetectors such as HgCdTe are available.<sup>[2]</sup> While the latter devices benefit from mature manufacturing processes developed in microelectronic industry, the ever increasing demand in consumer electronics, mobile devices, automobile, machine vision and security asks for novel device concepts, materials and fabrication processes. Of great interest are color sensing devices with narrowband sensitivity. In such photodetectors, the spectral width of the responsivity has a full-width at half-maximum (FWHM) of less than 100 nm.<sup>[3,4]</sup> This spectral selectivity leads to better imaging resolution and avoids interference from light with wavelengths not of interest. For

instance, in biological applications, it is important to have photodetectors with maximum selectivity in the NIR region (~800 nm) while being transparent in the visible. Such a feature will be helpful to image blood vessels without interference from ambient light. Besides their significance in biological applications, narrow-band photodetectors can find promising applications in optical communications, color imaging and security surveillance.

The industrially established path for narrowband responsivity uses broad band detectors with band-pass filters. The benefit of this rather expensive approach is a minimum response width that can be as small as 40 nm (FWHM) in a wide spectral range. Other strategies not involving external filters have also been devised. They are based on charge collection narrowing (CCN),<sup>[5]</sup> micro-cavities for harvesting charge-transfer (CT) states<sup>[6]</sup> and plasmon states<sup>[7]</sup> to limit the broadband detectors' response to a narrow range. Narrowband absorption materials with wavelength tunability such as colloidal quantum dots (CQD like PbS, CdSe(S), lead-halide perovskites) have been reported.<sup>[5,8]</sup> Beyond the wavelength of interest, such quantum dots have a broad S<sub>2</sub>-excitonic peak which is optically active for photo detection.<sup>[9]</sup> Using either CQD blends of different sizes or micro-meter thick films and integrating the CCN technique, the spectral response was controlled to a narrowband.<sup>[5,10,11]</sup> Paradoxically, mixing different sizes of these CQD blends have a narrowband photoresponse, while they are not transparent to wavelength not of interest due to the absorption of the device stacks (internal filtering). Moreover, it should be noted that the CCN technique significantly increases the response time and operating voltage and decreases the external quantum efficiency of the detector. For instance, Fang et al.<sup>[5]</sup> have shown ultrahigh narrowband single crystal perovskite films with FWHM < 20 nm. However, the EQE in these devices is less than 3% when biased at -4 V. Eventually, organic semiconductor materials are extremely interesting for narrowband photodetector devices due to the intrinsic narrowness of discrete optical  $\pi$ - $\pi^*$  transitions of its molecular constituents. Furthermore, due to the low charge carrier mobility in these devices, such devices are predestined for charge collection narrowing, where collection efficiency depends on the penetration depth of light into the semiconductor film.<sup>[12,13]</sup> Nevertheless, organic photodetectors (OPD) with a narrow spectral response (FWHM < 100 nm) performing with high EQE and at low voltage have yet to be realized.

Organic salts like cyanine dyes have recently been used for solar cell and photodetector applications in a wide spectral domain ranging from the ultra-violet to the near-infrared.<sup>[14–17]</sup> The synthesis of cyanine dyes has benefited from many decades of research and development in the field of photography, data storage and biolabeling.<sup>[18–20]</sup> While these dyes show a unique narrow absorption band in solution, their solid state thin film absorption shows a broadened spectrum as a result of intermolecular interactions.<sup>[21]</sup> Due to the very strong transition dipole moment of cyanine dyes, exciton coupling is particularly strong and for specific packing geometries, exciton bands due to H- or J-aggregates may dominate the absorption spectrum. The formation of H-aggregates is usually not desired, since they give rise to low lying dark excitonic states with non-radiative decay. On the other hand, J-aggregates give rise to emissive excitonic states. In tightly packed assemblies, coupling of transition dipole moments leads to extremely narrowband absorption (FWHM < 20 nm) along with coherent exciton diffusion.

Such features are highly desirable for narrowband photodetectors and this motivates the investigation of J-aggregates as the active layer in photodetectors. Osedach et al.<sup>[22]</sup> have shown that J-aggregates of cyanine dyes can be used in a near-infra red (NIR) photodetector with peak sensitivity at 756 nm. The device architecture included an optical spacer and a thick (200 nm) Ag electrode to enhance reflectivity. An EQE of around 15% at 0 V bias was achieved, however, due to interference effects from the cavity, the EQE spectrum was much broader and blue-shifted with respect to the J-aggregate peak absorption of the thin film. Furthermore, the exciton diffusion length in this device was estimated to be around  $2.0 \pm 0.4$  nm, which makes exciton recombination a limit for further enhancement of the external quantum efficiency in this device.

Organic semiconductors in general benefit from low-cost solution processability, which is an attractive feature for integration of such photodetectors in read-out integrated circuitry. This is particularly relevant when the photodetector device architecture can be printed with high spatial resolution.<sup>[23]</sup> Advantageously, aqueous J-aggregate inks can be produced which are suitable for inkjet printing. Patterned thin J-aggregate films using inkjet printing and their photo-voltaic properties were reported.<sup>[24,25]</sup> Although these reports show that the concept of using J-aggregates as active layer in devices has been realized before, the spectral characteristics of the J-aggregate had not been exploited efficiently for a narrowband photodetector.

In this work, we have explored the use of narrowband cyanine J-aggregates for photodetection at three different wavelengths from the visible to the NIR region. The variation of the polymethine chain length allows to span a considerable spectral region. A trimethine dye, pentamethine dye as well as a heptamethine dye are used for the formulation of J-aggregate inks to produce ultrathin films. The benefit of a robust device architecture with oxide layers for selective charge transport and its effect on external quantum efficiency is discussed. Eventually we show that the active materials used for the fabrication are fully compatible with inkjet printing and demonstrate a printed J580 ultra-narrowband (FWHM of the absorption band  $\sim 13$  nm) photodetector with higher EQE than the spin-coated (control) device.

## 4.2 Results and Discussion

### 4.2.1 Solvent engineering approach for J-aggregate thin films

From the class of cyanine dyes, we explore a trimethine (**J580**), a pentamethine (**J780**) and a heptamethine dye (**J980**) (Figure 4.1a –c) to investigate the formation of J-aggregates with the most narrow absorption band in thin films (Figure 4.1d). In aqueous solution, all three dyes form J-aggregates with peak positions at 586 nm (**J580**), 780 nm (**J780**) and 980 nm (**J980**), respectively. The absorption peaks are redshifted and significantly narrowed when compared to monomer absorption (Figure S4.1, Supporting Information). Methanol is a good solvent for all dyes and the dyes will remain in monomer form. Depending on the dye structure and its counter-ion, the J-aggregate formation in the solution can be influenced by the solvent. For



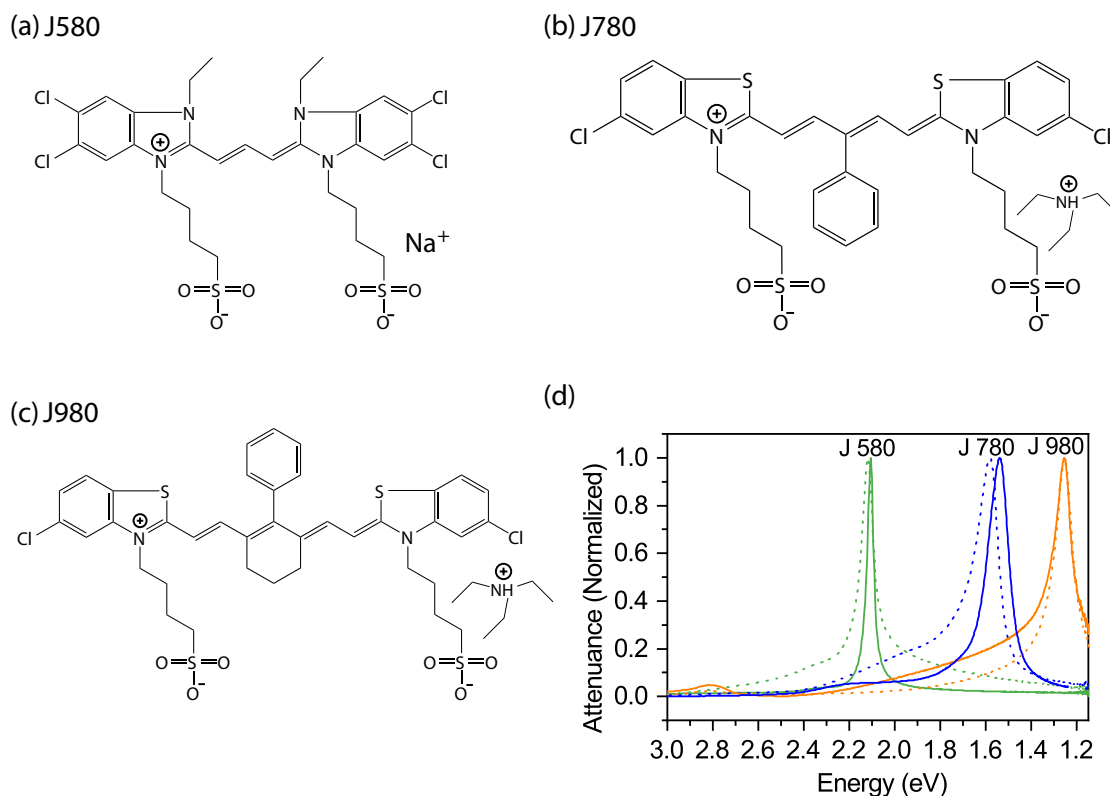


Figure 4.1 – Chemical structure of the (a) **J580**, (b) **J780** and (c) **J980** dye. (d) Comparison of attenuation peaks of aggregate thin films when suspended aggregates are directly deposited from solution (solid line) or obtained in-situ during spin coating from a monomer solution (dotted line).

instance, the **J580** dye is well-known to form J-aggregates in water.<sup>[13,26]</sup> On the other hand, the **J780** dye forms H-aggregates (J-aggregates) in water (acetate buffer) at low dye concentration (data not shown here). This confirms that the J-aggregate formation for the **J780** dye is highly favorable when the dye is dissolved in the acetate buffer medium. A similar observation was reported for the **J780** dye to form J-aggregates in water with narrow peak-width upon addition of sodium chloride.<sup>[27]</sup> Therefore, we have chosen water as solvent for J580 and acetate buffer for **J780** and **J980**.

One recurring challenge in fabricating organic thin film devices is to produce high quality thin films with low roughness and a minimum number of defects like grain boundaries or crystal interfaces. In solution, solvation and electrostatic forces are employed to control aggregation. When transferred to a substrate, the typical optical properties such as high oscillator strength and narrow absorption can be maintained. Commonly, when an aggregate containing solution is coated onto the substrate (direct method), the resulting film quality is poor with large domains and numerous pinholes (Figure 4.2a).<sup>[22]</sup> Other approaches include nucleation of aggregates of critical size on the substrate and then adsorption of the dye from a monomer solution, layer-by-layer deposition or Langmuir Blodgett techniques, which are all

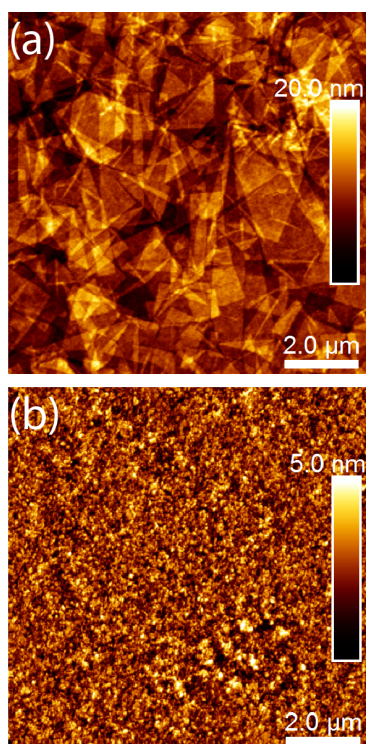


Figure 4.2 – Difference in film morphology of **J780** dye aggregates fabricated by the direct method (a) or in-situ method (b) from TFE solution on ITO/ TiO<sub>2</sub> substrates.

time consuming.<sup>[13,26,28]</sup> Alternatively, here we have explored a solvent (2,2,2, tri-fluoroethanol, TFE) with low boiling point and a larger dipole moment than water. The high solubility of the dye in TFE prevents aggregation, however, during spin-coating the dye concentration increases rapidly upon fast solvent evaporation thereby facilitating J-aggregate formation. This process (hereafter called in-situ method) rapidly forms J-aggregates in the thin films (Figure S4.2, Supporting Information). Furthermore, the uniformity of the film improves significantly in terms of reducing the crystallite sizes and porosity between the stacked sheets as shown in Figure 4.2b by AFM studies. The influence of this solvent engineering approach on device performance will be explained later. Concerning the properties of J-aggregates themselves - a large redshift, small FWHM and no shoulders in the absorption spectra are indicators for a film containing a monodisperse distribution of high quality aggregates. Attenuance spectra of the dye aggregates manufactured with the two different (direct and in-situ) methods are shown in Figure 4.1d. For the **J580** dye, the aggregate film deposited by the in-situ route has a smaller redshift, a much broader FWHM and a pronounced shoulder compared to the J-aggregates deposited directly from the solution. Convergence can be observed for the **J780** dye. While the aggregate film deposited directly from solution still has a larger red-shift, the FWHM is the same and only a small high energy shoulder exists in the in-situ film. Only for the **J980** dye the in-situ formed aggregates have superior optical properties over the directly formed aggregates. These observations suggest that the triethylammonium counterion as well as the additional cyclohexenyl group in the chromophore structure is beneficial for in-situ dye aggregation in

the film. The absorption coefficient ( $k$ ) of the thin films measured by ellipsometry is shown in Figure S4.3, Supporting Information. The FWHM of the J-aggregate absorption is narrow and similar to the attenuance spectra.

To summarize the results, the uniformity of films containing J-aggregates formed in-situ upon spin-coating from TFE is superior to films where J-aggregates are deposited directly from solution. On the other hand, the optical properties show a different trend for each dye: a narrower FWHM is observed for **J580** when deposited by the direct method, while **J780** shows a convergence between both methods and for **J980** the in-situ method is the best.

#### 4.2.2 Narrowband photodetectors

Devices with all three dyes were fabricated following an extremely simple device structure. The photoactive J-aggregate film is sandwiched between a  $\text{TiO}_2$  electron- and a  $\text{MoO}_3$  hole extraction layer. The entire detector is built on top of a glass-ITO electrode and completed with an Ag-electrode (Figure 4.3a and top-view for the electrode arrangement is shown in Figure S4.4a, Supporting Information). J-aggregate layers were fabricated by the in-situ and direct method. **J580** films were only manufactured by the direct method. To minimize the effect of shunts due to pin-holes in the J-aggregate layer we also report device results where an additional electron blocking layer (TAPC) is introduced between J-aggregate film and  $\text{MoO}_3$ . The energy diagram of the devices is shown in Figure 4.3b.

The data for the **J580** were taken from this reference work.<sup>[29]</sup> The J-V curves for all devices are shown in Figures 4.3c – f, Figures S4.4b – d and Figure S4.5. The dye **J580** showed high rectification and considerably low dark currents, but breakdown at -1 V. Adding TAPC as blocking layer deteriorated the diode character of the device. Dark current and photocurrent decreased drastically and there was only a small difference between the two of them (Figure 4.3d). The reason is low hole extraction efficiency due to energy (HOMO) misalignment of the TAPC layer compared to  $\text{MoO}_3$ .<sup>[30]</sup> Nevertheless, the  $J_{\text{light}}/J_{\text{dark}}$  ratio is higher than for **J580** without blocking layer and also it allowed to drive the photodetector at higher reverse bias (-2 V, in this case) without breakdown. The **J780** devices spin-coated from TFE solution showed a good rectification behavior with reduced number of shunts, in comparison to the J-aggregates spin-coated from acetate buffer solution (Figure 4.3e compared to Figure S4.4b, Supporting Information). For comparison, six out of eight cells perform similarly when spin-coated from TFE, while two cells (A1 and A8) which are close to the anode suffer little resistance from ITO (Figure S4.4c and d, Supporting Information). The **J980** devices showed improved rectification, with high  $J_{\text{sc}}$  and  $J_{\text{light}}/J_{\text{dark}}$  ratio for devices fabricated with the in-situ method (see Figure S4.5, Supporting Information). The integrated current density values from the EQE spectra (discussed later) measured at different bias voltage are shown in the J-V curves. Collectively, the results suggest that in devices where J-aggregates are spin-coated directly from solution an additional blocking layer is required (**J580**) to suppress the dark current. On the other hand, promoting in-situ J-aggregate formation on the substrates during spin-coating can overcome

the trap states like grain boundaries to enhance the short-circuit current.

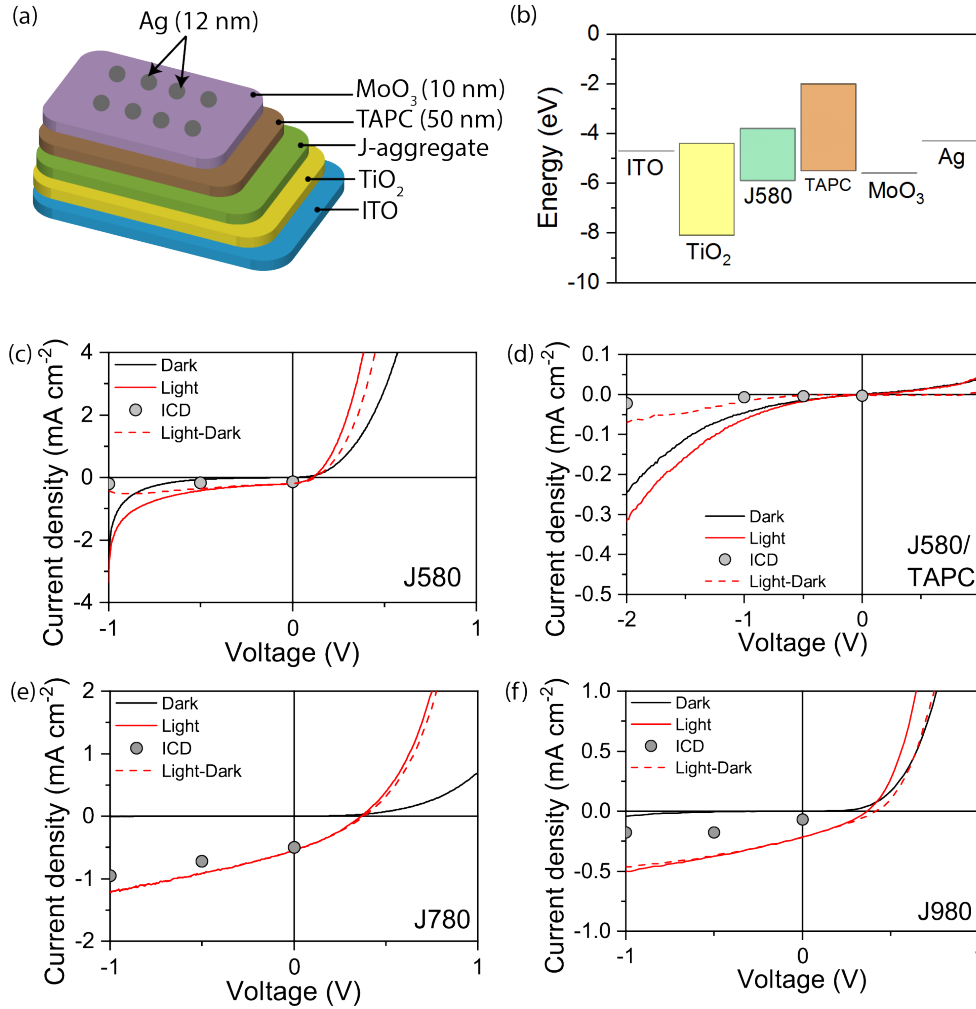


Figure 4.3 – (a) Device structure of narrowband photodetectors with J-aggregates as active layer investigated in this study. The device active area is  $3.1 \text{ mm}^2$ . (b) Energy level diagram of the device for **J580** (optical gap) with TAPC layer. Current density – voltage characteristics for the **J580** (c) **J580** with TAPC layer (d), **J780** (e) and **J980** (f) devices. The device structure is ITO/ $\text{TiO}_2$ /J-aggregate layer (**J580**, or **J580**+TAPC (50 nm) or **J780** or **J980**)/ $\text{MoO}_3$  (10 nm)/Ag (12 nm). The integrated current density (ICD) values calculated from the external quantum efficiency (shown later) are marked with filled circles over the J-V curves.

The external quantum efficiency (EQE) for the devices was measured under monochromatic light chopped at 85 Hz and at different bias voltages. The responsivity calculated from the EQE is shown on the right axis (Figure 4.4a – d). The EQE closely follows the absorption spectra for all the devices with similar FWHM values. It can be noted that the presence of the electron blocking layer (TAPC) in devices incorporating the **J580** dye leads to an increase in EQE from 8% (-0.5 V) to 16% (-2 V) with suppressed dark current. This is due to better hole extraction in the presence of a strong electric field at high reverse bias. We exclude the possibility of

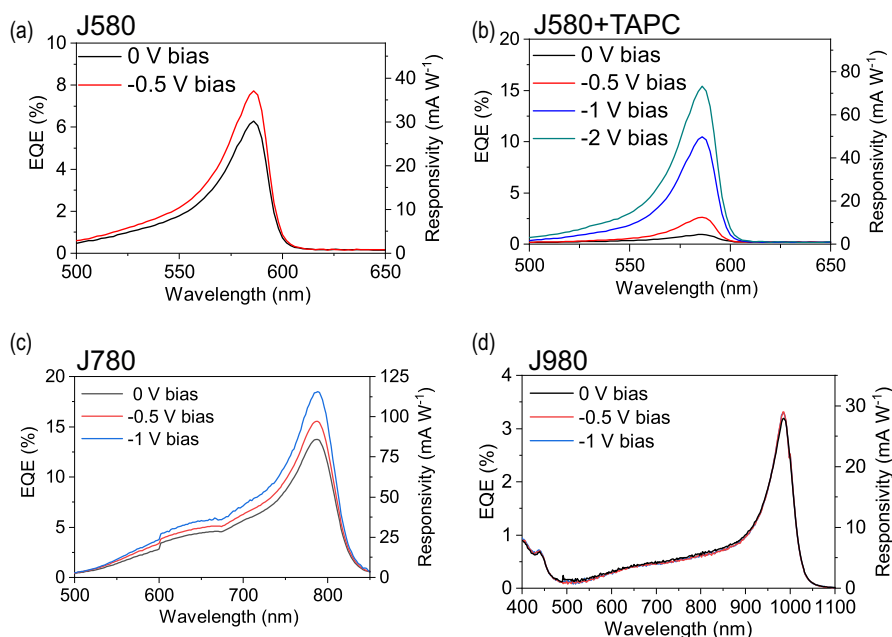


Figure 4.4 – External quantum efficiency (EQE) and responsivity (shown in open circles) of photodetectors showing wavelength-selectivity at 586 nm (a - without TAPC, b - with TAPC), 780 nm (c) and 980 nm (d) for **J580**, **J780** and **J980** respectively, measured at an interval of 2 nm at different bias voltage.

any gain mechanism as reported elsewhere, as our EQE did not exceed 100% at higher bias voltage.<sup>[31]</sup> Furthermore, **J780** photodetectors shows high EQE (15%) at -1 V reverse bias at 780 nm (Figure 4.4c). The peak maximum and FWHM of the EQE matches the absorption profile of **J780** (see Figure S4.6, Supporting Information), which is very different from the report by Osedach et al.<sup>[22]</sup> The difference comes from the thick top electrode (200 nm Ag) used in the latter work, which acts as optical cavity thereby introducing an interference effect. **J980** based photodetectors extend the peak wavelength to 980 nm showing a nominal EQE of 3.5% at -1V (Figure 4.4d). An increased non-radiative relaxation channel of the exciton in the low bandgap (**J980**) competes with charge generation, which explains the nominal EQE.<sup>[32]</sup> The **J980** photodetector shows a small EQE response at 450 nm from the S2 state.<sup>[33,34]</sup> The EQE from the S2 state is much lower than the S1 state unlike the strong response from the S2 state in quantum dot photodetectors.<sup>[35]</sup> The difference in the integrated current density values from the EQE and measured under AM1.5 solar irradiation intensity can arise from the narrowness of the J-aggregate absorption with respect to the spectral correction of the solar simulator to account for sharp emission peaks in the Xenon lamp (Figure 4.3f). Another reason could be the higher light intensity of the AM 1.5 solar irradiation which can induce photoconductivity.

### 4.2.3 Current noise

As suggested by Kim et al.<sup>[36]</sup>, the specific detectivity and noise equivalent power (NEP) was calculated from the current noise values. The noise power spectral densities ( $S_n$ ) for all four devices are shown in Figure 4.5(a-d). All spectra show a broadband bias independent increase in noise power spectral density at higher frequencies. This increase can be attributed to the fact that the impedance of the samples decreases in this frequency domain giving rise to an increasing thermal current noise which is further amplified by the high-frequency voltage noise of the current amplifier. The low frequency thermal noise also varies with frequency, but is expected to be less than  $1 \text{ pA}/\sqrt{\text{Hz}}$  and in this regime the noise is dominated by the  $1/f$  noise. Calculating from the DC current values, the expected range of the shot noise is at least one order of magnitude smaller than the observed noise levels in all cases.

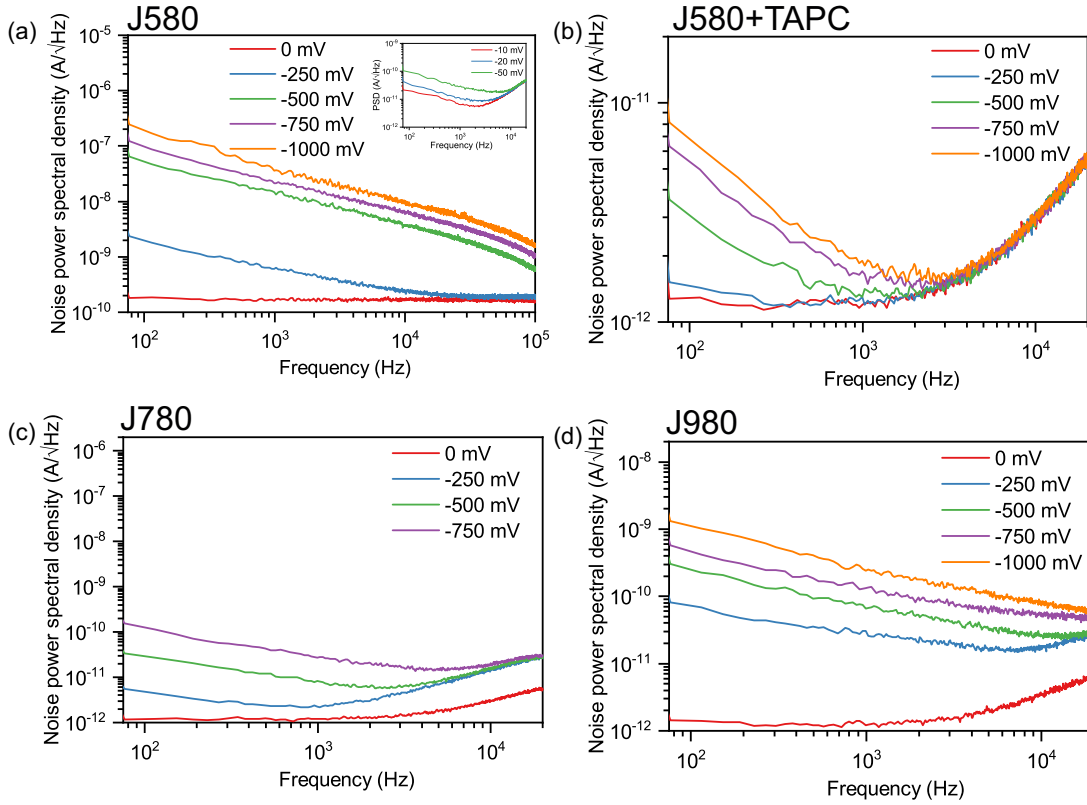


Figure 4.5 – Noise power spectral density recorded as a function of frequency for **J580** (a), **J580** with TAPC (b), **J780** (c) and **J980** (d) devices. The spectra were obtained at the indicated DC bias levels.

The role of TAPC in suppressing the dark current and allowing the device to be driven at higher bias voltage can be further verified from the current noise measurement. For instance, comparing the noise power spectral density at 100 Hz for **J580** and **J580** with TAPC layer at -1 V (0 V) shows a 4-order (2-order) difference in the  $1/f$  current noise (Figure 4.5a and b). It can be noticed that the  $1/f$  noise in the **J780** and **J980** devices is lower compared to the **J580** device.

This can be due to homogeneous J-aggregate film formation (to minimize contacts between  $\text{TiO}_2$  and  $\text{MoO}_3$ ) for **J780** and **J980** devices benefitting from the solvent engineering approach. The noise values at the -3dB values (as discussed below) have been taken to calculate the NEP and specific detectivity as summarized in Table 4.1.

#### 4.2.4 Response time and -3dB values

The response time of the detector was calculated from the rise time of the detector to reach from 10% to 90% of the maximum photocurrent. A frequency modulated square wave light pulse was used to determine the -3dB values. An example of such a measurement for the **J780** device measured at different bias voltage is shown in Figure 4.6a. A similar trend in rise and decay current with bias voltage was observed for **J580** and **J980**. Generally, light can influence the resistance and capacitance of the device even when measured at 0 V bias. With increasing light intensity, more excitons are created which leads to more charge generation. To evaluate this effect, we chose the **J580** device to measure the impedance at different light intensities (see Figure S4.7, Supporting Information). The increase in free charge carriers can decrease the resistance of the device, with a small increase in capacitance at low frequencies. A combined effect of resistance and capacitance influences the response time of the detector ( $\tau_r = RC$ ). In our case, we concluded that the resistance of the device is the dominant factor determining response time, which can be strongly influenced by light intensity, considering the high photoconductive nature reported in the cyanine devices when driven at high reverse bias.<sup>[37]</sup> For the -3dB measurement, the light intensity in our system was set to the level where the same  $J_{sc}$  values were obtained as measured with the AM1.5 solar simulator and the bias voltage was varied from 0 V to -1 V.

To investigate the effects of light and bias voltage on the device, the device was pre-conditioned for 120 s at -1 V and a light intensity leading to 70% of the integrated current density at 1 sun, followed by -3dB measurement at different bias voltage. The data plots for -3dB values for the devices measured with and without preconditioning are shown in the Supporting Information (Figure S4.8) and summarized in Figure 4.6b. The -3dB frequency becomes slightly higher with increase in bias voltage due to faster charge extraction, irrespective of the bias condition. It can be noted that the **J980** device shows the fastest response time compared to other photodetectors. With preconditioning the devices, there is a slight improvement in the response time as clearly evident in the **J780** devices. Nevertheless, the devices showed an upturn in the current attenuation in the low frequency regime at higher bias voltage. This can be due to counterion migration in the active layer which can form a space-charge layer thereby influencing the response time of the detector.<sup>[38]</sup> The -3dB values without pre-conditioning are summarized in Table 4.1 to calculate NEP and  $D^*$ .

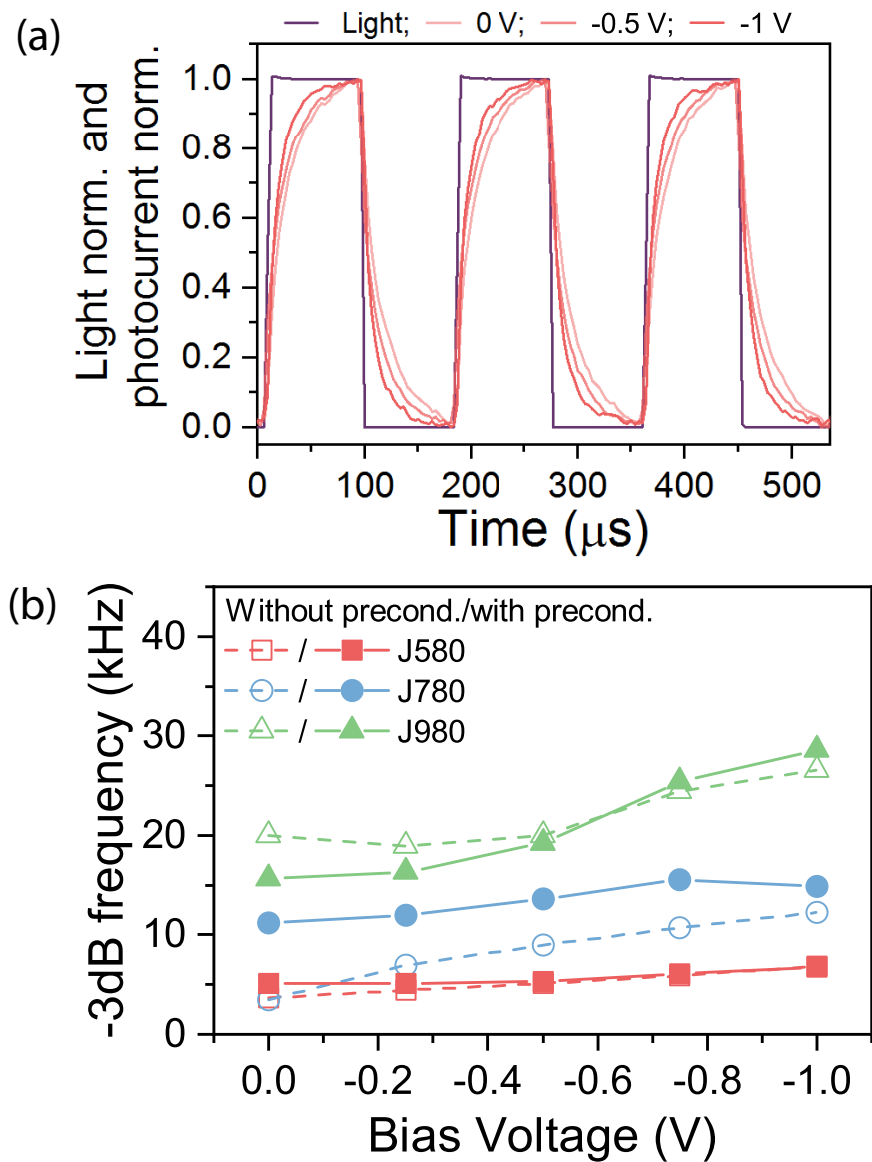


Figure 4.6 – Temporal response of the **J780** device illuminated with 10 kHz light pulse and measured at different bias voltage (a). Summary of -3dB values for all devices measured without and with preconditioning (b).



Table 4.1 – Summary of figures of merit for solution processed narrowband photodetectors with EQE &lt; 100 nm.

Device (film thickness)	Strategy	Response peak (nm)	FWHM of the EQE (nm)	Bias (V)	-3dB values (kHz)	EQE (%)	R (mA/W)	$S_n$ (A/ $\sqrt{Hz}$ ) @ 3dB value	NEP (W/ $\sqrt{Hz}$ )	D* (Jones or cm $\sqrt{A}/\sqrt{HzW}$ )
J580 (<10 nm)	This work - true absorption	586	28	0	3.61	6	29.68	1.64E-10	5.52E-09	3.19E+07
J780 (<10 nm)	This work - true absorption	780	72	-0.5	5.08	7.8	36.51	5.79E-09	1.59E-07	1.11E+06
J980 (<10 nm)	This work - true absorption	980	50	0	3.52	14	87.32	1.58E-12	1.81E-11	9.73E+09
Ketocyanines <sup>[39]</sup>	Optical cavity	525	90	-1	8.96	16.3	98.81	1.49E-11	1.51E-10	1.17E+09
Merocyanine J-aggregate <sup>[40]</sup>	True absorption	747	30	0	20	3.1	25.42	6E-12	2.36E-12	7.46E+08
Cyanine J-aggregate <sup>[40]</sup>	True absorption	750	65	-0.5	20	3.2	28.69	2.92E-11	1.02E-11	1.73E+08
J-aggregate <sup>[22]</sup> (<10 nm)	True absorption with optical cavity	756	125	0	20	17	7197.6	2.45E-13	3.40E-14	1E+11
Helical Nanoribbons <sup>[41]</sup> (1 $\mu$ m)	CCN	575 600 615 645	22 19 16 20	-3	-	-	8 7.3 3.4 1.1	-	-	2.6E+10 1.70E+10 1.10E+10 9.30E+09
P3HT:PCBM <sup>[42]</sup> (~ $\mu$ m)	Photo- multiplication type	650	29	-10	-	49	-	3E-14	1.5E-12	1.35E+11
BODIPY sensitized Zn <sub>0.9</sub> Mn <sub>0.1</sub> O <sup>[43]</sup>	True absorption	530	50	0.1 V/ $\mu$ m	0.001	1.9E+04	8E+06	-	-	1.70E+12

" - " means not mentioned

### 4.2.5 Demonstration of inkjet printed narrowband photodetectors

From the above optimized spin-coated devices, we have chosen one of the J-aggregates (**J580**) owing to their ultra-narrow FWHM of the EQE and environment friendly solvent (water) to demonstrate an inkjet printed device. Our main goal was to inkjet print the active J-aggregate film, to work towards an all-printed device. Nevertheless, we also inkjet printed the titania electron transporting layer. The inkjet printed device was completed by vacuum processing the top layers in the device stack as shown in Figure 4.7a. Generally, a solution available for spincoating needs to be adapted to also yield homogeneous films with inkjet printing. Good jetting is determined by the Webber and Reynolds number of the ink and defined in a stability window.<sup>[44–46]</sup> Droplet formation can be followed by stroboscopy and has been optimized for the inks used here (Figure S4.9). Secondly, the individual droplets need to merge into a uniform layer upon solvent evaporation. Devices manufactured with the compact TiO<sub>2</sub> (c-TiO<sub>2</sub>) layer alone showed a very poor performance. A single printed layer was less than 10 nm thick and the film remained porous even after wet-on-wet printing of several layers. The topography of the printed c-TiO<sub>2</sub> layer was imaged under AFM after annealing at 460 °C for 2 h (Figure S4.10a). To overcome this issue, we introduced a second, mesoporous TiO<sub>2</sub> layer (m-TiO<sub>2</sub>) on top of the non-homogeneously covered c-TiO<sub>2</sub> layer. The m-TiO<sub>2</sub> layer (~100 nm thick) homogeneously covered the c-TiO<sub>2</sub> layer and ITO substrate (Figure S4.10b). Subsequently, the J-aggregates were printed on the m-TiO<sub>2</sub> layer. The J-V curves of the printed devices are shown in Figure 4.7b. Upon addition of the meso-TiO<sub>2</sub> layer, an enhancement in  $J_{sc}$  and  $V_{oc}$  and suppression of dark current was observed. This can be due to complete coverage of meso-TiO<sub>2</sub> on the c-TiO<sub>2</sub> layer, which may have led to reduction in shunts between ITO/J-aggregates and improving the charge extraction between TiO<sub>2</sub>/J-aggregate interface. Moreover, the EQE of the J-aggregates printed on m-TiO<sub>2</sub> shows a 9-fold increase compared to the reference device (c-TiO<sub>2</sub>) at -1 V (Figure 4.7c and d). The introduction of a mesoporous layer is a well-known strategy used in dye sensitized solar cells (DSSC) for enhanced charge extraction from the device.<sup>[45,46]</sup> The broadening of the EQE in the presence of m-TiO<sub>2</sub> can be due to the increased adsorption of J-aggregates on mesoporous TiO<sub>2</sub>, which can itself act as light scatterer. Secondly, the thick top electrode (60 nm) with buffer layers (TAPC and MoO<sub>3</sub>) can introduce cavity effects where interference dominates the light absorption in the J-aggregate layer.<sup>[22]</sup> The response time of the inkjet printed device was measured (Figure 4.7e) and compared with the spin-coated **J580** device (Figure 4.7f). As shown in Section 4.2.3, addition of a TAPC layer significantly decreases the current noise. However, a thick electron blocking (TAPC) layer increases the resistance for hole extraction and is known to reduce the response time of the photodetector.<sup>[30]</sup> Here, we have observed a significant improvement in the response time due to the presence of an increased interface area between the TiO<sub>2</sub>/J-aggregate (upon addition of m-TiO<sub>2</sub> layer) leading to fast electron extraction, which speaks for overcoming the RC limit. To the author's knowledge, this may be the first inkjet printed, true ultra-narrowband photodetector with response speed ( $f_{-3dB}$ ) in the kHz regime operating at low bias voltage (-1 V).

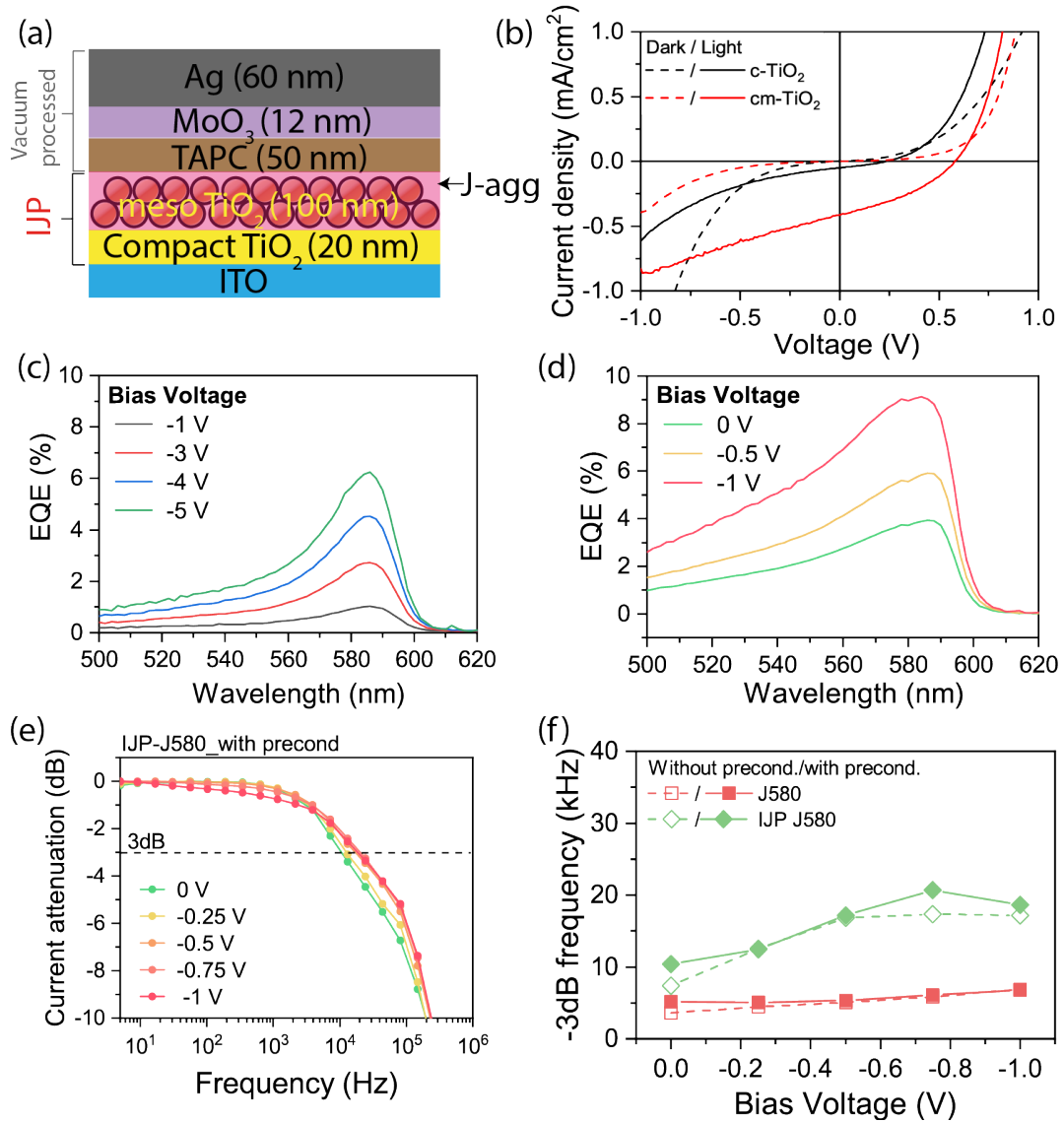


Figure 4.7 – Schematic of inkjet printed device (cross-section) structure showing printed layers (c-TiO<sub>2</sub>, m-TiO<sub>2</sub> and J-aggregate as active layer) followed by vacuum processed layers (a). Current density-voltage curves showing an increase in charge extraction upon addition of m-TiO<sub>2</sub> layer (b). EQE for inkjet printed device structure with J-aggregate as active layer on c-TiO<sub>2</sub> (c) and c-TiO<sub>2</sub>/m-TiO<sub>2</sub> (d). -3dB value recorded for inkjet printed device (IJP J580) with c-TiO<sub>2</sub>/m-TiO<sub>2</sub> at different bias voltage (e) and the values are shown in comparison with spin-coated device (without m-TiO<sub>2</sub> layer) (f).

### 4.3 Conclusion

We could realize narrowband organic photodetectors with optical response below 50 nm while keeping the thin films ~20 nm. We followed a not yet fully explored strategy to exploit the intrinsic narrow absorption width of a J-aggregate with high extinction coefficient. The peak EQE of the photodetector absorbing close to 1000 nm shows the narrow width of EQE (~38 nm) at low bias (-1 V), a fast response speed (20 kHz) and specific detectivity ( $\sim 10^8$  Jones) in good agreement with the current literature values. This strategy allowed for an extremely simple device structure making it a good candidate for large-area solution processing. We have demonstrated an inkjet printed device with better performance than the spin-coated devices from environmentally friendly solvents. We believe these findings will open new avenues to progress in developing narrowband photodetectors.

### 4.4 Experimental Section

**J-aggregate formation:** Three different cyanine dyes were procured from FEW Chemicals, Germany, namely - 5,6-dichloro-2-[[5,6-dichloro-1-ethyl-3-(4-sulfobutyl)-benzimidazol-2-ylidene]-propenyl]-1-ethyl-3-(4-sulfobutyl)-benzimidazolium hydroxide, inner salt, sodium salt (**J580**); 5-chloro-2-[5-[5-chloro-3-(4-sulfobutyl)-3H-benzothiazol-2-ylidene]-3-phenyl-penta-1,3-dienyl]-3-(4-sulfobutyl)-benzothiazol-3-ium hydroxide, inner salt, triethylammonium salt (**J780**); and 5-chloro-2-[2-(3-[2-[5-chloro-3-(4-sulfobutyl)-3H-benzothiazol-2-ylidene]-ethylidene]-2-phenylcyclohex-1-enyl)-vinyl]-3-(4-sulfobutyl)-benzothiazol-3-ium hydroxide, inner salt, triethylammonium salt (**J980**). They were used without further purification. 5 wt% of the **J580** dye was dissolved in water to form J-aggregates in solution. For **J780** and **J980**, the dye was dissolved in 100 mM acetate buffer to form J-aggregates in solution or in 2,2,2-tri-fluoroethanol (TFE) to prepare monomer solution. The solutions were stirred at 300 rpm overnight at room temperature to obtain stable J-aggregates in the solution before deposition.

**Fabrication of narrowband-photodetectors:** Indium Tin Oxide (ITO) substrates (Geomatec, resistivity  $\sim 11 \text{ Ohms}/\square$ ) were cleaned by ultrasonication in acetone, ethanol, Hellmanex, and water for 10 min separately. Titanium iso-proxide (Sigma Aldrich) was spin-coated on cleaned ITO substrates and subsequently annealed at 460 °C for 2 h to obtain a compact  $\text{TiO}_2$  layer as reported elsewhere.<sup>[47]</sup> Annealed  $\text{TiO}_2$  substrates were treated with oxygen plasma with a power setting of 45 W for 5 min. The J-aggregate solution was spin-coated on ITO/ $\text{TiO}_2$  substrates for 30 s at 4000 rpm. The device was completed with 50 nm of 4,4-Cyclohexylidenebis[N,N-bis(4-methylphenyl)benzenamine] (TAPC, Sigma Aldrich) as electron blocking layer and with 12 nm thick Molybdenum (VI) oxide ( $\text{MoO}_3$ , 99.97%, Sigma Aldrich) as hole extraction layer. A 12 nm Ag (Kurt J. Lesker) electrode was deposited through a shadow mask for cell definition with active areas of 3.1 and 7.1  $\text{mm}^2$ .

### Fabrication of inkjet printed photodetectors

**Preparation of inks:** Titanium diisopropoxide bis(acetylacetonate) with 75 wt. % in isopropanol (Sigma Aldrich) was further diluted in isopropanol to a ratio of 1:20 to use them as ink for a compact TiO<sub>2</sub> layer. Ink for a mesoporous TiO<sub>2</sub> layer was prepared from TiO<sub>2</sub> nanoparticle suspension (Ti-Nanoxide, Solaronix) with particle sizes ~15-20 nm dispersed in 18 wt% in terpineol medium and was diluted in terpineol to a 1:10 ratio. J-aggregates were prepared from the **J580** dye (FEW Chemicals, Germany) by dissolving 5 mg of the dye in 1 ml of Millipore water. The solutions were ultrasonicated for 5 min before printing the J-aggregates.

**Inkjet printing:** Indium Tin Oxide (ITO) substrates (resistivity ~11 Ohms/□) purchased from Geomatec were pre-cleaned as described above. Prior to inkjet printing, the substrates were cleaned by an oxygen plasma treatment for 5 min. The compact-TiO<sub>2</sub>, mesoporous-TiO<sub>2</sub> and J-aggregates were printed using the PiXDRO LP50 Inkjet system (Meyer Burger) equipped with a Spectra printhead module (SL-128 AA, 80 picoliter, Fujifilm Dimatix Inc.). Post-printing the compact-TiO<sub>2</sub> and mesoporous-TiO<sub>2</sub> layers, the substrates were annealed at 460 °C for 2 h followed by inkjet printing J-aggregates and drying at room temperature. Subsequently, the inkjet printed half-cells were transferred into a thermal evaporator chamber to complete the device by sequential thermal evaporation of 50 nm of TAPC, 10 nm of MoO<sub>3</sub> layer and 60 nm Ag.

**Characterization:** Attenuance of the film was measured using a Varian Cary 50 UV-vis spectrophotometer. J-V characteristics of the cell were studied by exposing the cells from the ITO side to AM 1.5 solar irradiation from a Spectra-Nova solar simulator. External quantum efficiency (EQE) of the cells was measured by calibrating the system to a Si photodiode. The responsivity (R) is calculated from the EQE ( $R = EQE \times \lambda / 1240$ ). The morphology of the thin films was studied using atomic force microscopy (Bruker Dimension Icon) in tapping mode.

The specific detectivity ( $D^*$ ) of a photodetector is given by the following expression:

$$D^* = \sqrt{A \Delta f R / i_n}$$

with A the area of the detector in cm<sup>2</sup>, R the responsivity in A/W and  $i_n$  the current noise in A integrated over the bandwidth  $\Delta f$ . In order to characterize the current noise of the system, the current was recorded as a function of time using a Stanford SR570 current amplifier while DC biasing the sample via the input of the amplifier. The noise power spectral density was calculated from the obtained data. The current noise values were chosen at the response speed ( $f_{-3dB}$ ) of the photodetector for calculating the noise equivalent power (NEP) and specific detectivity. The response speed of the photodetector was measured using a Paios (Fluxim, AG) system by modulating the frequency of the light pulse and recording the photocurrent at

different bias voltage. For impedance spectroscopy, the device was maintained at zero bias voltage while sweeping the frequency from 10 Hz to 10 MHz. The impedance was recorded with different light intensity to study the RC effect.

**Acknowledgements** The authors gratefully acknowledge funding from the Swiss National Science Foundation under grant numbers: 200021-157135 and 169695. We acknowledge the Scanning Probe Microscopy user laboratory at Empa for providing access to the instrument. S.B.A would like to thank Anand Verma for extending his support with the inkjet printing. We acknowledge the use of the facilities of the Coating Competence Center at Empa.

# Bibliography

- [1] L. Ma, W. Hu, Q. Zhang, P. Ren, X. Zhuang, H. Zhou, J. Xu, H. Li, Z. Shan, X. Wang, et al., *Nano Letters* **2014**, *14*, 694–698.
- [2] Hamamatsu, Classification and use of infrared detectors, Accessed: January 2019.
- [3] A. Liess, A. Lv, A. Arjona-Esteban, D. Bialas, A.-M. Krause, V. Stepanenko, M. Stolte, F. Würthner, *Nano Letters* **2017**, *17*, 1719–1726.
- [4] Hamamatsu, S7505-01 RGB color sensor, Accessed: January 2019, <https://www.hamamatsu.com/eu/en/product/type/S7505-01/index.html>.
- [5] Y. Fang, Q. Dong, Y. Shao, Y. Yuan, J. Huang, *Nature Photonics* **2015**, *9*, 679.
- [6] B. Siegmund, A. Mischok, J. Benduhn, O. Zeika, S. Ullbrich, F. Nehm, M. Böhm, D. Spoltore, H. Fröb, C. Körner, K. Leo, K. Vandewal, *Nature Communications* **2017**, *8*, 15421.
- [7] A. Sobhani, M. W. Knight, Y. Wang, B. Zheng, N. S. King, L. V. Brown, Z. Fang, P. Nordlander, N. J. Halas, *Nature Communications* **2013**, *4*, 1643.
- [8] K.-S. Cho, K. Heo, C.-W. Baik, J. Y. Choi, H. Jeong, S. Hwang, S. Y. Lee, *Nature Communications* **2017**, *8*, 840.
- [9] J. R. Manders, T.-H. Lai, Y. An, W. Xu, J. Lee, D. Y. Kim, G. Bosman, F. So, *Advanced Functional Materials* **2014**, *24*, 7205–7210.
- [10] Q. Lin, A. Armin, P. L. Burn, P. Meredith, *Nature Photonics* **2015**, *9*, 687.
- [11] K. Qiao, H. Deng, X. Yang, D. Dong, M. Li, L. Hu, H. Liu, H. Song, J. Tang, *Nanoscale* **2016**, *8*, 7137–7143.
- [12] J. R. Tischler, M. S. Bradley, V. Bulović, J. H. Song, A. Nurmikko, *Physical Review Letters* **2005**, *95*, 036401.
- [13] M. S. Bradley, J. R. Tischler, V. Bulović, *Advanced Materials* **2005**, *17*, 1881–1886.
- [14] T. Geiger, H. Benmansour, B. Fan, R. Hany, F. Nüesch, *Macromolecular Rapid Communications* **2008**, *29*, 651–658.
- [15] A. C. Véron, H. Zhang, A. Linden, F. Nüesch, J. Heier, R. Hany, T. Geiger, *Organic Letters* **2014**, *16*, 1044–1047.

- [16] H. Zhang, S. Jenatsch, J. De Jonghe, F. Nüesch, R. Steim, A. C. Véron, R. Hany, *Scientific Reports* **2015**, 5, 9439.
- [17] M. Bates, R. R. Lunt, *Sustainable Energy & Fuels* **2017**, 1, 955–968.
- [18] T. Tani in *J-aggregates*, World Scientific, **1996**, pp. 209–228.
- [19] R. S. Eachus, A. P. Marchetti, A. A. Muentner, *Annual review of physical chemistry* **1999**, 50, 117–144.
- [20] M. Shakiba, K. K. Ng, E. Huynh, H. Chan, D. M. Charron, J. Chen, N. Muhanna, F. S. Foster, B. C. Wilson, G. Zheng, *Nanoscale* **2016**, 8, 12618–12625.
- [21] N. A. Leclaire, M. Li, A. C. Véron, A. Neels, J. Heier, J. R. Reimers, F. A. Nüesch, *Physical Chemistry Chemical Physics* **2018**, 20, 29166–29173.
- [22] T. P. Osedach, A. Iacchetti, R. R. Lunt, T. L. Andrew, P. R. Brown, G. M. Akselrod, V. Bulović, *Applied Physics Letters* **2012**, 101, 113303.
- [23] F. P. G. de Arquer, A. Armin, P. Meredith, E. H. Sargent, *Nature Reviews Materials* **2017**, 2.
- [24] Y. Yu, I. Hajime, Y. Kenichi, K. Noriyuki, W. Hirofumi, M. Masaya, O. Yuji, *Japanese Journal of Applied Physics* **2010**, 49, 010204.
- [25] Y. Yang, S. Omi, R. Goto, M. Yahiro, M. Era, H. Watanabe, Y. Oki, *Organic Electronics* **2011**, 12, 405–410.
- [26] S. B. Anantharaman, T. Stöferle, F. A. Nüesch, R. F. Mahrt, J. Heier, *Advanced Functional Materials* **2018**, 1806997.
- [27] H. v. Berlepsch, C. Böttcher, *Physical Chemistry Chemical Physics* **2018**, 20, 18969–18977.
- [28] H. Aviv, Y. R. Tischler, *Journal of Luminescence* **2015**, 158, 376–383.
- [29] C.-H. Cheng, Z. Li, A. Hambarde, P. B. Deotare, *ACS Applied Materials & Interfaces* **2018**, 10, 39336–39342.
- [30] J. Li, Y. Zheng, D. Zheng, J. Yu, *Journal of Photonics for Energy* **2016**, 6, 035502.
- [31] J. W. Lee, D. Y. Kim, F. So, *Advanced Functional Materials* **2015**, 25, 1233–1238.
- [32] R. Englman, J. Jortner, *Molecular Physics* **1970**, 18, 145–164.
- [33] P.-A. Bouit, F. Spänig, G. Kuzmanich, E. Krokos, C. Oelsner, M. A. Garcia-Garibay, J. L. Delgado, N. Martín, D. M. Guldi, *Chemistry – A European Journal* **2010**, 16, 9638–9645.
- [34] C. Villegas, E. Krokos, P.-A. Bouit, J. L. Delgado, D. M. Guldi, N. Martín, *Energy & Environmental Science* **2011**, 4, 679–684.
- [35] J. W. Lee, D. Y. Kim, S. Baek, H. Yu, F. So, *Small* **2016**, 12, 1328–1333.
- [36] I. K. Kim, J. H. Jo, J. B. Lee, Y. J. Choi, *Organic Electronics* **2018**, 57, 89–92.
- [37] L. Wang, S. Jenatsch, B. Ruhstaller, C. Hinderling, D. Gesevičius, R. Hany, F. Nüesch, *Advanced Functional Materials* **2018**, 28, 1705724.



- 
- [38] S. Jenatsch, L. Wang, M. Bulloni, A. C. Véron, B. Ruhstaller, S. Altazin, F. Nüesch, R. Hany, *ACS Applied Materials & Interfaces* **2016**, 8, 6554–6562.
- [39] J. L. Lyon, D. M. Eisele, S. Kirstein, J. P. Rabe, D. A. VandenBout, K. J. Stevenson, *Journal of Physical Chemistry C* **2008**, 112, 1260–1268.
- [40] A. Liess, A. Arjona-Esteban, A. Kudzus, J. Albert, A.-M. Krause, A. Lv, M. Stolte, K. Meerholz, F. Würthner, *Advanced Functional Materials* **2018**, 0, 1805058.
- [41] Y. Zhong, T. J. Sisto, B. Zhang, K. Miyata, X. Y. Zhu, M. L. Steigerwald, F. Ng, C. Nuckolls, *Journal of the American Chemical Society* **2017**, 139, 5644–5647.
- [42] W. Wang, F. Zhang, M. Du, L. Li, M. Zhang, K. Wang, Y. Wang, B. Hu, Y. Fang, J. Huang, *Nano Letters* **2017**, 17, 1995–2002.
- [43] L. Gao, C. Ge, W. Li, C. Jia, K. Zeng, W. Pan, H. Wu, Y. Zhao, Y. He, J. He, et al., *Advanced Functional Materials* **2017**, 27, 1702360.
- [44] Y. Oh, H. G. Yoon, S.-N. Lee, H.-K. Kim, J. Kim, *Journal of the Electrochemical Society* **2011**, 159, B34–B38.
- [45] R. Cherrington, D. J. Hughes, S. Senthilarasu, V. Goodship, *Energy Technology* **2015**, 3, 866–870.
- [46] S. G. Hashmi, M. Özkan, J. Halme, S. M. Zakeeruddin, J. Paltakari, M. Grätzel, P. D. Lund, *Energy & Environmental Science* **2016**, 9, 2453–2462.
- [47] M. Alam, D. Cameron, *Journal of Sol-Gel Science and Technology* **2002**, 25, 137–145.

## 4.5 Supporting Information

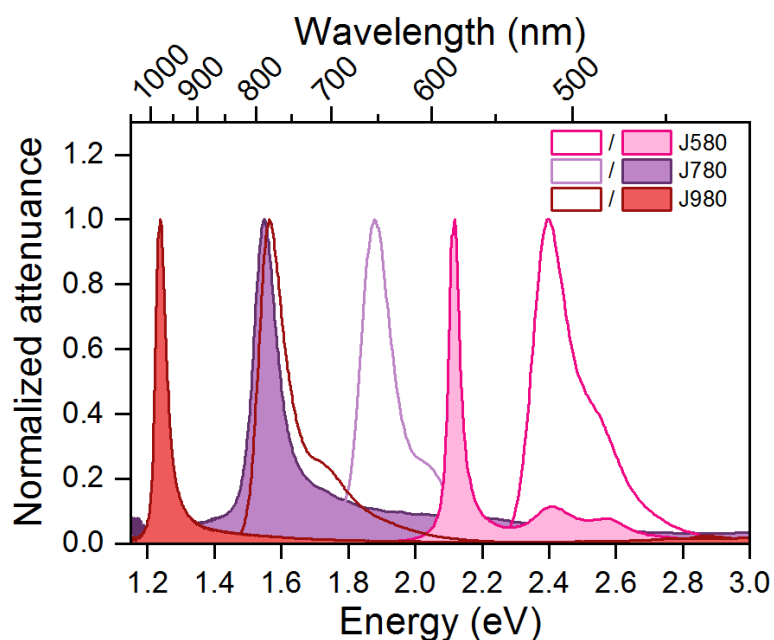


Figure S4.1 – Normalized monomer (open, in methanol) and J-aggregate (filled) absorption spectra of the three dyes in methanol solution. J-aggregate solution for **J780** and **J980** are obtained by dispersing the dye in acetate buffer. In the case of **J580**, J-aggregates were obtained by dispersing the dye in water.

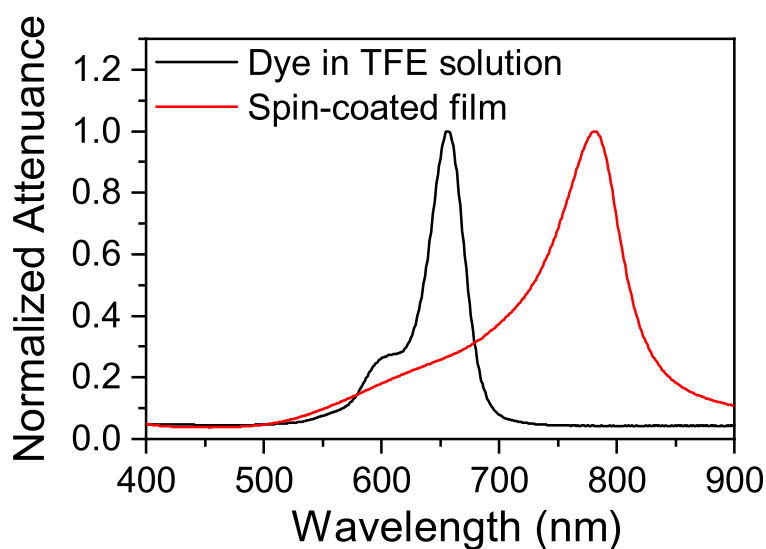


Figure S4.2 – Attenuance of **J780** dye in TFE solution and in thin film obtained by spin coating the solution on a glass substrate.

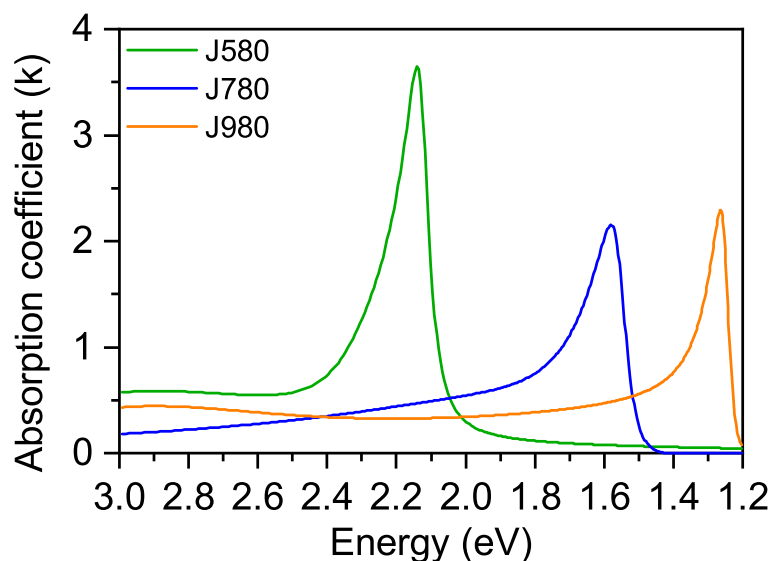


Figure S4.3 – The absorption coefficient calculated from ellipsometry for J-aggregate thin films spin-coated on  $\text{TiO}_2$  substrates are shown after subtracting the contribution from  $\text{TiO}_2$ .

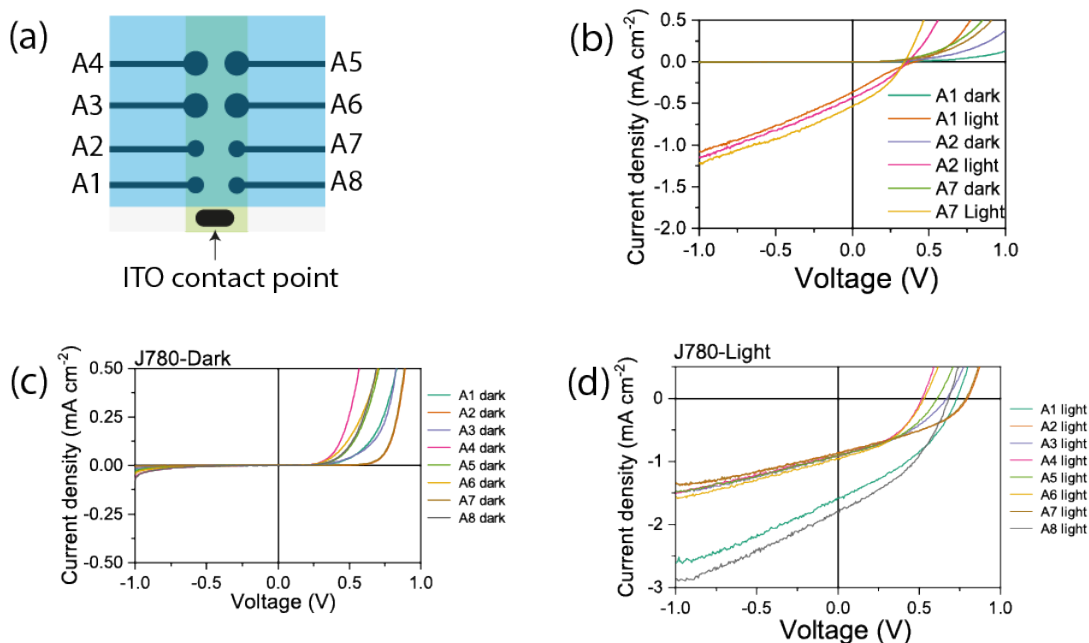


Figure S4.4 – Schematic of the device (top view) with electrodes (A1 to A8) and ITO contact point (a). Current density-voltage curves for **J780** spin coated from acetate buffer - direct method (b). In comparison, the J-V curves under dark (c) and light (d) are shown for **J780** spin-coated from TFE (in-situ method) for all the eight devices.

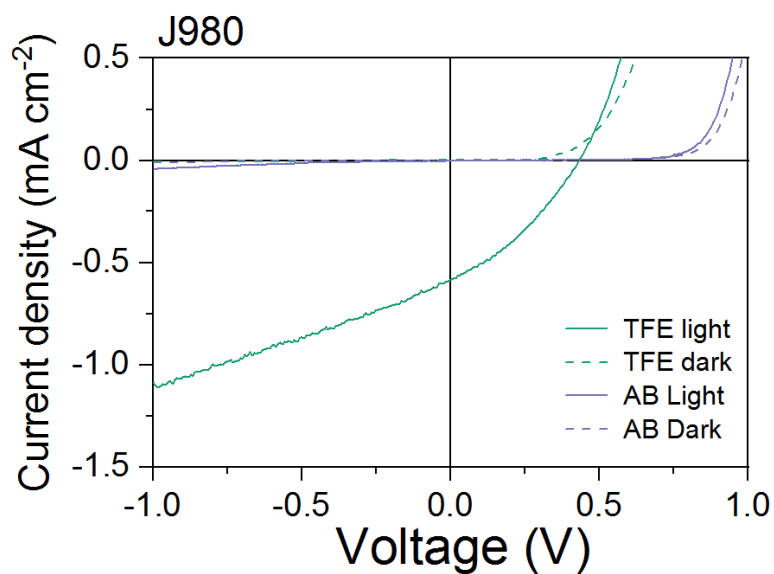


Figure S4.5 – Comparison of J-V curves for the **J980** devices spin-coated from TFE (in-situ method) and acetate buffer (AB, direct method) solution. The best device is reported here for J-aggregate films processed from the acetate buffer solution. The short-circuit current ( $J_{sc}$ ) shows a 60-fold increase from 0.01 to 0.58  $\text{mA cm}^{-2}$  while using the in-situ method.

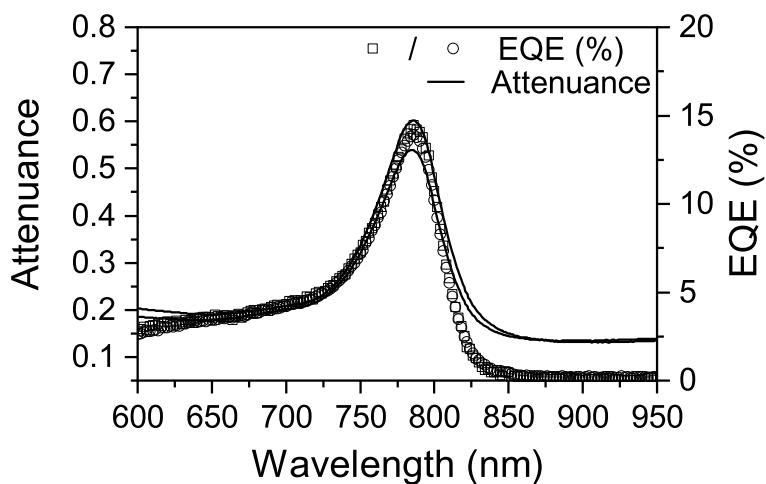


Figure S4.6 – Attenuance and EQE measured from two different batches (represented as open square and open circle) for **J780** devices.

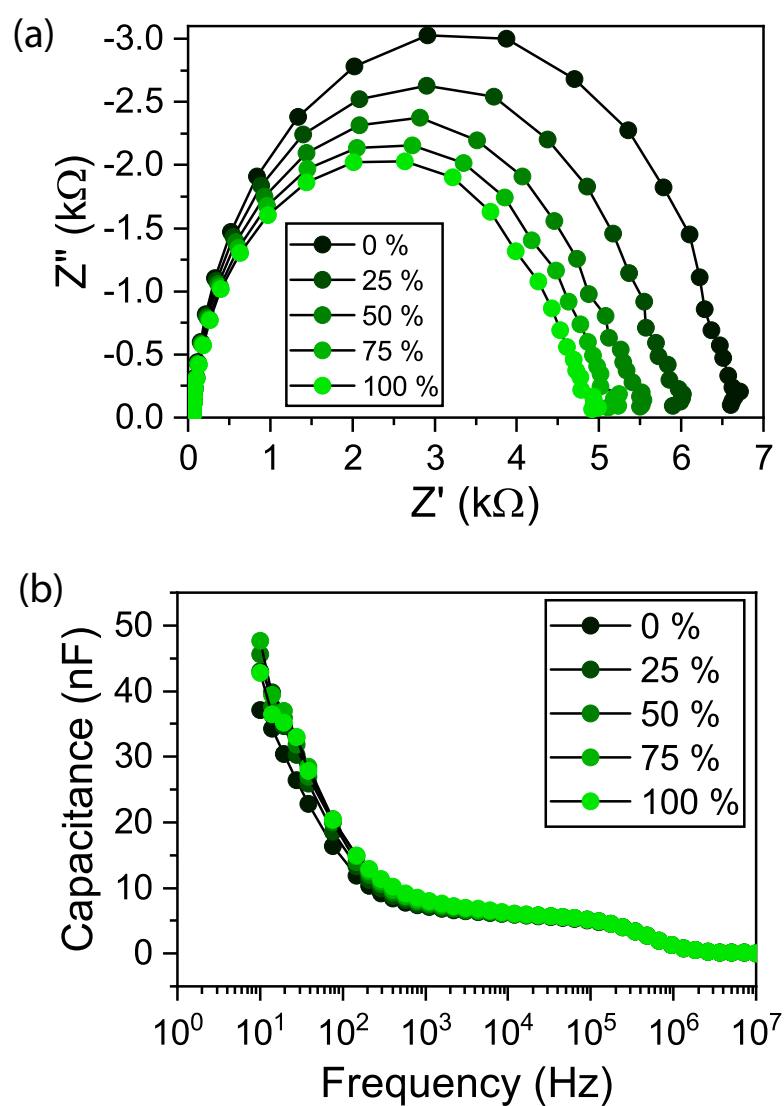


Figure S4.7 – Impedance (a) and capacitance (b) measured for **J580** devices at 0 V upon illumination with different light intensities.

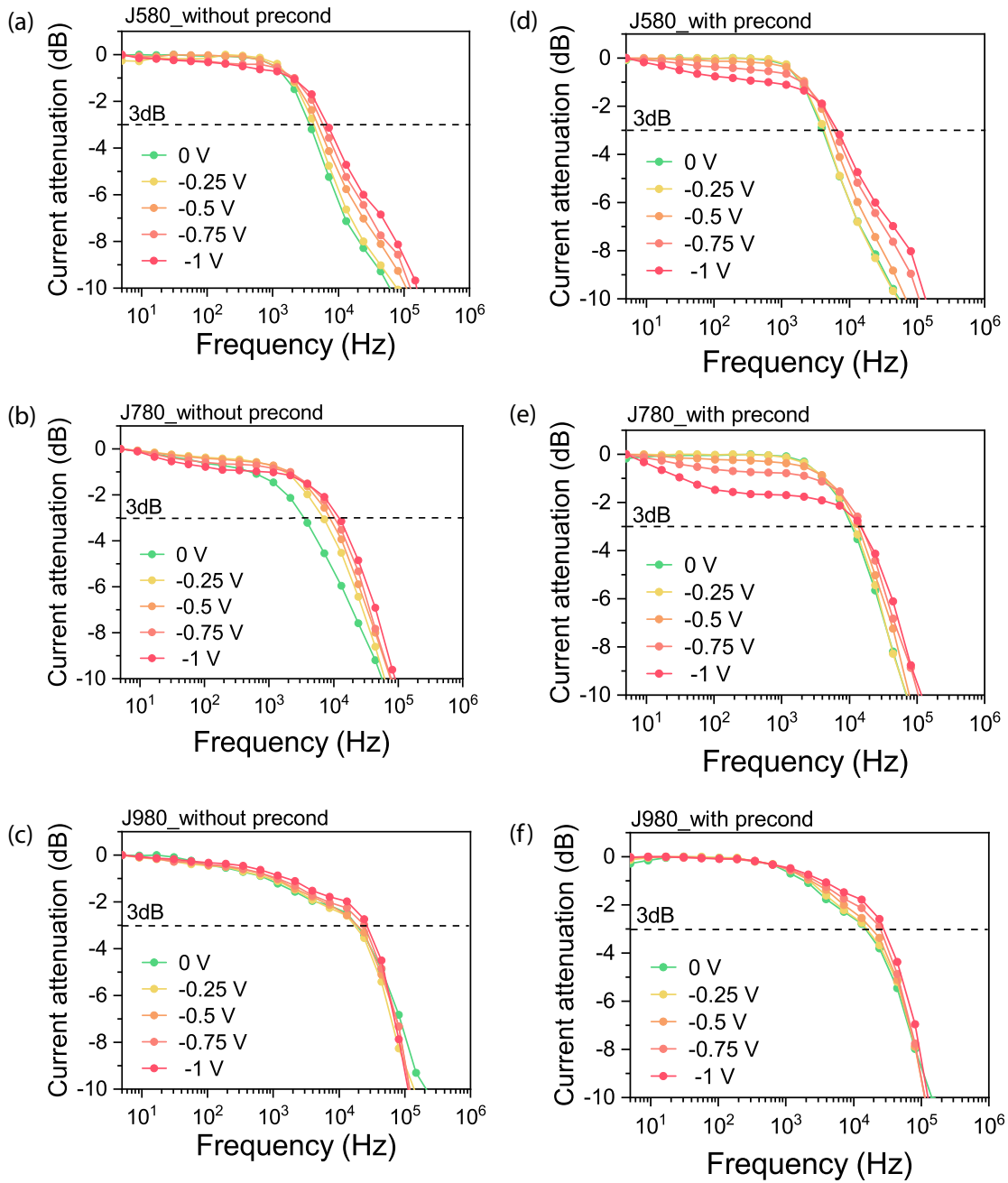


Figure S4.8 – Frequency response and -3dB values recorded without preconditioning for the **J580** (a), **J780**(b) and **J980** (c) and its corresponding values after preconditioning the devices for 120 s at -1 V (d-f).

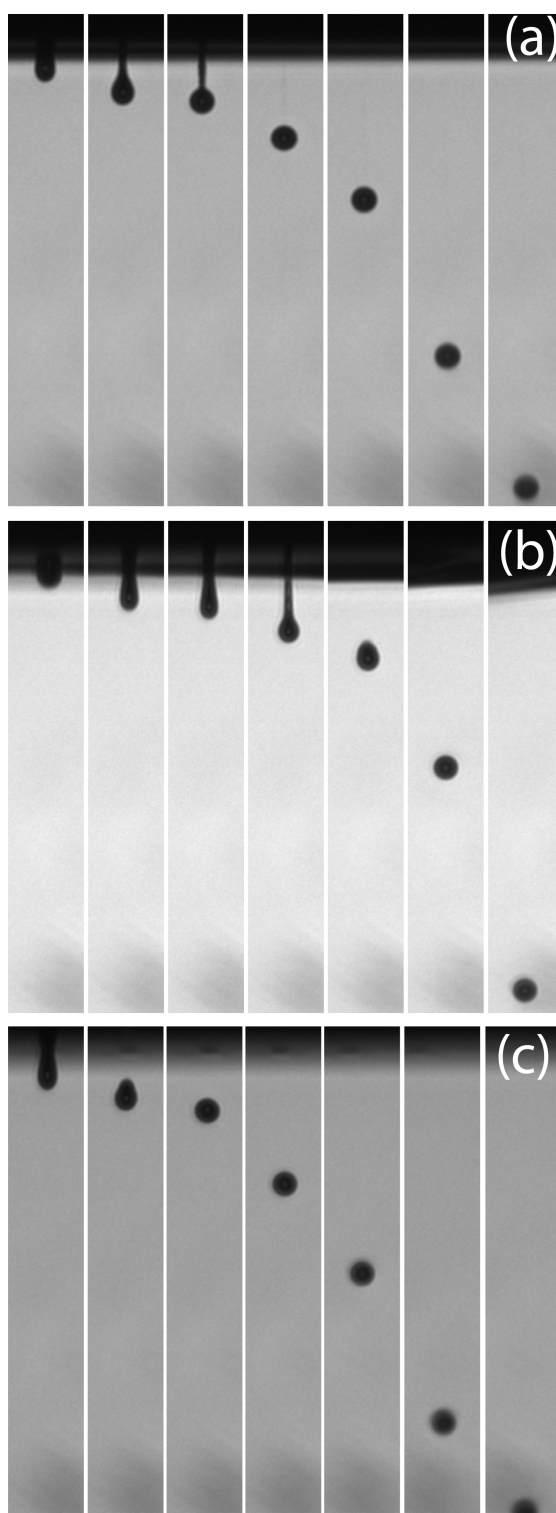


Figure S4.9 – Stroboscopic images of inkjet drop formation with c-TiO<sub>2</sub> ink (a), m-TiO<sub>2</sub> ink (b) and J-aggregate ink (c) at consecutive intervals (20  $\mu$ s) after the printing trigger pulse. The elongated tail associated with the ink droplet as observed in (a) and (b) quickly merges with the drop without forming any satellite drops.

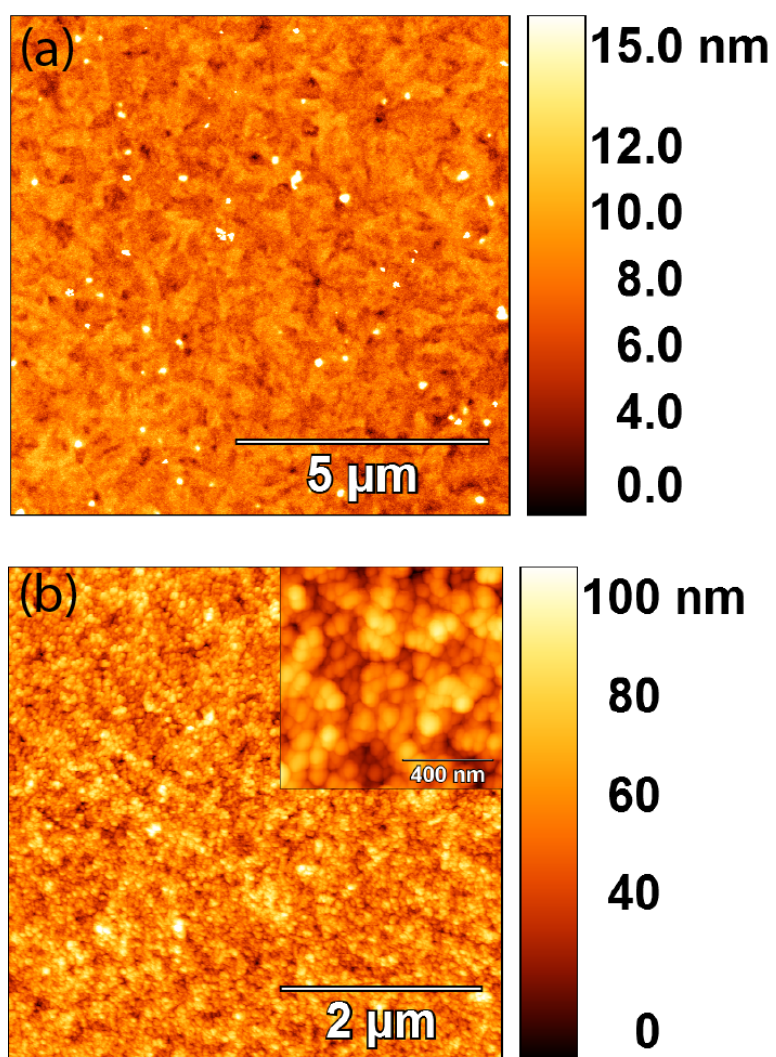


Figure S4.10 – Topographical images of inkjet printed c-TiO<sub>2</sub> on ITO substrates (a) and m-TiO<sub>2</sub> on c-TiO<sub>2</sub> coated ITO substrates (b).



## 5 Excitonic Channels from Bio-Inspired Templated Supramolecular Assembly of J-aggregate Nanowires

Surendra B. Anantharaman,<sup>1,2</sup> Daniel Messmer,<sup>3</sup> Amin Sadeghpour,<sup>4,5,6</sup> Stefan Salentinig,<sup>5,7</sup> Frank Nüesch,<sup>1,2</sup> and Jakob Heier<sup>1</sup>

<sup>1</sup>Laboratory for Functional Polymers, Empa, Swiss Federal Laboratories for Materials Science and Technology, Überlandstrasse 129, CH-8600 Dübendorf, Switzerland.

<sup>2</sup>Institut des Matériaux, Ecole Polytechnique Fédérale de Lausanne, EPFL, Station 12, CH-1015 Lausanne, Switzerland.

<sup>3</sup>Laboratory of Polymer Chemistry, Department of Materials, ETH Zurich, Vladimir-Prelog-Weg 5, 8093 Zürich, Switzerland.

<sup>4</sup>Center for X-ray Analytics, Empa, Swiss Federal Laboratories for Materials Science and Technology, Überlandstrasse 129, CH-8600 Dübendorf, Switzerland.

<sup>5</sup>Laboratory for Biointerfaces and <sup>6</sup>Laboratory for Biomimetic Membranes and Textiles, Empa, Swiss Federal Laboratories for Materials Science and Technology, Lerchenfeldstrasse 5, St. Gallen, CH-9014, Switzerland.

<sup>7</sup>Department of Chemistry, University of Fribourg, Chemin du Musée 9, 1700 Fribourg, Switzerland.

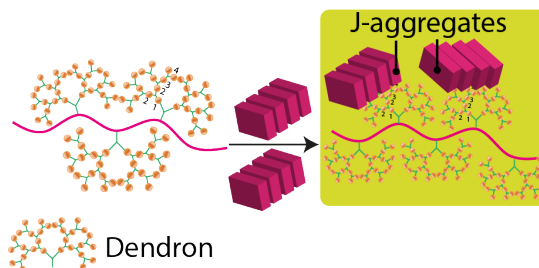
Reproduced by permission of The Royal Society of Chemistry  
©The Royal Society of Chemistry 2019

*Nanoscale*, **2019**, *11*, 6929-6938, DOI: 10.1039/C8NR10357G  
<https://pubs.rsc.org/en/content/articlehtml/2019/nr/c8nr10357g>

**Author Contributions:** J.H and F.N proposed the idea. D.M synthesized the dendronized polymers. S.B.A prepared all the samples and characterized them. A.S conducted the SAXS measurement and interpreted the data along with S.S. S.B.A discussed the results and wrote the manuscript with inputs from all co-authors.

### Abstract

Supramolecular assemblies with controlled morphology are of paramount importance for energy transport in organic semiconductors. Despite considerable freedom in molecular design, the preparation of dyes that form one dimensional J-aggregates is challenging. Here, we demonstrate a simple and effective route to functionalize dendronized polymers (DPs) with J-aggregates to construct tubular



DP/ J-aggregate nanowires. When J-aggregates are adsorbed onto DPs anchored to glass substrates, they assemble into microcrystalline domains typical for J-aggregates adsorbed on functionalized surfaces. Differently, the complexation between the dendronized polymer and J-aggregates in solution leads to dense packing of J-aggregate strands on the periphery of the DPs. Using a layer-by-layer (LBL) technique, DPs loaded with J-aggregates can also be adsorbed onto a DP monolayer. In this case, the thin film absorption spectra are narrower and indicate higher ratios of J-aggregate to monomer and dimer absorption than bare J-aggregates deposited similarly. The demonstration of J-aggregate adsorption on filamentous polymeric templates is a promising step toward artificial 1D light harvesting antennas, with potential applications in opto-electronic devices.

### 5.1 Introduction

The realization of artificial assemblies with efficient exciton transport properties is of utmost relevance to the development of future optoelectronic devices. Naturally occurring photosynthetic light-harvesting systems, like chlorophyll molecules in a protein scaffold, act as antennas for exciton harvesting and transport to the special pair at the reaction center of the photosystem. This exciton funneling occurs over distances of 20-200 nm with near-unity efficiency.<sup>[1,2]</sup> Inspired by these self-assembled antennae systems, synthetic supramolecular structures with strong transition dipole coupling have been a focus of recent research.<sup>[3]</sup> This coupling results in efficient resonance energy transfer, which can lead to coherent exciton motion. Two-dimensional, brickstone J-aggregates are one prominent example of such structures, featuring large coherent excited state domain sizes with exciton delocalization over more than 10000 molecules.<sup>[4]</sup> Recently, unprecedented exciton coherence in J-aggregates up to 1  $\mu\text{m}$  was realized,<sup>[5]</sup> thereby surpassing the exciton coherence length of chlorophyll systems.<sup>[2]</sup>

In parallel, several hybrid systems incorporating quantum dots (QDs) and J-aggregates were developed to study the energy transfer from J-aggregates to QDs and vice versa. Walker et al.<sup>[6]</sup> have reported 90% energy transfer efficiency from J-aggregates (donor) to QDs (acceptor) in a blend. Recently, Wang and Weiss<sup>[7]</sup> demonstrated that J-aggregates can act as “*exciton-bridge*” between lead sulfide donor and acceptor QDs. The presence of J-aggregate bridges resulted in a 20-fold higher energy transfer rate than QDs closely linked by a polyelectrolyte. This functionality of the J-aggregate when integrated into energy harvesting systems can play a pivotal role in exciton transport for building efficient devices. Interestingly, the above mentioned studies were conducted with J-aggregates from a class of cyanine dyes with tubular morphology, as exciton transport is superior along the tubular direction.<sup>[5,8]</sup> Despite extensive research into tubular J-aggregates,<sup>[8–16]</sup> they are scarce and tuning the morphology of J-aggregate remains challenging.<sup>[9,17,18]</sup> Given these structural restrictions of tubular J-aggregates it is challenging to tune optical properties without impacting J-aggregate morphology, limiting applications in devices relying on exciton transport. Furthermore, they are poorly soluble and cannot be processed into thin films. Here tubular aggregates share a general short-coming of J-aggregates. Spontaneous self-assembly of dye molecules in solution generally does not yield well-defined structures, but crystals that are rich in defects and show a high degree of disorder. Also here film formation properties are poor and coherence properties in the thin film are typically worsening compared to solution. LB techniques improve the quality of these assemblies, but they are labor intensive and the transfer to a substrate is unpractical.<sup>[19]</sup>

A way out of this dilemma is suggested by nature itself: in light harvesting antennas, protein scaffolds assemble chromophores in a fashion suitable for long-range exciton transport. This has inspired a number of research groups already. The scaffolding of cyanine dye molecules on one-dimensional templates including DNA,<sup>[20,21]</sup> viruses,<sup>[22]</sup> or proteins<sup>[23]</sup> has been widely studied. However, in these cases, the dye monomers are assembled on the scaffold. Given the limited spectral overlap of absorption and fluorescence, the Förster resonance energy transfer (FRET) rate in these systems is low. For instance, cyanine dye monomers coupled on DNA (with up to ~30 nm in length) have a transfer efficiency of ~2% in solution.<sup>[24]</sup> The mechanism of linear helical J-aggregate formation on DNA templates is a sequential process of inserting a co-facial (H-type) dimer into the minor groove of DNA, followed by dislodging the dimers into a higher-order aggregate (H- or J-). Consequently, the groove gets perturbed to facilitate binding to another dimer. In a cooperative fashion, this array of dimers forms an aggregate.<sup>[20,21]</sup> It can be postulated that the coupling between adjacent dimers is very weak, leading to exciton localization along the DNA. Moreover, the presence of J-dimers will adversely localize the exciton on the J-aggregate channel due to its lower optical bandgap.

We thus followed a different approach and anchored J-aggregates of a cyanine dye (Figure 5.1) dispersed in the solvent onto a template. As one-dimensional templates, we used dendronized polymers (DPs), a class of comb polymers where a linear backbone bears a dendritic (*i.e.* regularly and repeatedly branched) side chain on every repeating unit.<sup>[25,26]</sup> An important parameter for the description of these polymers is the dendritic generation number  $g$ , which corresponds to the number of branching points between a peripheral group and the focal

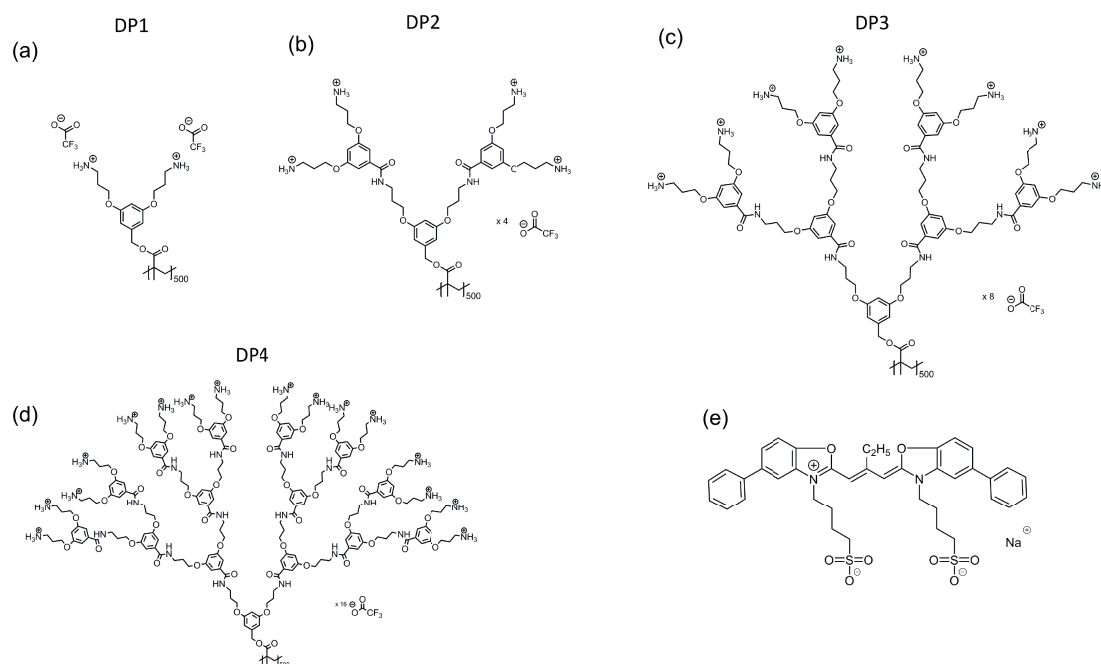


Figure 5.1 – Chemical structures of the DPs featured in this thesis (DP1, DP2, DP3 and DP4) as shown in (a-d) and the cyanine dye **J560** used for J-aggregate formation (e).

point by which the dendritic side groups are attached to their common core. By virtue of the very compact structure of the dendritic side chains, DPs are more shape resistant than other branched macromolecules such as bottle-brushes and the chain diameter becomes a parameter which can be varied in discrete steps by altering  $g$ .<sup>[27]</sup> Increasing thickness influences *e.g.* the overall stiffness of the polymers<sup>[27,28]</sup> and creates a separation between “interior” and “exterior” at sufficiently high  $g$ .<sup>[29,30]</sup> Another feature of interest is the large number of peripheral groups, which permits the facile modification of peripheral functionality. The DPs used in this thesis feature a methacrylate-based backbone and twofold-branching dendritic side chains bearing peripheral amines (in the form of their trifluoroacetate salts, see Figure 5.1). The synthesis of the DPs follows a bottom-up protocol as described in the Supporting Information - Section S1 and S2. In solution, the degree of protonation of primary and tertiary amines can be controlled via the pH, permitting easy control of the charge density of the DP. That also implies an easy control of the charge density of the DP. Furthermore, the DPs are water soluble and are adhering strongly to oxide surfaces.<sup>[31]</sup> These properties have previously been utilized to immobilize DP-enzyme conjugates on a variety of solid supports like mica, glass and silica.<sup>[32–35]</sup>

In this chapter, we investigate different aspects of the interaction of cyanine dye aggregates with DPs. The main goal of our work is to determine the conditions under which the DP template guides high quality J-aggregate assembly. The interaction between DPs and J-aggregates is mainly electrostatic, as the positively charged protonated peripheral amine groups of the DPs’ dendritic side chains can bond ionically to the negatively charged sulfonate groups of

the **J560** (Figure 5.1e) or its aggregates. We investigate in more detail the effect of line charge density, which differs greatly in the polymers DP2 and DP4. Adsorbing J-aggregates to DPs anchored to a surface does not improve J-aggregate crystal quality (morphology, optical properties) over other adsorption methods. In contrast, adsorbing J-aggregates onto the DPs in solution first and then anchoring the composite onto the substrate led to spectroscopically well-defined aggregates. Using small angle X-ray scattering (SAXS) we demonstrated that the aggregates indeed adsorb on the DPs in solution by forming tubular aggregates, as evident from the observed conformational changes. The J-aggregate nanowires maintain their spectroscopic properties when adsorbed onto a substrate.

## 5.2 Results and Discussion

### 5.2.1 Dye aggregation in solution

The specific dye (**J560**, for molecular structure see Figure 5.1e) was chosen for this investigation as it favors aggregation under acidic conditions, where amine groups in the DPs are fully protonated. First, J-aggregate formation in solution will be discussed. The process of J-aggregate self-assembly of the dye **J560** is a complex but hierarchical process influenced by solvent polarity, ionic strength, and the dye content. **J560** was dissolved in methanol ( $c_{J560} = 0.2$  mM), water ( $c_{J560} = 0.2$  mM) and 100 mM acetate buffer with pH  $\sim 3.5$ -4 ( $c_{J560} = 0.04$  mM). In methanol, only the monomer (*M*) form of the dye was observed with peak absorption at 504 nm (Figure 5.2). Even though the sulfonate groups (see Figure 1) render **J560** somewhat water solubility at the indicated concentration the monomers for J-aggregates (marked *J* in Figure 5.2) and H-type dimers (*D*), visible as red- and blue shifted peaks in the UV-vis spectrum next to remnant monomers. J-aggregates formed in acetate buffer have a higher quality than J-aggregates formed in water. Suspending **J560** in 100 mM acetate buffer led to complete formation of J-aggregates (peak absorption at 560 nm) with only a small amount of remnant monomers. Modifying the ionic strength of the buffer solution provides a further handle to alter the equilibrium between H-type dimers and J-aggregate (data not shown here). The molar extinction coefficient and full-width at half-maximum (FWHM) of the J-aggregate in acetate buffer was  $2.194 \times 10^5 \text{ M}^{-1} \text{ cm}^{-1}$  and 17.1 nm respectively.

### 5.2.2 Conformation of different generation DPs on glass substrates and anchoring J-aggregates

Glass substrates were functionalized with DPs by immersion into a DP solution ( $\sim 100 \text{ mg L}^{-1}$  in 100 mM acetate buffer) for 30 min, followed by rinsing with acetate buffer and water. The structure of the adsorbed layers here depends strongly on DP charge density with respect to the surface charge density.<sup>[36]</sup> The maximum line charge densities of fully protonated DPs are reported to decrease from  $60 \text{ nm}^{-1}$ , to  $30 \text{ nm}^{-1}$ ,  $15 \text{ nm}^{-1}$  and  $7.5 \text{ nm}^{-1}$  for DP4, DP3, DP2 and DP1, respectively.<sup>[37]</sup> The glass surface may have a density of  $\Gamma = 8 \text{ nm}^{-2}$

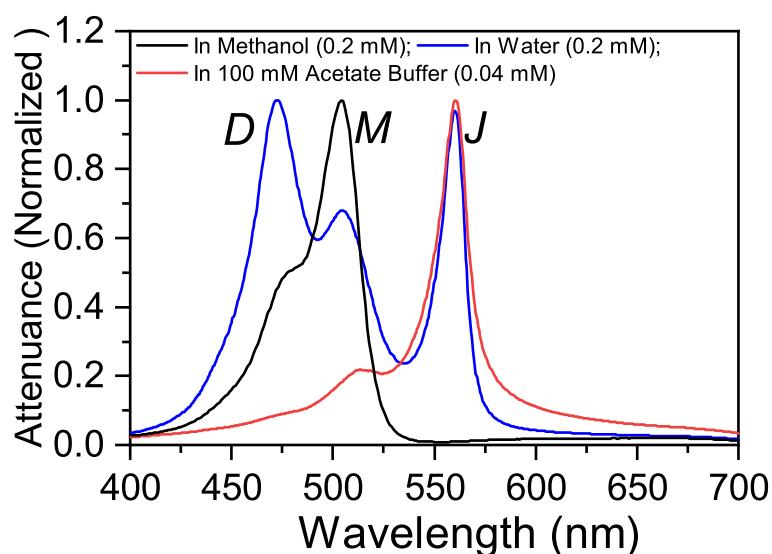


Figure 5.2 – Attenuance (normalized) for **J560** dye dissolved in methanol, water and 100 mM acetate buffer. The letters *D*, *M* and *J* stands for dimers, monomers and J-aggregates, respectively.

chargeable sites.<sup>[38]</sup> Under our experimental conditions the polymer chains of DP4 are highly positively charged and form a densely packed monolayer on glass or mica substrates as evident from AFM height images (Figure 5.3d). The DPs showed worm-like structures, with rather elongated chains (compared to less dense packed polymers at the same ionic strength) and almost equidistant spacing between neighbouring polymers.<sup>[39]</sup> For more information on the optimization conditions, please refer the Supporting Information, Section 5.5, Figures S5.2 to S5.6. We can assume that the majority of the segments of the DP are directly adsorbed to the surface, while a slight overcompensation of the charge maintains the worm-like structure. This slight charge overcompensation also prevents additional polymer to adsorb on top of the monolayer.

Under the same deposition conditions, films of DP3 formed a similar monolayer, but on top of that excess DPs collapsed into toroid shaped condensates (Figure 5.3c). We propose that the glass surface carries a higher charge density than a DP3 monolayer can compensate completely. In that case, DP3 adsorption is limited by steric interactions between adsorbed chains rather than by charge compensation. In that case the overall charge of the surface is still negative, facilitating the adsorption of further polymers to the DP3 monolayer.

The exact origin of this condensation is not clear, and also not subject of this thesis. Generally, long-range electrostatic interactions result in strongly correlated surface charge pattern that can lead to the formation of unexpected structures.<sup>[40]</sup> The similarity to DNA toroids, especially the monodispersity of the condensates as visible in the AFM images, speaks for a similar formation mechanism. DNA was reported to collapse into toroidal structures in solution upon the addition of covalent cations and other agents that mediate the attractive interaction

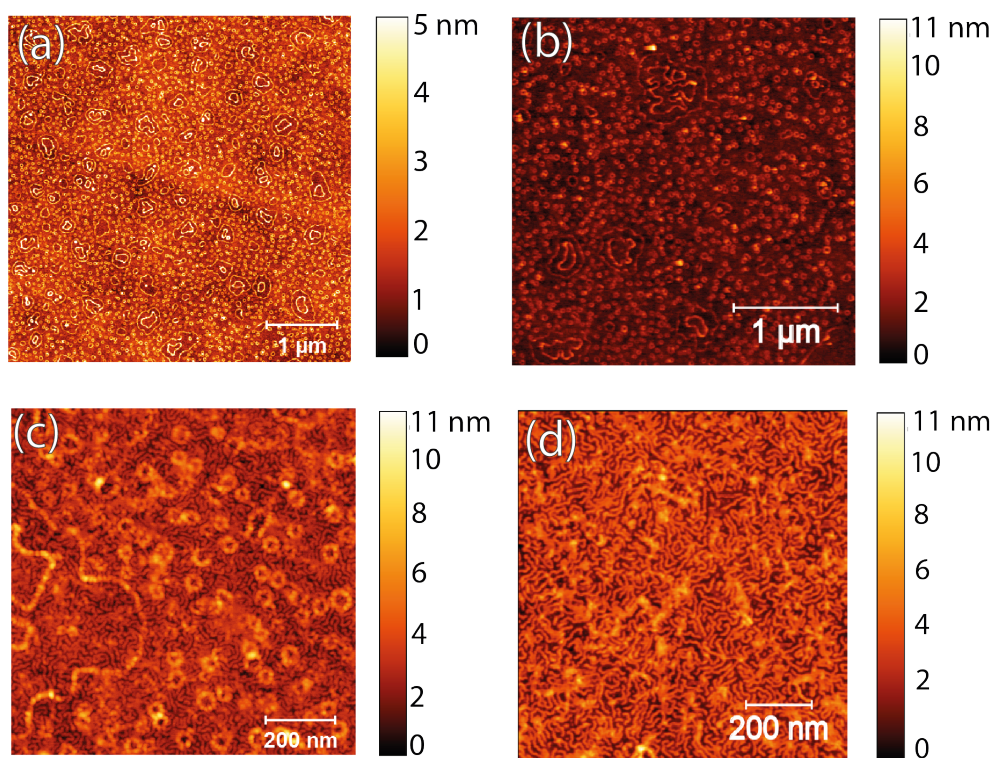


Figure 5.3 – AFM height images (tapping mode) of DPs – (a) DP1, (b) DP2, (c) DP3 and (d) DP4 deposited on glass.

between the chains.<sup>[41]</sup> Desorption of small cations from the glass surface may play that role. Ubbink and Odijk<sup>[41]</sup> calculated the stability conditions for DNA hexagonally packed within a toroid. It was found that toroids are the stable state for stiff enough chains. Toroidal structures may form in solution above the charged surface and then attach to the DP monolayer. The trend for ring structure formation on top of a first adsorbed DP monolayer continued for DP2 and DP1 (Figure 5.3 a and b). The even lower line charge densities ( $7.5$  and  $15 \text{ nm}^{-1}$  for DP1 and DP2, respectively)<sup>[39]</sup> still allows for electrostatically driven adsorption of DP to the substrate.<sup>[36]</sup> But, the reduced polymer charge density leads to less repulsion between the DP chains such that a dense monolayer can form. The dominating substrate charge density allowed for denser packing of the toroids. Toroidal DNA condensates have been identified as a method by nature to pack genomes at high density.<sup>[42]</sup> Line profiles of defects in the DP1 and DP2 layers show that indeed a monolayer of the polymers, about  $1 \text{ nm}$  in thickness is forming on the glass substrate. We show the film profiles together with cross sections of the toroidal structures (Figure S5.7, Supporting Information). To summarize, adsorbing DPs of different generation onto glass surfaces leads to different surface topographies and charge profiles. In the next section, we will discuss the deposition of J-aggregates on these DP films.

Glass substrates uniformly covered with DP films were immersed in **J560** ( $c_{\text{J560}} = 0.6 \text{ mM}$  in  $100 \text{ mM}$  acetate buffer,  $\text{pH} \approx 3.5\text{-}4$ ) and shaken overnight. Under these conditions the dye



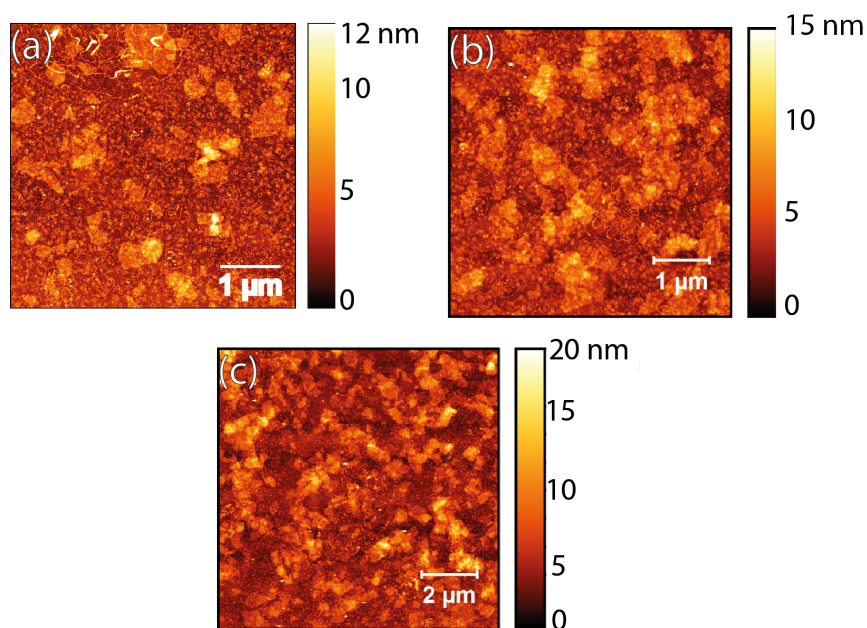


Figure 5.4 – AFM topographies (tapping mode) of J-aggregates deposited on DP2-functionalized glass substrates from (a) 0.2 mM, (b) 0.6 mM and (c) 2 mM solutions of J560 in 100 mM acetate buffer (pH  $\approx$  4).

is initially present in the form of dispersed J-aggregates (see section 5.2.1). The substrates were rinsed first with acetate buffer, then deionized water. At pH  $\approx$  3.5 - 4, the protonated peripheral amines of the DPs should interact with the sulphonate groups of the dye to anchor the J-aggregates. The attenuance spectra of the J-aggregate films are shown in Figure S5.8, Supporting Information. Compared to the solution spectra, the absorption peaks showed significant broadening and increased contributions from monomers and dimers. AFM images of the aggregates adsorbed from solution are shown in Figures 5.4 and S5.9. The aggregates adsorbed from solution crystallized into larger objects following a Volmer-Weber growth model and did not form conformal coatings on the DPs.<sup>[18]</sup> A crystal morphology of this type is characteristic for J-aggregates deposited onto functionalized substrates, and a direct advantage of using DPs over e.g. dendrimers cannot be recognized.<sup>[18,43]</sup> Also, this process was independent of DP generation and dye solution concentration. The attenuance spectra of J-aggregates on DPs of different generation reveal further information. The contributions of total attenuance attributed to monomer or J-aggregates as well as the ratio between these contributions are shown in Figure 5.5. No adsorption of J-aggregates on glass substrates was observed in the absence of DP layer. The J-aggregate peak intensity was largest for DP2, as was the ratio between monomer and J-aggregate contribution. This observation suggests a correlation between the conformation of the DP and the aggregation behavior. The dye formed better (*i.e.* high *J-/M-* ratio) J-aggregates on the toroidal structures DPs (DP1 and DP2) than on the rod-like DPs (DP3 and DP4). It can also be seen that the dimer (*D*) absorption started to increase with DP3 and DP4. Effectively, the J-aggregate films on DP3 and DP4 showed



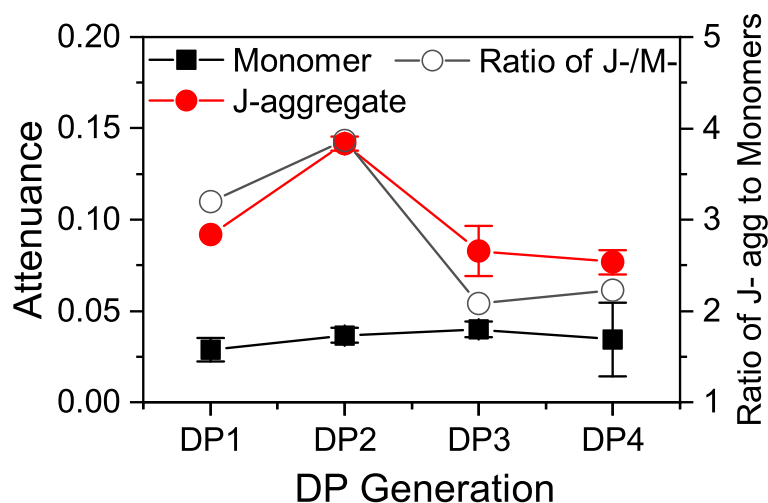


Figure 5.5 – Attenuance of monomers and J-aggregates deposited on DP functionalized glass substrates from  $c_{J560} = 0.6$  mM dye solution in 100 mM acetate buffer.

a higher dimer and monomer fraction than the starting solution. The adsorption onto DP monolayers is therefore different from the cooperative mechanism cyanine dye complexation with DNA,<sup>[20,21]</sup> where initially formed dimers act as nucleation sites for J-aggregate growth.

Small-angle x-ray scattering studies (see section 5.2.3) indicate, that the density of dendrons packed in a DP increases with DP generation. The shape of the DP2 surface seems to be most compatible with the conformation of the aggregates and fewer monomers or dimers find room to also adsorb to the DP. Indeed, when using a solution with higher dye concentration ( $c_{J560} = 2$  mM dye in 100 mM acetate buffer), resulting in larger aggregates, a further decrease in J-aggregate absorption was observed (Figure S5.8b and d). As the DPs were strongly adsorbed on the glass surface which limits their conformational J-aggregate growth does not seem to be directed by the molecular nature of polymers, but J-aggregate growth follows a Volmer-Weber growth mode. J-aggregation is even more prominent on low generation DPs than higher generation DPs.

### 5.2.3 Complexation of J-aggregate and dendronized polymers in solution studied by SAXS

To avoid the conformational constraints in the deposited DP films and to allow the polymers to act as true templates, we moved on to complexing DPs and J-aggregates in solution. DP2 and DP4 in 100 mM acetate buffer solutions were prepared and different amounts of J-aggregate in acetate buffer solutions were added to obtain 0.2 mM, 0.6 mM and 2 mM dye concentration (See Supporting Information, Figure S5.10). The solutions were stirred overnight and filled into quartz capillaries for the SAXS measurements.

The solution containing dendronized polymers of second generation (DP2) was characterized

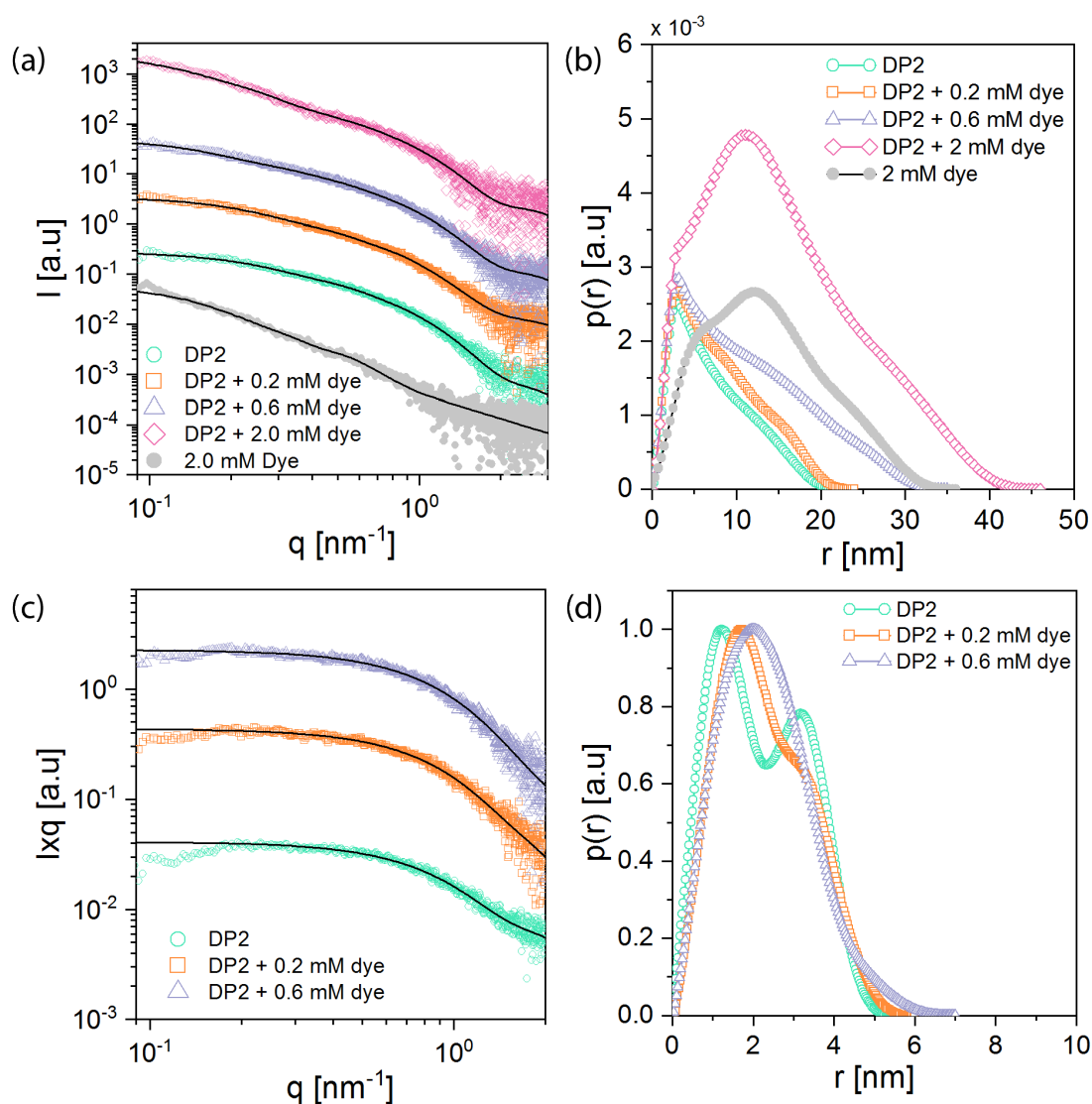


Figure 5.6 – (a) The experimental  $I(q)$  profiles of DP2 and its mixture with **J560** dye shown in dots, and their corresponding theoretical curves shown as solid lines calculated from the IFT analysis. For better representation, the curves are shifted vertically. (b)  $p(r)$  functions corresponding to the theoretical curves shown (a). (c)  $I \times q$  versus  $q$  curves for DP2 and polymer-dye mixtures representing cross-section scattering intensities. These curves analyzed by IFT to obtain detailed cross sectional information. For better representation, the curves are shifted vertically. (d)  $p(r)$  functions, obtained by IFT assuming cylindrical symmetry for the  $I \times q$  shown in (c).

with increasing amounts of dye molecules added to the sample. The SAXS scattered intensities as a function of the scattering vector magnitude,  $q$ , for those samples and the pure dye sample at 2 mM concentration are presented in Figure 5.6a together with their corresponding simulated curves. Fits of the corresponding pair-distance distribution functions,  $p(r)$ , are shown in Figure 5.6b, as obtained from indirect Fourier transformation (IFT) analysis of scattering data; these plots aid in the interpretation of the system's structural behavior in real space. The  $p(r)$  from the pure polymer shows asymmetric behavior. A maximum appears at around 2.9 nm while a (semi-)linear decay shows up at higher dimensions, reaching zero at around 22 nm. Such  $p(r)$  behavior is typically for elongated particles (cylindrical structures) with maximum dimension ( $D_L$ ) of about 22 nm. To obtain further information about the cross section of the cylindrical structures, before and after loading with dye molecules, the scattering from the cylinder cross-section,  $I_{cs}(q)$  was separated from the cylinder length (proportional to  $q^{-1}$ ) via  $I_{cs}(q) = I(q) \times q$ . The resulting  $I_{cs}(q)$  curves are shown in Figure 5.6c. These corresponding  $p(r)$  functions correspond to the spatially averaged convolution square of electron density fluctuations within the cross section of polymer chains. The cross-sectional  $p(r)$  for the pure polymer shows a bimodal distribution with a maximum cross-section dimension ( $D_{cs}$ ) of 5.3 nm.

A similar behavior has been observed for polymer samples loaded with 0.2 and 0.6 mM of dye; the  $p(r)$  presented in Figure 5.6d shows an increase in  $D_L$  up to 33 nm. Consistent with the increase in overall particle dimension,  $p(r)$  of the cross-section also demonstrates a slight increase after adsorption of dye molecules on the polymer chains (from  $D_{cs} = 5.3$  nm for pure polymer to 6.6 nm in presence of 0.6 mM of dye). Interestingly, the bimodal feature present in pure DP2 in  $p(r)$  disappears with increasing dye concentration and a uniform electron density distribution across the polymer was observed eventually (Figure 5.6d). The coverage of the DP surface with J-aggregates through charge-charge interactions and hydrophobic effects may result in expulsion of water to form a homogeneous scattering volume thus suppressing the bimodal feature upon addition of dyes in DP2.

At very high concentrations of dye (2 mM), the scattering patterns resemble the ones obtained for pure dye aggregates, only with extension to higher  $D_{max}$  (see a broad distribution peak at around 12 nm in Figure 5.6b, blue and gray curves). This indicates that at such high concentrations of dye, the polymer is saturated and cannot adsorb additional dye molecules, and hence considerable numbers of standard J-aggregates form in the medium. It can be noted that the trend observed in attenuation for the J-aggregates deposited on DP2 pre-functionalized substrates shown in Figure S5.8b matches the SAXS measurement in solution: at the optimized dye concentration of 0.6 mM, the J-aggregate size is such that DP and aggregate can adapt their conformation without too high penalty in energy. Increasing the dye concentration to 2 mM, drastically increased the J-aggregates size in solution, which inhibited its adsorption to the amine groups of the DP, leading to a decrease of J-aggregate adsorption (Figure S5.8b).

SAXS measurements on the DP4 samples (Figure 5.7) revealed similar trends.  $D_L$  for DP4 showed similar values as DP2, an increase in  $D_L$  for pure polymer from around 23.5 nm to 33.5

Table 5.1 – Maximum elongated dimension ( $D_L$ ) and maximum cross-section dimension ( $D_{cs}$ ) for DP2 and DP4 at different dye loadings. Note that these dimensions are underestimates, due to the inherently limited access to low  $q$  values in the Guinier regime.

Sample details	Maximum elongated dimension ( $D_L$ ), [nm]		Maximum cross-section dimension ( $D_{cs}$ ), [nm]	
	DP2	DP4	DP2	DP4
Pure DP	22	23.5	5.3	8.8
DP + 0.2 mM dye	23	25	5.7	9.7
DP + 0.6 mM dye	33	29	6.6	9.7
DP + 2 mM dye	35	53	NA	NA

nm for polymer subjected to 0.6 mM dye (Figure 5.7a and b). As expected the cross-sectional dimensions were significantly larger:  $D_{cs} = 8.8$  nm for pure polymer increasing to  $D_{cs} = 9.7$  nm for polymer in the presence of 0.6 mM dye. Such increased cross-sectional dimensions are in good agreement with our estimations from the molecular structure of the polymer. In further similarity to the observations made for DP2, the initially present bimodal feature in cross sectional  $p(r)$  of DP4 diminished after adsorption of dye (Figure 5.7d), indicating a transformation of the cross-section from a core-shell structure to a homogeneous electron density, indicative of the replacement of initially present water with tightly interacting dye molecules. The outcome of SAXS studies for both DP2 and DP4 are summarized in Table 5.1.

#### 5.2.4 Layer-by-layer deposition of DP/J-aggregate nanowires

SAXS experiments proved that for a dye concentration of  $c_{J560}$  dye aggregates are homogeneously covering the DP's exterior surfaces. Also, the SAXS measurements showed an overall increase in elongated dimension for both the DP2 and DP4 generation upon addition of dye. We next tested a layer-by-layer (LBL) approach to adsorb the nanowires onto a substrate. The J-aggregate/DP nanowires did not adsorb onto neat glass substrates, but they adhered well on substrates functionalized with DPs. From here we can conclude that the J-aggregate/DP nanowires bear overall negative charge, *i.e.* that the nanowires bear  $> 0.5$  equiv. of J560 per amine of the central DPs. To deposit the nanowires, glass substrates were functionalized with monolayers of DP (as shown in Figure 5.3), exposed to the J-aggregate/DP nanowire solution for 24 h and then rinsed with water. AFM images revealed a low density of thick, individual. J-aggregate/DP nanowires adsorbed on the DP2 functionalized surface (Figure 5.8a). They showed a more elongated rod-like shape than the underlying DPs. The structure is also very different from the J-aggregates adsorbed onto a DP functionalized surface (Figure 5.5) .

Corroborating the SAXS results, this suggests the formation of a DP/J-aggregate nanowire whereby the DP chains stretch upon dye loading. A direct comparison between the DP/J-aggregate nanowires in solution and the ones adsorbed to the substrate is difficult because the substrate has a major influence on the conformation. But, the AFM images clearly show that the DP/J-aggregate nanowires as whole adsorb to the substrate. It can be noted that

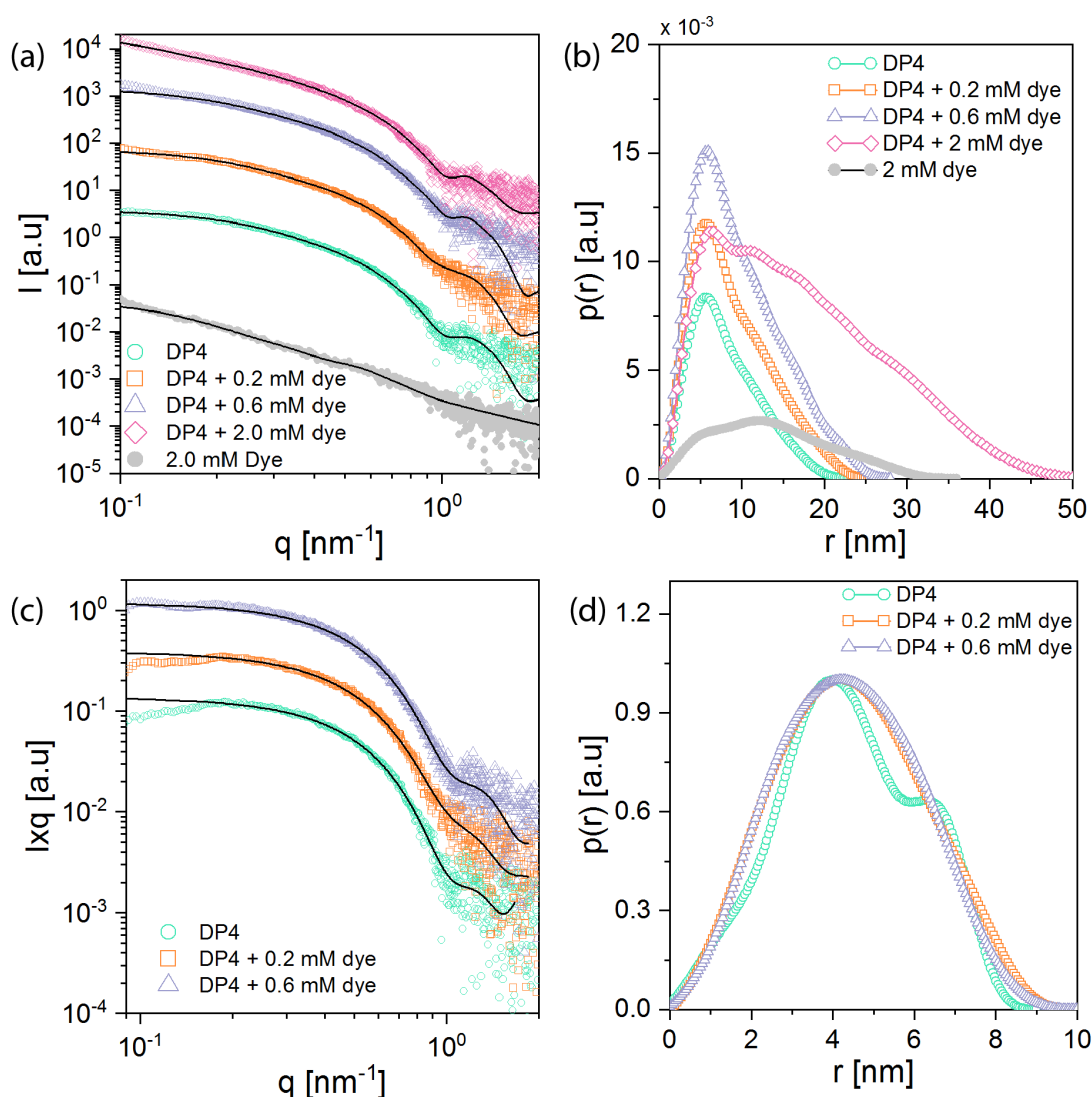


Figure 5.7 – (a) The experimental  $I(q)$  profiles of DP4 and its mixture with **J560** dye shown in dots, and their corresponding theoretical curves shown as solid lines calculated from the IFT analysis. For better representation, the curves are shifted vertically. (b)  $p(r)$  functions corresponding to the theoretical curves shown (a). (c)  $I \times q$  versus  $q$  curves for DP2 and polymer-dye mixtures representing cross-section scattering intensities. These curves analyzed by IFT to obtain detailed cross sectional information. For better representation, the curves are shifted vertically. (d)  $p(r)$  functions, obtained by IFT assuming cylindrical symmetry for the  $I \times q$  shown in (c).

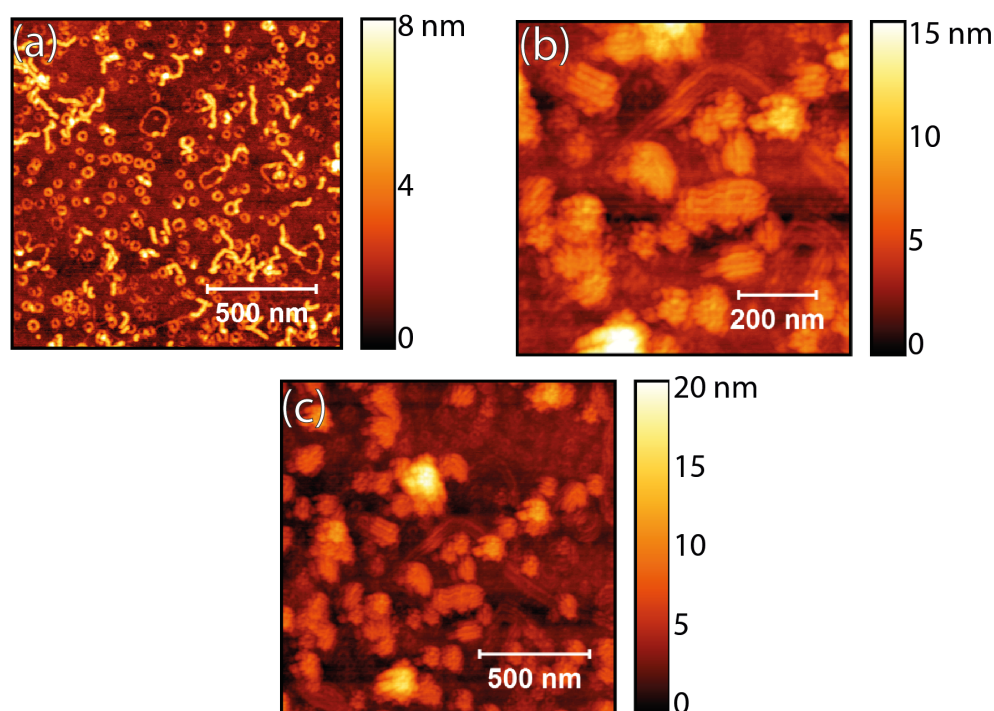


Figure 5.8 – Elongated DP2 (a) and DP4 (b) deposited from complexed DP and J-aggregate solution ( $c_{J560} = 0.6$  mM dye in acetate buffer) on their corresponding DP pre-functionalized glass substrates. For DP4, *super-structures* were observed with local ordering when they are covered with dye molecules as shown in (c).

the nanowires preferentially adsorb on top of the “isolated” rings, in-line with our earlier interpretation that the potential at the monolayer level is negative, while the top surface of the toroids is positive. We can also note that the surface is free of J-aggregate crystals as observed in the experiments described in section 5.2.2. This also means that all J-aggregates are complexed with the DPs to form DP/J-aggregate nanowires

The morphology of DP4/J-aggregate nanowires analogously prepared was markedly different: DP4/J-aggregate nanowires were not found to adhere individually, but assembled into *bundle-like* structures when deposited on the substrate (Figure 5.8b and c). This can be explained by a reduction of electrostatic repulsion between J-aggregate/DP nanowires, the positive charge of the DPs is compensated by the negative charge of the dye aggregates anchoring on the DP surface. This type of nanotubular bundles are also famously present for tubular J-aggregates.<sup>[44]</sup> Another type of structure - *supercoiling*, is influenced by the DPs interaction with substrates.<sup>[45]</sup> Also, a block co-polymer coupled to DP is known to generate nanoscale building block materials.<sup>[46]</sup> In a similar fashion, complexing the cyanine dye J-aggregates with DP4, showed a supercoiling effect, which is reflected in the topography (Figure 5.8c).

Also here, and differently from the aggregates directly assembled onto a substrate (Figures 5.5 and S5.9), no platelet-shaped crystals were observed. Larger J-aggregate crystallites are

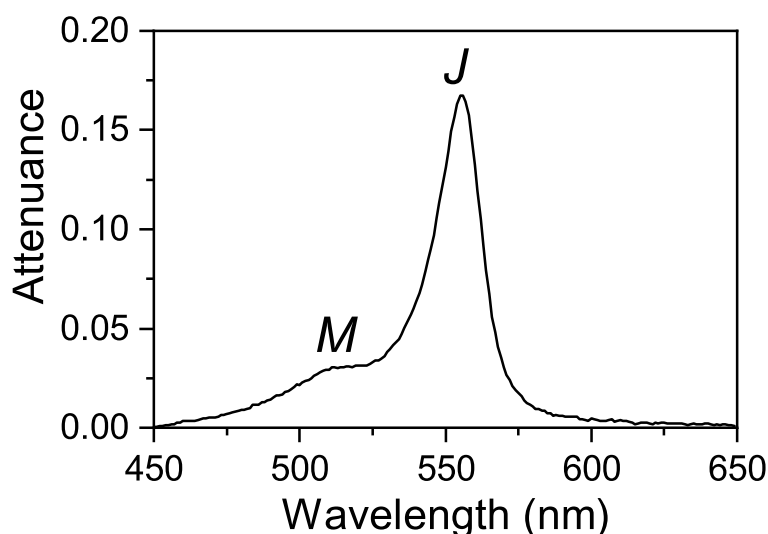


Figure 5.9 – Attenuance for DP4-premixed with dye solution ( $c_{J560} = 0.6$  mM) and deposited on DP4 functionalized glass substrates.

prone to self-quenching at defects like grain boundaries resulting from the spontaneous self-assembly process. Moreover, static disorder is one of the limiting factors for extended diffusion length in large aggregate crystals. Next to the absence of polycrystalline domains, a J-aggregate of “high quality” shows characteristic features in UV-Vis spectroscopy. The FWHM of the absorbance peak is narrow and the fraction of monomer and dimer absorbance is low. Absorbance spectra of the J-aggregate/DP nanowires in thin films are shown in Figure 5.9. It can be noticed that the J- to M- intensity is much higher in J-aggregate/DP nanowires compared to J-aggregates deposited on DPs (Figure S5.8d) for the same dye concentration ( $c_{J560} = 0.6$  mM). Also, the dimer absorption is negligible when using the solution complexation route (Figure 5.9) compared to depositing the aggregates on DP functionalized substrates (Figure S5.8d). This underscores the significance of initial conformational flexibility of the polymer, which is required for templated J-aggregation (Figure 5.8) as opposed to mere adsorption (Figure 5.4). In fact, the DPs acted as a much better linear template for J-aggregates than conventional DNA assemblies, which are difficult to functionalise with J-aggregates already present in the solution.

### 5.3 Conclusion

We here demonstrated the potential of complexing DPs and J-aggregates in solution as a new method to form coherent tubular aggregates with improved properties in thin film. Critical for the ability of the J-aggregate to anchor to the dendrons of the DP is the dye concentration (size of aggregates) and generation of the DPs. The net negatively charged J-aggregate/DP nanowires can be easily deposited onto a positively charged substrate, maintaining a high fraction of J-aggregates in the film. Adsorbing J-aggregates from solution onto substrates

functionalised with DPs is not a promising route to fabricate high quality J-aggregate films.

The complexation route allows to disperse J-aggregates into other matrix materials, where they could act as energy transport channels in FRET mode. Moreover, due to the versatility of this technique, J-aggregates could be grown on defined pathways which provides exciting opportunities for building optoelectronic devices. The next steps will be to study the properties of these tubular aggregates as excitonic channels in excitonic transistors. Specifically, we believe that this method can be extended to study donor-acceptor systems for energy transfer studies and in photovoltaics.

### 5.4 Experimental Section

Dendronized polymers of generation 1-4 were synthesized by following solid state peptide synthesis as described elsewhere.<sup>[31]</sup> Glass substrates were cleaned in acetone, ethanol, Hellmanex soap solution and water (3 times) with 5 min ultrasonication for each step separately. The substrates were dried using a N<sub>2</sub> gas stream and treated with oxygen plasma for 5 min to remove any organic residues. To deposit the DP on glass, the substrates were immersed in a solution of DP (1 mg mL<sup>-1</sup>) dissolved in 100 mM acetate buffer for 30 min and rinsed with acetate buffer followed by rinsing in water and N<sub>2</sub> drying. Cyanine dye (5-Phenyl-2-[2-[[5-phenyl-3-(4-sulfobutyl)-3H-benzoxazol-2-ylidene]-methyl]-but-1-enyl]-3-(4-sulfobutyl)-benzoxazolium hydroxide, inner salt, sodium salt) abbreviated as **J560**, was dissolved in methanol, water and acetate buffer at different concentrations to study the monomer to J-aggregate formation in solution. To achieve DPs covered with J-aggregate assemblies, the dye solution and DP solution were mixed together. The surface topography of the adsorbed layers was studied using atomic force microscopy (Bruker Dimension Icon) with an Antimony-doped Si cantilever (RTESP 300, tip radius of 12 nm, force constant of 40 Nm<sup>-1</sup>, resonant frequency 300 kHz) procured from Bruker and images were analyzed using the Nanoscope software. UV-Visible spectra for J-aggregate were acquired using a Varian Cary 50 UV-Vis spectrophotometer.

The SAXS experiments were performed using a Nanostar SAXS system (Bruker AXS GMBH, Karlsruhe, Germany) equipped with microfocussed X-ray source (Cu K<sub>α</sub> radiation) and MONTEL optics providing a point-focused X-ray beam with 0.154 nm wavelength. A VÅNTEC-2000, Xe-based gaseous avalanche detector capable of photon counting with 0.5 s temporal resolution, positioned at sample to detector distances of about 67 cm was used to acquire the scattering patterns. The acquisition time was 2 h. The setup is optimized and aligned to achieve the minimum scattering vector modulus of 0.1 nm<sup>-1</sup>. All the experiments were performed at room temperature.

The DP samples and its mixtures with dye solution were transferred into disposable quartz capillaries of 1.5 mm in outer diameter (Hilgenberg GmbH, Malsfeld, Germany). The capillaries were sealed prior mounting in the sample chamber. The scattering patterns from empty capillary and acetate buffer filled ones were also recorded for background subtraction.



**Acknowledgements** The authors gratefully acknowledge funding from the Swiss National Science Foundation grant numbers: 200021-157135 and 169695 to conduct this research work. We acknowledge the Scanning Probe Microscopy user laboratory at Empa for providing access to the instrument. The authors gratefully acknowledge Prof. Dr. A. Dieter Schlüter for his valuable inputs and discussion.



# Bibliography

- [1] E. Romero, V. I. Novoderezhkin, R. van Grondelle, *Nature* **2017**, 543, 355–365.
- [2] T. Mirkovic, E. E. Ostroumov, J. M. Anna, R. van Grondelle, Govindjee, G. D. Scholes, *Chemical Reviews* **2017**, 117, 249–293.
- [3] T. Kobayashi, *J-Aggregates*, World Scientific, **1996**.
- [4] D. Möbius, *Advanced Materials* **1995**, 7, 437–444.
- [5] D. M. Eisele, J. Knoester, S. Kirstein, J. P. Rabe, D. A. Vanden Bout, *Nature Nanotechnology* **2009**, 4, 658–663.
- [6] B. J. Walker, V. Bulović, M. G. Bawendi, *Nano Letters* **2010**, 10, 3995–3999.
- [7] C. Wang, E. A. Weiss, *Nano Letters* **2017**, 17, 5666–5671.
- [8] K. A. Clark, E. L. Krueger, D. A. Vanden Bout, *The Journal of Physical Chemistry Letters* **2014**, 5, 2274–2282.
- [9] H. von Berlepsch, C. Böttcher, A. Ouart, C. Burger, S. Dähne, S. Kirstein, *The Journal of Physical Chemistry B* **2000**, 104, 5255–5262.
- [10] E. Lang, A. Sorokin, M. Drechsler, Y. V. Malyukin, J. Köhler, *Nano Letters* **2005**, 5, 2635–2640.
- [11] N. Kameta, K. Ishikawa, M. Masuda, M. Asakawa, T. Shimizu, *Chemistry of Materials* **2012**, 24, 209–214.
- [12] D. M. Eisele, C. W. Cone, E. A. Bloemsma, S. M. Vlaming, C. G. F. van der Kwaak, R. J. Silbey, M. G. Bawendi, J. Knoester, J. P. Rabe, D. A. Vanden Bout, *Nature Chemistry* **2012**, 4, 655–662.
- [13] K. A. Clark, C. W. Cone, D. A. Vanden Bout, *The Journal of Physical Chemistry C* **2013**, 117, 26473–26481.
- [14] J. Yuen-Zhou, D. H. Arias, D. M. Eisele, C. P. Steiner, J. J. Krich, M. G. Bawendi, K. A. Nelson, A. Aspuru-Guzik, *ACS Nano* **2014**, 8, 5527–5534.
- [15] D. M. Eisele, D. H. Arias, X. Fu, E. A. Bloemsma, C. P. Steiner, R. A. Jensen, P. Rebentrost, H. Eisele, A. Tokmakoff, S. Lloyd, *Proceedings of the National Academy of Sciences* **2014**, 111, E3367–E3375.

## Bibliography

---

- [16] J. L. Banal, T. Kondo, R. Veneziano, M. Bathe, G. S. Schlau-Cohen, *The Journal of Physical Chemistry Letters* **2017**, 8, 5827–5833.
- [17] H. v. Berlepsch, C. Böttcher, *Physical Chemistry Chemical Physics* **2018**, 20, 18969–18977.
- [18] S. B. Anantharaman, T. Stöferle, F. A. Nüesch, R. F. Mahrt, J. Heier, *Advanced Functional Materials* **2018**, 1806997.
- [19] A. V. Sorokin, N. V. Pereverzev, I. I. Grankina, S. L. Yefimova, Y. V. Malyukin, *The Journal of Physical Chemistry C* **2015**, 119, 27865–27873.
- [20] M. Wang, G. L. Silva, B. A. Armitage, *Journal of the American Chemical Society* **2000**, 122, 9977–9986.
- [21] K. C. Hannah, B. A. Armitage, *Accounts of Chemical Research* **2004**, 37, 845–853.
- [22] C. M. Soto, A. S. Blum, G. J. Vora, N. Lebedev, C. E. Meador, A. P. Won, A. Chatterji, J. E. Johnson, B. R. Ratna, *Journal of the American Chemical Society* **2006**, 128, 5184–5189.
- [23] K. D. Volkova, V. B. Kovalska, A. O. Balanda, R. J. Vermeij, V. Subramaniam, Y. L. Slominskii, S. M. Yarmoluk, *Journal of Biochemical and Biophysical Methods* **2007**, 70, 727–733.
- [24] S. A. Díaz, S. M. Oliver, D. A. Hastman, I. L. Medintz, P. M. Vora, *The Journal of Physical Chemistry Letters* **2018**, 9, 3654–3659.
- [25] H. Frauenrath, *Progress in Polymer Science* **2005**, 30, 325–384.
- [26] A. D. Schlüter, A. Halperin, M. Kröger, D. Vlassopoulos, G. Wegner, B. Zhang, *ACS Macro Letters* **2014**, 3, 991–998.
- [27] B. Zhang, R. Wepf, M. Kröger, A. Halperin, A. D. Schlüter, *Macromolecules* **2011**, 44, 6785–6792.
- [28] Y. Guo, J. D. van Beek, B. Zhang, M. Colussi, P. Walde, A. Zhang, M. Kröger, A. Halperin, A. Dieter Schlüter, *Journal of the American Chemical Society* **2009**, 131, 11841–11854.
- [29] C. Gstrein, P. Walde, A. D. Schlüter, T. Nauser, *Photochemical & Photobiological Sciences* **2016**, 15, 964–968.
- [30] C. Gstrein, B. Zhang, M. A. Abdel-Rahman, O. Bertran, C. Alemán, G. Wegner, A. D. Schlüter, *Chemical Science* **2016**, 7, 4644–4652.
- [31] B. Zhang, R. Wepf, K. Fischer, M. Schmidt, S. Besse, P. Lindner, B. T. King, R. Sigel, P. Schurtenberger, Y. Talmon, Y. Ding, M. Kröger, A. Halperin, A. D. Schlüter, *Angewandte Chemie International Edition* **2011**, 50, 737–740.
- [32] F. Sara, B. T. E., Z. Baozhong, S. A. Dieter, W. Peter, *Macromolecular Bioscience* **2011**, 11, 1052–1067.
- [33] F. Sara, K. Phillip, L. Dario, S. A. Dieter, P. Dittrich, W. Peter, *ChemPlusChem* **2012**, 77, 98–101.

- 
- [34] A. Küchler, J. Adamcik, R. Mezzenga, A. D. Schlüter, P. Walde, *RSC Advances* **2015**, 5, 44530–44544.
- [35] A. Küchler, D. Messmer, A. D. Schlüter, P. Walde in *Methods in enzymology*, Vol. 590, Elsevier, **2017**, pp. 445–474.
- [36] O. J. Rojas, M. Ernstsson, R. D. Neuman, P. M. Claesson, *Langmuir* **2002**, 18, 1604–1612.
- [37] L. Grebikova, S. Kozhuharov, P. Maroni, A. Mikhaylov, G. Dietler, A. D. Schlüter, M. Ullner, M. Borkovec, *Nanoscale* **2016**, 8, 13498–13506.
- [38] S. H. Behrens, D. G. Grier, *The Journal of Chemical Physics* **2001**, 115, 6716–6721.
- [39] L. Grebikova, S. Kozhuharov, P. Maroni, A. Mikhaylov, G. Dietler, A. D. Schlüter, M. Ullner, M. Borkovec, *Nanoscale* **2016**, 8, 13498–13506.
- [40] Z. Yao, M. O. De La Cruz, *Physical Review E* **2013**, 87, 012603.
- [41] J. Ubbink, T. Odijk, *Biophysical Journal* **1995**, 68, 54–61.
- [42] C. C. Conwell, I. D. Vilfan, N. V. Hud, *Proceedings of the National Academy of Sciences* **2003**, 100, 9296–9301.
- [43] M. S. Bradley, J. R. Tischler, V. Bulović, *Advanced Materials* **2005**, 17, 1881–1886.
- [44] K. A. Clark, E. L. Krueger, D. A. Vanden Bout, *The Journal of Physical Chemistry C* **2014**, 118, 24325–24334.
- [45] V. Percec, C. H. Ahn, B. Barboiu, *Journal of the American Chemical Society* **1997**, 119, 12978–12979.
- [46] C. Li, A. D. Schlüter, A. Zhang, R. Mezzenga, *Advanced Materials* **2008**, 20, 4530–4534.

## 5.5 Supporting Information

### S1. Details concerning dendronized polymer synthesis and characterization

The dendronized polymers (DPs) employed in this work were prepared in a bottom-up approach, building the side chains by adding exactly one layer of dendritic monomers, i.e. DP1 served as the precursor to DP2, DP2 as the precursor for DP3, etc.<sup>[S1,S2]</sup> This mode of synthesis guarantees 1) that main-chain length within such a homologous series of DPs is essentially conserved, facilitating comparisons between DPs of differing *g*, and 2) that the dendritic side-chains are virtually defect-free, as quantified using a colorimetric defect labeling approach.<sup>[S3,S4]</sup> The N-protected precursor polymers of samples used in this thesis have been characterized elsewhere; DP1 has a molar mass of 259 kDa ( $P_n \approx 500$ ) as determined by GPC (Figure. S5.1), and chain length is conserved through-out the homologous DP series as evidenced by AFM imaging.<sup>[S5]</sup> GPC data does not provide a reliable measure of chain lengths particularly for high *g* DPs, as they feature very large molar masses per repeat unit (several kDa) and appropriate molar mass standards are not available; the results in Figure S5.1 rely on universal calibration using PMMA standards.

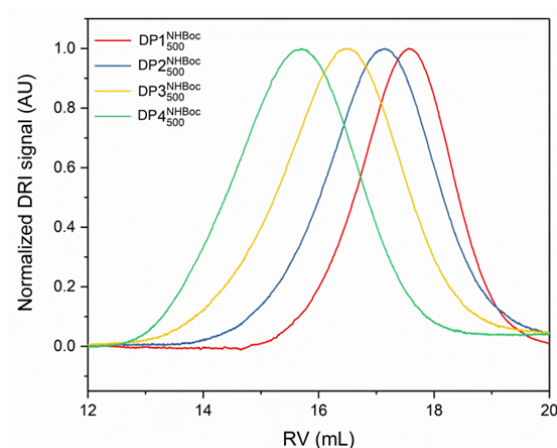


Figure S5.1 – Normalized GPC curves (DMF with 0.1 % LiBr, 45 °C, DRI detector) of the N-protected precursors DP1-DP4 to the polyelectrolytes DP1-DP4 used in this thesis, constituting a homologous series of DPs and corresponding numerical data (based on universal calibration using PMMA standards).

Table S5.1 – Outcome from Figure S5.1

DP	Mn [kDa]	D
DP1	259	1.72
DP2	665	1.57
DP3	1686	1.51
DP4	3805	1.26

## S2. Optimization conditions for obtaining monolayer DP on solid substrates

In preliminary explorations, the adsorption of DP4 was investigated in order to arrive at suitable conditions for the coating of other silicate surfaces. Mica was chosen as a substrate for these studies as it is atomically flat, permitting facile observation of adsorbed features by AFM, and as qualitatively it behaves quite similar to *e.g.* glass in that the surfaces exposes net negative charges, providing good adsorption of the polycationic dendronized polymers. The  $g = 4$  representative of the series was selected as due to its high diameter (*ca.* 5 nm) it can without any difficulty be observed in AFM. A number of parameters pertaining to the adsorption process was investigated, with the aim of developing a procedure which reliably provides densely coated substrates, as the goal was initially to prepare substrates suitable for the deposition and controlled growth of J-aggregates rather than to prepare self-assembled structures in solution.

Generally, AFM samples described below were prepared by submerging a freshly cleaved platelet of mica (*ca.* 5 mm x 5 mm, Plano GmbH) into the solution in question, then gently agitating the vessel for the indicated duration. Thereafter, the platelet was removed from solution, rinsed with copious amounts of pure solvent or buffer, affixed to a magnetic specimen disk (12 mm, Ted Pella Inc.) by means of a small piece of double-sided tape, and dried in a stream of dry N<sub>2</sub> for at least 1 h. AFM was performed on a NanoScope Multimode IIIa (Digital Instruments) using a 10  $\mu\text{m}$  x 10  $\mu\text{m}$  "E" scanner (Digital Instruments) using silicon cantilevers with a typical resonance frequency of 300 MHz and a typical spring constant of 26  $\text{Nm}^{-1}$  (OMCL-160TS-R3, Olympus). Images were processed using NanoScope Analysis (Bruker) and Fiji.<sup>[S6]</sup>

### 1. Solvent

The polyelectrolytic DPs are soluble in MeOH and water, as well as in a number of polar aprotic solvents such as DMSO or DMF, which due to their very high boiling points are however difficult to remove, particularly from strongly interacting surfaces such as mica or glass. A suitable solvent was evaluated first by immersing mica specimen into fairly concentrated solutions of DP4 (*ca.* 100  $\text{mg L}^{-1}$  in MeOH or deionized water) and then rinsing with the respective solvent. As is evident from Figure S5.2, this resulted in a fairly well-behaved monolayer of the dendronized polymer in the case of the aqueous solution, however for the methanolic solution no dense coverage was observed, and only individual polymers or small aggregates remained behind after washing.

### 2. pH

For the purpose of synthesizing covalent DP-enzyme conjugates, as well as for the immobilization of these conjugates, slightly basic aqueous buffers are usually employed as solvents. In order to provide quantitatively improved solubility of the DPs discussed here and in order to

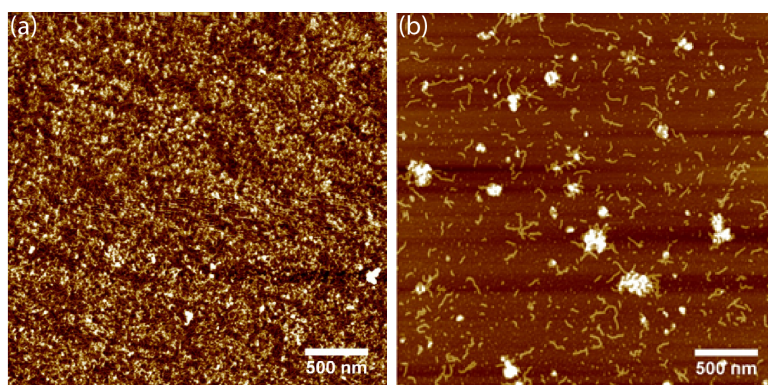


Figure S5.2 – AFM height images of DP4 deposited from  $100 \text{ mg L}^{-1}$  solutions in a) deionized water and b) methanol. The samples were removed from the solution and rinsed after 100 min. This observation agrees with the generally better solubility of DP4 and its lower *g* analogues in methanol than in water: Likely, a significant portion of initially deposited DP molecules is washed off by rinsing with methanol, whereas the dense layer deposited from aqueous solution remains in place.

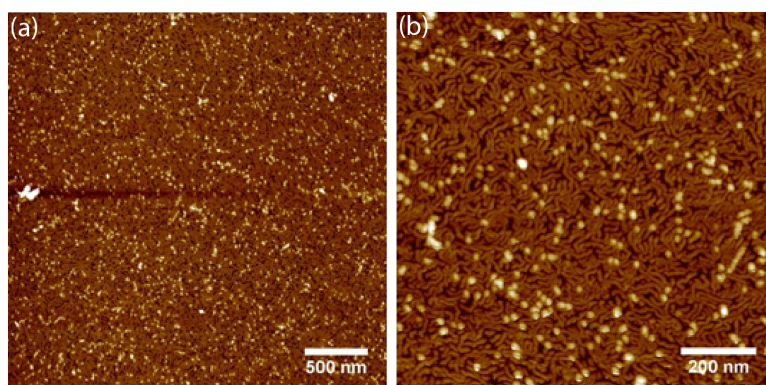


Figure S5.3 – AFM height images of DP4 deposited from  $100 \text{ mg L}^{-1}$  solutions in 100 mM acetate buffer at pH = 4 during 1 h. a) overview image, b) zoom revealing structural details.

fully protonate the peripheral amines, more acidic solutions in 100 mM acetate buffers of pH = 4 and pH = 5 were prepared. Using solutions containing  $100 \text{ mg L}^{-1}$  of DP4, both buffers were found to result in the deposition of dense layers of DPs. However, the layers in the case of pH = 4 were much more regular, appearing as essentially densely packed monolayers of DP chains with the occasional protruding coil or chain-crossover (Figure S5.3).

### 3. Immersion time

Initially, fairly long immersion of the mica platelets in DP4 solutions was used. It was found that exposure times as short as 5 min (Figure S5.43a and b) are entirely sufficient in order to produce complete adlayers of DP at  $100 \text{ mg L}^{-1}$ , and that prolonged exposure is not necessary.



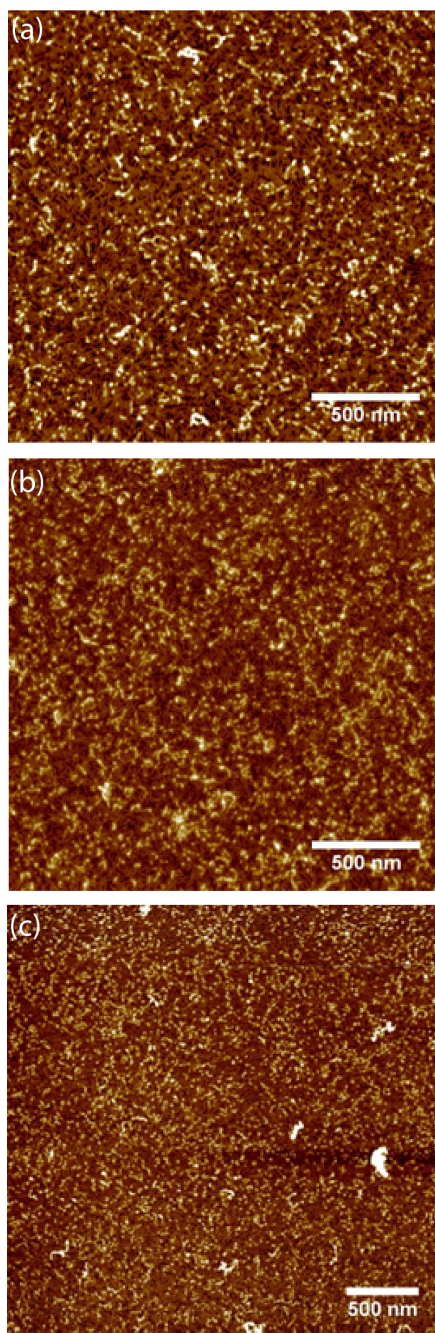


Figure S5.4 – AFM height images of DP4 deposited from  $100 \text{ mg L}^{-1}$  solutions in 100 mM acetate buffer at  $\text{pH} = 4$  with a) 5 min, b) 10 min and c) 20 min immersion time

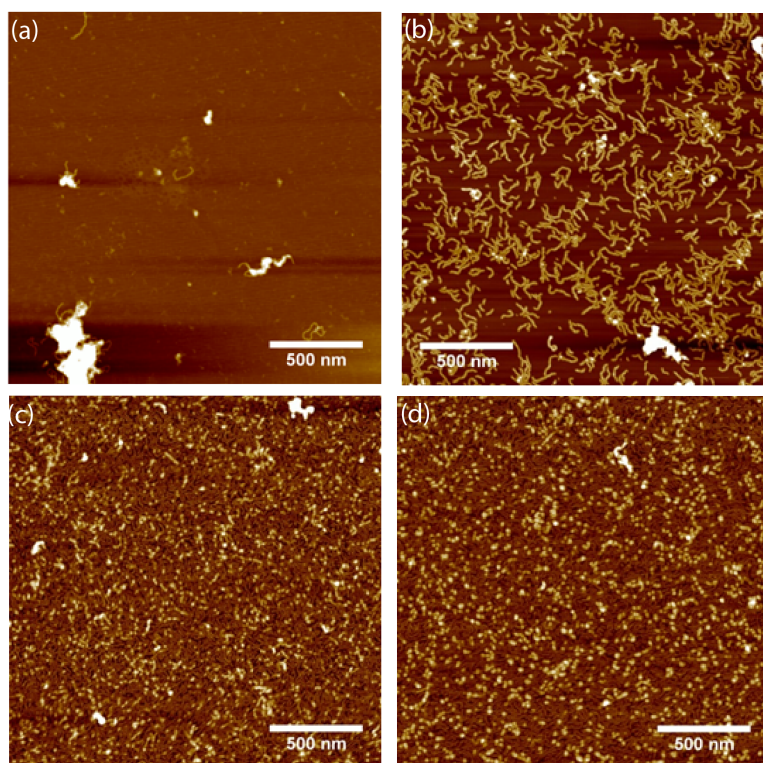


Figure S5.5 – AFM height images of mica substrates immersed for 15 min into solutions (100 mM acetate buffer, pH = 4) containing a) 10 mg L<sup>-1</sup>, b) 20 mg L<sup>-1</sup>, c) 50 mg L<sup>-1</sup> and d) 100 mg L<sup>-1</sup> DP4.

#### 4. Concentration

At 100 mg L<sup>-1</sup>, a fair amount of polymer is employed; considering the quite strong adhesion in the case of aqueous solutions and the fact that in drop-casting of solutions fairly dense surface coverage may be achieved already at concentrations of around 10 mg L<sup>-1</sup> for DPs comparable to DP4, the polymer concentration was varied. While very low concentrations employed for drop-casting were insufficient (1 mg L<sup>-1</sup> – 20 mg L<sup>-1</sup> Figure S5.5a and b) – likely in part due to loss of material by adsorption to the walls of the vessel in which the solution was prepared – concentrations starting at 50 mg L<sup>-1</sup> (Figure S5.5c and d) produced complete adlayers.

#### 5. Ionic Strength

The buffer solutions employed up to this point were not adjusted for ionic strength; Figure S5.6 displays the result of such adjustments to ionic strengths of 20 mM, 50 mM, 100 mM, and 200 mM by addition of NaCl to the acetate buffer. Rather than leading to a further improvement of the homogeneity of the adlayers, increasing ionic strength appears to be counterproductive, likely due to shielding of the peripheral ammonium cations of the DPs which reduce adhesion

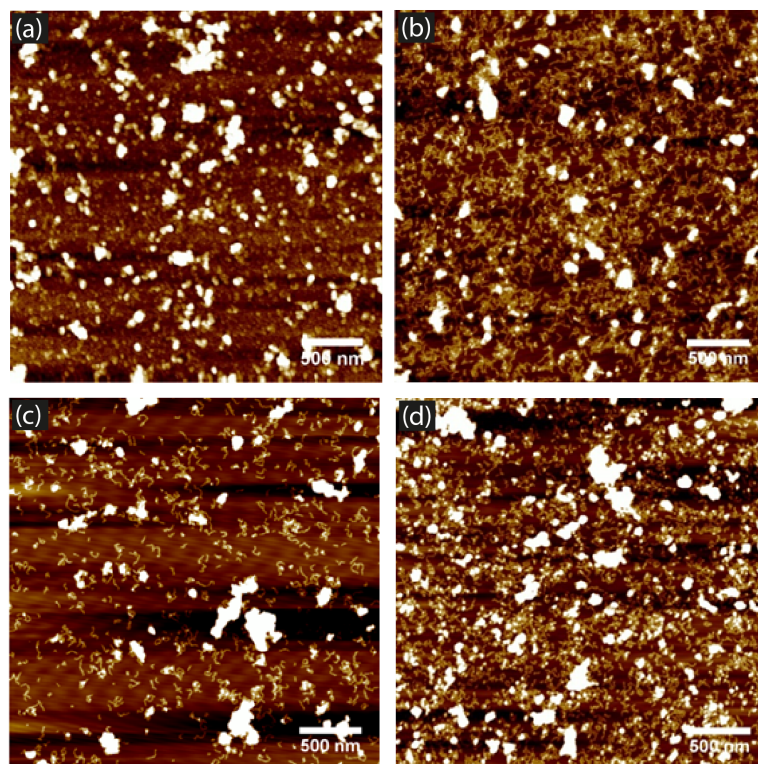


Figure S5.6 – AFM height images of mica substrates immersed into solutions of DP4 (50 mg L<sup>-1</sup> in acetate buffer, pH = 4), adjusted with NaCl to ionic strengths of (a) 20 mM, (b) 50 mM, (c) 100 mM, (d) 200 mM.

and DP interactions: Instead of homogenous adlayers, large aggregates appear and coverage becomes much looser than in the standard buffer. Additionally, large aggregate structures – possibly salt deposits – can be found in all samples where NaCl was added. No adjustment of ionic strength therefore appears necessary or helpful.

### Subbibliography

- [S1] B. Zhang, R. Wepf, K. Fischer, M. Schmidt, S. Besse, P. Lindner, B. T. King, R. Sigel, P. Schurtenberger, Y. Talmon, Y. Ding, M. Kroeger, A. Halperin and A. D. Schluter, *Angewandte Chemie-International Edition* **2011**, 50, 737-740.
- [S2] A. Kuchler, D. Messmer, A. D. Schluter and P. Walde, in *Nanoarmoring of Enzymes: Rational Design of Polymer-Wrapped Enzymes*, ed. C. V. Kumar, **2017**, 590, 445-474.
- [S3] L. J. Shu, I. Gossel, J. P. Rabe and A. D. Schluter, *Macromolecular Chemistry and Physics* **2002**, 203, 2540-2550.
- [S4] B. Zhang, H. Yu, A. D. Schluter, A. Halperin and M. Kroeger, *Nature Communications* **2013**, 4.



[S5] D. Messmer, M. Kroger and A. D. Schluter, *Macromolecules* **2018**, 51, 5420-5429.

[S6] J. Schindelin, I. Arganda-Carreras, E. Frise, V. Kaynig, M. Longair, T. Pietzsch, S. Preibisch, C. Rueden, S. Saalfeld, B. Schmid, J.-Y. Tinevez, D. J. White, V. Hartenstein, K. Eliceiri, P. Tomancak and A. Cardona, *Nature Methods* **2012**, 9, 676.

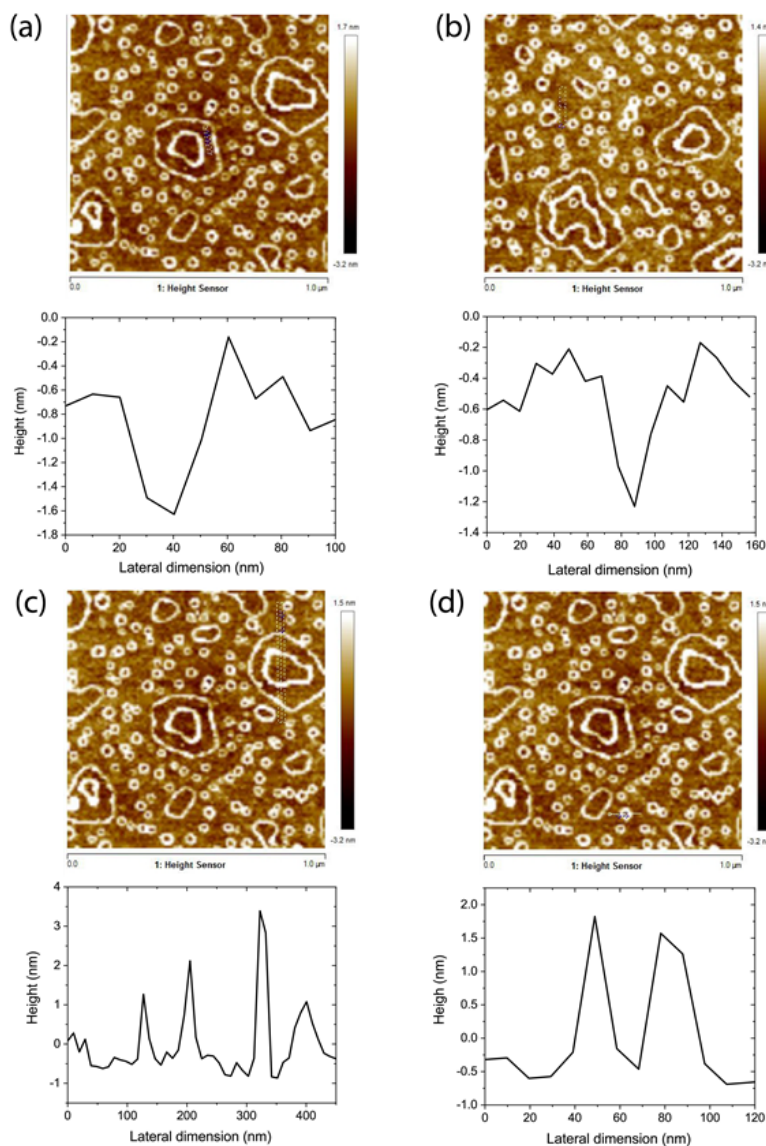


Figure S5.7 – AFM images and profiles of different sections of DP1 deposited on glass substrates. (a) and (b): Scans through defects in the DP1 monolayer show that the DP1 monolayer is about 1 nm thick. (c) Profile through the larger ring features. The height of these ring features is up to 4 nm on top of the base monolayer. (d) Profile through a small toroidal ring. The ring features are about 2 nm high.

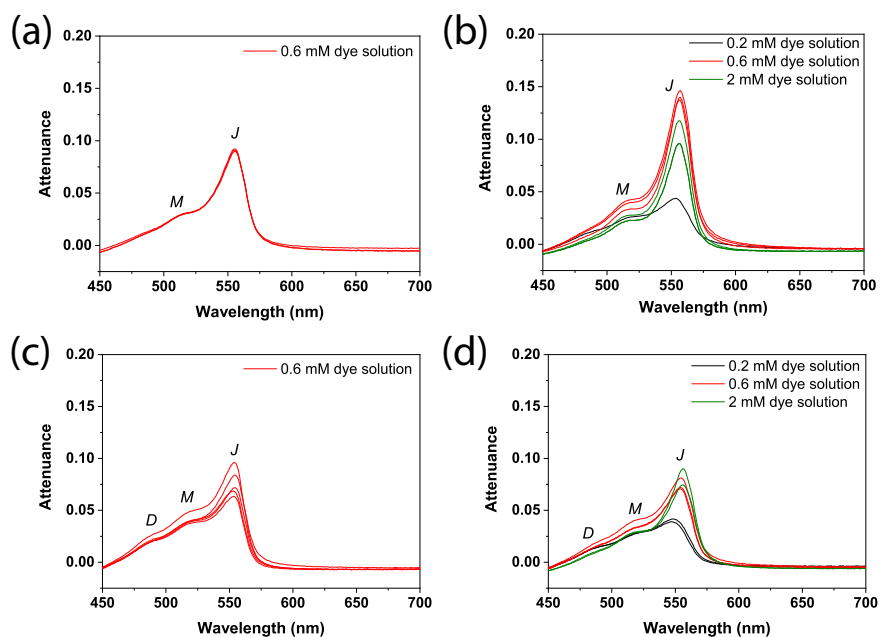


Figure S5.8 – Attenuance of monomers and J-aggregates deposited on glass substrates pre-functionalized with (a) DP1, (b) DP2, (c) DP3 and (d) DP4.

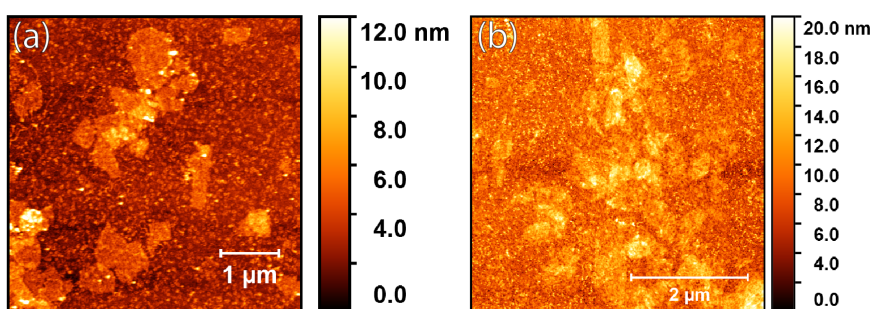


Figure S5.9 – AFM height images of DP2 (a) and DP4 (b) functionalized glass with J-aggregates deposited from dye solution

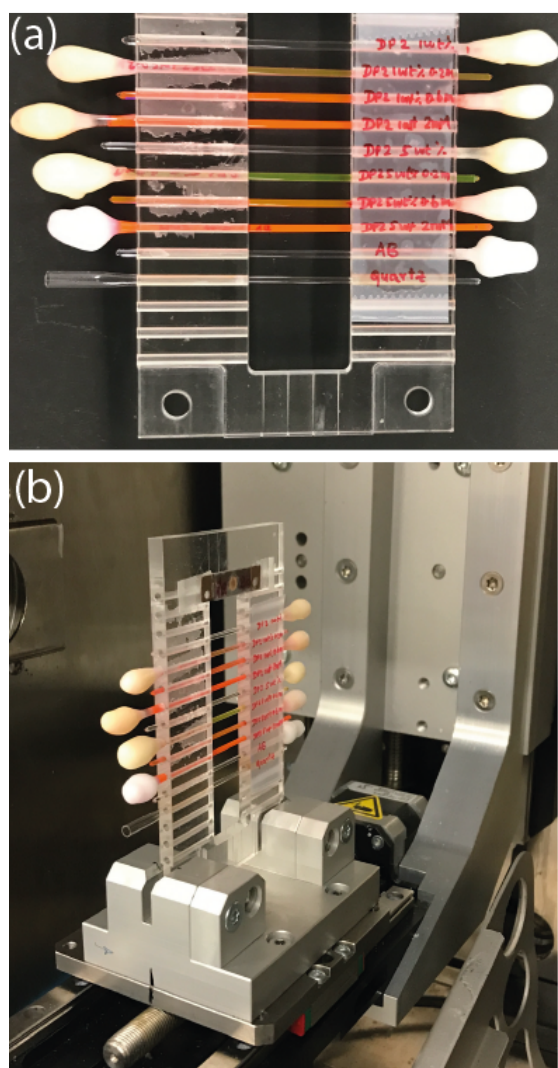


Figure S5.10 – SAXS measurement set-up for quartz capillaries filled with DP2 (1 wt% and 5 wt%) with 0.2 mM, 0.6 mM and 2 mM dye solution (a) loaded in the measurement set-up (b).

## 6 Strongly Red-Shifted Photoluminescence Band Induced by Molecular Twisting in Cyanine (Cy3) Dye Films

Surendra B. Anantharaman,<sup>†,§</sup> Sergii Yakunin,<sup>‡,⊥</sup> Chuyao Peng,<sup>†</sup> Marcus Vinícius Gonçalves Vismara,<sup>#</sup> Carlos E. O. Graeff,<sup>#</sup> Frank A. Nüesch,<sup>†,§</sup> Sandra Jenatsch,<sup>†,§</sup> Roland Hany,<sup>†</sup> Maksym V. Kovalenko,<sup>‡,⊥</sup> and Jakob Heier<sup>†</sup>

<sup>†</sup>Laboratory for Functional Polymers and <sup>‡</sup>Laboratory for Thin Films and Photovoltaics, Swiss Federal Laboratories for Materials Science and Technology, Überlandstrasse 129, CH-8600 Dübendorf, Switzerland.

<sup>§</sup>Institut des Matériaux, Ecole Polytechnique Fédérale de Lausanne, EPFL, Station 12, CH-1015 Lausanne, Switzerland.

<sup>⊥</sup>Laboratory of Inorganic Chemistry, Department of Chemistry and Applied Biosciences, ETH Zürich, CH-8093 Zürich, Switzerland.

<sup>#</sup>Faculdade de Ciências, Universidade Estadual Paulista Júlio de Mesquita Filho (UNESP), 17033-360 Bauru, Brazil.

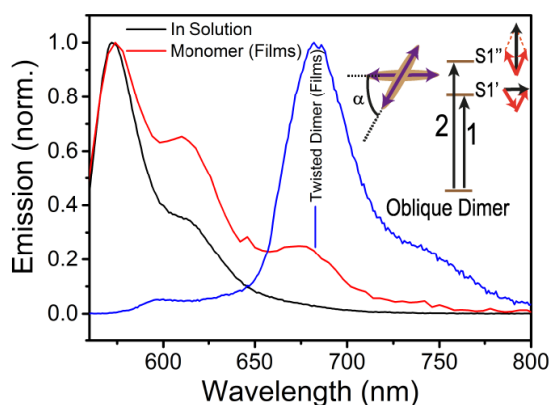
Adapted with permission from Journal of Physical Chemistry C  
©2017 American Chemical Society

*J. Phys. Chem. C*, **2017**, *121* (7), 9587-9593, DOI: 10.1021/acs.jpcc.7b01412  
<https://pubs.acs.org/doi/abs/10.1021/acs.jpcc.7b01412>

**Author Contributions:** J.H proposed the idea. J.H and S.B.A prepared the samples and planned the measurements. S.Y and J.H conducted temperature dependent PL measurement supervised by M.V.K. M.V.G.V and C.F.O.G performed ESR measurements. C.P provided the data for counter-ion effect. S.J provided Cy3-P samples and PL for NOPF<sub>6</sub>/Cy3-P blends. S.B.A wrote the manuscript with inputs from all co-authors.

### Abstract

Cyanine dye molecules, used as monomers or in aggregate form, find interesting applications in optoelectronic devices. Among the various aggregate species incorporating organic dyes, centrosymmetric dimers are known as nonluminescent. They can act as exciton quenchers due to a low-energy optically forbidden excited state. In this study, however, we show that a dimer species in thin films exhibits efficient and strongly red-shifted photoluminescence. When the films were excited, a monomer emission at 590 nm along with a second emission peak at 680 nm was observed. A close relation between the dye concentration and the emission showed that a new emission at 680 nm corresponds to the dimer emission. Circular dichroism (CD) spectroscopy reveals that a fraction of the dimers exist in a twisted dimer configuration. Stable, long-lived, and quenchable fluorescence with high quantum yield is attributed to this dimer emission.



### 6.1 Introduction

Organic dyes such as oxazines, rhodamines, cyanines, and merocyanines are used as energy transport medium in various applications including optoelectronic devices, light harvesting antennas, photography, and dye lasers.<sup>[1,2]</sup> Monomer emission is strongly diminished when surrounded by aggregate trap states (aggregation-caused quenching, ACQ).<sup>[3]</sup> Absorption and fluorescence of these dye molecules in different molecular configurations (dimers, H- or J-type) are dictated by the net transition dipole moments of the optical transitions between ground state  $S_0$  and excited state  $S_n$  and largely follow Kasha's rule.<sup>[4]</sup> In homodimers and H-aggregates, the net transition dipole moment is zero, which renders them nonfluorescent. However, transitions to/from the excited ( $S_1'$ ) state are fully forbidden only for a perfect parallel or antiparallel alignment of dye molecules.<sup>[5]</sup>

It is highly desirable in this context to learn more about H-aggregate dimer trap states and their role in excited-state deactivation in organic amorphous films. Highly luminescent



H-aggregates and dimers have been reported in solution<sup>[6–8]</sup> and thin films.<sup>[9,10]</sup> This phenomenon was ascribed to the small distortion between two dye molecules along the chromophore axis resulting in the rotational twist ( $\alpha$ ) by 10°. Rigidification of these twisted dye molecules in the solid state can result in an enhancement of fluorescence,<sup>[11]</sup> obviating the effect of ACQ and forbidden transitions.

Cyanines, rhodamine, and rubrene have shown anomalous photoluminescence (PL) bands in the solid state.<sup>[12–14]</sup> For example, PL was studied for pseudoisocyanine dyes adsorbed into microcrystalline cellulose.<sup>[12]</sup> Upon excitation at 532 nm, a new emission peak at 680 nm was observed in these films along with a monomer emission (620 nm). The emission intensity scaled well with the dye concentration and excitation intensity. The authors hypothesized that the emission at 680 nm could be due to dimer formation at high laser fluences. In contrast to this, there are also reports indicating triplet formation in cyanine dimers, which can lead to this second emission.<sup>[15–17]</sup> Similarly, the formation of excimers has been observed.<sup>[18]</sup> It is still unclear what the underlying mechanisms are for additional emission bands in the films.

In the present study, a detailed investigation is carried out using different spectroscopic techniques such as electron spin resonance (ESR), CD, and fluorescence to identify the origin of an unexpected emission in the Cy3 dye 1,1'-diethyl-3,3',3'-tetramethylcarbocyanine. In the thin film, an emission band at 680 nm (red-shifted by 100 nm from the monomer band) is significantly more intense than the monomer emission. However, this emission is not observed in solution. Our investigations support the hypothesis that the second emission originates from dimers in the sample that are present in a twisted dimer configuration. The fraction of dimers in that configuration is low. Guidelines for achieving high quantum efficiency of dimers compared to the normal monomer emission and the possibility to harvest this emission is presented. The development of efficient solid state emitters is a prospering research field as a result of the numerous technological applications employing luminescent materials in thin films.<sup>[19]</sup>

## 6.2 Results and Discussion

Cy3 dyes with different counterions like  $\Delta$ -TRISPHAT (Cy3-T), iodide (Cy3-I), hexafluorophosphate (Cy3-P), and tetraphenyl borate (Cy3-B) were coated from suitable solvents to prepare thin films. Cy3-T in chlorobenzene (CB) gives a monomer absorption peak at 559 nm and a vibronic peak at 526 nm (Figure 6.1a). Upon excitation at 550 nm, an emission was observed at 572 nm, which is assigned to monomer fluorescence in solution. Spin-coated films prepared from the same dye solution show monomer and dimer absorptions at 577 and 529 nm, respectively. In the PL spectra, the peak at 588 nm is assigned to monomer emission. In solution and in films, a vibrational shoulder to the monomer peak was observed at higher wavelength. However, the dye films show a strong dimer emission at 680 nm, which is red-shifted from the monomer peak.

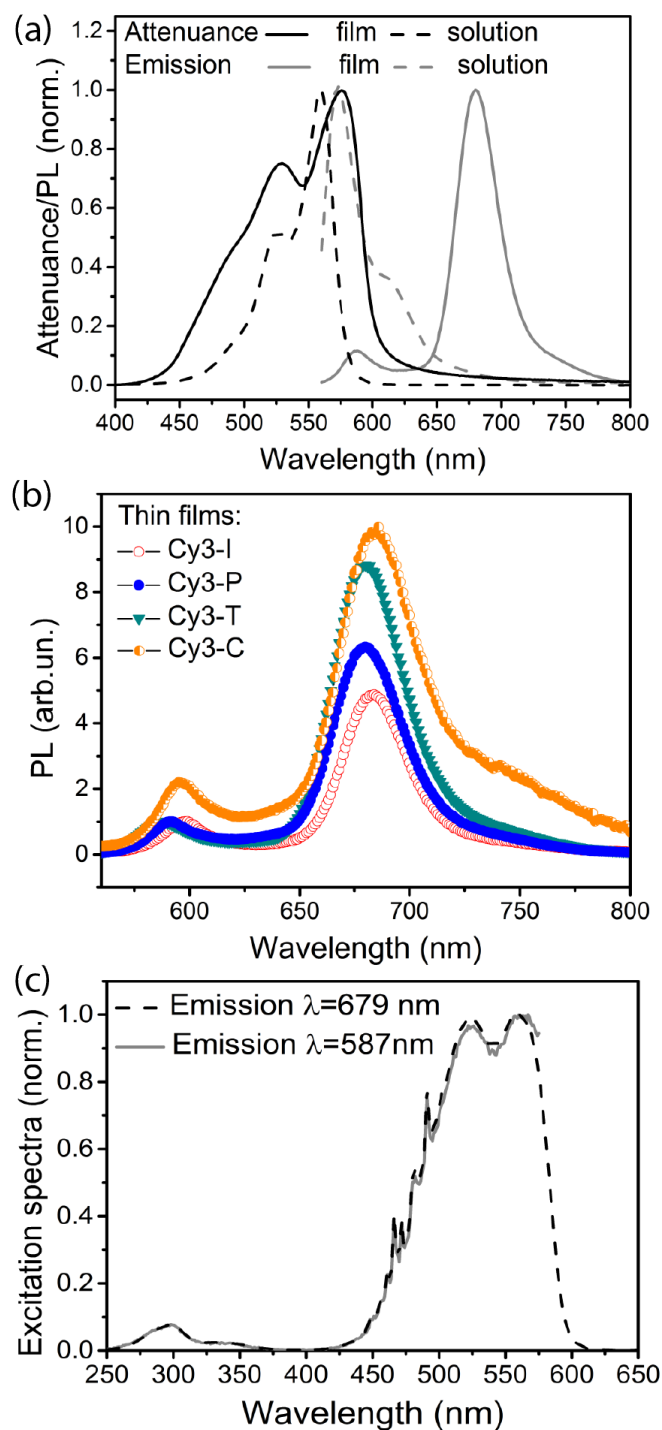


Figure 6.1 – Attenuance and PL spectra for Cy3-T in CB solution and spin-coated film (a). PL spectra from cyanine films with different counterions (b). Excitation spectra for Cy3-T films when emission was monitored at the monomer (587 nm) and dimer (679 nm) peak (c).

The dimer emission peak (680 nm) was present in all the cases, irrespective of the counterion (Figure 6.1b). However, the intensity of the dimer emission peak differs with counterion although any determinant role of counterion toward the dimer emission peak can be excluded. In addition to the counterion, the nature of the heteroaromatic moiety may also influence the dimer emission (see Figure S1).

The ratio of the intensities of the two emissions did not change when the excitation wavelength was varied from 450 to 580 nm. Also, the excitation spectra acquired at 587 and 679 nm are similar (Figure 6.1c). The latter double peak corresponds to the absorption spectra of monomer and dimer. From this observation, it can be concluded that we are dealing with an excited state process.

The absorption spectrum and excitation spectra obtained for both monomer and dimer emissions resemble each other, but the ratio of the intensities of the two bands differs. While in absorption the main band is more intense than the dimer band, in excitation the bands have similar intensities. The disparity between the absorption and excitation spectra arises because UV-vis measurements (Figure 6.1a) record a ground state absorption process while the excitation spectra (Figure 6.1c) are acquired in the excited state. The latter case also probes energy exchange between both monomer and dimer. This will show different amounts of monomer and dimer species, on comparing the excitation and absorption spectra. As the population of the emissive dimer species is not the only deactivation pathway, the fraction of emissive dimers cannot be quantified. But direct excitation of the dimer emission cannot be observed, indicating a low fraction of the latter. Although dimer emission (in parallel arrangement) is generally optically forbidden, it can be hypothesized that the distortion of the molecule can break the selection rule that forbids transition, giving rise to an emission. Emission from the *trans*-triplet state of a structurally very similar dye has been measured in methanol at 77 K and found to be around 722 nm.<sup>[20]</sup> This emission is significantly more red-shifted than the dimer emission in this work and represents one of many arguments against triplet emission as an explanation.

For all dyes, at temperatures between 77 and 300 K, no paramagnetic species were identified by ESR or LESR either in *g* close to 2 (singlet) or 4 (triplet). However, the measurement of dye Cy3-T at 6.5 K under illumination showed the presence of two ESR signals attributed to cationic and anionic dyes. Again, no triplet signals could be observed (*g* close to 4). The signals were weak with *g* = 2.0026 and line width of 0.6 mT from the anion and *g* = 2.0023 with line width of 2.3 mT from the cation. The origin of the signals is attributed to charge transfer of the photoexcited electron or hole between dye molecules generating paramagnetic species, cations, and anions. This observation was possible due to the effects of low temperature. At 6.5 K the photogenerated charges have relatively long recombination times and thus are more stable. This result also indicates that no triplet state is generated.

Determining the effect of temperature on emission signals can assist in analyzing the spectra. For example, triplet population is generally a temperature-dependent phenomenon.<sup>[21]</sup> In

addition, cis–trans isomerization of the molecules is hindered at lower temperatures. Spectra were measured while the samples were cooled by adiabatic compression from room temperature (RT) to 92 K. Spectra were also taken during the warm-up phase back to RT and then during heating to 340 K. The samples were excited at 480 nm, and the two emission peaks at 600 and 680 nm were observed (Figure 6.2a). Upon cooling, in the range from 300 to 180 K both peaks increase in intensity. Between 180 and 92 K, the monomer peak intensity increases while the second emission decreases (Figure 6.2a,b). The cooling–heating cycle shows some hysteresis. Upon heating, between 92 and 120 K (Figure 6.2c), both peaks initially decrease in intensity. The intermediate heating regime where the monomer emission decreases and the second peak emission increases are evident between 130 and 240 K (Figure 6.2d). Between 290 and 340 K again both peak intensities decrease in intensity (Figure 6.2e). Outside of the intermediate cooling and heating regime, the sample shows a regular temperature response: fluorescence increases with decreasing temperature because nonradiative processes become less effective. The unusual temperature response of the second emission in the intermediate temperature range is consistent with a model where thermal motion of the molecule annuls the geometrical restrictions that makes the  $S_1'-S_0$  transition impossible. Alternatively, the energy transfer to the emissive species can also be temperature dependent. The regular monomer emission undergoes an irreversible red-shift during the cooling cycle. It was also observed that the monomer emission is composed of two peaks that we identified as 0–0 and 0–1 (vibrational) transitions. Upon cooling to 92 K (Figure 2c), the vibronic shoulder becomes stronger in intensity causing the red-shift. This effect requires further attention and could be related to an isomeric phase transition that the molecules undergo during thermal excursion favoring the 0–1 transition. The second emission remains unaffected.

Dimerization in thin films cannot be avoided by spin-coating the dye from more dilute solutions. Dimer formation could be reduced by dispersing the Cy3-P dye at different concentration of 2, 1, 0.5, 0.05, 0.02, and 0.01 wt % in a PVME polymer matrix. Absorbance measured on the spin-coated films is shown in Figure S6.2. Reduced dimerization is observed in samples with lower dye content (0.01 and 0.02 wt %). The samples were placed into an integrating sphere and excited within the monomer absorption band.

The intensity of the dimer emission (680 nm) increases with increasing dye concentration as shown in Figure 6.3a. At the lowest dye concentrations (0.01 wt %), significant monomer emission was detected, which decreases when increasing the dye concentration. Above 0.5 wt %, monomer emission is fully quenched. The remaining small peak at 590 nm could originate from the vibronic peak or is due to energy exchange between dimer to monomer. At low dye concentrations, monomer emission is high because the monomers are not surrounded by dimers that would quench the emission. Increasing the dye concentration increases the probability for energy transfer from an excited monomer to a dimer, resulting in a strong dimer emission. When the emission intensity is normalized by the dye concentration, emission from both monomer and dimer is strongly concentration dependent in the low concentration regime, signifying the importance of dilution (Figure 6.3b). In the high concentration regime, the dimer emission is nearly constant. The fraction of dimers that are emissive remains

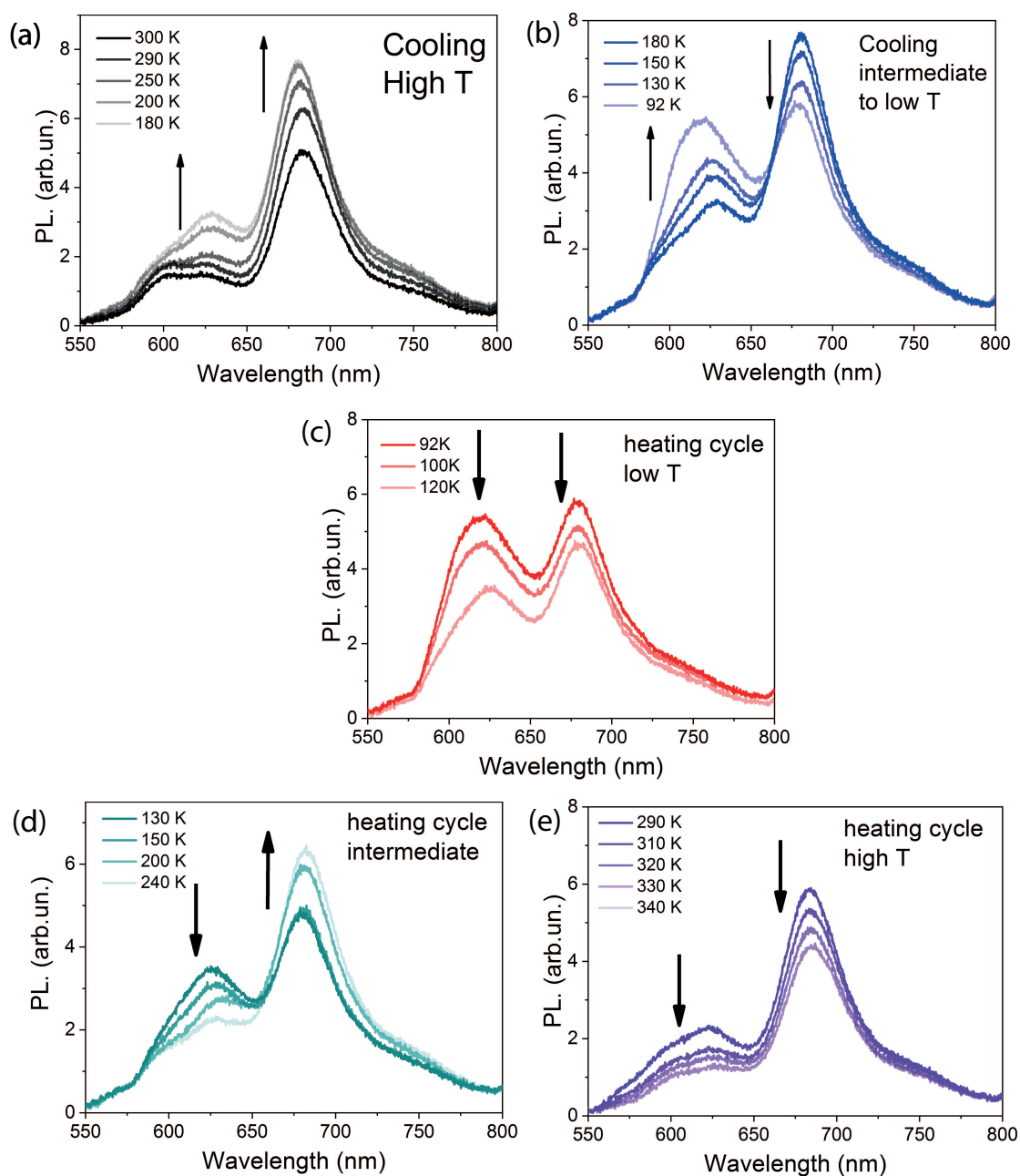


Figure 6.2 – Temperature-dependent fluorescence studies of the cyanine films (Cy3-T) recorded from 92 K to room temperature on cooling (a, b) and on heating (c, d, e).

constant with dye concentration. The deviation from proportionality with dye concentration above 1 wt % is due to H-aggregate formation that quenches the emission further.

As hypothesized above, the reason for dimer emission could be the twisting of molecules against each other in the film. In that case, the excited states can obtain rotatory strength. In the CD spectrum, exciton coupling can be displayed as classic Cotton effect, with positive and negative contributions at different energies.<sup>[22,23]</sup> The films described here show signatures from H-aggregate and dimer configurations and are thus not easy to interpret (Figure 6.3c). At low dye concentrations, the signal is positive in the H-aggregate and dimer absorption region. Increasing the dye concentration to 1 wt %, the dimer signal turns negative, while the H-aggregate has a bisignate signal with a positive contribution at lower wavelength and a negative contribution at higher wavelength (merging with the dimer signal). The samples with high dye concentration (2 wt %) in the PVME matrix showed a strong negative signal (510 nm) at the dimer peak position (Figure 6.3c) but no positive contribution from the H-aggregate. This negative signal in the dimer position was observed irrespective of the matrix, i.e., when the dye was dispersed in a PMMA matrix (see Figure S3) during preparation of the thin films. Buss<sup>[24]</sup> reported a similar observation when dispersing cyanines in  $\gamma$ -cyclodextrin in solution. With decreasing dimer concentration, the CD signal showed a transition from negative to positive apex. This behavior was explained by proposing that the dimers were trapped with a twisted sandwich configuration in the matrix. A similar observation here validates our hypothesis that dimers are twisted in oblique configuration in the films.

We can only speculate on the different molecular configurations of the dyes at different degrees of packing. However, the signals observed in the negative or positive apex of the dimer peak position indicate that some dimers are packed such that they become optically active, which results in different absorption of light in right-circular and left-circular directions. This difference in absorption also indicates that the net transition dipole moments are not parallel unlike the normal transition in the classical dimers. Therefore, a small resultant transition dipole moment results in absorption of light along with fluorescence.

An equally viable reason for the role of excimer is the twisting of molecules in the excited state. The difference between a twisted dimer and an excimer can be resolved with the following argument: If indeed a stable excimer (excited dimer) configuration existed, it would give rise to much broader and unstructured band.<sup>[25]</sup> However, this is not observed in our study, as shown in Figure 6.3a where the dimer emission is narrow with a vibronic band in the film. This supports the role of molecular twisting which is preserved in films and not in solution. The lifetime of the dimer emission peak was always longer than the monomer emission peak. For instance, in the case of Cy3-T films, the monomer shows a lifetime of 0.085 ns, whereas the dimer shows a lifetime of 1.069 ns. The lifetime of the dimer emission peak in Cy3-P was 0.668 ns (Figure 6.4). Because of the limited resolution of the instrument (100 ps), the direct Cy3-P fluorescence could not be measured (lifetime around 50 ps).<sup>[26]</sup> Thus, the lifetime of the dimer emission is approximately 1 order of magnitude longer than the monomer emission. The dimers are more stable in the presence of oxygen as detailed in the Figure S6.4, SI.

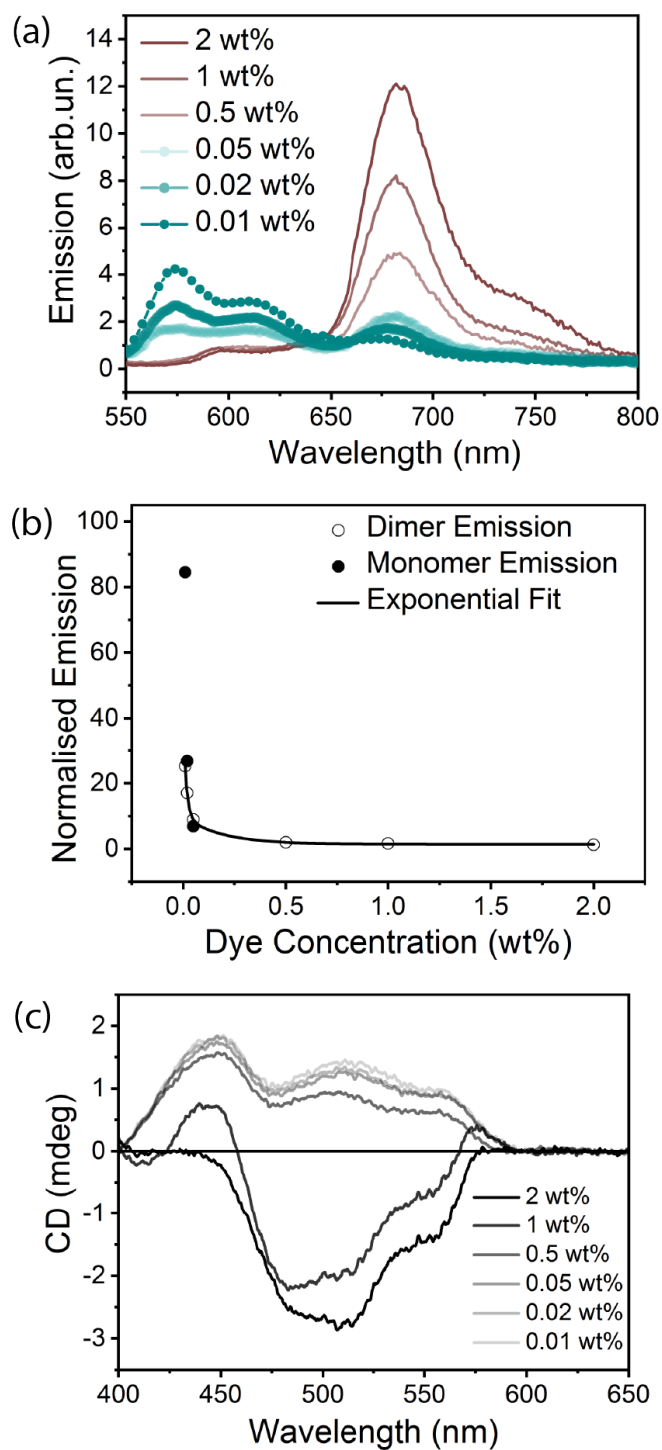


Figure 6.3 – Emission spectra for different concentrations of Cy3-P dye dispersed in a PVME matrix (a). The dimer and monomer emission are normalized with the dye concentration in the PVME matrix (b). Circular dichroism (CD) spectra for different concentration of Cy3-P dye dispersed in the PVME matrix (c).

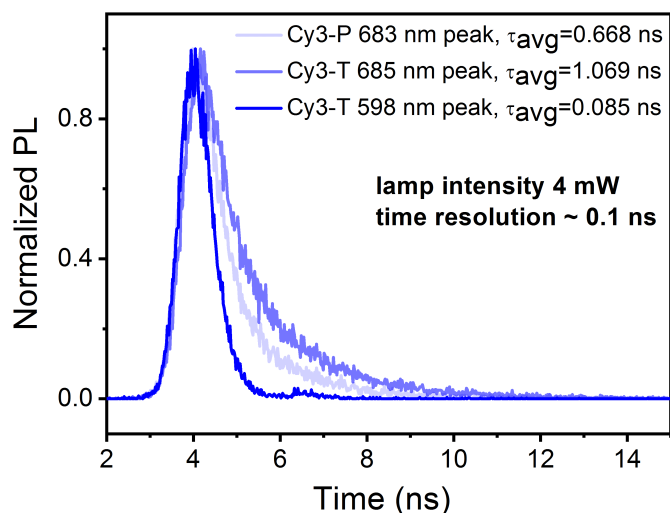


Figure 6.4 – Lifetime measurement for the monomer and dimer emission from Cy3-T and Cy3-P spin-coated films.

Fluorescence quenching is a powerful tool to measure exciton diffusion lengths and also to assess whether the excitons are diffusive or localized species.<sup>[27]</sup> Two experiments were performed on a model system for a doped dye film and a bilayer device. In the first experiment, the dye layer was blended with NOPF<sub>6</sub> at different concentrations.<sup>[28]</sup> In the second experiment, a C<sub>60</sub> fluorescence quenching layer was deposited on top of dye layers of different thickness. The sample was illuminated from the dye side. Both materials have been shown to quench both emissions, but the dimer emission is expected to be quenched more efficiently, as during its longer lifetime it has a higher probability to react with the quenching site.

The results of the first experiments show that when the dye film is p-doped at the lowest doping (NOPF<sub>6</sub>/Cy3-P = 0.05), the dimer emission is already fully quenched, whereas the monomer emission is only fully quenched at NOPF<sub>6</sub>/Cy3-P = 1 (Figure 6.5a). In addition, the film morphology changes upon heavy doping. In the second experiment, the fraction of the unquenched emission of monomer to dimer increased as the dye film became thinner (Figure 6.5b).

This observation supports the proposal that the dimer emission is quenched more efficiently than the monomer emission. The second experiment suggests that the excited emitting dimer state is localized near the C<sub>60</sub> interface while the monomer exciton is allowed to diffuse. As the dye film thickness increases (30 and 55 nm), the fraction of quenched emitting dimers decreases. For very thick films (100 nm, not shown here), the light absorption region moved away from the dye/C<sub>60</sub> interface, and the emission behavior of pure Cy3 films was recovered. On the other hand, thinner films (20 nm) show a stronger decrease in dimer emission than monomer. The ratio of monomer to dimer unquenched emission (as shown in the inset, Figure 6.5b) first decreases exponentially as a function of dye film thickness but then approaches a maximum value. The data are consistent with a model where the second emission is quenched



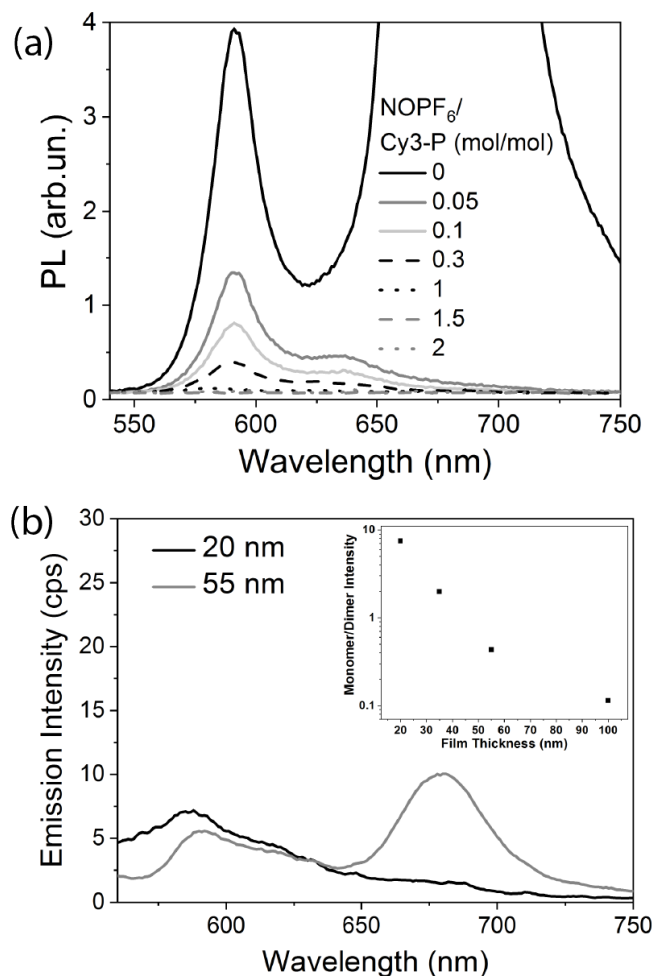


Figure 6.5 – Blends of NOPF<sub>6</sub>/Cy3-P show that the dimer is quenched more efficiently than the monomer emission (a). Nonquenchable emission intensity from Cy3-P films spin-coated on C<sub>60</sub> decreases with increase in the film thickness. The ratio of monomer to dimer intensity with film thickness is shown in the inset (b).

very efficiently only from localized sites next to the C<sub>60</sub> interface, while the monomer emission is more efficiently quenched over a large distance through the film (exciton diffusion). At 100 nm (not shown here) dye film thickness, the sample shows the pure dye layer behavior as no light is absorbed near the quenching sites. The typical quantum efficiency in a thin cyanine film with only monomer emission is around 1.5%, while the dimer emission alone contributes 8.5%.<sup>[29]</sup> Also, the dimer emission decreases exponentially with the dye concentration in solid matrices (Figure 6.3b). Given the assumption that there is a low fraction of emitting dimer species, concentration quenching can be overcome leading to higher quantum yield. We propose that this sets a lower limit to the concentration of emitting dimer species. Assuming half of the dye molecules are assembled into a dimer, and the transfer rate from monomer to dimers as well as fluorescence quantum efficiency is near 100%, a high estimate of the fraction of emissive dimers could be 10%.

### 6.3 Conclusion

A red-shifted PL band in thin film samples of a cyanine dye was observed and arises from a low fraction of dimers that are present in a twisted configuration. Without this twisted configuration the net transition dipole moment would be zero. The existence of these states is confirmed by CD measurements. Dispersing either monomer or dimer in a matrix at low concentration can be a means to overcome selfquenching resulting in strong fluorescence, as observed in this study. Temperature-dependent emission shows that dimer-to-monomer emission is dominant at room temperature and weak at low temperatures. Also, the lifetime of the dimer in the excited state is longer than for the monomer, more stable in the presence of oxygen and quenchable at room temperature, which satisfies the most important prerequisites for application in devices. We propose that engineering the molecular stacking in the film and harvesting this strong fluorescence as demonstrated in this study can overcome the limitation of ACQ to improve the performance of the devices built with cyanine dyes.

### 6.4 Experimental Section

**Materials:** Trimethine cyanine dyes (Cy3) 1-ethyl-2-[3-(1-ethyl-1,3-dihydro-3,3-dimethyl-2H-indol-2-ylidene)-1-propen-1-yl]-3,3-dimethyl-3H-indolium with the counterions hexafluorophosphate (Cy3-P), iodide (Cy3-I), and tetraphenylborate (Cy3-B) were procured from FEW Chemicals, Germany. Two counterions, perchlorate (Cy3-C) and  $\Delta$ -TRISPHAT (Cy3-T), accompanying the same chromophore were synthesized in our laboratory as reported elsewhere.<sup>[29]</sup> Trimethine dyes 3-ethyl-2-[3-(3-ethyl-3H-benzothiazol-2-ylidene)propenyl]benzothiazol-3-ium perchlorate and 3-ethyl-2-[3-(3-ethyl-3H-benzooxazol-2-ylidene)propenyl]benzothiazol-3-ium perchlorate were purchased from FEW Chemicals, Germany.

The purity of the synthesized dye were verified by NMR spectroscopy (not shown here). The highest purity dyes procured from FEW chemicals showed similar results. Suitable solvents

were chosen to dissolve the dyes along with two different polymers, either poly(methyl vinyl ether) (PVME) or poly(methyl methacrylate) (PMMA), separately.

**Film Formation:** Glass substrates were cleaned in acetone, ethanol, and Hellmanex solutions before spin-coating with the dye solution. The dye solution was spin-coated at 2000 rpm for 2 min on glass substrate to obtain a homogeneous film. For fluorescence quenching studies, the dye was blended with NOPF<sub>6</sub> in the solution and spin-coated on the glass substrates.

**Characterizations:** The absorption spectra for the films were acquired using a Varian Cary 50 UV–vis spectrometer. Fluorescence spectroscopy (Horiba Jobin Yvon Fluorolog equipped with integrating sphere) was used to obtain the excitation and emission scans from the dye films. Fluorescence quantum efficiencies were measured following the procedure of deMello.<sup>[30]</sup> Fluorescence quenching was studied for the films deposited from the blend of dye/NOPF<sub>6</sub> to determine the characteristics of energy transfer. Subsequently, temperature-dependent fluorescence studies were conducted for the dye films to determine the role of a thermally activated process in the emission. Spin-coated films were mounted into a self-built cooling station facilitated with an adiabatic compression cooling to reach the desired temperature. Fluorescence signals were collected at different intervals while monitoring the substrate temperature when cooling and heating the sample between room temperature and 92 K. The lifetime of the emission signal was monitored at room temperature using the Quantaaurus–Tau fluorescence lifetime spectrometer from Hamamatsu Photonics, K.K. Japan. A xenon lamp source with lamp intensity of 4 mW was used to excite the film at different wavelengths, and fluorescence signals were collected with a time resolution of 0.1 ns. The lifetime and emission wavelength can be used to classify the role of different species present in the film. To further understand the stability of the signals to light and oxygen, the processed films were kept in a nitrogen environment and stored in the dark and in daylight separately for 30 days. At different time intervals, the emission from these samples was monitored to determine the stability of the emitting species. Circular dichroism spectroscopy (JASCO J-815 CD spectrometer) was used to characterize the spin-coated films at room temperature from 400 to 650 nm with a scan rate of 100 nm/min and pitch for 0.2 nm.

Cyanine dyes Cy3-I, Cy3-C, Cy3-P, and Cy3-T were studied by electron spin resonance (ESR) and by light-induced electron spin resonance (LESER) at temperatures from 77 to 298 K. In addition, Cy3-T was studied at a temperature of 6.5 K. For the LESER measurements with temperature between 77 and 298 K, a Miniscope MS300 spectrometer from Magnettech (X-band and 9.3–9.55 GHz) was used. For measurements at 6.5 K, a Bruker Elexsys E580 spectrometer (X-band) was used, and the temperature was controlled by a continuous flow of liquid Helium using an Oxford cryogenic system, model ITC503. The microwave power used was between 0.100 and 31.62 mW. Samples were illuminated by a 140 W xenon lamp from a Newport solar simulator using an AM 1.5 filter. The samples were illuminated inside the ESR

cavity. Diphenylpicrylhydrazyl (DPPH) with  $g = 2.0036$  was used as  $g$ -factor reference. The ESR spectra were simulated using the software EasySpin implemented in MATLAB (MathWorks, Inc.).

**Acknowledgements** We gratefully thank Prof. Dr. Raffaele Mezzenga and Ms. Wenjie Sun from ETH Zürich, for extending their support to access the CD spectroscopy in their lab. We acknowledge the financial support received from the Swiss National Science Foundation (SNF) Grants 200021-157135 and 200021-144120 for conducting this work. C.F.O.G. acknowledges the financial support from FAPESP (2013/07296-2) and CNPq.

## Bibliography

- [1] T. Kietzke, *Advances in OptoElectronics* **2007**, 1–15.
- [2] T. Tani, *Photographic Science Advances in Nanoparticles, J-Aggregates, Dye Sensitization, and Organic Devices*, Oxford University Press, **2011**.
- [3] S. Varghese, S. Das, *The Journal of Physical Chemistry Letters* **2011**, 2, 863–873.
- [4] M. Kasha, H. R. Rawls, M. Ashraf El-Bayoumi, *Pure and Applied Chemistry* **1965**, 11, 371–392.
- [5] R. W. Chambers, T. Kajiwara, D. R. Kearns, *The Journal of Physical Chemistry* **1974**, 78, 380–387.
- [6] U. Rösch, S. Yao, R. Wortmann, F. Würthner, *Angewandte Chemie International Edition* **2006**, 45, 7026–7030.
- [7] F. Würthner, S. Yao, *Angewandte Chemie International Edition* **2000**, 39, 1978–1981.
- [8] S. Zeena, K. G. Thomas, *Journal of the American Chemical Society* **2001**, 123, 7859–7865.
- [9] M. Matsui, S. Ando, M. Fukushima, T. Shibata, Y. Kubota, K. Funabiki, *Tetrahedron* **2015**, 71, 3528–3534.
- [10] Y. Chen, B. Lee, D. Fu, V. Podzorov, *Advanced Materials* **2011**, 23, 5370–5375.
- [11] F. Würthner, T. E. Kaiser, C. R. Saha-Möller, *Angewandte Chemie International Edition* **2011**, 50, 3376–3410.
- [12] L. F. V. Ferreira, A. S. Oliveira, F. Wilkinson, D. Worrall, *J. Chem. Soc. Faraday Trans.* **1996**, 92, 1217–1225.
- [13] M. L. Ferrer, F. del Monte, D. Levy, *Langmuir* **2003**, 19, 2782–2786.
- [14] Z. Chen, A. Lohr, C. R. Saha-Moller, F. Wurthner, *Chemical Society Reviews* **2009**, 38, 564–584.
- [15] A. K. Chibisov, *High Energy Chemistry* **2007**, 41, 200–209.
- [16] A. Ferencz, D. Neher, M. Schulze, G. Wegner, L. Viaene, F. C. De Schryver, *Chemical Physics Letters* **1995**, 245, 23–29.
- [17] M. Asano-Someda, T. Ichino, Y. Kaizu, *The Journal of Physical Chemistry A* **1997**, 101, 4484–4490.

## Bibliography

---

- [18] A. V. Sorokin, B. A. Gnap, I. I. Bessalova, S. L. Yefimova, Y. V. Malyukin, *Journal of Luminescence* **2016**, 179, 171–177.
- [19] J. Mei, Y. Hong, J. W. Y. Lam, A. Qin, Y. Tang, B. Z. Tang, *Advanced Materials* **2014**, 26, 5429–5479.
- [20] K. Jia, Y. Wan, A. Xia, S. Li, F. Gong, G. Yang, *The Journal of Physical Chemistry A* **2007**, 111, 1593–1597.
- [21] A. Köhler, H. Bässler, *Materials Science and Engineering: R: Reports* **2009**, 66, 71–109.
- [22] S. F. Mason, *Journal of the Chemical Society Chemical Communications* **1973**, 239–241.
- [23] N. Berova, L. D. Bari, G. Pescitelli, *Chemical Society Reviews* **2007**, 36, 914–931.
- [24] V. Buss, *Angewandte Chemie International Edition in English* **1991**, 30, 869–870.
- [25] M. Sims, D. D. C. Bradley, M. Ariu, M. Koeberg, A. Asimakis, M. Grell, D. G. Lidzey, *Advanced Functional Materials* **2004**, 14, 765–781.
- [26] J. De Jonghe-Risse, J. Heier, F. Nuesch, J.-. E. Moser, *Journal of Materials Chemistry A* **2015**, 3, 10935–10941.
- [27] R. R. Lunt, N. C. Giebink, A. A. Belak, J. B. Benziger, S. R. Forrest, *Journal of Applied Physics* **2009**, 105, 053711–7.
- [28] B. Fan, F. A. de Castro, J. Heier, R. Hany, F. Nüesch, *Organic Electronics* **2010**, 11, 583–588.
- [29] S. Jenatsch, L. Wang, M. Bulloni, A. C. Véron, B. Ruhstaller, S. Altazin, F. Nüesch, R. Hany, *ACS Applied Materials & Interfaces* **2016**, 8, 6554–6562.
- [30] J. C. de Mello, H. F. Wittmann, R. H. Friend, *Advanced Materials* **1997**, 9, 230–232.

## 6.5 Supporting Information

### S1. Non-emissive dimers

Structural motifs dictate the molecular packing thereby influencing the dimer emission. This is because of the well-known reasoning that modifying the quinoline ring in a cyanine dye can affect the aggregation nature.<sup>[S1,S2]</sup> To verify this, we studied a Cy3 benzoxazol dye, where the dimethyl group is replaced by oxygen in the quinoline ring. The film forming properties of this dye are very poor, for that we dispersed the dye in a PVME polymer. In that matrix the dye shows even stronger dimer absorption (Figure S6.1a) compared to the other Cy3 dyes shown earlier in this study. When excited at the dimer wavelength (520 nm), the film shows a small monomer emission but no second emission was observed (Figure S6.1b). Introducing oxygen in the motif will decrease the steric hindrance for parallel alignment of the dye molecules, thereby reducing the torsional angle between dimers, prohibiting potential emission from the dimer. Conversely, we can say that the presence of hydrocarbon chains induces strong dimer emission. This goes in hand with the observation by Sorokin et al.,<sup>[S3]</sup> where a long hydrocarbon tail in the DiI dye has shown a strong dimer emission. This observation looks still valid, on comparing the LB films studied by Debnath et al.,<sup>[S4]</sup> where excimers are observed even in a monolayer film. From this observation, we argue that long hydrocarbon chains can have strong interaction with the neighboring dye molecules, leading to more unique way of packing the molecules. To see whether changing the polymer matrix can help in dispersing this dye, we chose PMMA, which has better dispersion properties than PVME. It can be seen from Figure S6.1b, the dispersing matrix has no effect in tuning the second emission. Furthermore, this point was verified by choosing another dye by replacing oxygen with sulphur (benzothiazol), which confirms that the non-emissivity is not due to internal quenching. Therefore, we can conclusively say that structural motifs can influence the dimer emission.

### S2. Stability of monomer and dimer emission in the influence of light and oxygen

Having said that the second emission peak obtained in the film can have longer lifetime than a monomer emission, the atmosphere in the film storage can also influence the lifetime. If this is due to a triplet emission, atmospheric oxygen can also quench the fluorescence. To investigate this, the films were stored in dark and in daylight in the presence of oxygen. The monomer and dimer emission were monitored periodically for 30 days. It was observed that when samples were preserved in dark and in the presence of oxygen, the emission measured for 30 days is almost within the standard deviation of the light signal of the instrument (Figure S6.4a). We can say that the second emission signal is stable in the presence of oxygen, which again disowns the role of triplet state. However, when exposed to daylight and in the presence of oxygen, the intensity of both monomer and dimer decreases (Figure S6.4b). This can be due to accelerated photobleaching of cyanine dyes in the presence of oxygen and light. Finally, this shows that samples preserved in dark has a stable dimer emission.

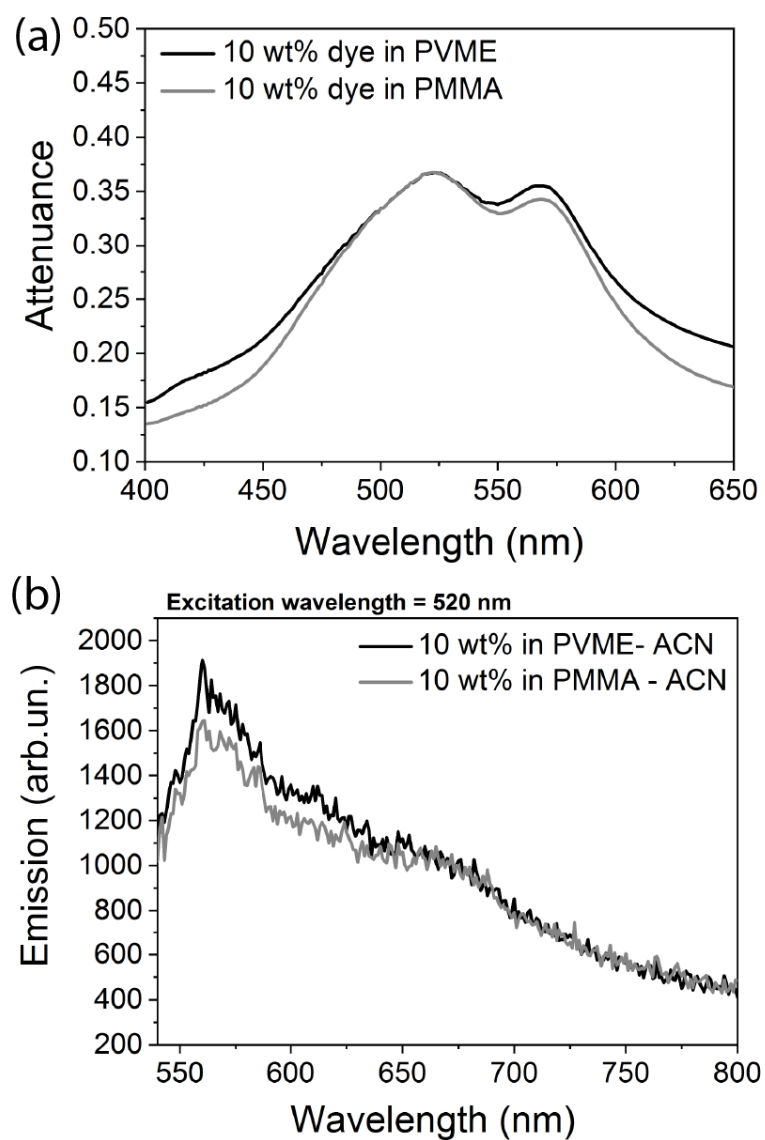


Figure S6.1 – Attenuance (a) and emission (b) of non-emissive dimers.



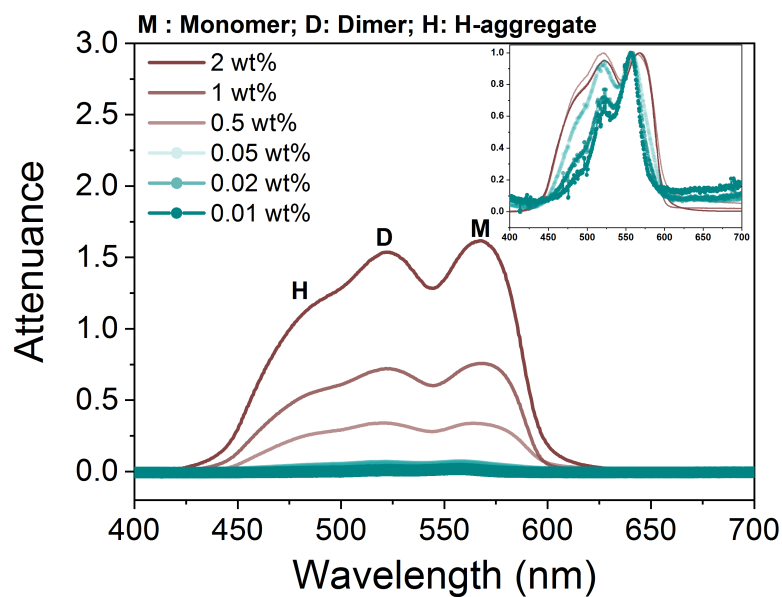


Figure S6.2 – Attenuance for different concentrations of Cy3-P dye dispersed in a PVME matrix.

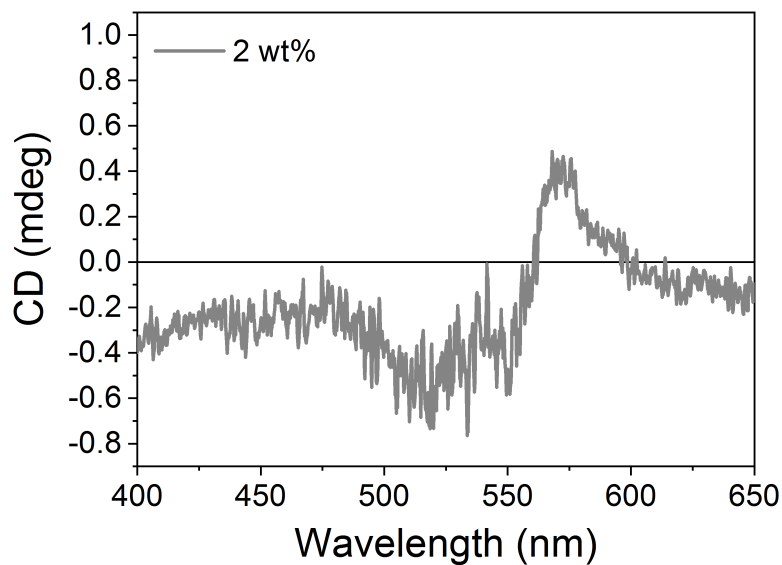


Figure S6.3 – Circular dichroism (CD) spectroscopy for 2 wt% of Cy3-P dye dispersed in the PMMA matrix.

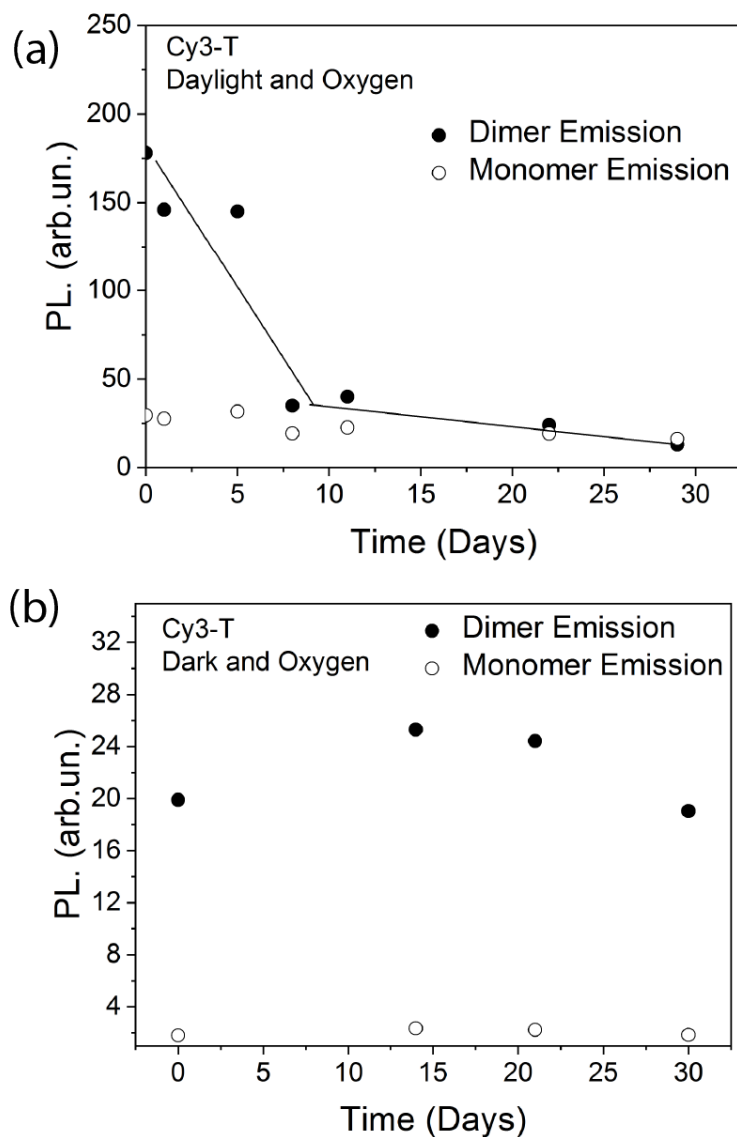


Figure S6.4 – Stability study of the dimer and monomer emission peak from Cy3-T dye films monitored for 30 days when preserved in dark (a) and in daylight (b) in the presence of oxygen. The line is guide to the eye.

### Subbibliography

[S1] Mobius, D., *Adv. Mater.* **1995**, 7, 437-444.

[S2] Matsui, M.; Ando, S.; Fukushima, M.; Shibata, T.; Kubota, Y.; Funabiki, K., *Tetrahedron* **2015**, 71, 3528-3534.

[S3] Sorokin, A. V.; Gnap, B. A.; Bepalova, I. I.; Yefimova, S. L.; Malyukin, Y. V., *Journal of Luminescence* **2016**, 179, 171-177.

[S4] Debnath, P.; Chakraborty, S.; Deb, S.; Nath, J.; Bhattacharjee, D.; Hussain, S.A., *J. Phys. Chem. C* **2015**, 119, 9429-9441.



## 7 Conclusion and Outlook

The next generation optoelectronic devices using organic semiconductors demand coherent exciton migration in thin films and high photoluminescence quantum yield (PLQY) for light harvesting and light emitting devices, respectively. Although J-aggregates are well-known for coherent coupling of dye molecules favoring exciton migration and narrow emission linewidth, growing 2D J-aggregates with high PLQY has been a missing link in realizing efficient optoelectronic devices. Addressing the fundamental challenges from the viewpoint of growing high quality J-aggregate thin films to overcome exciton quenching sites can be one approach. This thesis work follows this approach in a systematic way, by growing 2D J-aggregate thin films to suppress non-radiative decay channels, improving the J-aggregate PLQY in solution and realization of narrowband photodetector with a prototype demonstrating additive manufacturing capability. In chapter 2, a new growth route with controlled phases (monomers and J-aggregates) in solution is shown to result in large coherent J-aggregate domains in thin films. The large coherent domains suppressing non-radiative recombination of excitons at the grain boundaries and increasing the PLQY were evident from the photoluminescence studies. A direct correlation established here between the crystalline order and PLQY at room temperature is in agreement with temperature dependence studies. An increase in relative quantum yield from twofold (300 K) to sevenfold (6 K) due to reduced exciton-phonon coupling was observed. Using time-resolved photoluminescence spectroscopy, the charge-exciton quenching was identified to be an additional non-radiative decay channel impeding exciton migration in thin films. As the results from this chapter explain growth mechanism and the exciton dynamics in J-aggregate thin films, it opens new ideas for further studies. Benefitting from the large micron-scale dimension of the 3D J-aggregate crystals with high PLQY, a next step could be to selectively functionalize the substrate to grow J-aggregates for organic light-emitting transistors (OLETs). Furthermore, the exciton migration length can be estimated from exciton-exciton annihilation studies or using super resolution fluorescence microscopy.

Although the PLQY of J-aggregate thin films was improved to ~5% at room temperature by overcoming the grain boundary quenching, further improvements focused on studying the PLQY of J-aggregate solutions as described in Chapter 3. Upon addition of alkylamines to

pristine J-aggregate solutions, a drastic improvement in PLQY from ~5% to ~60% was achieved. Addition of dye to alkylamines showed a clear affinity between dye molecules and amine groups. Small-angle neutron scattering studies to probe the internal arrangement in a ternary system (dye-hexylamine-water) was achieved. Without dye molecules, the binary system (hexylamine-water) showed a local arrangement of water droplets confined in a hexylamine matrix with polar amine groups towards the water/hexylamine interface. Upon addition of dye molecules, the J-aggregates adhered mostly to the water/ hexylamine interface with monomers stabilized at the alkylchain ends. It can be concluded that monomers or dimers present at the edges of J-aggregate crystals can quench or inhibit exciton migration. Increasing the monomer stability at the alkyl chain edges compared to J-aggregate crystal edges can reasonably explain the enhancement in PLQY. With a careful assessment of dye structure and counter-ion influence, this approach to significantly enhance the PLQY of J-aggregate is believed to be extendable to other class of cyanine molecules demanding high PLQY. Moreover, it can be envisaged that by tuning the electrostatic stabilization between dye and alkylgroups to integrate with metal atoms can open new areas for applying high PLQY J-aggregates in the field of hybrid plasmonic devices.

In chapter 4, a true ultra-narrowband (FWHM <100 nm) absorbing material for narrowband photodetection with selective response from visible to near-infrared region was realized. A new approach was shown to alter the aggregation rapidly during spin-coating. By choosing suitable solvents like 2,2,2-trifluoroethanol, facilitates in-situ J-aggregate formation during solvent evaporation while dispersing them as monomers in solution. This approach to achieve a continuous J-aggregate film is important for good device performance, different from the previous approach followed in Chapter 2, to grow large coherent domains for exciton diffusion. From J-V, EQE and current noise results, this solvent engineering approach obviates the shunts in the device, improves  $J_{sc}$  complementing EQE and decreasing current noise, respectively. As this work recognized a route to achieve true ultra-narrowband photodetectors with an environmentally friendly solvent (water) process, the synergistic combination led to successfully demonstrate an inkjet printed device with even better figure of merits, signifying a substantial technological advancement. This demonstration can be appealing to a wide research community or industry seeking true narrowband photodetectors which are printable for large-scale without compromising the figure of merits. The remaining challenge in achieving a fully-printable photodetector lies in printing the buffer layer and top electrode. This challenge can be addressed in future work with a combination of aerosol and inkjet printing.

Exploring dendronized polymers (DP) for its wide range of process tunability in modifying the surface functional groups, its density on the poly-methacrylate backbone, and controlled chain length from DP generation, had added advantage to investigate DPs as 1D template for self-assembly of dye molecules and is described in Chapter 5. A common solvent (acetate buffer) identified to form cyanine J-aggregates in acidic pH (~4-4.5) while protonating the peripheral amines of DPs proved suitable to anchor J-aggregates on the DPs by a simple complexation route. This route is different from J-aggregates grown on well-known DNA templates, where a systematic anchoring of dimers forms a J-aggregate. The anchoring of

J-aggregates on dendronized polymer leading to stiffening of the polymer was clearly observed with small-angle x-ray scattering (SAXS) studies. Furthermore, the J-aggregate nanowires deposited on functionalized substrate showed a high quality of J-aggregates (high J-/M- ratio). With the advantage of depositing monolayers on substrates, studying exciton migration length will form the foundation to build excitonic transistors using J-aggregate nanowires. Moreover, dispersing these J-aggregate nanowires as highway excitonic channels in solar cells with monomers as matrix can benefit in efficiently transporting the excitons to a charge-transfer interface while broadening the absorption window from the monomers.

In chapter 6, the cyanine dye molecules dispersed in a polymer matrix helps overcome the forbidden dimer emission. A strongly red-shifted photoluminescence from the monomer peak emerges from cyanine thin films. Circular dichroism spectroscopy studies confirmed a twisted packing of dye molecules, which guarantees an optical allowed transition state. A longer exciton lifetime confirmed from TRPL studies, stability towards oxygen atmosphere and good energy transfer as a donor molecule (Cy-3P) to guest (NOPF<sub>6</sub>) even in small amount (0.05%) satisfies important pre-requisite for devices. An application of this result was followed in another work to achieve a good electroluminescence in organic light emitting electrochemical cells.





# Curriculum Vitæ

---

---

## Personal Details

Name Surendra Babu Anantharaman  
Address Zwinggartenstrasse 53, 8600 Dübendorf  
Telephone +41 77 956 4962  
E-Mail surendrababu87@gmail.com  
Date of Birth 1<sup>st</sup> February 1987 in Thiruvurur, India  
Nationality Indian  
Marital Status Single

---

## Education

01/2015 – till date **École Polytechnique Fédérale De Lausanne (EPFL), Switzerland**  
Ph.D Candidate, Materials Science and Engineering  
06/2009 – 06/2012 **Indian Institute of Technology Madras (IIT), India**  
M.S (By Research), Metallurgical and Materials Engineering  
08/2007 – 05/2009 **College of Engineering, Anna University, India**  
M.Sc, Materials Science  
08/2003 – 06/2007 **University of Madras, India**  
B.Sc, Physics

---

## Scholastic Achievements

12/2018 **US Patent** (US 10,145,371 B2) on Ultrahigh vacuum apparatus having a cryopump nanostructured material" by **Surendra Babu Anantharaman**, W.C. Yang, T.N. Kao, Victor Y. Lu, Wei Chin  
07/2018 Student Perspective Article on Hybrid solar cells and beyond: Spanning ceramics and organic molecules, published in **American Ceramics Society Bulletin**  
04/2018 **China Patent** (CN 104564597 B) for US 10,145,371 B2 patent family  
03/2017 Received funding from the **SNF funding scheme R'EQUIP** for the first joint proposal submitted on IR-AFM studies for phase separation in organic blends  
10/2016 – 12/ 2016 Recipient of **Swiss-Japan Researchers Exchange** under JSPS Program  
06/2009 – 06/2012 Recipient of **half-time research assistantship (HTRA)** from Department of Ministry of Human Resource Development, Government of India to conduct research during my MS at IIT Madras

---

## Research Experience

01/2015 – till date **École Polytechnique Fédérale De Lausanne (EPFL) and Swiss Federal Laboratories for Materials Science and Technology, Switzerland**

*Zwinggartenstrasse 53 – 8600 Dübendorf*  
☎ +41 77 956 4962 • ✉ surendrababu87@gmail.com

Thesis title (tentative)	Exciton Dynamics in 2D Organic Assemblies and Realization of Next-generation Opto-electronic Devices
Thesis Advisors	Prof. Frank Nüesch and Dr. Jakob Heier
Projects	<ul style="list-style-type: none"> <li>• To study the exciton dynamics in J-aggregate thin films at low temperatures using ultrafast spectroscopy (In collaboration with <b>IBM Zürich, Quantum Optics Research Lab</b>)</li> <li>• Suppressing the non-radiative decay channels has shown an unprecedented increase in PLQY to 60% at room temperature (In collaboration with <b>Paul Scherrer Institute</b>)</li> <li>• Understanding the dynamics of dendronized polymers conformation when interacting with J-aggregates in solution (In collaboration with <b>Laboratory of Polymer Chemistry, ETH Zürich</b> and <b>Center of X-ray analytics, Empa, St. Gallen</b>)</li> <li>• Developed ultranarrowband photodetectors with FWHM &lt; 20nm and inkjet printed a prototype using the facility at the <b>Coating Competence Center, Empa, Dübendorf</b></li> </ul>
07/2009 – 05/ 2012	<b>Indian Institute of Technology Madras (IIT), India</b>
Thesis title	Electrolyte Materials for Intermediate Temperature Solid-Oxide Fuel Cells (IT-SOFC)
Thesis Advisor	Prof. Ranjit Bauri
Projects	<ul style="list-style-type: none"> <li>• Developed oxygen-ion conductors for IT-SOFCs using rare earth oxides doped and co-doped ceria</li> <li>• Enhancing stability and protonic conductivity for rare earth doped perovskites</li> </ul>

## Work Experience

01/2015 – till date	<b>Swiss Federal Laboratories for Materials Science and Technology, Switzerland</b> Research Assistant
10/2016 – 12/ 2016	<b>Tokyo University of Agriculture and Technology (TUAT), Japan</b> Internship: Design and fabrication of nano-scale transistor for organic materials Supervisor: Prof. Takeshi Shimomura
11/2013 – 12/ 2014	<b>Indian Institute of Technology Madras, India</b> Project Associate: Developing environmental barrier coatings for SiC composites Supervisor: Prof. Ashutosh S. Gandhi
08/2012 – 10/ 2013	<b>Taiwan Semiconductor Manufacturing Company, Ltd. (TSMC), Taiwan</b> Process Engineering: Handling thin film fabrication in PVD, CVD and ALD tools Equipment Engineering: Developed new ideas to enhance the performance of ultra-high vacuum pumps.
07/2009 – 06/ 2012	<b>Indian Institute of Technology Madras, India</b> Half-time Research Assistant – Teaching Assistant for SEM and XRD labs for graduate students

## Publications

13. **Surendra B. Anantharaman**, D. Messmer, A. Sadeghpour, S. Salentinig, F. Nüesch, J. Heier. Excitonic channels from bio-inspired templated supramolecular assembly of J-aggregate nanowires, *Nanoscale*, **2019** 11, 6929-6938.

Zwinggardenstrasse 53 – 8600 Dübendorf

☎ +41 77 956 4962 • ✉ surendrababu87@gmail.com

12. **Surendra B. Anantharaman**, T. Stöferle, F. Nüesch, R. F. Mahrt, J. Heier. Exciton Dynamics and Effects of Structural Order in Morphology Controlled J-aggregate Assemblies, *Advanced Functional Materials*, **2018** (Accepted). **Features in the Cover Page.**
11. K. Strassel, A. Kaiser, S. Jenatsch, A. Véron, **Surendra B. Anantharaman**, E. Hack, M. Diethelm, F. Nüesch, R. Aderne, C. Legnani, S. Yakunin, M. Cremona, R. Hany, Squaraine Dye for a Visibly Transparent All-Organic Optical Upconversion Device with Sensitivity at 1000 nm, *ACS Applied Materials & Interfaces*, **2018** 10 (13) 11063-11069.
10. M. Makha, P. Schwaller, K. Strassel, **Surendra B Anantharaman**, F. Nüesch, R. Hany, J. Heier. Insights into photovoltaic properties of ternary organic solar cells from phase diagrams, *Science and Technology of Advanced Materials*, **2018** 19 (1), 669-682.
9. **Surendra B. Anantharaman**, V.B. Rajkumar, S. Raghunandan, K.C. Hari Kumar, R. S. Kumar, A.S. Gandhi. Role of Submerged Miscibility Gap in Phase Formation in Sol-gel Synthesis of Yttrium Silicates, *Journal of the European Ceramic Society*, **2017** 37 (15), 5001-5007.
8. **Surendra B. Anantharaman**, S. Yakunin, C. Peng, M. Vismara, C. F.O. Graeff, F. Nüesch, S. Jenatsch, L. Wang, R. Hany, M. Kovalenko, J. Heier . Strongly Red-Shifted Photoluminescence Band Induced by Molecular Twisting in Cyanine (Cy3) Dye Films, *J. Phys. Chem. C*, **2017** 121 (17), 9587–9593.
7. S. Jenatsch, L. Wang, N. Leclaire, E. Hack, R. Steim, **Surendra B. Anantharaman**, J. Heier, B. Ruhstaller, L. Penninck, F. Nüesch, R. Hany. Visible light-emitting host-guest electrochemical cells using cyanine dyes, *Organic Electronics*, **2017** (48), 77–84.
6. M. Makha, P. Testa, **Surendra B. Anantharaman**, J. Heier, S. Jenatsch, N. Leclaire, J.-N. Tisserant, A. Véron, L. Wang, F. Nüesch, R. Hany. Ternary semitransparent organic solar cells with a laminated top electrode, *Science and Technology of Advanced Materials*, **2017** 68 – 75. **Editor's choice.**
5. **A.S. Babu**, R. Bauri, G. S. Reddy. Processing and Conduction Behavior of Nanocrystalline Gd-doped and Rare Earth Co-doped Ceria Electrolytes, *Electrochimica Acta*, **2016** 209, 541-550.
4. **A.S. Babu**, R. Bauri. Phase Evolution and Morphology of Nanocrystalline BaCe<sub>0.9</sub>Er<sub>0.1</sub>O<sub>3</sub> Proton Conducting Oxide Synthesised by a Novel Modified Solution Combustion Route, *Journal of Physics and Chemistry of Solids*, **2015** 87, 80 – 86.
3. **A.S. Babu**, R. Bauri. Synthesis, Phase Stability and Conduction Behavior of Rare Earth and Transition Elements doped Barium Cerates, *International Journal of Hydrogen Energy*, **2014** 39, 14487-14495.
2. **A.S. Babu**, R. Bauri. Effect of Sintering Atmosphere on Densification, Redox Chemistry and Conduction Behavior of Gd-doped CeO<sub>2</sub> Electrolytes, *Ceramics International*, **2013** 39, 9421 – 9428.
1. **A.S. Babu**, R. Bauri. Rare Earth Co-doped Nanocrystalline Ceria Electrolytes for Intermediate Temperature Solid Oxide Fuel Cells (IT-SOFC), *ECS Transactions*, **2013** 57, 1115-1123.

Zwinggardenstrasse 53 – 8600 Dübendorf

☎ +41 77 956 4962 • ✉ surendrababu87@gmail.com

---

## Conferences

- 2018** EDMX Research Day 2018, EPFL – Surendra Anantharaman, T. Stöferle, F. Nüesch, R. F. Mahrt, J. Heier. Enhancing Solid-State Luminescence in Supramolecular Assemblies by Suppressing Non-radiative Decay - *Oral Presentation*
- 2018 MS&T, Columbus – Surendra Anantharaman et al., Role of submerged miscibility gap in phase formation in sol-gel synthesis of yttrium silicates - *Poster Presentation*
- 2018 MRS Spring Meeting & Exhibit, Arizona – Surendra Anantharaman, T. Stöferle, F. Nüesch, R. F. Mahrt, J. Heier. Enhancing the exciton diffusion in the supramolecular assemblies by suppressing the non-radiative decays - *Oral Presentation*
- 2018 MRS Spring Meeting & Exhibit, Arizona – Surendra Anantharaman, A. Verma, M. Makha, R. Hany, F. Nüesch, J. Heier. Inkjet-printed narrowband organic photodetectors with color selective responsivity - *Poster Presentation*
- 2018 ICSM, South Korea – Surendra Anantharaman, K. Strassel, M. Makha, R. Hany, F. Nüesch, J. Heier. Filter-free narrowband photodetectors with color selective responsivity - *Oral Presentation*
- 2018 ICSM, South Korea – Mohammed Makha et al., Phase Control in a Ternary oPV Blend System by Ionic Interactions and Correlation between Phase and Efficiency - *Oral Presentation*
- 2017** EMPA PhD Symposium 2017 – Surendra Anantharaman, T. Stöferle, F. Nüesch, R. F. Mahrt, J. Heier. Morphology Controlled Growth of 2D J-aggregate Films and Its Role on Exciton Diffusion - (*Oral Presentation*)
- 2017 International Conference on Physical and Theoretical Chemistry, Dublin. – Surendra Anantharaman et al., Strongly red-shifted photoluminescence band induced by molecular twisting in cyanine (Cy3) dye films (**Invited Oral**)
- SAOG 2017 – Surendra Anantharaman et al., Unravelling the Growth Mechanism of 2D J-aggregate Monolayers and Nanocrystals on Modified Surfaces - (*Poster Presentation*)
- 2016** 2016 ICSM, China – Surendra Anantharaman, Frank Nüesch and Jakob Heier. Growth and morphology of J-aggregates on solid substrates - *Poster Presentation*
- 2016 ICMST, Kerala, India – Surendra Anantharaman, Frank Nüesch and Jakob Heier. Unravelling the Growth Mechanism of 2D J-aggregate Monolayer and Nanocrystals on Modified Surfaces - *Oral Presentation*
- 2013** 2013 WHTC, China – A.S. Babu and Ranjit Bauri. Synthesis, phase stability and conduction behavior of co-doped and doped barium cerates - *Oral Presentation*

---

## Professional Activities

- 2017 – 2019 **American Ceramics Society (ACerS)** – President's Council of Student Advisors (PCSA) as Programming Committee Member representing EPFL in the ACerS

Zwinggertenstrasse 53 – 8600 Dübendorf

☎ +41 77 956 4962 • ✉ surendrababu87@gmail.com



